Terrain déformation du rift de Corinthe (Grèce) et ses environs, en utilisant l'interférométrie SAR

Elias Panagiotis




A dissertation of the Ecole Doctorale des Sciences de la Terre
(ED 109 – IPGP – Paris VII – ENS) and the University of Patras

Presented by:

Panagiotis ELIAS, MSc

For the degree of Doctor of Ecole Normale Supérieure, France

and the University of Patras, Greece

In the discipline of Geosciences

Ground deformation observed in the western Corinth rift (Greece) by means of SAR interferometry

Defended on June, 20, 2013 in front of a jury composed of:

Alex RIGO (Observatoire Midi-Pyrénées,Toulouse, France) .....Reporter

Daniel RAUCOULES(BRGM, Orléans, France) .....Reporter

Issaak PARCHARIDIS (Harokopio University of Athens, Athens, Greece).....Examiner

Pascal BERNARD (IPGP, Paris, France).....Examiner

Michel SEBRIER (CNRS, Université Paris VI, Paris, France).....Examiner

Sébastien ROHAIS (IFP Energies nouvelles, Rueil-Malmaison, France).....Invited

Vassilis ANASTASSOPOULOS (University of Patras, Patras, Greece) ..... Co-director of thesis

Pierre BRIOLE (CNRS, ENS, Paris, France) ..... Co-director of thesis

The dissertation was prepared in the National Observatory of Athens (IAASARS) and in the Laboratory of Geology of the Ecole Normale Supérieure

στον πατέρα μου που μου έμαθε να σκέφτομαι

to my father who taught me to think

à mon père qui m'a appris à penser

Abstract

The rift of Corinth (Greece) has been long identified as a site of major importance in Europe due to its intense tectonic activity. It is one of the world's most rapidly extending continental regions and it has one of the highest seismicity rates in the Euro-Mediterranean region. The GPS studies conducted since 1990 indicate a north–south extension rate across the rift of ~1.5 cm year-1 around its western termination. Geological evidences show that the south coast of the rift is uplifting whereas the north part is subsiding.

The western termination of the rift in the Patras broader area, with many active faults lying very close and inside the city of Patras, presents major scientific and socio-economic importance. Recent seismicity has affected this end of the rift with the Movri (Achaia) earthquake in June 2008 and a seismic swarm around Efpalio (Fokida) in January 2010. Additionally, the presence of a plurality of geophysical phenomena and morphological features renders this area and the Gulf of Corinth generally, as natural laboratory, a place of international initiatives as the Corinth Rift Laboratory and a case study for the EO Supersites initiative.

Seismic and geodetic ground measurements from permanent networks (since 2000) and measuring campaigns (since 1990) have been (and are) performed. Moreover dense SAR data are available since 1992 and the ERS1 mission.

Motivated by the lack of precise and extended mapping of the vertical deformation of the area and by the limitations of the GPS network (in terms of density of points) we investigate, model and interpret a large set of SAR interferometry data completed by the GPS data. The SAR interferometry data are very powerful for measuring vertical motions, for mapping localized deformations across faults or other features and for mapping and modeling the co-seismic deformation produced by earthquakes.

We processed ascending and ascending acquisitions of ASAR/ENVISAT in the period between 2002-2010, to produce Persistent Scatterers and Small Baseline Subsets deformation rates maps. These products have been combined together but also constrained with a number of GPS observations in order to extract the precise Up-Down and East-West deformation components field. The methodology chain performed globally well over the area (despite the vegetation cover and slopes) and provides accurate and robust results in many areas. We verified the agreement between GPS and the InSAR deformation field rates. We also compared them with remote sensing and ground observations of independent studies.

We focused in specific case studies and presented the deformation rates along cross sections inside the city of Patras, around the Rion-Antirion bridge, around the urban areas of Psathopyrgos, Aigion, Sellianitika, Nafpaktos, Ακratas, the island of Trizonia, and the river deltas of Psathopyrgos, Sellianitika, Aigion, Mornos, Marathias and Akrata.

Significant ground deformation is observed within the city of Patras itself, due not only to urban subsidence often seen elsewhere, but also to the motion of shallow structures likely to be induced by deep tectonic movements at the junction of the right lateral strike-slip fault linked to the Movri and penetrating inland between Rio and Patras (trans-tensional fault of Rio Patras), and the Psathopirgos normal fault at the entrance of the Corinth Rift. The Rio-Patras fault is a transition, oblique, structure, connecting the strike-slip zone to the south and the extensional area to the east.

The Aigion fault appears very active with uplift rate of about 2mm/an, the highest rate across the Corinth Rift in the sample period, this uprising damping in the three kilometers separating this fault from the West Helike fault to the south.

The observed discontinuities of the deformation field are not always correlated with seismic activity at the same place in the sampled period.

The Temeni-Valimitika delta, east of Aigion, is the only delta of the area not subsiding (at least at its bigger part). We think that this is because it is located on the footwall of the Aigion fault with the delta compaction/subsidence balanced by the tectonic uplift. All the other deltas are subsiding due to the compaction of their sediments, and in the big ones it is possible to observe a linear increasing rate as approaching their coastal borders.

The 2008 and 2010 seismic events which occurred in the study area are modeled by inversion of their sources parameters using a model of dislocation in a homogenous elastic half-space constrained by the seismic, the GPS and the SAR interferometry data.

At the broad scale, most of our studied tectonic features are pieces of a (diffuse) triple junction between micro-plates at the boundary between the rift of Corinth to the east and the termination of the Hellenic arc to the west. We briefly investigated and discussed the Trikonida and Aitoliko valley deformation field in the northwest of the triple junction area.

Finally, for the sake of completeness and in order to assess the capabilities of the space geodesy we presented some inferred discontinuities occurred by landslides and some by unclear origin and requiring further investigations.

Résumé

Le rift de Corinthe (Grèce) a été depuis longtemps identifié comme un site d'importance majeure en Europe en raison de son activité tectonique intense. Il est l'une des régions continentales s'étendant plus rapidement dans le monde et il a l'un des taux les plus élevés de sismicité dans la région euro-méditerranéenne. Les études menées par GPS depuis 1990 indiquent un taux d'extension nord-sud à travers le rift d'environ 1,5 cm/an à son extrémité occidentale. Les observations géologiques montrent que la côte sud du rift connaît un mouvement de surrection alors que la côte nord est en subsidence. A la terminaison occidentale du rift, plusieurs failles actives se situent au voisinage ou à l'intérieur même de la ville de Patras qui se trouve exposée à un aléa sismique important. Le séisme de Movri (Achaïa) en juin 2008 et l'essaim sismique d'Efpalion (Fokida) en janvier 2010, survenus à quelques dizaines de kilomètres de Patras, ont attiré l'attention scientifique et sociétal sur cette région et apporté des éléments nouveaux à la connaissance géophysique de la région. La présence d'une pluralité de phénomènes géophysiques et les caractéristiques morphologiques font de cette région de Patras, et plus généralement du rift de Corinthe, un laboratoire naturel exceptionnel qui est devenu depuis vingt ans le lieu d'initiatives internationales coordonnées dans le Laboratoire du Rift de Corinthe et reconnu comme un Supersite par les agences spatiales.

Sur le terrain des campagnes de mesures géodésiques et sismologiques ont eu lieu depuis 1990 et des réseaux permanents ont été déployés à partir de 2000. Dans le domaine de la télédétection, des données SAR sont disponibles depuis 1992 et la mission ERS1.

Motivé par l'absence d'une cartographie précise et étendue de la déformation verticale de la zone et par les limitations du réseau GPS (en termes de densité de points) nous étudions, modélisons et interprétons un nombre important de données d'interférométrie SAR complétées par les données du réseau GPS. Les données d'interférométrie SAR sont très puissantes pour mesurer les mouvements verticaux, pour cartographier les déformations localisées sur des discontinuités, failles ou autres, pour cartographier et modéliser la déformation co-sismique produite par les tremblements de terre.

Nous avons traité des données ascendantes et descendantes du capteur ASAR embarqué sur ENVISAT dans la période 2002-2010, et produit des cartes de vitesses (et séries temporelles) de points persistants (Permanent Scatterers) d'une part, de régions cohérentes (SBAS, Small Baseline Subsets) d'autre part. Ces deux types de cartes ont été combinés ainsi que contraint par les observations GPS afin d'en extraire les composantes verticales et est-ouest du champ de vitesses. Dans l'ensemble la chaîne de calcul fonctionne convenablement sur la région pourtant affectée par de nombreuses zones couvertes de végétation et par un relief important. Les résultats paraissent précis et robustes dans de nombreuses zones dans lesquelles le mouvement du sol était auparavant inconnu ou mal connu. Nous avons vérifié

l'accord entre le GPS et les vitesses déduites de l'interférométrie radar, et comparés nos résultats avec ceux d'études indépendantes.

Nous nous sommes concentrés sur des études de cas spécifiques et nous présentons les taux de déformation le long des sections transversales dans les zones de la ville de Patras, des abords du pont de Rion-Antirion, des centres urbains de Psathopyrgos, Aigion, Sellianitika, Nafpaktos, Akrata, de l'île de Trizonia ainsi que des deltas de Psathopyrgos, Sellianitika, Aigion, Mornos, Marathias et Akrata.

Des déformations du sol apparaissent à l'intérieur même de la ville de Patras. Il s'agit non seulement de subsidences urbaines souvent observées ailleurs, mais aussi de mouvements de blocs superficiels vraisemblablement induits par les mouvements tectoniques profonds à la jonction entre une zone de faille décrochante, provenant de la zone de Movri et entrant à terre entre Rio et Patras (faille en trans-tension de Rio-Patras), et la faille normale de Psathopirgos à l'entrée du rift de Corinthe. La faille de Rio-Patras apparaît comme une structure de transition, oblique, entre le décrochement au sud et l'extension à l'est.

La faille d'Aigion apparaît très active avec un taux de soulèvement d'environ 2mm/an, le taux le plus élevé observé dans l'ensemble du rift de Corinthe dans la période échantillonnée, ce soulèvement s'amortissant dans les trois kilomètres séparant cette faille de celle d'Hélike ouest.

Les discontinuités observées dans le champ de déformation ne sont pas toujours corrélées avec une activité sismique enregistrée dans la même zone au cours de la période d'investigation.

Le delta de Temeni-Valimitika, à l'est d'Aigion, est le seul delta de la zone qui ne subside pas (au moins dans sa plus grande partie). Nous pensons que c'est parce qu'il est situé sur le 'footwall' de la faille d'Aigion et que le processus de compaction/subsidence y est compensé par le processus de soulèvement tectonique dû à la faille. Tous les autres deltas sont en subsidence, en raison vraisemblablement du tassement de leurs sédiments, et dans les plus grands d'entre eux, il est possible d'observer une augmentation linéaire du taux de subsidence entre le bord intérieur du delta et sa côte.

Les séismes survenus en 2008 et 2010 dans la zone d'étude sont modélisés par inversion de leurs paramètres de sources en utilisant un modèle de dislocation dans un demi-espace élastique homogène contraint par les données sismologiques, les données GPS et les données d'interférométrie SAR.

La plupart des objets tectoniques que nous avons étudiés sont des éléments d'un point triple (diffus) séparant trois micro-plaques situées à la frontière entre le rift de Corinthe à l'est et la terminaison de l'arc hellénique à l'ouest. Nous avons brièvement étudié et discutons les déformations observées par interférométrie radar au sud de lac Trichonis et dans le graben Aitolien au nord d'Etoliko, c'est-à-dire dans la partie nord-ouest du point triple

Enfin, pour être complet, et afin d'évaluer les capacités de la géodésie spatiale, nous présentons des discontinuités probablement dues à des glissements de terrain et quelques-unes d'origine incertaine et requérant des investigations plus approfondies.

Περίληψη

Η ρηξιγενής ζώνη της Κορίνθου (Ελλάδα) έχει από καιρό αναγνωριστεί ως μια περιοχή μείζονος σημασίας στην Ευρώπη, λόγω της έντονης τεκτονικής της δραστηριότητας. Είναι μία από τις πιο ταχέως εφελκούμενες ηπειρωτικές περιοχές στον κόσμο και παρουσιάζει έναν από τους υψηλότερους ρυθμούς σεισμικότητας στον Ευρω-μεσογειακό χώρο. Μελέτες GPS που διεξάγονται από το 1990 εκτιμούν το ρυθμό εφελκυσμού περί τα 1.5 εκατοστά ανά έτος γύρω στο δυτικό πέρας του. Γεωλογικές μελέτες δείχνουν ότι η νότια ακτή του ανυψώνεται, ενώ η βόρεια υποχωρεί.

Το δυτικό πέρας της ρηξιγενής ζώνης στην ευρύτερη περιοχή της Πάτρας, με πολλά ενεργά ρήγματα που βρίσκονται πολύ κοντά και μέσα στην πόλη, παρουσιάζει σημαντικές επιστημονικές και κοινωνικο-οικονομικές προεκτάσεις. Η πρόσφατη σεισμικότητα έχει εκδηλωθεί σε αυτήν την περιοχή με το σεισμό της Μόβρης (Αχαΐα) τον Ιούνιο του 2008 και με τη σεισμική ακολουθία κοντά στο Ευπάλιο (Φωκίδα) τον Ιανουάριο του 2010. Επιπλέον, η παρουσία ενός πλήθους γεωφυσικών φαινομένων και γεωμορφολογικών χαρακτηριστικών καθιστά την εν λόγω περιοχή, αλλά και τον Κορινθιακό Κόλπο εν γένει, ένα φυσικό εργαστήριο, μια περιοχή μελέτης για διεθνείς πρωτοβουλίες, όπως το Corinth Rift Laboratory και μια περιπτωσιολογική μελέτη της πρωτοβουλίας 'EO Supersites'.

Σεισμικές και γεωδαιτικές επιτόπιες παρατηρήσεις από μόνιμα δίκτυα (από το 2000) και δειγματοληπτικές μετρήσεις (από το 1990), συνεχίζονται να διενεργούνται από το 2000 και 1990, αντίστοιχα. Επιπλέον, πυκνές λήψεις δεδομένων SAR είναι διαθέσιμες από το 1992 από την αποστολή του ERS-1.

Παρακινούμενοι από την έλλειψη μιας λεπτομερούς, ακριβούς και εκτεταμένης χαρτογράφησης της κάθετης παραμόρφωσης στην περιοχή ενδιαφέροντος και τους περιορισμούς του δικτύου GPS (από την άποψη της πυκνότητας της δειγματοληψίας), ερευνούμε, μοντελοποιούμε και ερμηνεύουμε ένα μεγάλο σύνολο δεδομένων διαφορικής συμβολομετρίας SAR και μετρήσεων GPS. Τα δεδομένα διαφορικής συμβολομετρίας μπορούν να αξιοποιηθούν για την ακριβή μέτρηση κατακόρυφων μετακινήσεων, για τη χαρτογράφηση τοπικών παραμορφώσεων εκατέρωθεν ρηγμάτων ή άλλων σχηματισμών και για τη χαρτογράφηση και μοντελοποίηση της ενδο-σεισμικής παραμόρφωσης.

Επεξεργαστήκαμε δεδομένα ανοδικής και καθοδικής τροχιάς του δέκτη ASAR / ENVISAT της περιόδου μεταξύ 2002-2010, για την παραγωγή χαρτών ρυθμού παραμόρφωσης Σταθερών Σκεδαστών (Persistent Scatterrers) και υποσύνολα μικρών χωρικών γραμμών βάσης (Small Baseline Subsets – SBAS). Τα προϊόντα συνδυάστηκαν κατάλληλα, αλλά και διορθώθηκαν από μια σειρά από παρατηρήσεις GPS, προκειμένου να εξαχθεί το ακριβές πεδίο παραμόρφωσης κατά την κατακόρυφη και κατά την διεύθυνση Ανατολής-Δύσης συνιστώσα. Η ακολουθούμενη μεθοδολογία λειτούργησε καλά σε ευρεία κλίμακα στην περιοχή ενδιαφέροντος (παρά την κάλυψη της βλάστησης και το έντονο ανάγλυφο) και παρείχε ακριβείς και αξιόπιστες εκτιμήσεις σε πολλές επί μέρους περιοχές. Επαληθεύσαμε τη συμφωνία μεταξύ των πεδίων παραμόρφωσης των παρατηρήσεων GPS και

συμβολομετρίας. Επίσης, τα συγκρίναμε με δεδομένα τηλεπισκόπησης και επίγειες παρατηρήσεις από ανεξάρτητες μελέτες.

Εστιάσαμε σε συγκεκριμένες περιπτωσιολογικές μελέτες και παρουσιάσαμε τους ρυθμούς παραμόρφωσης μαζί με διατομές μέσα στην πόλη της Πάτρας, γύρω από τη γέφυρα Ρίου-Αντιρρίου, γύρω από τις αστικές περιοχές του Ψαθόπυργου, Αίγιου, Σελλιανίτικων, Ναυπάκτου, Ακράτας, νήσου Τριζονίων, και τα ποτάμια δέλτα του Ψαθόπυργου, Σελλιανίτικων, Αιγίου, Μόρνου, Μαραθιά και Ακράτας.

Σημαντική παραμόρφωση του εδάφους παρατηρείται μέσα στην πόλη της Πάτρας, οφειλόμενη όχι μόνο στην αστική καθίζηση (όπως συμβαίνει συχνά), αλλά και στην μετακίνηση των ρηχών δομών που ενδέχεται να προκαλούνται από βαθιές τεκτονικές μετακινήσεις στην επαφή του δεξιόστροφου ρήγματος πλευρικής ολίσθησης που συνδέεται με τον σεισμό της Μόβρης. Το τελευταίο διεισδύει στη ξηρά και συνδέεται μεταξύ Ρίου και Πάτρας (ρήγμα πλάγιας ολίσθησης) και στη συνέχεια με το κανονικό ρήγμα του Ψαθόπυργου στην είσοδο της ρηξιγενής ζώνης της Κορίνθου. Το ρήγμα Ρίου-Πάτρας αποτελεί μια ζώνη μετάβασης, συνδέοντας την ζώνη πλευρικής ολίσθησης στο Νότο με τις ρηξιγενείς δομές εφελκυσμού στην Ανατολή.

Το ρήγμα του Αιγίου παρουσιάζει υψηλή ενεργητικότητα με ρυθμό ανύψωσης περί τα 2 χιλιοστά ανά έτος, ο υψηλότερος στην ρηξιγενή ζώνη της Κορίνθου κατά την περίοδο δειγματοληψίας, ο οποίος αποσβένει στα τρία χιλιόμετρα που χωρίζουν αυτό το ρήγμα με το Δυτικό τμήμα του ρήγματος της Ελίκης στο νότο.

Οι παρατηρούμενες ασυνέχειες του πεδίου παραμόρφωσης δεν σχετίζονται πάντα με τη σεισμική δραστηριότητα κατά την περίοδο της μελέτης.

Το δέλτα της Τέμενης-Βαλιμίτικων, ανατολικά του Αιγίου, είναι το μόνο δέλτα της περιοχής που δεν υποχωρεί (τουλάχιστον κατά τη μεγαλύτερη έκτασή του). Πιστεύουμε ότι αυτό οφείλεται στο ότι βρίσκεται στον πόδα του ρήγματος του Αιγίου με τη συμπίεση/καθίζηση του δέλτα να εξισώνεται με την τεκτονική ανύψωση. Όλα τα άλλα δέλτα υποχωρούν λόγω της συμπίεσης των ιζημάτων τους και στα μεγαλύτερα είναι δυνατόν να παρατηρηθεί ένας γραμμικώς αυξανόμενος ρυθμός παραμόρφωσης καθώς προσεγγίζουμε το προδέλτα του.

Τα σεισμικά γεγονότα του 2008 και 2010 που έλαβαν χώρα στην περιοχή μελέτης μοντελοποιήθηκαν με αναστροφή των παραμέτρων της πηγής παραμόρφωσής τους, χρησιμοποιώντας ένα μοντέλο της μετατόπισης σε ένα ομογενές ελαστικό ημιχωρικό μέσο με χρήση σεισμικών, GPS και συμβολομετρικών δεδομένων.

Σε ευρεία κλίμακα, οι περισσότερες υπό μελέτη τεκτονικές δομές αποτελούν τμήματα μιας (διάχυτης) τριπλής επαφής μεταξύ των μικρο-πλακών στο όριο ανάμεσα στη ρηξιγενή ζώνη της Κορίνθου στα Ανατολικά και στον τερματισμό του Ελληνικού τόξου προς τα δυτικά. Ερευνήσαμε συνοπτικά και συζητήσαμε το πεδίο παραμόρφωσης της λίμνης Τριχωνίδας και της κοιλάδας του Αιτωλικού στα βορειοδυτικά της περιοχής της τριπλής επαφής.

Τέλος, χάρη πληρότητας και για την αξιολόγηση των δυνατοτήτων της διαστημικής γεωδαισίας παρουσιάσαμε μερικές ασυνέχειες, οι οποίες, άλλες προκλήθηκαν από κατολισθήσεις και άλλες με ασαφή προέλευση, οι οποίες χρήζουν περαιτέρω έρευνας.

Acknowledgements

I would like to express my gratitude to my supervisors, Research Director Pierre Briole, Professor Vassilis Anastasopoulos, Senior Researcher Thanassis Rontogiannis and Professor Sergios Theodoridis for their guidance and support during my study. I also would like to acknowledge my examiners, Issaak Parcharidis, Pascal Bernard and Michel Sebrier, as well as the rest of the jury in Paris, Alex Rigo, Daniele Raucoules and Sébastien ROHAIS, especially those that didn't put me on the top of the wall during my defense! Moreover I would like to thank the rest of the jury members in Patras, Stathis Stiros and Thimios Sokos.

I gratefully acknowledge the permission for the realization of the thesis of my employer, National Observatory of Athens. Moreover, I would like to thank the members of my hosting Institute for Astronomy, Astrophysics, Space Applications and Remote Sensing, Penteli, Greece and especially Ioannis Daglis, Olga Sykioti and Dimitris Paronis.

I would like to thank the entire staff of the Laboratory of Geology of the Ecole Normale Supérieure, Paris, France.

Special thanks to Helene Lyon-Caen, Anna Serpetzidaki, Maya Illieva, Dimi Dimitrov, Ann Deschamps, Maurin Vidal, Alex Nercesian, Eugenie Perouz, Antonios Mouratidis, Omiros Giannakis, Akis Panagis, Margarita Segou and to all the CRL community who sustain the CRL 'idea'.

I am deeply grateful to my companion Annita Panteleli for her great support, encouragement, help and patience during my PhD study.

Most of the figures were obtained by employing the GMT freeware package by [Wessel and Smith, 1998].

I would like to thank ESA and JAXA for providing us with SAR data from ASAR/ENVISAT (ESA-AOE 766) and PALSAR/ALOS (ALOS science project 167).

Contents

List of Figures

List of Tables

1. Introduction

1.1. Geodesy

Geodesy is the science of accurately measuring and understanding three fundamental properties of the Earth: (1) its gravity field, (2) its geometrical shape and (3) its orientation in space [Torge, 2001]. In the recent decades the growing emphasis has been on the time variation of these 'three pillars of geodesy' [Beutler et al., 2004], which has become possible owing to the accuracy of new space-based geodetic methods and also owing to a truly global reference system that only space geodesy can realize [Altamimi et al., 2001, 2002]. As each of these three properties are connected by physical laws and are forced by natural processes of scientific interest [Lambeck, 1988], space geodesy has become a highly interdisciplinary field, intersecting with a vast array of geophysical disciplines, including tectonics, Earth structure, seismology, oceanography, hydrology, atmospheric physics, meteorology, climate change and more. This richness of diversity has provided the impetus to develop space geodesy as a precise geophysical tool that can probe the Earth and its interacting spheres in ways never before possible [Smith and Turcotte, 1993]. The following is just a few examples of geophysical applications of space geodesy: plates tectonics, by tracking the relative rotations of clusters of space geodetic stations on different plates; interseismic strain accumulation, by tracking the relative velocity between networks of stations in and around plate boundaries; earthquake rupture parameters, by inverting measurements of co-seismic displacements of stations located within a few rupture lengths of the fault; postseismic processes and rheology of the Earth's topmost layers, by inverting the decay signature (exponential, logarithmic, etc.) of station positions in the days to decades following an earthquake; magmatic processes, by measuring time variation in the position of stations located on volcanoes or other regions of magmatic activity, such as hot spots; rheology of the Earth's mantle and ice-sheet history, by measuring the vertical and horizontal velocities of stations in the area of postglacial rebound (glacial isostatic adjustment); mass redistribution within the Earth's fluid envelope, by measuring time variation in Earth's shape, the velocity of the solid-Earth center of mass, Earth's gravity field, and Earth's rotation in space; Global change in sea level, by measuring vertical movement of the solid Earth at tide gauges, by measuring the position of space-borne altimeters in a global reference frame, and by inferring exchange of water between the oceans and continents from mass redistribution monitoring; Hydrology of aquifers by monitoring aquifer deformation inferred from time variation in 3-D coordinates of a network of stations on the surface above the aquifer; providing a global reference frame for consistent georeferencing and precision time tagging of nongeodetic measurements and sampling of the Earth, with applications in seismology, airborne and space-borne sensors and general fieldwork [Herring 2007].

1.2. Earthquakes

Earthquakes are sudden and violent phenomena and many times have catastrophic consequences in terms of human lives and economic disaster. The common scope of predicting tectonic activity fortifies the public health and benefits the socioeconomic welfare of a community residing in a seismotectonically active region. This scope presents many and various difficulties, both theoretical and practical. Empirical models which are fed by various measurements (recent instrumentally recorded events, accounts of historical earthquakes and geomorphological evidence) are critical in order to improve our knowledge of the mechanisms that are activated during the seismic events. The characteristics of the mechanisms are estimated by measurements acquired from a large number of in-situ and remote sensors. In each seismotectonic event the gained experience is used to quantify the seismic hazard of a region and promotes the scientific knowledge towards the common scope.

An earthquake is a sudden movement of the Earth's surface, caused by a release of strain built up over long periods on faults. The rocks are elastic and can store energy in the same way as a compressed spring. Earthquakes are focused on faults in the rock mass. Most have foci (focus point) within the crust but a few, in plate boundary zones and beneath stable cratonic (old and stable part of the continental lithosphere) areas (where they are related to events in nearby subduction (Figure 1-1) zones), have foci at great depths, down to about 700 km, in the mantle; beyond this depth the rock mass is insufficiently rigid to rupture.

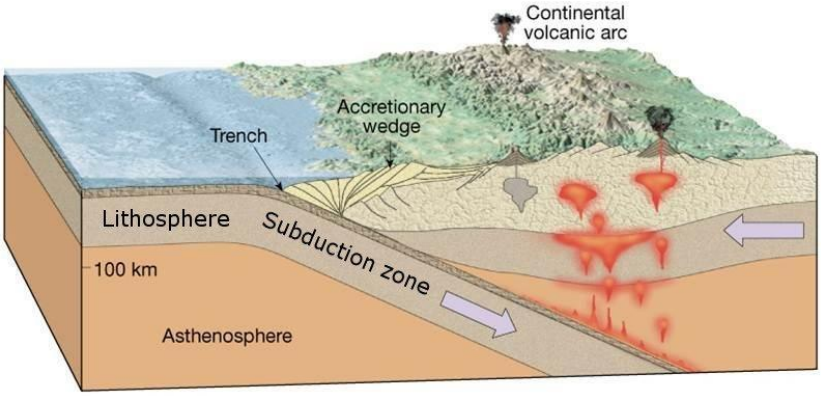

Figure 1-1. The Lithospheric subduction zone.

Not all the built-up strain is relieved by earthquakes; part of it can be relieved by continual small adjustments, a process of creep. However, where friction prevents such accommodation, the strain builds up until something has to give, and there is a sudden rupture of the weakest part of the solid rock, the forces being accommodated by sudden dislocation of the rocks on either side of the fault plane. This process can happen on all three types of fault: normal (Figure 1-2a), reverse (Figure 1-2b), left-lateral strike slip (Figure 1-2c) and right-lateral strike slip (Figure 1-2d).

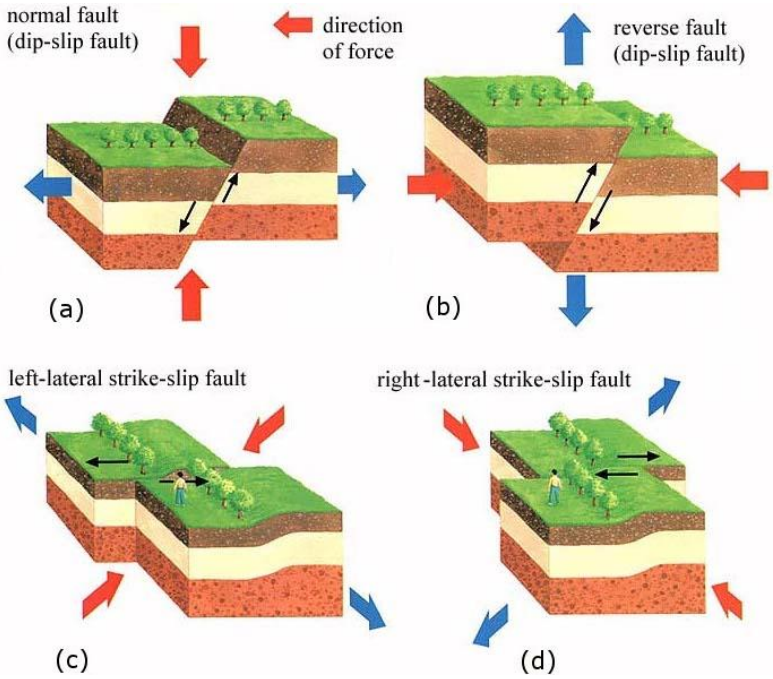

Figure 1-2. Type of faults: (a) normal, (b) reverse, (c) left-lateral and (d) right-lateral.

Moreover it can be a mixture of normal/reverse and strike slip (oblique). The point directly above the focus is called the epicentre; here, the effects of the earthquake will be greatest. If the focus is shallow, the effects will be greater than if it is deep.
The elastic-rebound model of earthquakes assumes that between earthquakes material at a distance from the fault undergoes relative motion. Because the fault is locked, featuresacross it that were originally linear (Figure 1-3a), such as a fence, are slowly deformed with time (Figure 1-3b). Finally, the strain becomes so great that the fault breaks in an earthquake, offsetting the features (Figure 1-3c).

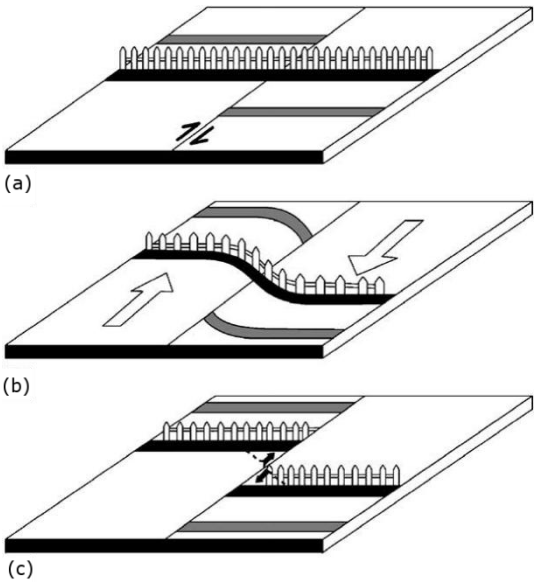

Figure 1-3. The elastic-rebound model of earthquakes. [Stein and Wysession 2003]

Additionally, phenomena that are partly related to earthquakes are landslides. A landslide phenomenon includes a wide range of ground movement, such as rockfalls, deep failure of slopes, shallow debris flows, and land instability which can occur in offshore, coastal and onshore environments. Landslides are recognized as natural hazards, with significant or high social-economic impact in many countries and represent a significant risk for citizens as well as infrastructures.

1.3. Context of the Corinth Rift.

The tectonics of the Eastern Mediterranean region is very complex. It has been studied intensely for the last 40 years since initiation of the plate-tectonic concept. The Eastern Mediterranean region, which defines the region lying between the Caspian Sea and the Adriatic Sea through Caucasus, Anatolia, Aegean Sea and Greece, is the one of the world's most seismically active regions with deadly earthquakes occurring often.

The tectonic framework of the eastern Mediterranean is dominated by the collision of the Arabian and African plates with Eurasia [McKenzie, 1970; Jackson and McKenzie, 1984, 1988]. Plate tectonic models [DeMets et al., 1990; Jestin et al., 1994] based on analysis of global seafloor spreading, fault systems, and earthquake slip vectors indicate that the Arabian plate is moving in a north-northwest direction relative to Eurasia at a rate of about 18-25 mm year^{-1}, averaged over about 3 Myr (Figure 1-4).

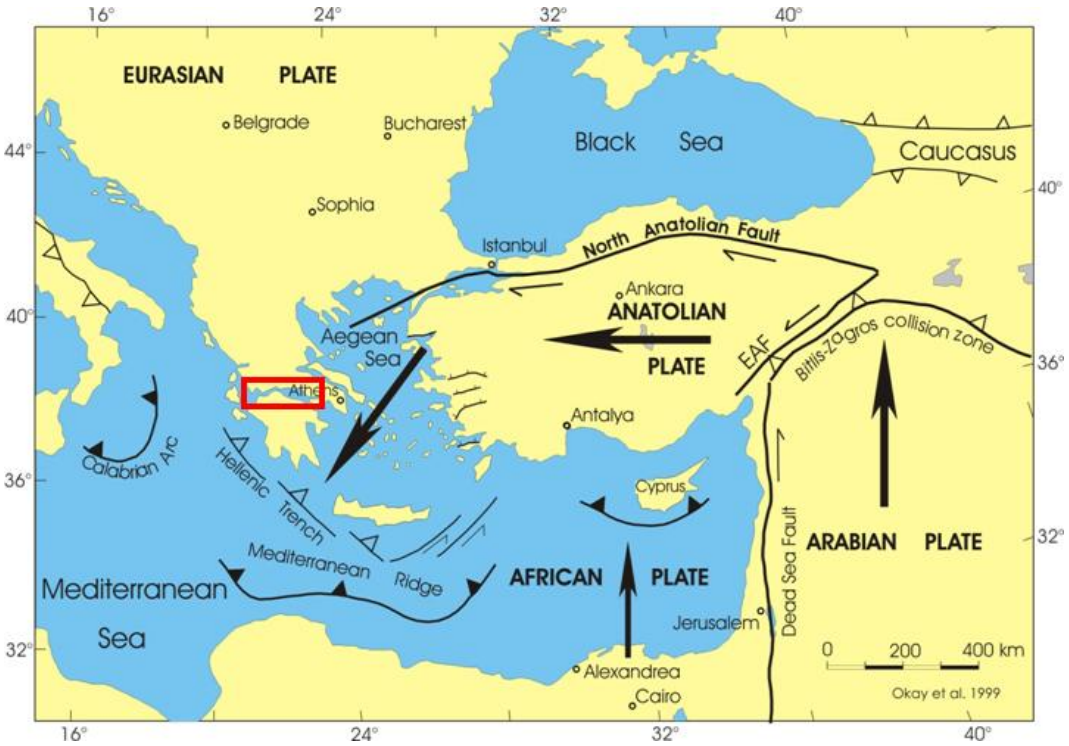

Figure 1-4. The plate tectonic context around the Gulf of Corinth.

Ten mm year^{-1} of this rate is absorbed by shortening the Caucasus. These models also indicate that the African plate is moving in a northerly direction relative to Eurasia at a rate of about 10 mm year^{-1} (at 30°N, 31°E). Differential motion between Africa and Arabia (~10-

15 mm year^{-1}) is thought to be taken up predominantly by left-lateral motion along the Dead Sea transform fault. The analysis of 1988-1994 GPS measurements in Turkey has shown that the Anatolian block is undergoing counter-clockwise rotation about a pole located north of Sinai (33.4°E, 31.1°N), [Reilinger et al. 1995]. This northward motion results in continental collision along the BitlisZagros fold and thrust belt, intense earthquake activity and high topography in eastern Turkey and the Caucasus mountains and westward extrusion of the Anatolian plate [McKenzie, 1970]. The Anatolian block escapes from Eastern Anatolia due to Eurasia and Arabian collision and moves onto the African oceanic plate along the Hellenic arc. The leading edge of the African plate is being subducted along the Hellenic arc at a higher rate than the relative northward motion of the African plate itself, requiring that the arc moves southward relative to Eurasia proper [e.g., Sonder and England, 1989; Royden, 1993]. Subduction of the African plate is also thought to occur along the Cyprean arc and/or the Florence rise south of Turkey, although it is less well defined in these regions than along the Hellenic arc.

The Gulf of Corinth (GoC) lies between the subducting Africa and Anatolian plates (Figure 1-4). It has been long identified as a site of major importance due to its intense past geophysical activity [Clarke et al., 1997]. It is one of the world's most rapidly extending continental regions and it has one of the highest seismicity rates in the Euro-Mediterranean region.

Previous geodetic studies conducted, which were based on GPS observations and Interferometric Synthetic Aperture Radar (DInSAR) observations, revealed North – South extension rates across the gulf of up to about 1.5 cm year^{-1} [Briole et al., 2000;Avallone 2003] during the last 20 years. The rifting mechanism observed is crucial for the stability of the region as it can lead to submarine slope failures and it has been long identified as a site of major importance due to its intense past geophysical activity [Briole et al., 2000]. A number of earthquakes with magnitude greater than 5.8 have been occurred: Alkyonides (1981, M=6.7), Aigio (1995, Mw=6.1), and Galaxidi (1992, Mw=5.8), Efpalio (2010, Mw=5.3). In an average, one earthquake having Mw>6 is occurring every six years in the GoC. The rifting mechanism observed is crucial for the stability of the region as it can lead to submarine slope failures and possible damaging tsunamis. On land, the same fault system causes landslides. Moreover, the south coast of the Corinth rift is uplifting whereas the north part is subsiding [Elias et al., 2009, Palyvos et al., 2007]. GoC has a large number of off-shore and on-shore (well visible at the surface) long faults, most of them striking E-W. Large earthquakes occurs also on the faults located around the GoC and connected to it, like the Movri earthquake in 2008 (Mw=6.4)

In the present study we investigate the ground deformations in the area of the western end of the Gulf or Corinth (GoC) by exploiting satellite geodesy. Conventional [Massonnet and Feigl., 1998] and advanced Differential Interferometric technics – i.e. PSI, SBAS – of Synthetic Aperture Radar data acquisitions ASAR/ENVISAT sensor, as well as GPS observations [Briole et al. in preparation] has been carried out, acting in synergy for the reconnaissance of these aseismic discontinuities.

The Gulf of Corinth (GoC) with the older seismicity in the area is illustrated in Figure 1-5.

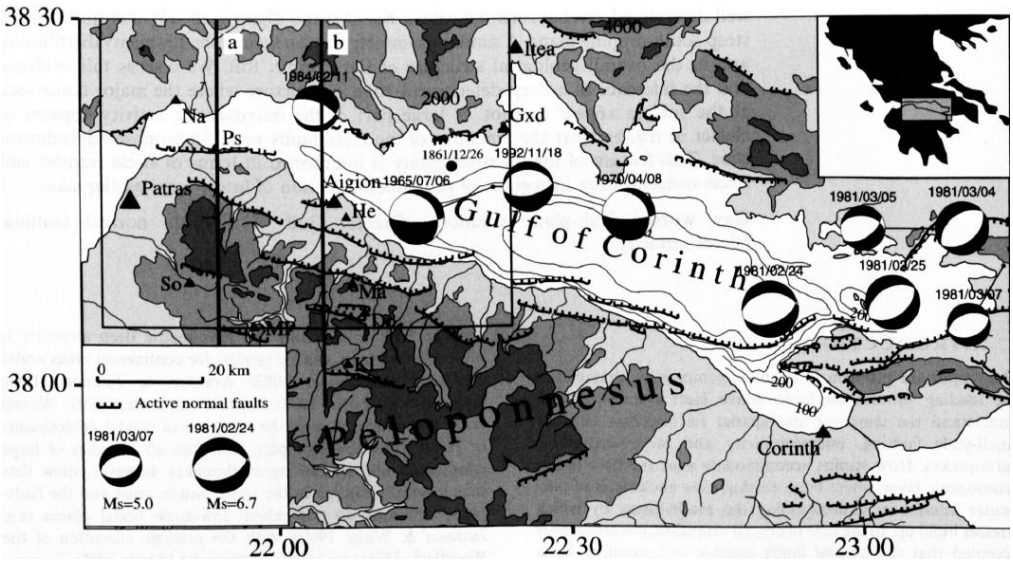

Figure 1-5. Courtesy of [Rigo et al., 1996]. Seismicity of the central and Eastern GoC since 1996.

Recent seismicity has been mitigated towards the Western GoC with the last two recent moderate earthquakes of the GoC to have occurred there (Figure 1-6).

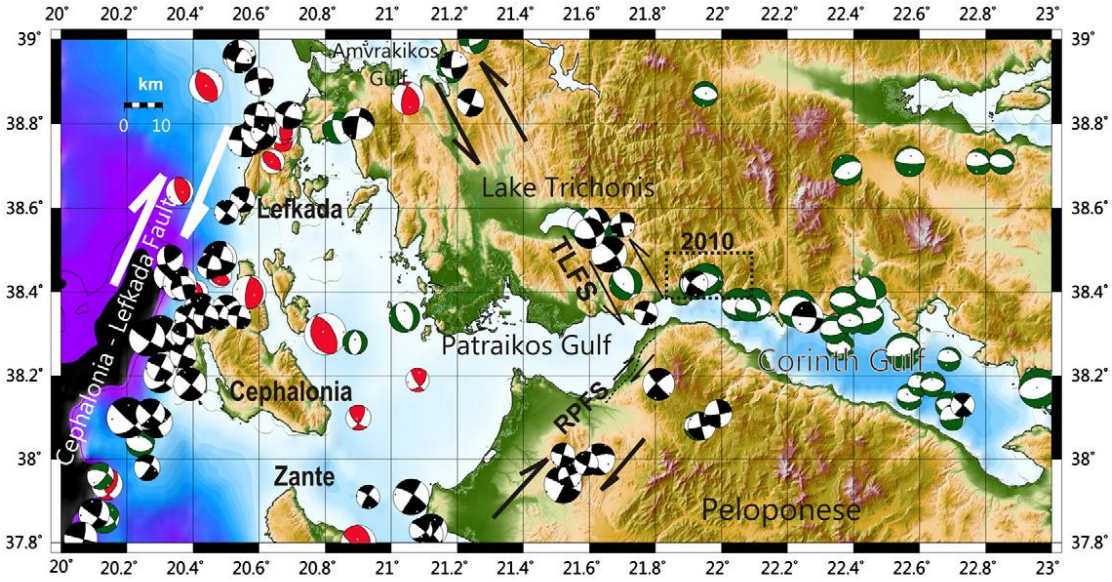

Figure 1-6. Courtesy of [Sokos et al. 2012]. Recent seismicity in extended GoC area.

1.4. Rationale

The area of the GoC that presents a major scientific and/or socio-economic interest and is the most active seismically, presenting strong micro-seismicity, is its westernmost part. This area includes the city of Patras, the Rion-Patras fault zone, the Rion-Antirrion bridge, the Psathopyrgos fault zone which is considered to be a presently active structure [Flotte et al., 2005], Lambiri-Rofodafni, Helike, Pyrgaki on-shore and coastal fault systems. Psathopyrgos fault zone acts as a transfer zone between the Corinth and Patras rift [Flotte et al., 2005].

According to [Palyvos et al., 2007] not known earthquakes have been occurring by this fault for the last 400 years (strong evidence for a seismic gap, considering the slip of neighbour segments). Patras is the third most populated city in Greece with more than 200,000 citizens. The bridge of Rion-Antirrion is 2,880m long (its width is 28m) and connects the eastern and western Greece. The bridge has been designed and constructed taking into consideration the raised seismicity of the area. The population in the city and the suburbs of Patras and many other towns around the Western end of the Gulf of Corinth, along with the bridge or Rio-Antirrio are subjected to geophysical hazards.

At the western end of the rift, we consider the presence of a triple junction zone with part of the relative micro-plate motion being accommodated across a strike-slip zone passing beneath Patras and connected to the area of the 2008 earthquake and part of the relative motion transferred towards NW to the Trichonidas graben [Kiratzi et al., 2008], the Agrinion area and the Aetoliko valley until Amfilochia and the Amvrakikos gulf.

The “triple junction” area is characterized by the presence of a large city (Patras) and large infrastructures (bridge, tunnels) all exposed to the seismic hazard Figure 7-1.

This “triple junction” as well as the western part of the rift where extension is fast, seismic gaps are inferred, densely populated constitute the area of the CRL (Corinth Rift Laboratory) where various European scientists collaborate to gather data and improve the knowledge of the mechanisms of the deformation.

The Western GoC are presents a plurality of geophysical phenomena and morphological features (strike / normal faulting, triple junction, submarine and onshore landslides, high seismicity, high extension rates, subsiding deltas, high slopes, intense relief, aseismic faults, urban faults, coastal uplift). This variety of phenomena renders the Western GoC (but also the GoC generally) as natural laboratory. For this reason this area has drawn the attention of many international research groups and is included in the schedule of many educational courses throughout European Universities.

This area is among the most intensive studied areas in Europe because of its considerable tectonic activity. Consequently it is very well covered with ground measuring networks and many measuring campaigns are being performed (i.e. GPS, on shore/submarine seismometers, strain gauges, tidal meters, inclinometers, electric resistivity meters etc.).

Moreover, GoC is a place of international initiatives as Corinth Rift Laboratory (CRL) project at Patras (http://crlab.eu) with a strong EO component and a link with the EO Supersites initiative (http://supersites.earthobservations.org).

All the forth mentioned reasons are leading to the fact that the Western GoC is a tectonically active area, presenting high risk due to a big variety of geophysical phenomena, requiring a uninterruptable monitoring and study to advance the knowledge of the thematic and methodology context.

The lack of a clear detailed and accurate deformation mapping with high resolution for such an important area as the GoC was the motivation for the present thesis. This achievement could only be successfully accomplished by combing EO and in-situ data, in the specific case satellite active microwave data of Synthetic Aperture Radar (SAR) sensor processed with

advanced differential interferometry methodologies (i.e. PSI and SBAS) and long-term permanent and campaign GPS observations.

1.5. Novelty

Since the early 90s, DInSAR data have been acquired over the CRL area with various sensors/satellites (SAR/ERS-1 SAR/ERS-2 and ASAR/ENVISAT).

Here we present and discuss the DInSAR observations in the triple junction area where DInSAR is useful to map the deformation field (for the on-shore areas) in complement to GPS data that are available at a limited number of sites only that are crucial to provide the overall deformation pattern [Briole et al., in prep] but cannot be dense enough to assess the fault motions at shallow depth.

The combination of high spatial density measurements provided by Earth Observation (EO) data and the accurate point wise measurements acquired by GPS and other in-situ instruments is necessary in order to map and understand in detail the deformation mechanism lying underneath. This knowledge will lead us to quantify the stress accumulated along and across features and to estimate how it will be either diffused violently leading either to interseismic sequence, or absorbed slowly as a creeping procedure. Moreover, it will reveal us how it will act as a transfer zone mitigating the stress to other neighbouring features.

In the field of earthquake fault parameters estimation we achieved the constraint of moderate earthquake (Mw ~ [5.5 6.5]) fault parameters with space geodesy with accuracy of ±2 km for length and ±1 km for depth.

In the present thesis we used the combination of PSI and SBAS methodology of a large volume of both ascending and descending ASAR/ENVISAT acquisitions. We constrained these with the available permanent and campaign GPS network observations and finally we combined the ascending and descending track to extract the East-West component (EWc) and Up-Down component (UDc). With the proposed methodology we have calculated the spatially distributed deformation field of an extended area of the GoC, with high accuracy of almost 1 mm $year^{-1}$ and common reference to ITRF frame. Cross section profiles are drawn for a number of detected discontinuities. Their distribution reveals the rate and the range of depth of their deformation source. By using this information, in-situ visits and morphological evidence we can propose characterizations (e.g. striking, ground deformation rate, range of depth) of each detected discontinuity.

Additionally, in the city of Patras, where there is no morphological evidence due to its dense construction - in the contrary the proposed combined methodology benefits from the urban environment - we provide a big volume of accurate deformation rates.

1.6. Imposed questions

Some questions that were guided our study are following:

- How can we discriminate the effect of different deformation mechanism?
- Do Creeping faults exist in GoC? Which are and what are their characteristics?
- What are the rates of the creeping faults?
- What are the depths of the deformation sources?
- How the geodetic data combined with seismic observations constrain the fault characteristics in case of earthquakes even with no surface rupture and small ground deformation?
- How the GPS and InSAR observations could be implemented? What are the benefits of this?

1.7. Current status and our vision

Until now the geodetic observation of the Western Gulf of Corinth was done mainly by long-term permanent and campaign GPS [Briole et al., 2000;Avallone 2003], observations and from DInSAR that was dealing with shallow earthquake events of moderate magnitude with considerable ground deformations. Moreover, some study exploits high resolution SAR data over two decades but targeting a few case studies with a single track and in the LOS direction, not enlightening the overall context of the Western GoC. We envisage to promote the knowledge towards this scope and provide an accurate deformation field with common reference, separating the UDc and EWc and contributing to the understanding of the dominate tectonic context.

The Geodetic GPS network of the Gulf of Corinth provides very accurate horizontal deformation measurements but its vertical component suffers from lower accuracy. Moreover, this measurement is only achievable with permanent GPS stations, operating continuously after a long period of time for almost a decade. Additionally, the observations are pointwise so their spatial density is limited. Due to the variety of ground deformations occurring in the Gulf of Corinth, in terms of scale, source mechanism, velocity, land cover and geometry there is the need to fill this gap. This gap is filled with Earth Observation and specifically with Satellite Synthetic Aperture Radar interferometry (InSAR).

2. Methodology

2.1. Differential Interferometry

A Synthetic Aperture Radar (SAR) is a coherent airborne or space borne (and sometimes ground based) side looking radar system which utilizes the flight path of the platform to simulate an extremely large antenna or aperture electronically, and that generates high-resolution remote sensing imagery. Over time, individual transmit/receive cycles (PRT's) are completed with the data from each cycle being stored electronically. The signal processing uses magnitude and phase of the received signals over successive pulses from elements of a synthetic aperture. After a given number of cycles, the stored data is recombined (taking into account the Doppler effects inherent in the different transmitter to target geometry in each succeeding cycle) to create a high resolution image of the terrain being over flown.

Synthetic Aperture Radar Interferometry (InSAR) is a technique which is applied to phase component of two SAR images acquired from relatively close positions to distinguish and study the interference patterns between the two images. Synthetic Aperture Radar Differential Interferometry (DInSAR) is the same interferometric technique but having the topographic effect minimized. InSAR can provide spatially continuous measurement of deformed fields [Massonnet and Feigl, 1998]. Monitoring of geological phenomena induced by tectonic [Elias et al., 2009; Elias et al 2008], volcanic [Briole et al, 2008; Elias et al, 2008; Sykioti et al, 2006; Massonnet et al, 1995] or other geodynamic [Massonnet and Feigl, 1998; Zebker et al., 1994] or human induced processes such as subsidence due to exhaustion of oil [Amelung et al., 1999], natural gas and water reservoirs [Fruneau et al., 1999], deformation due to water vapor injection for increasing oil productivity, large scale constructions, tunneling and road constructions [Van der Kooij, 1999] are the main applications of satellite Differential Interferometry using SAR sensors .

In Figure 2-1 we can see a few useful geometrical features concerning acquisitions of SAR satellites. As the satellite is moving along its ascending or descending track, in the azimuth direction of the formed image, it transmits microwave pulses with a certain incidence angle (that in the usual case is 23°) either to the right or the left side, which are reflected by the ground and received back by the satellite. The vector between the satellite and the ground target is in the Line of Sight (LOS). The swath width depends from the Antenna footprint. The echoes are sorted in the azimuth direction by the Doppler effect and in the range direction by the delay of the arrival of the backscatter. The inclination of the orbit is in the usual cases ~ -8.5°.

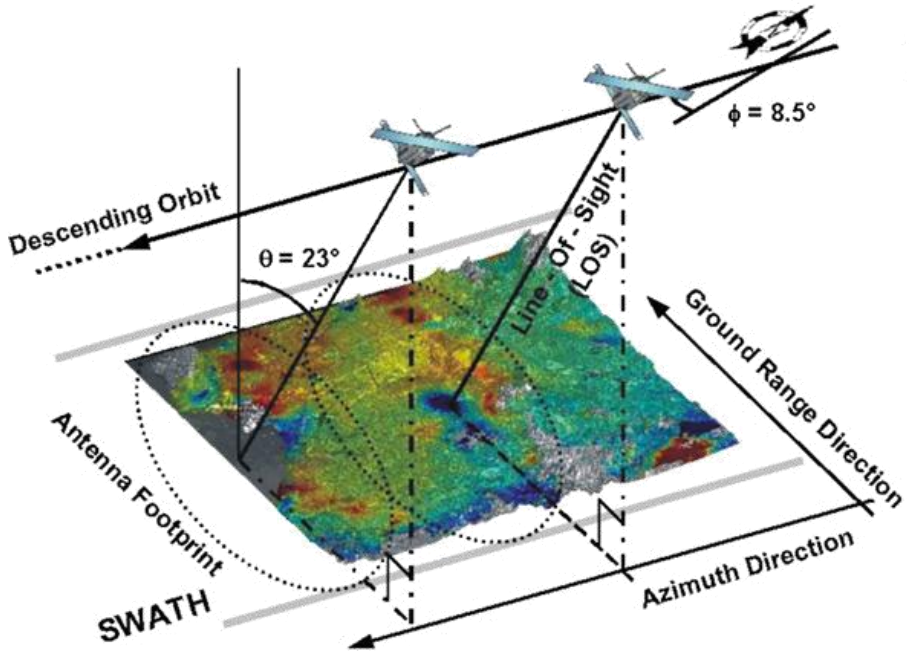

Figure 2-1. Geometrical issues concerning the satellite orbit and the reception of a SAR satellite [Courtesy of Colesanti and Wasowski, 2006].

According to the methodology of SAR interferometry the interference of signal detected from two different passes of the platform, from the same track, will be calculated, having the effect of the topography eliminated (differential interferometry).

The classic DInSAR technique has offered numerous examples for the reliable measurement of abrupt ground deformations. A single interferometric observation provides measurements of ground deformation on the line of sight of the satellite – target (scatterer). For the estimation of the deformation projected on the Cartesian reference system, at least three linearly independent observations are needed. Given the possibility of viewing the target from different angles and sides, this is feasible only from the satellite measurements. The accuracy of this method though, is limited by components relating to spatial and temporal decorrelation, signal delay due to tropospheric and ionospheric disturbances, orbital errors as well as Digital Elevation Model (DEM) artifacts.

Thus, almost any interferogram contains large areas where the signals decorrelate and no measurement is possible. If the surface is vegetated, weathers appreciably or is prone to snow coverage, the scattering properties change with time leading to a loss of interferometric coherence, a phenomenon known as temporal decorrelation [Li and Goldstein, 1990; Zebker and Villasenor , 1992]. Decorrelation also results in variations in imaging geometry. If the perpendicular baseline between the spacecraft position at the two times at which the images are acquired is non-zero, the difference in incidence angle alters the coherent sum of wavelets from the many small scattering elements within a resolution cell, so that measurements do not repeat exactly. This phenomenon, referred to as spatial decorrelation [Zebker and Villasenor, 1992], increases as the baseline increases. Thus, poor orbit control produces candidate InSAR pairs with excessive baselines that cannot be used to produce interferograms. A corresponding decorrelation results in changes in squint angle, the angle with which the spacecraft is pointed forward or backward. A change in squint angle alters the SAR Doppler frequency range leading to decorrelation. The squint angle on

the ERS-2 and Radarsat-1 satellites has, at times, not been well constrained. Although these decorrelation effects can be reduced by filtering, there are critical values of baseline and squint angle difference beyond which there is complete loss of interferogram coherence [Zebker and Villasenor , 1992]. In summary, even if SAR data are regularly acquired, temporal and spatial decorrelation limit the number of possible interferograms and hence temporal resolution.

After decorrelation, the next most significant limitation of conventional InSAR is the variation in the delay of the signal as it propagates through the atmosphere, which leads to an additional phase term that varies over the image [Hanssen, 2001]. Most of the variation in this term over the typical dimensions of an interferogram is due to variation in the distribution of water vapor in the atmosphere. The atmospheric phase term is, locally, correlated in space with the spectral power of the spatial variation in phase delay generally approximating a power law for areas lacking in significant topography. Where there is significant topography, there is further variation that correlates with surface height. As the time between spacecraft passes is of order of one month, the atmospheric signal is effectively decorrelated in time. A common method for reducing atmospheric signal is, therefore, to stack multiple interferograms acquired over time. However, any variation in the spatial or temporal nature of deformation over the period of the stack is then lost.

2.1.1. Interferometry Equations

Mathematical theory of InSAR has been elaborated in a number of references in details [Franceschetti et Lanari, 1999] and one can refer to them for more details. Certain equations, however, have key importance for the current research and are therefore referenced from the work of [Rosen et al., 1996], to support interpretation of the measurements and results.

The phase difference between the two scenes of an interferometric pair contains the variations of the satellite-ground distance during the acquisition time interval which is mainly projection of coseismic displacement vector on the satellite LOS direction.

The measured phase difference between two corresponding pixels is expressed by interferometry equation after precise co-registration of the two images, as follows:

$$\Delta\varphi = \varphi_{topo} + \varphi_{flat} + \varphi_{disp} + \varphi_{orbit} + \varphi_{atm} + \varphi_{noise} \quad (2.1)$$

where φ_{topo} is topography phase signature, φ_{flat} is flat earth phase caused by the imaging geometry, φ_{disp} is differential displacement pattern, φ_{orbit} is phase error caused by inaccurate orbit parameters, φ_{atm} is atmospheric artefacts and φ_{noise} refers to noise contribution.

Figure 2-2 shows interferometric geometry of two imaging Radar systems separated by baseline vector $\boldsymbol{B}$ which are in trajectories perpendicular to the page plane. Position 1 and

position 2 depicts the base (master image) and the nearly repeating its track imaging system (slave image), respectively.

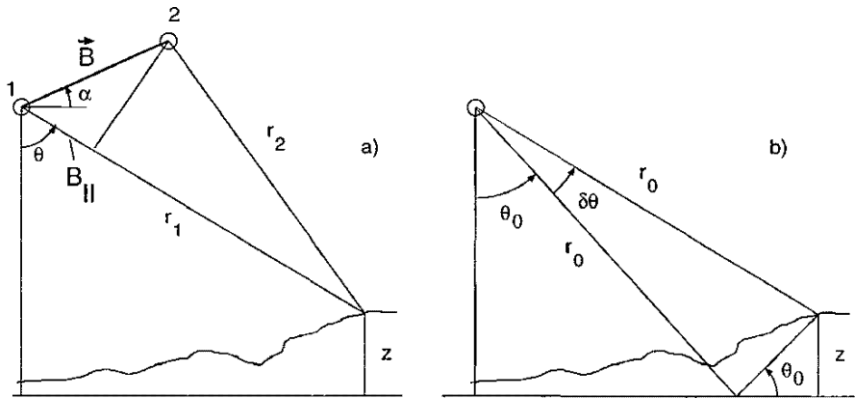

Figure 2-2. Courtesy of [Rosen et al. 1997] Interferometric geometry. (a) Two apertures separated by a baseline *B*, are flying into the paper imaging a swath on the ground (b) Conventions in linearizing the interferometer equations. The general term *Θ* is the angle of the Line of Sight.

The phase at each Radar image pixel is the sum of the backscattered and propagated phase (φ_{b_i} and φ_{p_i}, respectively). Propagated phase is equal to $4\ \frac{\pi}{\lambda}\ r_i$ where, r_i is the range from antenna i to the imaged point. The backscattered phase is nearly equal for two Radars imaging the same scene with same frequency and similar imaging geometry ($\varphi_{b_1} = \varphi_{b_2}$). By assuming these conditions - actually the SAR systems measuring the phase term in modulo 2π (one fringe) and a variation of one fringe corresponds to a variation in range along the Line of sight of $r_1 - r_2 = \lambda\ 2$ - the phase difference between the two Radar images at a given point can be calculated by the following equation.

$$\Delta\varphi = \varphi_1 - \varphi_2 = -\frac{4\pi}{\lambda}(r_1 - r_2) \tag{2.2}$$

In the case of satellite imaging geometry, where $B \ll r$, the previous equation can be written as:

$$\Delta\varphi = -\frac{4\pi}{\lambda} B\ l = -\frac{4\pi}{\lambda} B\ \sin(\theta - \alpha) \tag{2.3}$$

Where *l* is the unit vector in the LOS. Because :

$$B_{/\!/} = Bsin(\theta - \alpha) \tag{2.4}$$

Equation 2.3 implies that the phase difference is directly proportional to the component of $\boldsymbol{B}$ in the look direction. Equation is the so-called 'parallel ray approximation' which has been used by [Zebker et Goldstein, 1986]. In order to relate this phase to topography, a terrain surface without local topographic variations is considered. Thus,

$$\Delta\varphi_0 = -\frac{4\pi}{\lambda} B \sin(\theta_0 - \alpha) \quad (2.5)$$

where θ_0 is the look (or incidence) angle to a given point. When the topography is present, the look angle for a given range is altered by $\delta\varphi$ as shown in Figure 2-2. In this new condition, Equation 2.5 will change to:

$$\Delta\varphi_0 = -\frac{4\pi}{\lambda} B \sin(\theta_0 + \delta\theta - \alpha) \quad (2.6)$$

If flat earth phase component is removed from Equation 2.6, the 'flattened' phase difference is remained:

$$\Delta\varphi_{flat} = \Delta\varphi - \Delta\varphi_0 \cong -\frac{4\pi}{\lambda} B\, cos(\theta_0 - \alpha)\delta\theta \quad (2.7)$$

and because :

$$B_\perp = Bcos(\theta_0 - \alpha) \quad (2.8)$$

Equation 2.7 implies that flat earth phase component is directly proportional to the first order of perpendicular component of the baseline referenced to the flat earth and to the small angle, which is in turn proportional to topographic height z:

$$\delta\theta \cong \frac{z}{r_0 sin\theta_0} \quad (2.9)$$

The term 'height ambiguity' is equal to the change in elevation required to alter the phase difference by one cycle (2π radians) and is given by:

$$h_a = \frac{\lambda r_0 sin\theta_0}{2B_{\perp 0}} \quad (2.10)$$

The phase difference in repeat-pass interferometry measures all ground displacement between two passes, as well as topography. In the second image, the change in range due to displacement (Δ_r), enters into the phase difference equation directly:

$$\Delta\varphi_{flat} = -\frac{4\pi}{\lambda} B \cos\ \theta_0 - \alpha\ \ \frac{z}{r_0 sin\theta_0} + \frac{4\pi}{\lambda}\Delta_r \quad (2.11)$$

Equation 2.11 implies that in far range, phase difference is more sensitive to surface displacement than to topography itself. In this equation $\Delta_r = \lambda/2$ gives one cycle of phase difference, while *z* should change by $h_a$to make the same change.

The InSAR technique measures earth surface deformations along the satellite LOS direction (slant range) and is partially sensitive to variations perpendicular to this direction (azimuth). The range change observed with InSAR is projection of the displacement vector (**d**) on the sensitivity vector (**v**) as follows:

$$r = -\boldsymbol{v}^T \boldsymbol{d} \tag{2.12}$$

Where $\boldsymbol{d} = (d_x, d_y, d_z)^T$ is vector of east, north and vertical displacement of a point at the earth surface, and $\boldsymbol{v} = (v_x, v_y, v_z)^T$ is the unit LOS vector (sensitivity vector) expressed in the same local reference system, pointing from ground to the satellite.

2.1.2. Simple Stacking of interferometric products

This method is the temporal averaging of unwrapped and linear trend removed differential interferograms in order to increase the S/N ratio in cases of a rapid/episodic deformation event as an earthquake [Elias et al., 2006].

In the present thesis we have used the following procedure. The selected differential interferograms have been unwrapped by SNAPHU software [Chen et Zebker 2002]. From all the interferograms we have excluded from any posterior calculations the pixels falling into the sea, the areas without the existence of deformation information and the areas where the absolute modeled deformation value is above 10mm. In order to minimize any linear orbital and low frequency tropospheric effect we have followed the following procedure. We partitioned each interferogram in a number of horizontal and vertical zones of 50 pixels, each. Then, for all the interferograms we applied a linear least square fitting to remove any N-S trend slope of the average values of the horizontal zones. The same procedure has been followed for the E-W trend with the vertical zones. Simultaneously the mean value of each interferograms has been set to zero.

Additionally, in the case of Movri earthquake we removed the linear correlation between the topography and the deformation.

2.1.3. Multi-temporal InSAR techniques (PSI/SBAS)

Multi-temporal InSAR techniques, involving the processing of multiple acquisitions in time, provide one way to address these issues. Currently, there are two broad categories: Persistent Scatterer methods including those that identify pixels based primarily on their phase variation in time [e.g., Ferretti et al., 2001; Kampes, 2005] and those that use primarily correlation of their phase in space [e.g., Hooper et al., 2004; van der Kooij et al., 2006], and small baseline methods [e.g., Berardino et al., 2002; Schmidt and Burgmann, 2003]. The naming of the categories is inconsistent in that ‘Persistent Scatterer’ refers to the type of pixel that is identified whereas ‘Small Baseline’ refers to the methodology of interferogram formation [Hooper et al., 2008].

Persistent Scatterer InSAR (PSI) is an extension to the conventional InSAR techniques described above, which addresses the problems of decorrelation and atmospheric delay. The degree of decorrelation within a pixel depends on the distribution of scattering centers on the ground that contributes to that pixel. In a radar image, the reflected wave from a resolution element is the coherent sum of individual wavelets scattered by many discrete scatterers. Constructive and destructive interference of these wavelets gives rise to variation in the phase and amplitude of the pixel with both different viewing angle and relative movement of the scatterers. if the individual scatterers contribute to the pixel move randomly over time, by large distances compared to the radar wavelength or are viewed from considerably different angles due to a too large $B_{/\!/}$, its phase echoes will simulate complete temporal decorrelation, although simulating complete spatial decorrelation would produce the same variation in phase, that is, phase that varies over the full $\pm\pi$ radians range and is effectively random. In contrast, if one of the scatterers contributing to the pixel is much brighter and stable in time than the others, the largest contributor to the phase is the wavelet from the brighter scatterer and there is little interference from the other scatterers. The signal received for this pixel varies little as the other scatterers move around, and any motion of the scatterer can be readily measured by the phase of the radar echo.

If the phase of a pixel was determined by just one point scatterer, the decorrelation would be reduced to zero and all radar images of the area would form usable interferograms. Although this is rarely the case, there are pixels where one scatterer dominates the echo and which behave somewhat like point scatterers, so that decorrelation is greatly reduced. This is the model for a PS pixel. Physically this might be the corner of a building, a tree trunk dominating contributions from smaller branches and leaves, or a single large rock or facet amidst rubble on a lava flow. One can thus obtain useful data from all image pairs enabling the formation of a series of interferograms, all referenced to the same “master” scene. The atmospheric delay signal can then be estimated and removed by filtering of the resulting phase time series obtained for each of the PS pixels.

An algorithm to exploit PS pixels was first achieved by Ferretti et al. [2000, 2001]. They have patented this procedure and refer to it as the “permanent scatterers’ technique”. It is based on the identification of target-scatterers with a stable radiometric behavior in time (therefore, being less influenced by the environing natural parameters and preserving their reflective properties constant in time) and by estimating and removing part of the noise, rendering them reliable points of measurement. This technique insures the minimization of noise and the measurement of linear or nonlinear deformation phenomena in the Line Of Sight of the satellite which in case of I2 acquisition mode of ASAR/ENVISAT is almost vertical, in the scale of a few mm $year^{-1}$. PS (Persistent of Permanent Scatterers according to the methodology used) pixels are identified as those pixels whose phase histories match an assumed model of how displacement varies with time. This functional model of temporal displacement (e.g. linear model) to identify PS pixels, approximate knowledge of how the deformation varies with time is required a priori. Commonly, deformation is assumed to be steady-state or periodic in nature. However, in deformation studies the temporal nature of the deformation is usually one of the phenomena that we wish to determine. Volcanoes, for example, often deform in a very episodic and non-steady fashion. The temporal pattern of deformation during transient fault slip events and postseismic deformation is also not known a priori.

Since then, in literature other research teams have developed slightly different or similar approaches aiming to noise minimization and signal enhancement by using large SAR data volumes having similar detection characteristics (side-looking and observation angle, signal frequency, satellite system, signal polarity) [Kampes 2005; Lanari et al., 2004; Crosetto et al. 2003 ; Werner et al. 2003a, 2003b; Lyons and Sandwell 2003;Van der Kooij, 2003; Duro et al., 2003, Usai 2003, 2002; Le Mouélic et al., 2003; Costantini et al., 2001, 2002].

In addition to the PS approach, Small BAseline Subset (SBAS) method [Bernardino et al., 2002], which is based on different combination of the available SAR interferograms relative to a study area, will be used. The SBAS technique relies on an appropriate combination of differential interferograms characterized by a small orbital separation. This reduces the spatial decorrelation phenomena. This technique provides two key advantages: (1) increased sampling rate by using all the acquisitions included in the small baseline subsets and (2) preserved the capabilities of the system to provide spatially dense deformation maps, which is a key issue of the conventional InSAR method [Casu et al., 2006].

This technique is ideal for measuring small-scale ground deformation due to displacements in active fault zones [Colesanti at al., 2003 ; Crosetto et al., 2003] or to subsidence occurring from manmade constructions and drilling activities.

There has been some debate about the relative merits of PS and SB approaches. However, as they are optimized for different models of ground scattering, the two approaches are in fact complementary, at least in the usual case where a data set contains pixels with a range of scattering characteristics. In the thesis we have used the approach of PSI and SBAS of [Hooper 2008]. This approach also maximizes the spatial sampling of the useable signal. Improvement of the spatial sampling is important not only because the resolution of any deformation signal is increased, but also because it allows for more reliable estimation of integer phase-cycle ambiguities present in the data (phase unwrapping).

Other methodologies are squeeSAR, for combining PS and DS (Distributed Scatterers), which has been proposed by [Ferretti et al., 2011] and Interferometric Point Target Analysis (IPTA), a specific method of PSI to exploit temporal and spatial characteristics of interferometric signatures collected from point targets to map scatterer deformation history [Werner et al., 2003].

The PSI/SBAS software used in the present work is StaMPS/MPI. StaMPS (Stanford Method for Persistent Scatterers) is a software package that implements an InSAR persistent scatterer method developed to work even in terrains devoid of man-made structures and/or undergoing non-steady deformation. StaMPS/MTI (Multi-Temporal InSAR) [Hooper 2010, Hooper 2008; Hooper et al. 2007; Hooper et al., 2004] is an extended version of StaMPS that also includes a small baseline method and a combined multi-temporal InSAR method.

StaMPS also computes the standard deviation of the deformation rate using the bootstrap technique. The idea of this technique is to find the sample distribution using a number samples as the statistical inference is based on the sample distribution. This is achieved by resampling i.e., by selecting random samples from population. In this case resampling is done with replacement. The re-sampled populations are then used to estimate the linear

regression coefficients. Hence, the deformation rate is computed for each time the resampling was done. The deviation of these mean values gives the standard deviation (σ) of the deformation rate.

Some of the PSI/SBAS output maps present artifacts and specifically trend slopes (ramp) across the longitude dimensions (as in Figure 2-22). The correction of this artifact is performed by the proposed method.

2.2. GPS

The GPS consists of almost 27 active satellites that can be used to position a geodetic receiver with an accuracy of millimeters within the ITRF. To do this requires geodetic-class receivers (operating at two frequencies, and with antennas designed to suppress signal multipath), currently costing a few thousand US dollars, and geodetic research-class software (developed by various universities and government institutions around the world). Such software embody leading-edge models (of the solid Earth, atmosphere and satellite dynamics) and data processing algorithms (signal processing and stochastic parameter estimation).

Many of the models have been developed as a result of much research conducted by the international geodetic and geophysical community, often specifically to improve the accuracy of GPS. Today it is even possible for a nonexpert to collect GPS data and produce receiver positions with centimeter accuracy by using an Internet service for automatic data processing.

In geophysics, GPS measurements have been widely used over the past decade to monitor crustal displacements, with precision levels on the order of 2-3 mm/yr (horizontally) now routinely achieved.

As pointed, Geodesy can be used to investigate motions of the Earth's surface on timescales of seconds to decades, and so is an appropriate tool to study all phases of the earthquake cycle [Hammond, 2005]. Figure 2-3 schematically illustrates the expected characteristics of geodetic position time series as a function of time and distance from a fault through the earthquake cycle. In this specific example, the fault is strike slip (Figure 2-4) with two stations either side of the fault located at equal distance normal to the fault strike.

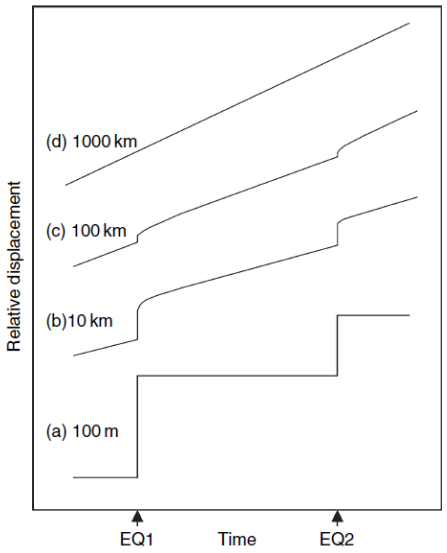

Figure 2-3. Courtesy of [Blewitt 2007]. Schematic illustration of the effect of the earthquake cycle on geodetic station positions.

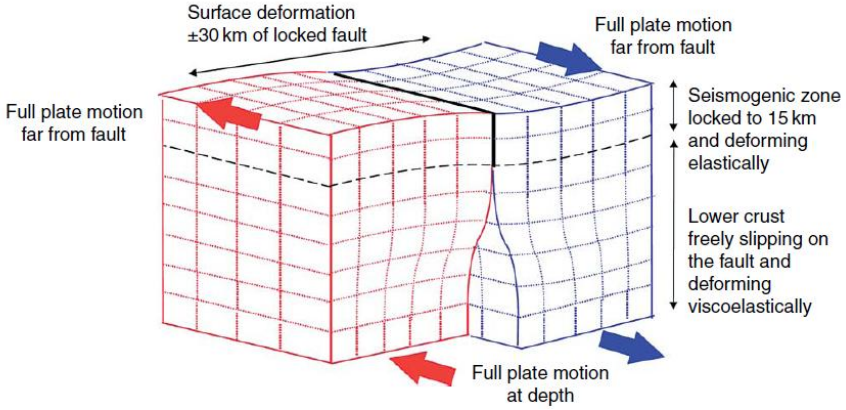

Figure 2-4. Courtesy of [Blewitt 2007]. Deformation around a transform plate boundary, such as the San Andreas Fault.

'Displacement' is defined as the relative position of the two stations in the direction parallel to the strike of the fault. Each curve represents a different distance from the fault (that is, half the distance between stations). For purposes of illustration, the plot is not to scale. The plot shows the time of characteristic earthquakes EQ1 and EQ2, which are of the largest magnitude that can typically occur on this particular fault, because smaller earthquakes produce displacements so small that they can be neglected for purposes of illustrating the earthquake cycle. Thus EQ1 and EQ2 represent the start and end of an earthquake cycle. The size of these earthquakes (M_W~7) is sufficient and they rupture from seismogenic depth through to the surface, with co-seismic slip approximately constant with depth. Case (a) at distance 100m shows a displacement equal to the co-seismic slip on the rupture plane. In between earthquakes, the distance between stations is so small that no deformation is detected. Hence case (a) is effectively equivalent to a geological determination of co-seismic fault slip. In the opposite extreme, case (d) at 1000 km from the fault in the far field shows no detectable co-seismic displacement. (This assumes naively that this is the only active fault

in the region of this scale or any ground surface deformation from other sources). This displacement represents the far-field driving force transmitted through the crust that ultimately causes the earthquakes. In a sense, the earthquake represents the crust 'catching up' to where it would be if the fault was continuously sliding as a frictionless plane. Thus, case (d) shows the same average displacement per year as would a regression to curve (a) over a sufficient number of earthquake cycles. Thus, case (d) also represents: (1) the slip rate at depth below the locked (seismogenic) portion of the crust, assuming the crust behaves perfectly elastically; and (2) the mean slip rate inferred by geological observations of recent Quaternary earthquakes over several earthquake cycles, assuming that the activity of this fault is in steady state equilibrium and is not evolving in time. Case (b) represents the strain accumulation and release where strain rates are highest in the near-field of the fault. In this case, the co-seismic displacement is slightly damped due to the co-seismic rupture being of finite depth. On the other hand, the time series captures subsequent near-field postseismic effects following each earthquake [Pollitz, 1997]. These processes include afterslip (creep) caused by a velocity-hardening rheology, and poroelastic relaxation in response to co-seismic change in pore pressure. Significant aftershock might in some cases be a contributing factor. These processes affect GPS position time series in the days to months following the earthquake [Kreemer et al., 2006]. Over periods of years to decades, the strain for case (b) is slowly released in the viscoelastic layers beneath the crust which will affect the time series. This occurs because at the time of the earthquake, the crust displaces everywhere and stresses the layers beneath. These layers react instantly as an elastic medium, but as time increases, they start to flow viscously. As the time series ages toward the second earthquake EQ2, most of the viscoelastic response has decayed, and the time series becomes flat. This represents the phase of interseismic strain accumulation. However, the slope of this part of the curve is significantly lessened owing to transient postseismic processes earlier in the earthquake cycle. Thus, near field measurements of strain alone can significantly underestimate the seismic hazard unless this is taken into account. This dampening phenomenon also makes it more difficult to pinpoint the location of active faults capable of generating large earthquakes. Stations in case (c) are still sufficiently close that co-seismic displacements can be detected but are far enough from the rupture that near-field relaxation does not contribute to the time series. On the other hand, the crust in this intermediate field responds significantly to deep viscoelastic relaxation at the base of the crust and beyond, into the upper mantle. Precisely how the pattern of deformations looks in the years after a large earthquake depends on the relative effective viscosity of these various layers [Hetland and Hager, 2006]. Thus GPS networks with stations at various distances about a recently ruptured fault can be used to probe rheology versus depth. Note that in going from EQ1 to EQ2 the relative velocity between the pair of stations decreases in time. Thus, the strain rate can depend considerably on the phase of the earthquake cycle (Dixon et al., 2003). Thus, in regions of low strain were there are many faults that rupture infrequently (such as the Great Basin, western USA) it is not uncommon to observe strain rates that are almost entirely transient in nature and can exceed interseismic strain by an order of magnitude [Hetland and Hager, 2003; Gourmelen and Amelung, 2005). This makes it more difficult to interpret strain-rate maps in terms of seismic hazard, except in those cases where the strain rates are so large that logically they must be dominated by interseismic strain accumulation on dominant faults [Kreemer et al., 2006]. Such analysis is

on the leading edge of research, and requires careful modeling of the earthquake cycle in any given region of interest.

2.3. Data Description

2.3.1. Digital Elevation Model

For the shaded reliefs and the processing of ASAR data we have used Ktimatologio DEM, (original in 5mx5m cell size), created for the needs of Hellenic Cadaster by aerial photogrammetry. For the PSI/SBAS processing the same DEM has been reprojected from traverse Mercator projection of GGCS87 Datum with cell size of 5mx5m to geographic projection of WGS84 datum with cell size 0.0002°N x 0.0002°E by using a bilinear interpolation.

2.3.2. Synthetic Aperture Radar Earth Observation data

For the present study we have used SAR ASAR/ENVISAT (C-band) data of both ascending and descending tracks and ascending PALSAR/ALOS (L-band) acquisitions. The main findings and all the PSI/SBAS maps were rendered with ASAR data. The PALSAR data have been used for the inspection of the detection of Movri 2008 earthquake deformation field, exploiting its advantage (over C-band) of L-band resulting to interferograms with better coherence.

For the area on the GoC and for the PSI/SBAS processing we have used 35 acquisitions of descending track 279 (dated between 20/10/2002 and 3/10/2012) and 29 of ascending 415 (dated between 11/2/2003 and 9/2/2012) (Figure 2-5). The acquisition dates versus the baselines and the interferograms calculated for SBAS processing of the descending track are shown in Figure 2-6 and for the ascending in Figure 2-7. Their volume is 252 and 123 for descending and ascending track, respectively.

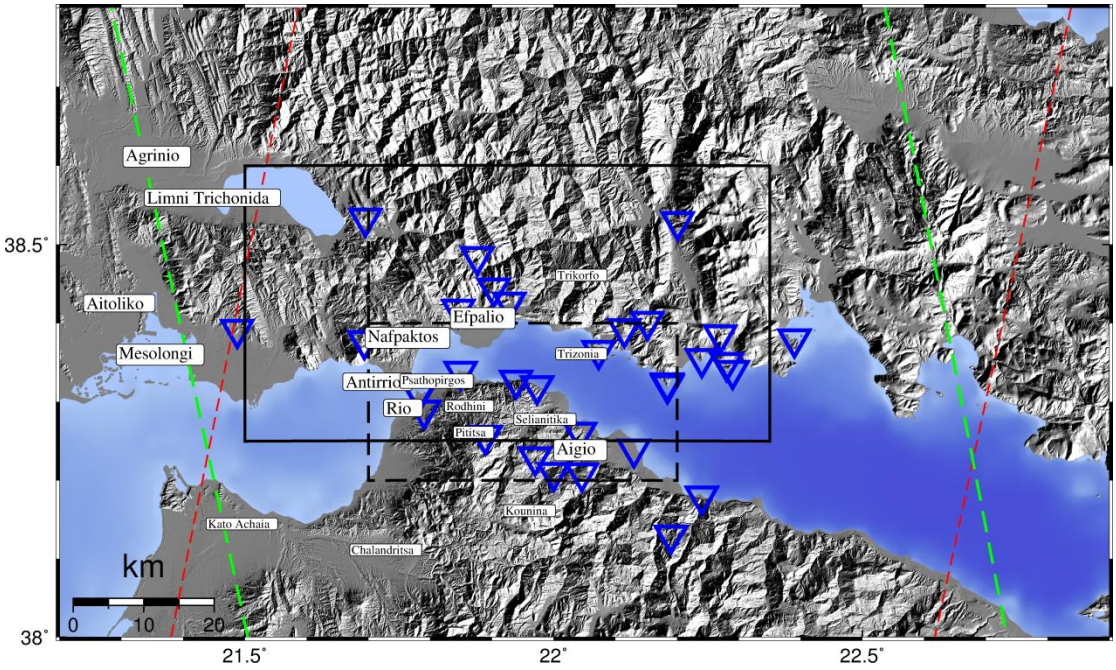

Figure 2-5. Shaded relief of the western GoC area. In solid black line the North Side of GoC that is investigated is marked. In dashed black line the South side of GoC that is investigated is marked. Red dashed lines indicate

the swath of the descending tracks track no. 279. Green dashed lines indicate the swatch of the ascending track no. 415. Reversed blue triangles spot the locations of the GPS measurements used in the thesis.

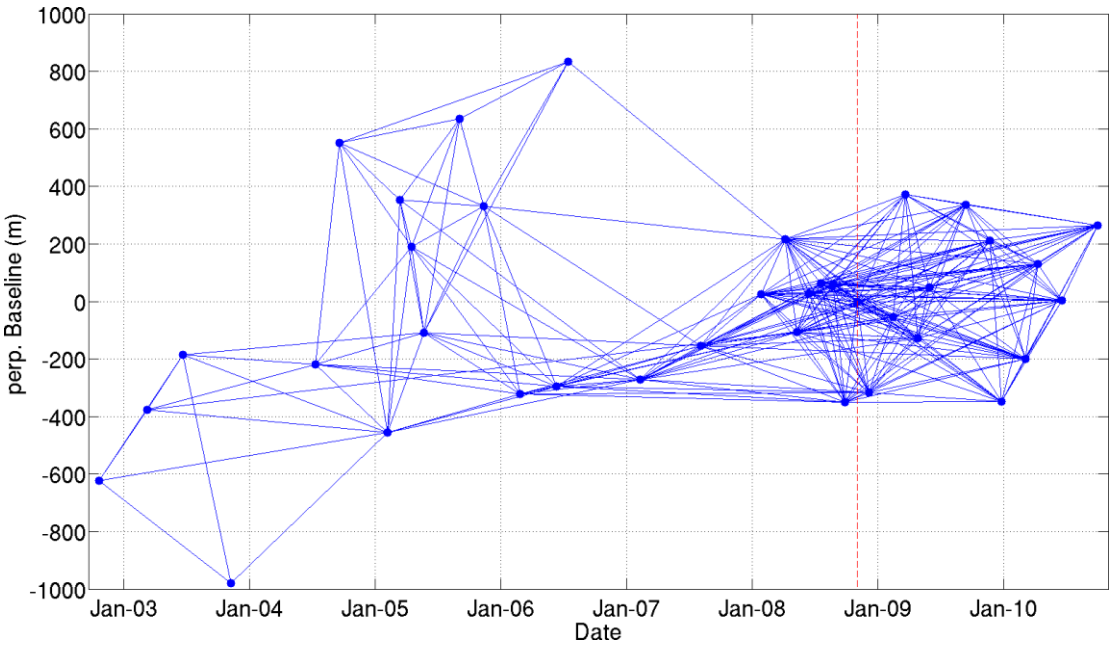

Figure 2-6. The acquisition dates versus the baselines for the descending ASAR track 279 are shown in points. The interferograms calculated for SBAS processing are indicated with lines. The dotted red vertical line represents the date of the master acquisition used in the PS processing.

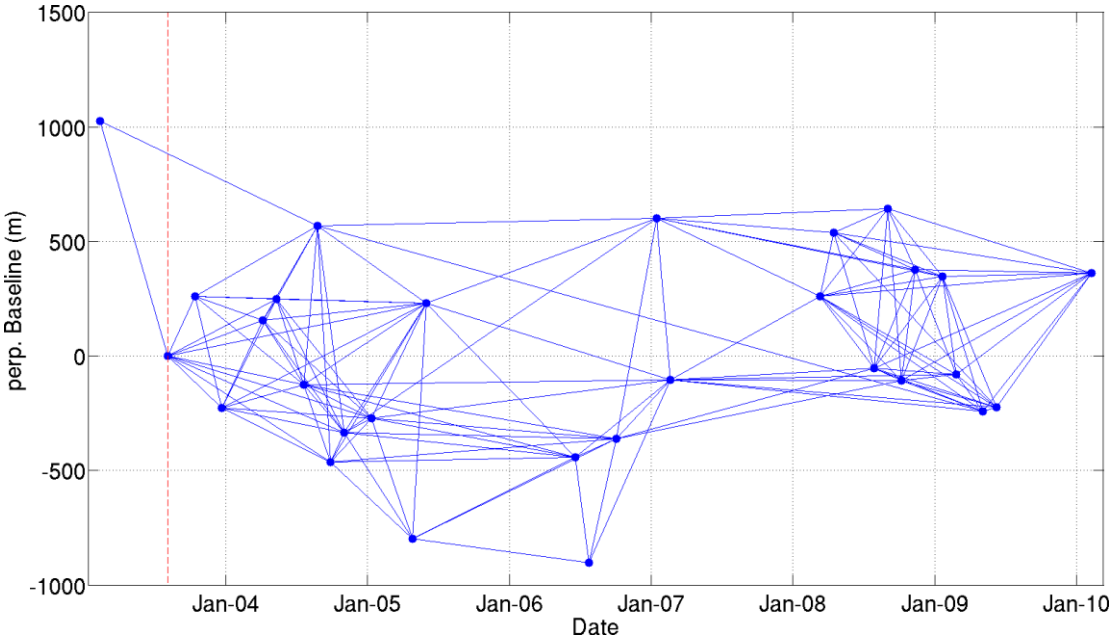

Figure 2-7. The acquisition dates versus the baselines for the ascending ASAR track 415 are shown in points. The interferograms calculated for SBAS processing are indicated with lines. The dotted red vertical line represents the date of the master acquisition used in the PS processing.

For the area of Aetoliko (Figure 2-8) and for the PSI/SBAS processing we have used 25 acquisitions of descending track 50 (dated between 2/5/2003 and 4/6/2010) and 25 of ascending track no. 186 (dated between 17/11/2002 and 19/4/2009). The acquisition dates versus the baselines and the interferograms calculated for SBAS processing of the descending track are shown in Figure 2-9 and for the ascending in Figure 2-10. Their volume

is 86 and 116 for descending and ascending track, respectively. The master acquisition (19/8/2005) has been selected such that it forms the most proper baselines (ideally 100m<$B_{\perp}$<300m) with the rest of them.

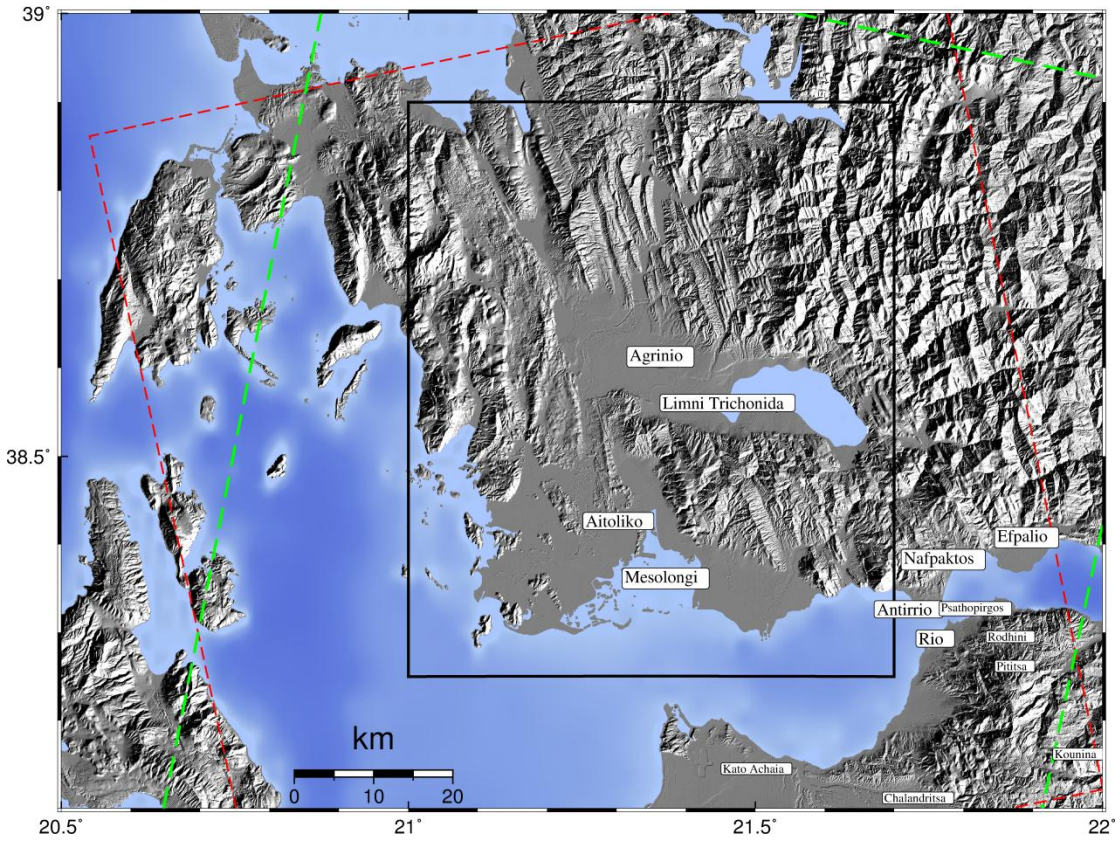

Figure 2-8. Shaded relief of Aetoliko (North-West of GoC) area. In solid black line the area of Aetoliko that has been investigated is marked. Red dashed lines indicate the swath footprint of the descending ASAR tracks no. 50. Green dashed lines indicate the swatch of the ASAR ascending track no. 186.

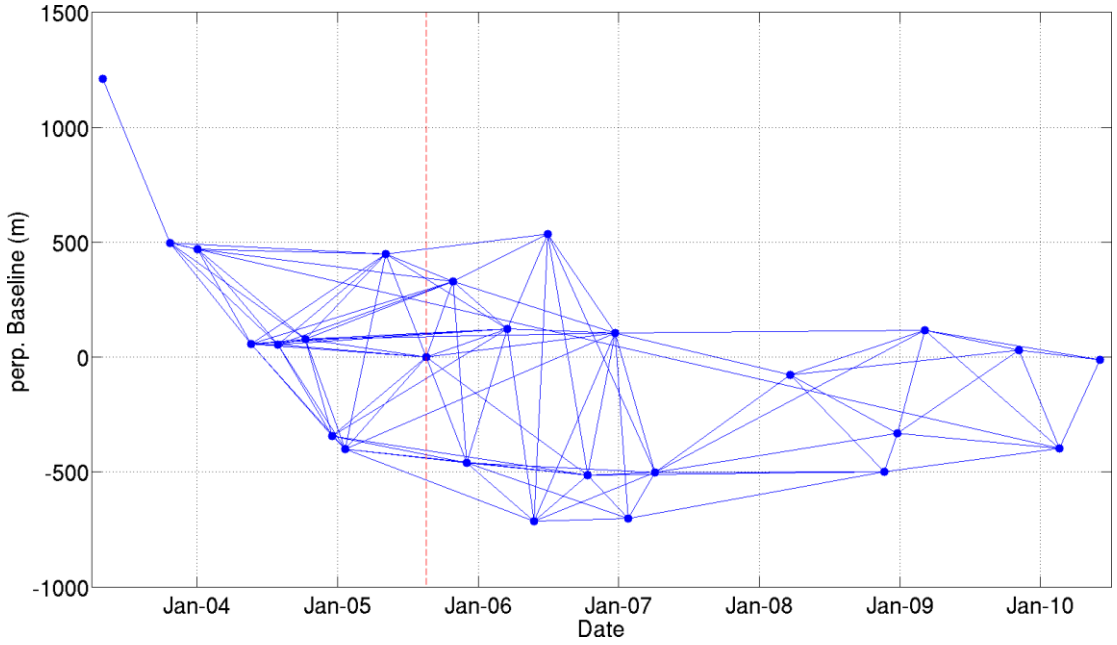

Figure 2-9. The acquisition dates versus the baselines for the descending ASAR track 50 are shown in points. The interferograms calculated for SBAS processing are indicated with lines. The dotted red vertical line represents the date of the master acquisition used in the PS processing.

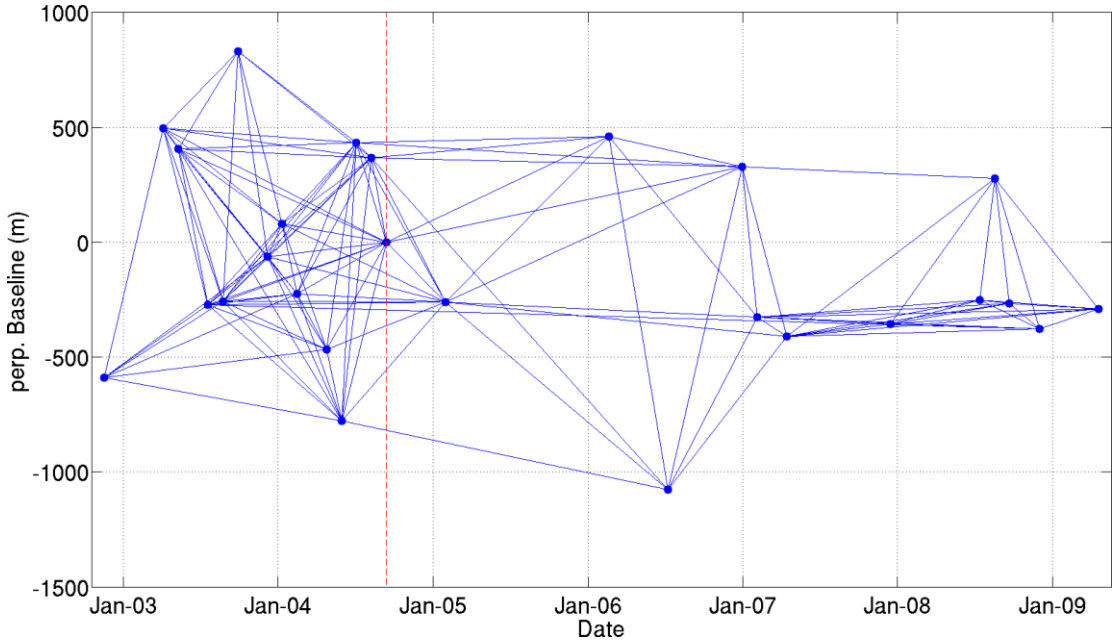

Figure 2-10. The acquisition dates versus the baselines for the ascending ASAR track 186 are shown in points. The interferograms calculated for SBAS processing are indicated with lines. The dotted red vertical line represents the date of the master acquisition used in the PS processing.

For the Processing of PALSAR/ALOS interferograms (for the Movri 2008 earthquake we have used a set of 15 ascending acquisitions of Track624, having incidence angle of 34°, dated between 21/12/2006 and 31/3/2010.

2.3.3. GPS data

The GPS data used in the thesis (Figure 2-5) are from campaign network [Briole et al. 2000; Avallone, 2003; Muller 2011] since 1990 and permanent network [Briole et al. 2000; Avallone, 2003] since 2000. The permanent network includes the stations, KOUN, TRIZ, LIDO, EYPA, PSAR and LAMP (Figure 2-28, Figure 2-35). These stations could provide a good estimation of the Up-Down component also. The non-permanent (campaign) stations provided only planar components. Deformations induced by episodic events, as the Movri 2008 earthquake, have been removed from the observation sequence. By default the GPS measurements have been transformed from ITRF2008 to stable Achaia by shifting the East component by -8.5 mm and the North component by 10.5 mm. Where stated the GPS measurements have been transformed from stable Europe to stable Fokida by shifting the East component by -12 mm and the North component by -3 mm.

The GPS data used are mainly of two kinds (a) from permanent GPS stations and (b) from GPS campaigns (including static and kinematic) that were organized from time to time.

The permanent stations (Figure 2-11) can provide, of course, continuous and more precise data since almost the only main noise component is the atmospheric disturbances. The standard deviation of the vertical is ~2 cm. In ten years of measurements the level of 2mm $year^{-1}$ is achievable in the ideal case. The permanent network used can be seen in Figure 2-28 and Figure 2-35.

Figure 2-11. Permanent station of Psaromita cape. The antenna is visible on the edge of the building roof.

The campaign GPS measurements are the second type of GPS observation. It demands very good preparation and a lot of resources in terms of manpower, materials and time. Many practical issues may arise and the surveyor should be prepared in advance. Generally, there are three ways of setting the GPS antenna in the reference point. The acquisition accuracy depends on the type of it and of course on the experience and the concentration of the surveyor. These are:

- Mounting the antenna on the reference point. In this case the antenna is screwed on the pillar (Figure 2-12a) or on the rock (Figure 2-12b). This is the most accurate method used for the planar measurements. For the UDc is also the most accurate if the antenna plate is leveled. It is possible to fine tune the leveling because the antenna is screwed on the reference point. Slight offset from the right leveling will produce errors mainly in the UDc.
- Placing the antenna on a triblock (Figure 2-13), performing centering to the referencing point, leveling the antenna plate and measuring the height of it from the top surface of the pillar. There is almost always a horizontal misfitting of at least ~2 mm. Considering that a good record of the antenna height from the top of the pillar surface will always be kept the fact that the leveling is possible makes the measuring of the UDc more accurate.
- Stabilizing the antenna over the reference point in a tripod (Figure 2-14). This procedure demands a lot concentration and experience. It may produce large errors but it is the only way to have dense measurements.

All the GPS measurements are provided with uncertainty values. For all the measurements much effort has been put in in order to keep the irregularities of the equipment as few as possible, the antennas were all of the same type, photographic and written records as well as tracking of all the actions that have been performed and the materials and the equipment that have been used, in the field, have been kept.

(a) (b)

Figure 2-12. GPs antenna mounted on (a) pillar and (b) solid rock.

Figure 2-13. Placing the antenna over triblock and over pillar.

(a)

(b)

Figure 2-14. Stabilizing the antenna over the reference point with two different kinds of tripods.

2.3.4. Seismic data

The relocated seismic data for the investigation of Movri 2008 earthquake has been provided from [Serpetzidaki et al., in preparation ; Ilieva 2011]. Aftershocks have been recorded using a local network installed one week after the mainshock for a period of 4 months. The map and cross section show the relocated seismicity, colors correspond to various clusters identified.

The relocated seismic data for the investigation of Efpalio 2010 concern aftershocks that have been recorded by the permanent stations of CRL plus two additional stations installed on January 22, 2010 [Lyon-Caen et al., in preparation].

2.3.5. Fault vectors

The CRL (Corinth Rift Laboratory) fault vectors that have been used in the map or the current study are from project "*Hazard, seismogenic dynamics, and seismic/aseismic coupling of an active fault system in the western Rift of Corinth, Greece (SISCOR)"*.

2.4. ASAR/ENVISAT PSI/SBAS processing

Following the STaMPS procedure we calculated the initial combined PSI/SBAS deformation maps for both ascending and descending tracks for the South and the North Gulf of Corinth area as defined in Figure 2-5. Note that all the values correspond to linear deformation rate in mm year^{-1} with arbitrary reference point and along the LOS direction.

2.4.1. South Gulf of Corinth

For the South GoC (Figure 2-5) we have combined the descending track no. 279 (Figure 2-6) and ascending track no. 415 (Figure 2-7).

For the acquisitions of South GoC the one of 2/11/2008 has been used as master for the PS processing (Figure 2-6). For the PS map with an amplitude dispersion index of 0.4, a number of 27850 PSs have been calculated. For the SBAS processing with an amplitude dispersion index threshold of 0.6, minimum coherence threshold 0.5, time for total decorrelation threshold 1500 days and a critical baseline 1070m a number of 252 interferograms have been processed and 45358 PSs have been calculated. After the merging of them a number of 71195 PSs have been finally calculated. Its standard deviation map is shown in Figure 2-15. Note that due to the color scaling that is extended it is not easy to discriminate all the inferred discontinuities. In the following sections focus will be given to each area and a more appropriate color scale will be given.

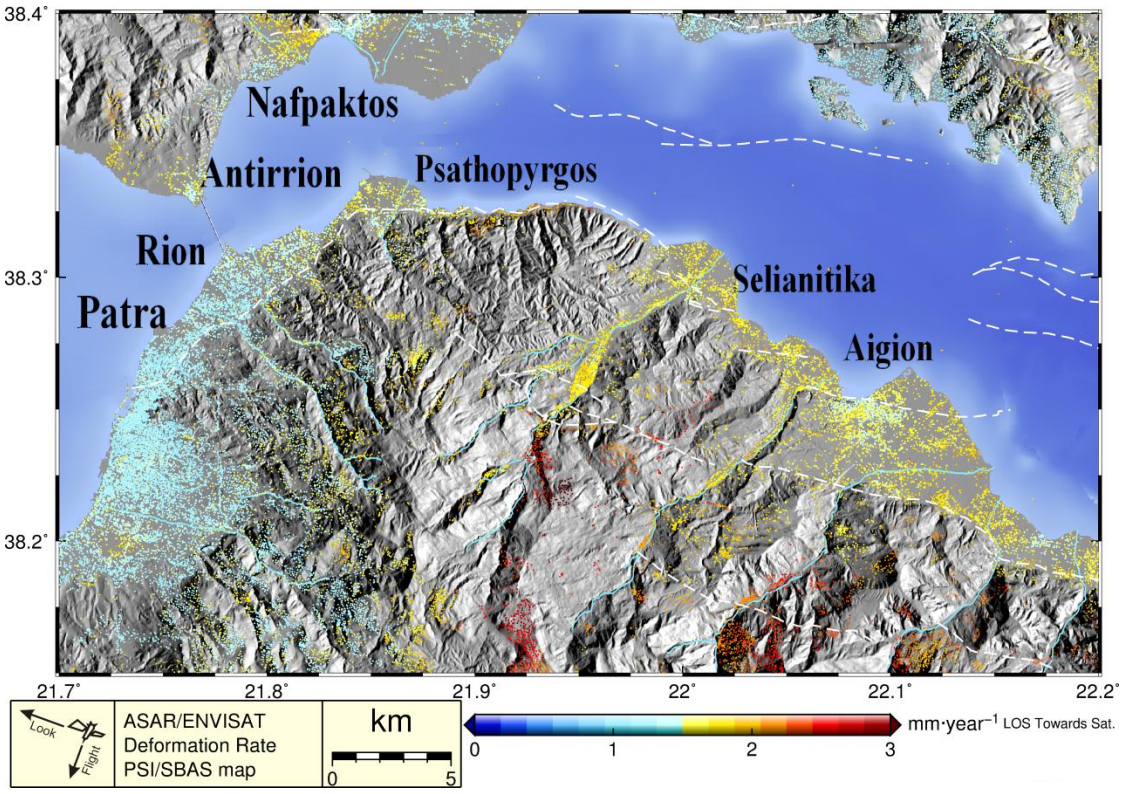

Figure 2-15. PSI/SBAS Standard deviation map of the South study area, descending track no. 279.

Its deformation rate map is shown in Figure 2-16. In this map we can clearly see discontinuities in the city of Patras, Rio, Psathopyrgos, and Sellianitika.

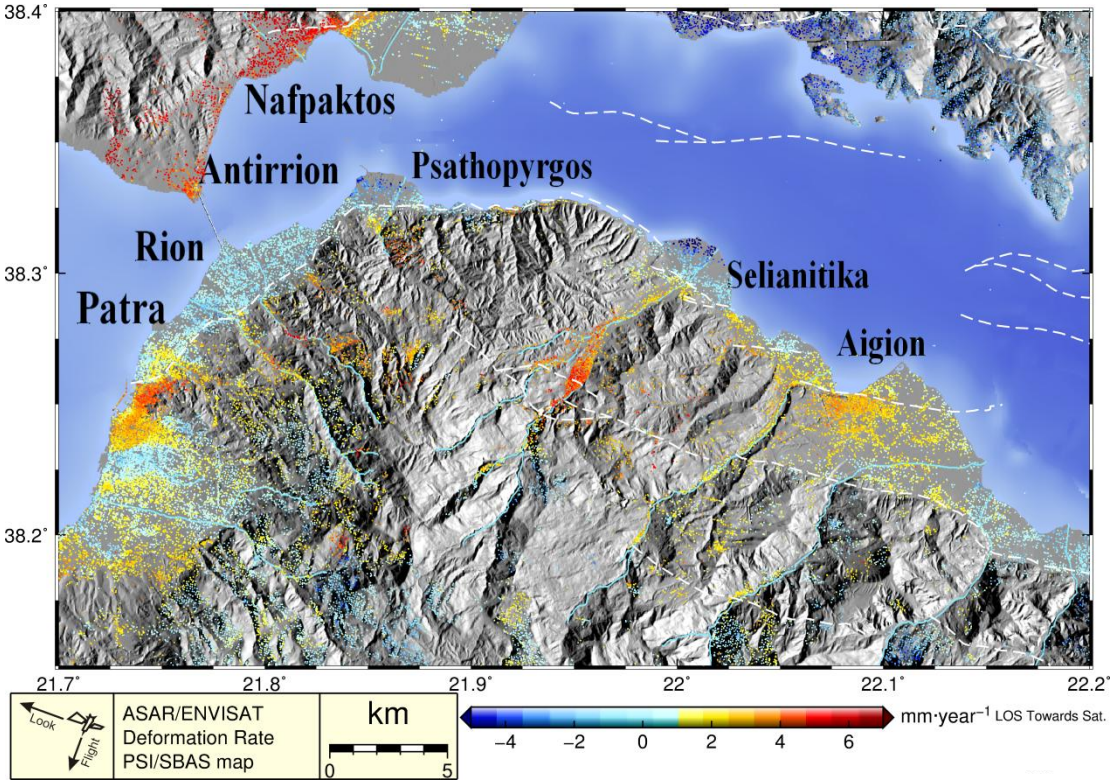

Figure 2-16. PSI/SBAS LOS rate map of the South study area, descending track no. 279.

The high vegetated land cover, the increased abrupt slopes, the high precipitation rates and the increased moisture levels of the area away from the coast are sources of temporal decoherence for the PSI/SBAS chain. For this reason we have quite few Persistent Scatterers left mainland and more in the coast where at least the abrupt slopes are much less.

For ascending track no. 415 the acquisitions of 5/8/2003 have been used as master for the PS processing. For the PS map with an amplitude dispersion index of 0.4, a number of 29171 PSs have been calculated. For the SBAS processing with an amplitude dispersion index threshold of 0.6, minimum coherence threshold 0.5, time for total decorrelation threshold 1700 days and a critical baseline 1070m a number of 123 interferograms have been processed and 37438 PSs have been calculated. After the merging of them a number of 64322 PSs have been finally calculated.

Its standard deviation map is shown in Figure 2-17. Its deformation rate map is shown in Figure 2-18.

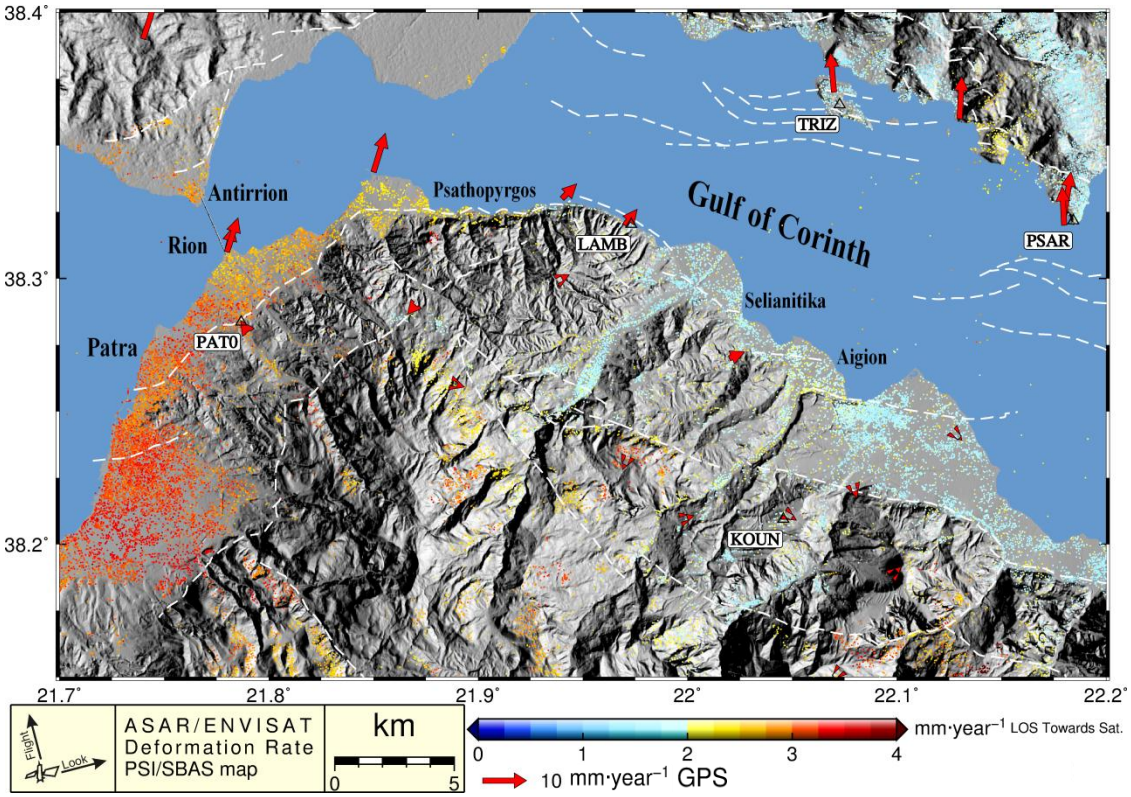

Figure 2-17. PSI/SBAS Standard deviation map of the South study area , ascending track no. 415.

In this map we can clearly spot discontinuities in the city of Patras, Rio, Psathopyrgos, and Aigion.

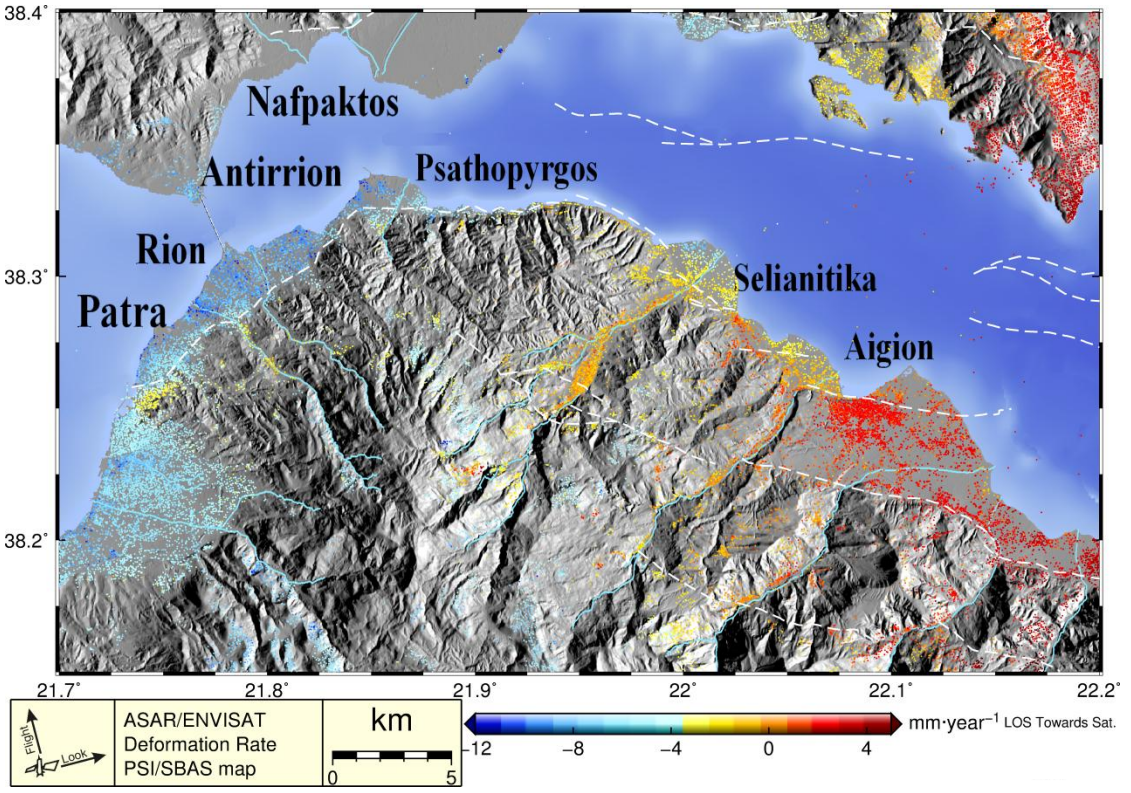

Figure 2-18. PSI/SBAS LOS rate map of the South study area, ascending track no. 415.

2.4.2. North Gulf of Corinth

For the North GoC (Figure 2-5) we have combined as it will be explained later the descending track no. 279 (Figure 2-6) and ascending track no. 415 (Figure 2-7).

For descending track no. 279 the acquisition of 2/11/2008 has been used as master for the PS processing. For the PS map with an amplitude dispersion index of 0.4, a number of 31022 PSs have been calculated. For the SBAS processing with an amplitude dispersion index threshold of 0.6, minimum coherence threshold 0.5, time for total decorrelation threshold 1500 days and a critical baseline 1070m a number of 252 interferograms have been processed and 56009 PSs have been calculated. After the merging of them a number of 85049 PSs have been finally calculated. Its standard deviation map is shown in Figure 2-19.

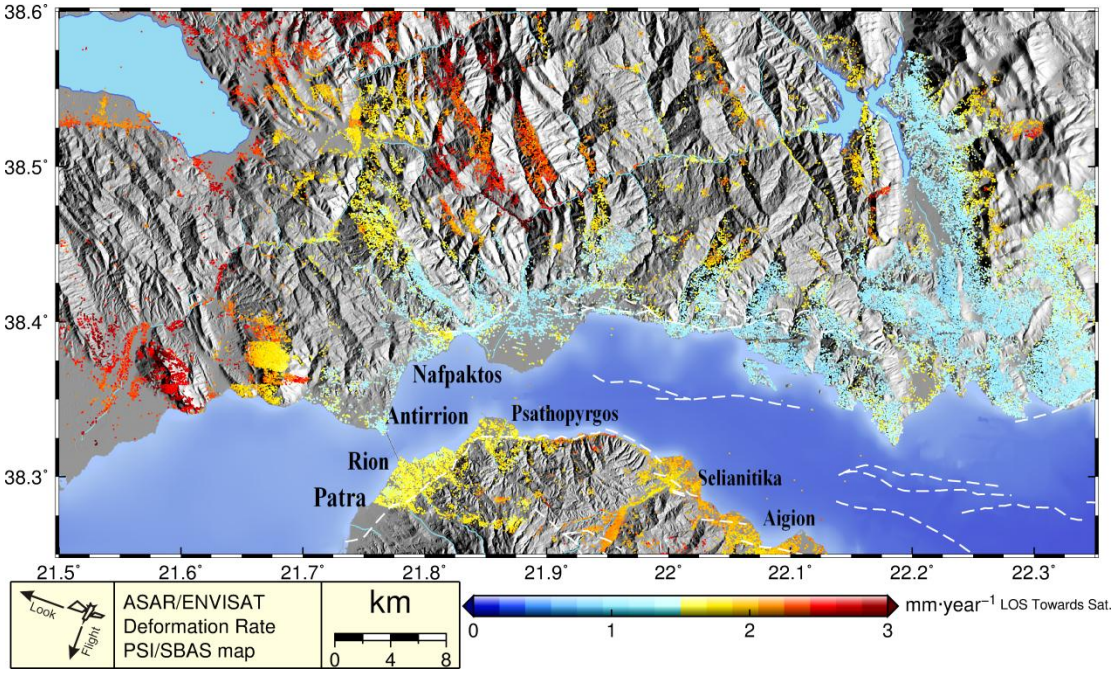

Figure 2-19. PSI/SBAS Standard deviation map of the North study area, descending track no. 279

Its deformation rate map is shown in Figure 2-20. In this figure we can spot main discontinuities in Nafpaktos, Thichonida Lake and some local ones that could be landslides.

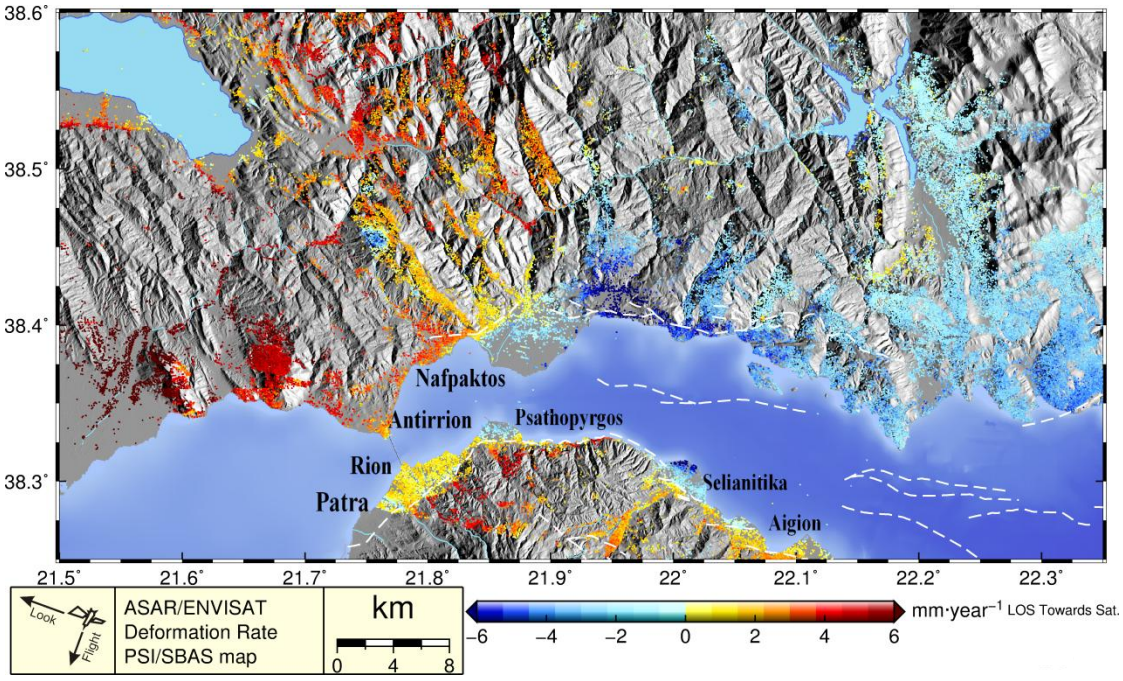

Figure 2-20. PSI/SBAS LOS rate map of the North study area, descending track no. 279

For ascending track no. 415 the acquisitions of 5/8/2003 have been used as master for the PS processing. For the PS map with an amplitude dispersion index of 0.4, a number of 51890 PSs have been calculated. For the SBAS processing with an amplitude dispersion index threshold of 0.6, minimum coherence threshold 0.5, time for total decorrelation threshold 1700 days and a critical baseline 1070m a number of 122 interferograms have been processed and 57669 PSs have been calculated. After the merging of them a number of 105299 PSs have finally been calculated. Its standard deviation map is shown in Figure 2-21.

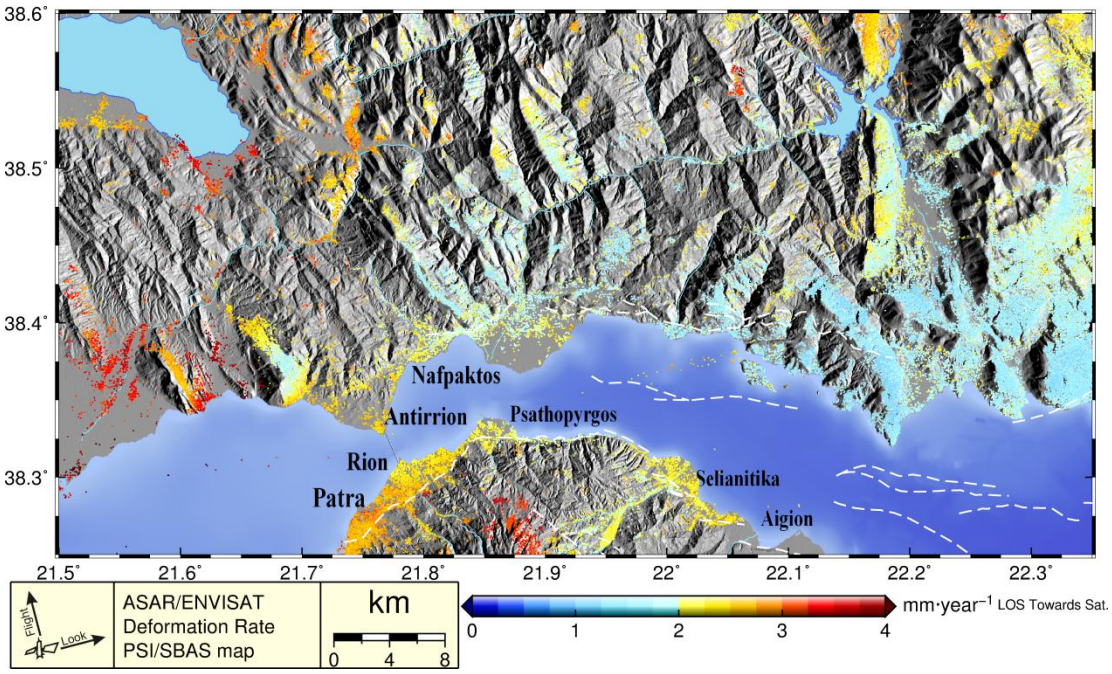

Figure 2-21. PSI/SBAS Standard deviation map of the North study area, ascending track no. 415.

Its deformation rate map is shown in Figure 2-22. In this figure we can spot a general E-W trend which doesn't correspond to reality and will be corrected according to the proposed methodology.

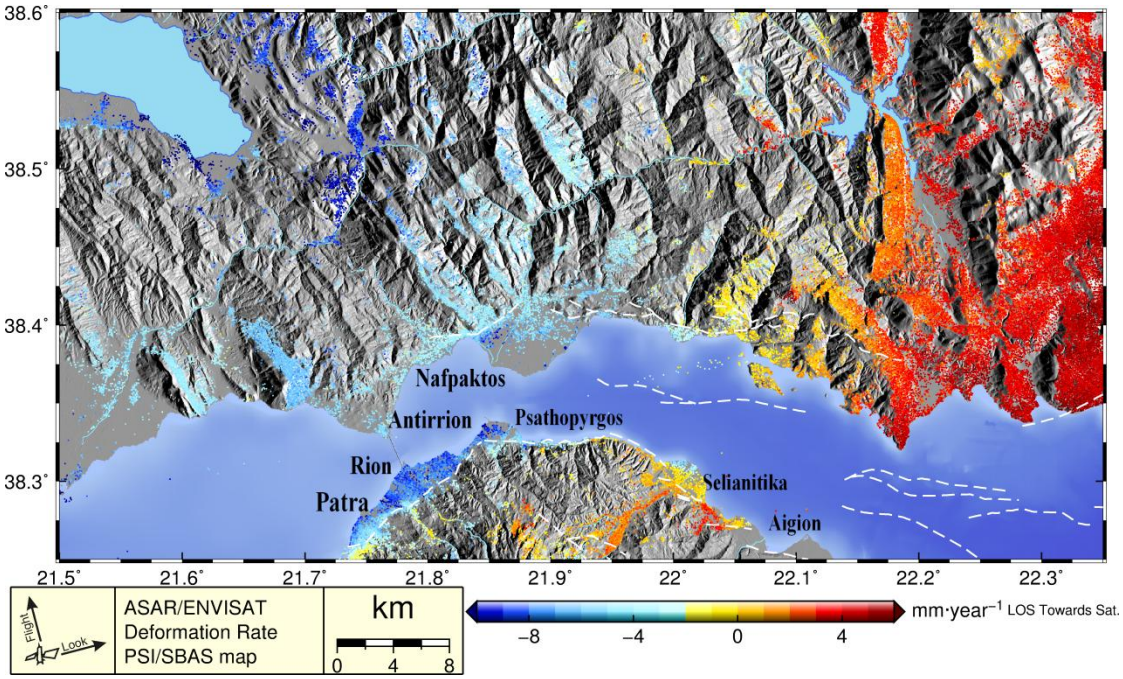

Figure 2-22. PSI/SBAS LOS rate map of the North study area, ascending track no. 415.

2.4.3. Aetoliko

For the Aetoliko area (Figure 2-8) we have calculated the descending track no. 50 and ascending track no. 186.

For descending track no. 50 the acquisition of 19/8/2005 has been used as master for the PSI/SBAS processing (Figure 2-9). For the PS map with an amplitude dispersion index of 0.4, a number of 85908 PSs have been calculated. For the SBAS processing with an amplitude dispersion index threshold of 0.6, minimum coherence threshold 0.45, time for total decorrelation threshold 1500 days and a critical baseline 1070m a number of 86 interferograms have been processed and 59053 PSs have been calculated. After the merging of them a number of 135088 PSs have finally been calculated. The PSI/SBAS map of descending track 50 is show in Figure 6-5.

For ascending track no. 186 the acquisition of 12/9/2004 has been used as master for the PSI/SBAS processing (Figure 2-10). For the PS map with an amplitude dispersion index of 0.4, a number of 68785 PSs have been calculated. For the SBAS processing with an amplitude dispersion index threshold of 0.6, minimum coherence threshold 0.4, time for total decorrelation threshold 1600 days and a critical baseline 1400m a number of 116 interferograms have been processed and 47961 PSs have been calculated. After the merging of them a number of 107913 PSs have finally been calculated.

2.5. Constraining PS with GPS and decomposing

In this chapter we will describe the correction procedure of the PSI/SBAS map using the available horizontal deformation rates of the campaign and permanent GPS Observations. As forthmentioned the GPS measurements are translated from ITRF2008 frame to stable Achaia (by shifting -8.5mm year^{-1} the East and 10.5mm year^{-1} the North component), unless stated differently. The vertical component is referenced to the permanent GPS Station KOUN (located inside Stable Achaia) at 38.2095°N, 22.0458°E, since the ITRF2008 vertical component is zero. After the correction the UDc of the PSI/SBAS maps are referenced to Stable Achaia, even if only the horizontal rates of the GPS station has been used in the correction procedure. Indeed this will be confirmed in §2.5.3.

Herein we will introduce the term Expected UDc value and how we computed it. Considering a typical sensitivity vector of the ASAR/ENVISAT LOS, I2 mode:

$$\vec{\boldsymbol{U}} = \begin{bmatrix} U_{east} \\ U_{north} \\ U_{up} \end{bmatrix} \sim \begin{bmatrix} \pm 0.38 \\ 0.09 \\ 0.92 \end{bmatrix}$$

and the representation of the LOS deformation vector as:

$$\left\{ \begin{matrix} V_{LOS}^{asc} = \begin{bmatrix} V_{east}^{asc} \\ V_{north}^{asc} \\ V_{up}^{asc} \end{bmatrix} \cdot \begin{bmatrix} U_{east}^{asc} & U_{north}^{asc} & U_{up}^{asc} \end{bmatrix} \\ V_{LOS}^{desc} = \cdots \end{matrix} \right\} \Rightarrow$$

where $\begin{bmatrix} V_{east}^{asc} \\ V_{north}^{asc} \\ V_{up}^{asc} \end{bmatrix}$ is the observed deformation vector

we will solve for UDc of the deformation for ascending and descending V_{up}^{asc} and V_{up}^{desc}, respectively :

$$\left\{ \begin{matrix} V_{up}^{asc} = \dfrac{V_{LOS}^{asc} - \begin{bmatrix} V_{east}^{asc} \\ V_{north}^{asc} \end{bmatrix} \cdot \begin{bmatrix} U_{east}^{asc} & U_{north}^{asc} \end{bmatrix}}{U_{up}^{asc}} \\ V_{up}^{desc} = \cdots \end{matrix} \right\} \xrightarrow{\begin{matrix} V_{east}^{asc}, V_{east}^{desc} = V_{east}^{gps} \\ V_{north}^{asc}, V_{north}^{desc} = G_{up}^{gps} \\ V_{up}^{asc} = V_{expected}^{asc} \\ V_{up}^{desc} = V_{expected}^{desc} \end{matrix}}$$

Replacing the EWc and NSc of the ascending and descending tracks with the corresponding GPS rates as $\begin{Bmatrix} V_{east}^{asc}, V_{east}^{desc} = V_{east}^{gps} \\ V_{north}^{asc}, V_{north}^{desc} = V_{up}^{gps} \end{Bmatrix}$ and setting the UDc of both tracks to the expected ones as : $\begin{Bmatrix} V_{up}^{asc} \equiv V_{expected}^{asc} \\ V_{up}^{desc} \equiv V_{expected}^{desc} \end{Bmatrix}$

We get the expected UDc for the ascending and descending tracks as:

$$V_{expected}^{asc} = \frac{V_{LOS}^{asc} - \begin{matrix} V_{east}^{gps} \\ V_{north}^{gps} \end{matrix} \cdot \begin{matrix} U_{east}^{asc} & U_{north}^{asc} \end{matrix}}{U_{up}^{asc}}$$

$$V_{expected}^{desc} = \frac{V_{LOS}^{desc} - \begin{matrix} V_{east}^{gps} \\ V_{north}^{gps} \end{matrix} \cdot \begin{matrix} U_{east}^{desc} & U_{north}^{desc} \end{matrix}}{U_{up}^{desc}}$$

Actually the expected UDc is the value that we get if we force the horizontal PSI/SBAS components to be equal to the corresponding GPS ones. Thus, in the following procedure we will use the horizontal components of the GPS (which are more accurate compared to InSAR) to calculate the UDc (but also the EWc) from PSI/SBAS where the InSAR is more accurate than GPS.

For both, ascending and descending tracks, we have followed the described underneath procedure for the South and the North Gulf of Corinth area as defined in Figure 2-5. Note that all the values correspond to linear deformation rate in mm year^{-1}.

2.5.1. South Gulf of Corinth

For each GPS point location we have calculated the median LOS values (of both tracks) of a formed patch containing the deformation rate values of the PS lying within a range of 400 m. close to the GPS location. By forcing each EWc and NSc (North-South component) values of each patch to match that of the GPS values, we have calculated the corresponding expected UDc values. Note that for each patch as LOS value we have used the average of all PS LOS values inside it (Figure 2-23a and Figure 2-23b) for ascending and descending respectively. Then for each permanent GPS Station (where the UDc can be extracted, since their measurements is spanning almost ten years) that lays inside the study area, we have calculated a linear fitting along the longitude dimension between the expected UDc values and the GPS ones (Figure 2-23c and Figure 2-23d). The permanent station of GPS that its UDc components have been used for both ascending and descending tracks was PSAR, TRIZ and KOUN. These linear trends (red lines) are fitting well with the difference between the expected and GPS EWc and NSc values (Figure 2-23a and Figure 2-23b).

From a total number of 139 GPS measurements we have used 25 (Table 1).

In the next step we have removed the linear trend between the expected and GPS UDc values, resulted to the Figure 2-23e and Figure 2-23f. In both tracks we can see a clear residual trend (shown with blue lines) that has opposite signs.

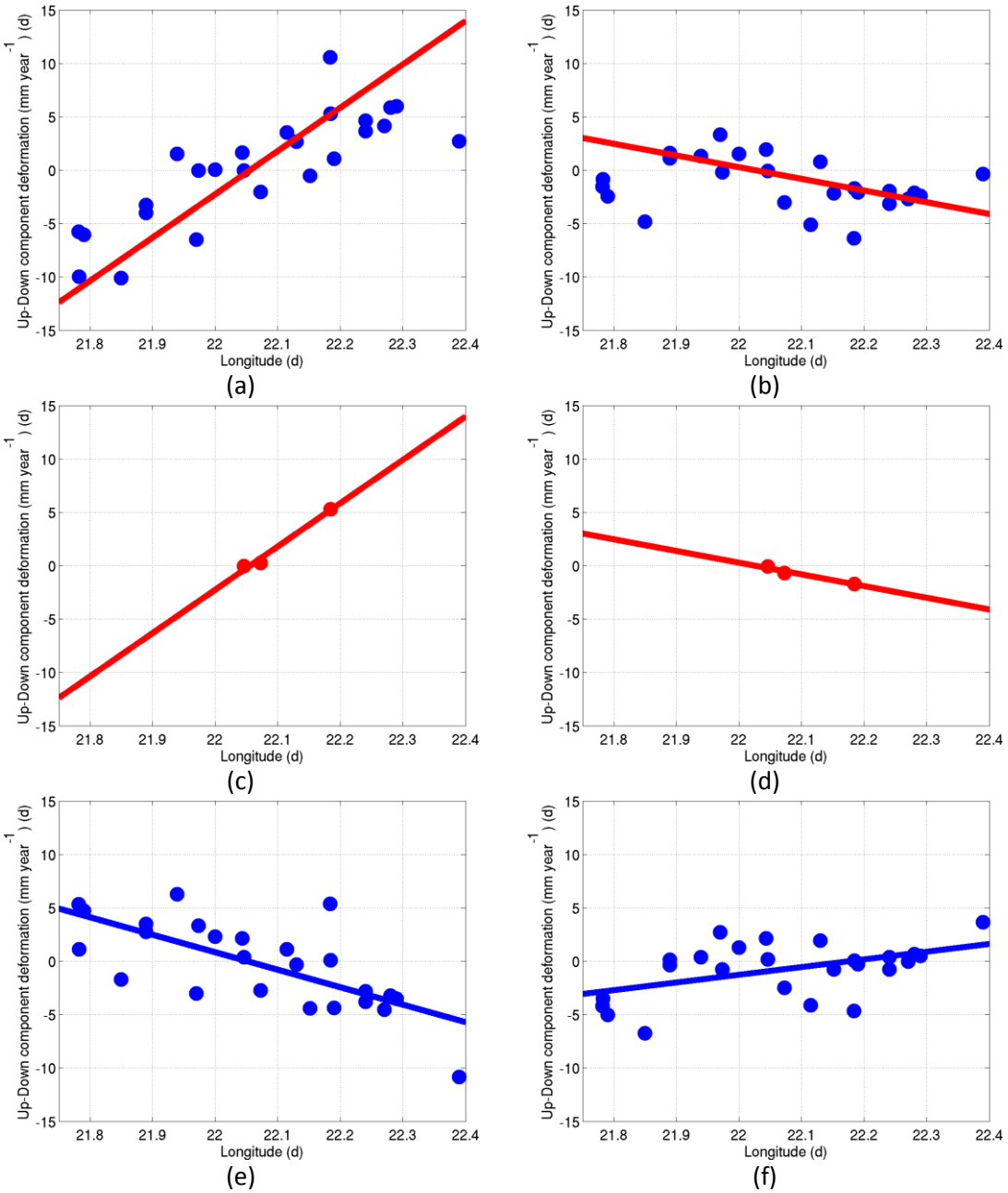

Figure 2-23. For the South GoC : (a) The expected values along the longitude dimension of ascending track , with red line the trend calculated from the UDc of the GPS is shown, (b) the expected values of descending track , with red line the trend from calculated from the UDc of the GPS is shown, (c) the difference between the expected and the GPS UDc values and its trend line in red, (d) the difference between the expected and GPS UDc values and its trend line in red, (e) the expected UDc values after the linear trend correction of ascending track, with red line the residual trend is shown and (f) the expected UDc values after the linear trend correction of descending track, with blue lines the residual trend is shown.

Figure 2-24a shows the difference between the corrected expected ascending and descending UDc values along the longitude dimension. Ideally if p was the expected UDc, the condition 1.13 is true and can be used to corrected these trends (red lines of Figure 2-23e and Figure 2-23f) by forcing them both to be at zero slopes (Figure 2-24c and Figure 2-24d).

$$\forall\, p_i^{asc}, p_i^{desc} : p_i^{asc} - p_i^{desc} \approx 0, i = 1 \dots 25 \qquad (2.13)$$

The condition of course has many solutions and the common trend slope could be different than zero but because of the lack of large GPS UDc measurements volume, we have to assume that this trend slope is zero. In Figure 2-24b the difference between the corrected expected UDc values of ascending and descending tracks is shown. The trend slope along longitude dimension has been minimized for both tracks. The patterns of both tracks are pretty much the same (Figure 2-24c and Figure 2-24d). Their σ (standard deviation of PSI/SBAS procedure) before the correction was 6.3 mm year^{-1} and after is 3.9 mm year^{-1}.

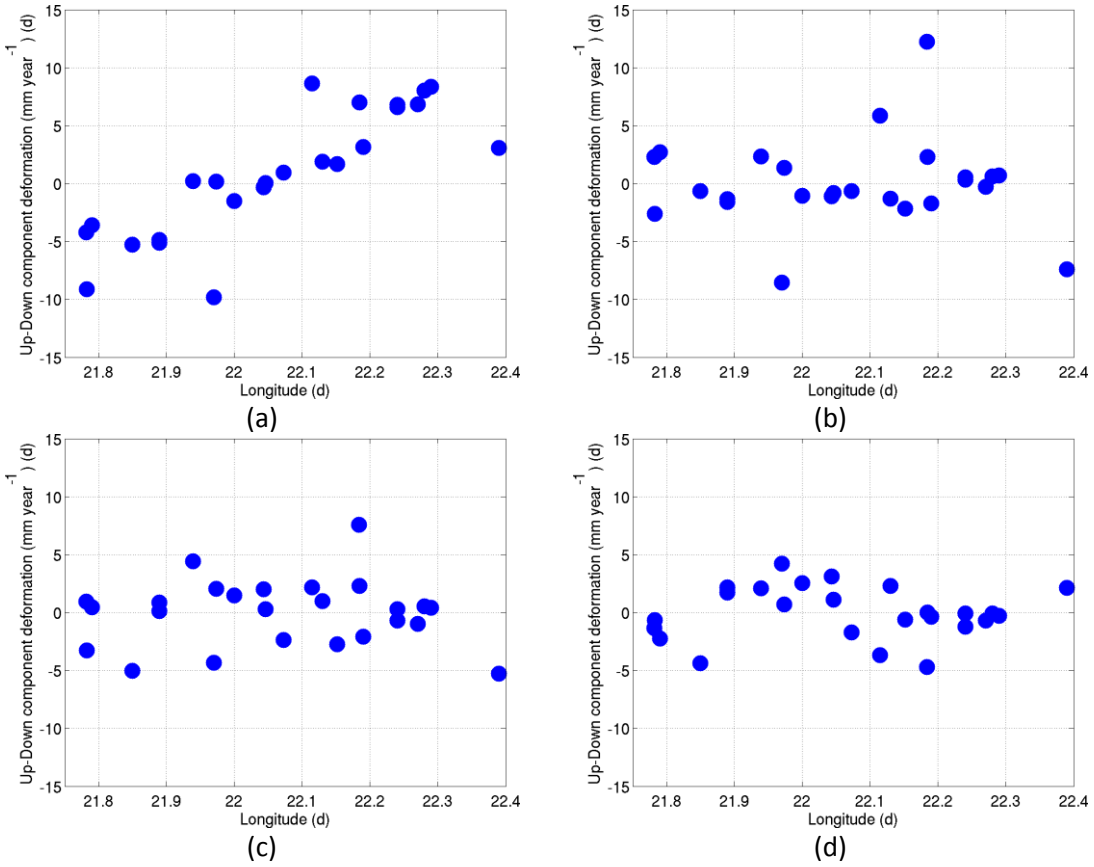

Figure 2-24. (a) The difference between the corrected expected ascending and descending UDc patch values along the longitude dimension, (b) the difference between the corrected expected ascending and descending UDc patch values after the residuals correction, (c) the expected UDc values after the residuals trend correction of ascending track and (d) the expected UDc values after the residuals trend correction of descending track.

The rms between the corrected expected and the GPS UDc value was 3.1 mm year^{-1} and 1.1 mm year^{-1} and after the correction is 1.3 mm year^{-1} and 0.7 m year^{-1} for the ascending and descending track respectively.

In Figure 2-25a and Figure 2-25b the expected UDc values of both tracks along the latitude dimension are presented. In Figure 2-25c and Figure 2-25d the expected UDc values of both tracks after the correction are shown. In the descending track there is an obvious shift of the values lying between latitude 38.2°N and 38.25°N, but there are not opposite slope trends between ascending and descending tracks as it was the case along the longitude dimension. No correction has been applied along the latitude dimension.

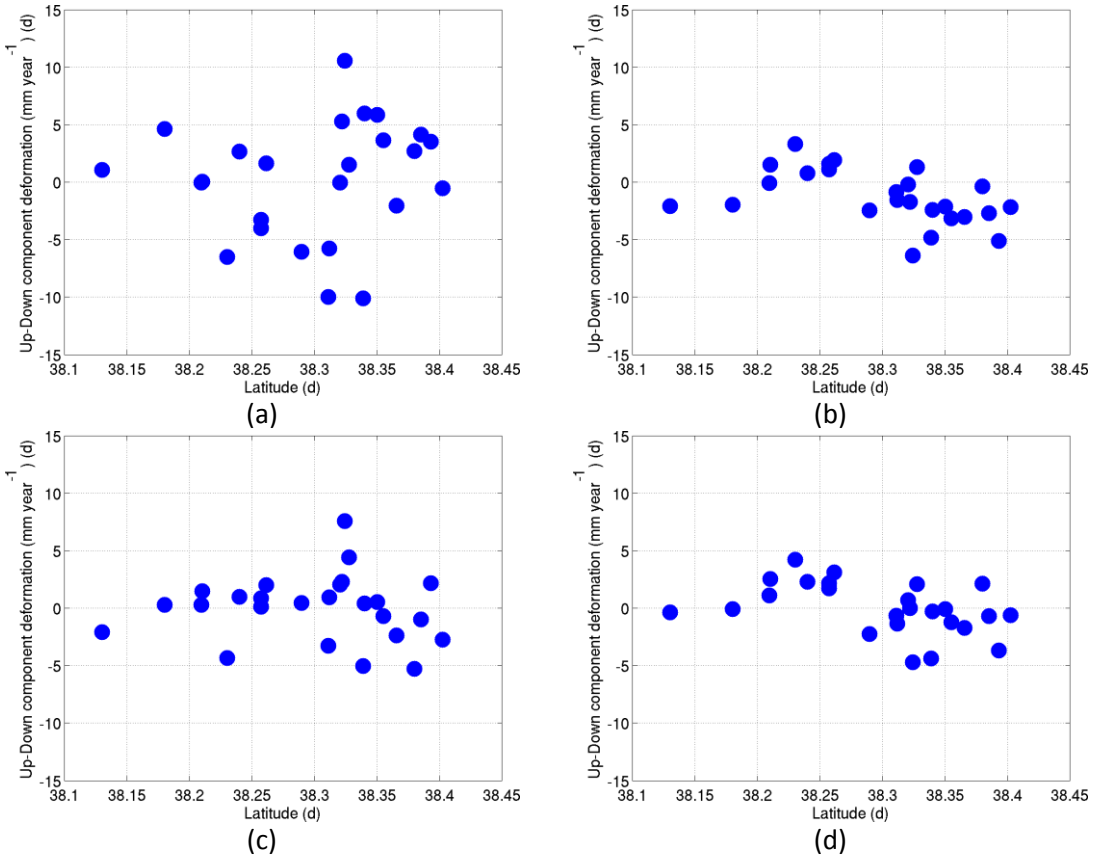

Figure 2-25. The expected UDc values of ascending track along the latitude dimension, (b) the expected UDc values of descending track, (c) the expected UDc values after the residual trend correction of ascending track and (d) the expected UDc values after the residual trend correction of descending track.

In Figure 2-26a and Figure 2-26b the difference between expected and GPS UDc values of both tracks along the latitude dimension are shown. In Figure 2-26c and Figure 2-26d the difference between expected and GPS UDc values of both tracks along the latitude dimension after the correction are shown.

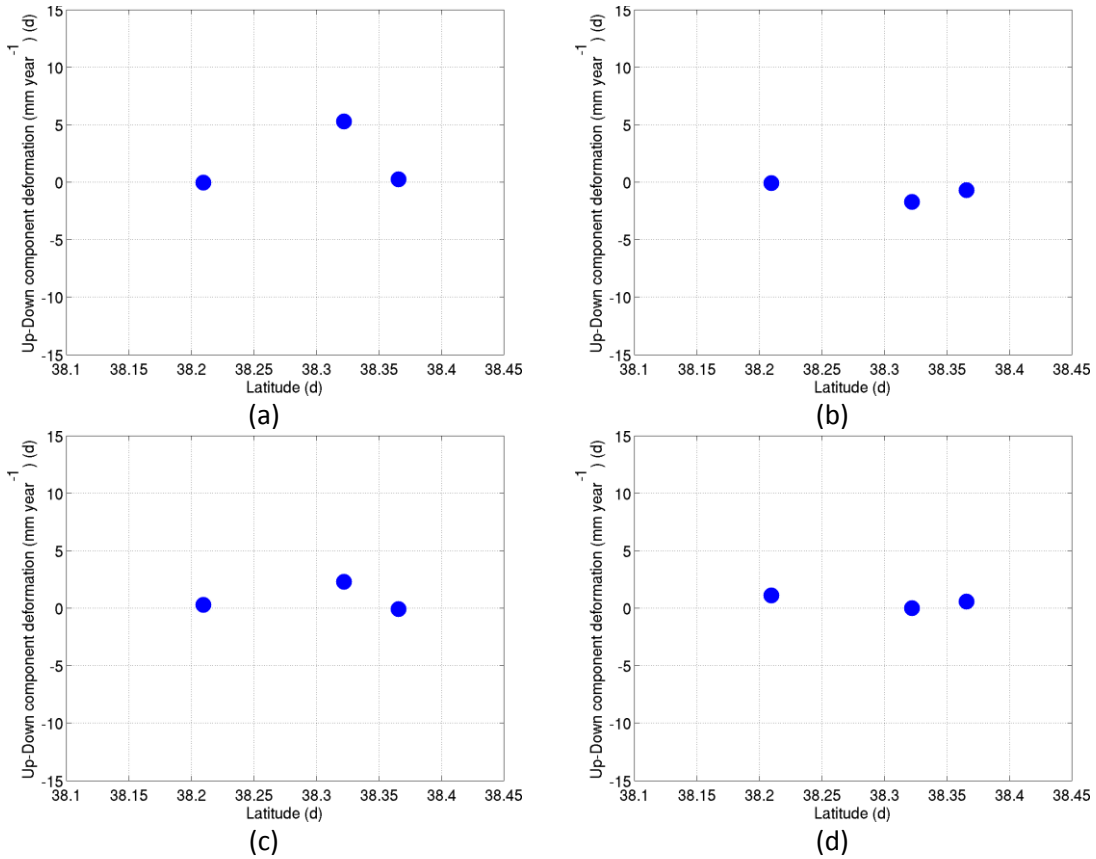

Figure 2-26. The difference of the expected and the GPS UDc values of ascending track along the latitude dimension, (b) the difference of the expected and the GPS UDc values of descending track, (c) the difference of the expected and GPS UDc values after the residual trend correction of ascending track and (d) the difference of the expected and GPS UDc values after the residual trend correction of descending track.

Unfortunately, the volume of the GPS of which the UDc exists is very small and it can't form a statistically robust group. If the volume was high the slopes of the values of the Figure 2-23e and Figure 2-23f would be expected to coincide and their slope would be either 0, which means that there is no real linear trend in the Up-Down component or different than zero, which means that there is real linear trend along the longitude dimension.

The corrected expected values of Figure 2-24c and Figure 2-24d (along longitude) and Figure 2-25c and Figure 2-25d (along latitude), provide estimates of the UDc in the GPS locations. Neglecting any real linear trends along the two dimensions the table of the estimations of the UDc in the GPS locations and their σ are shown in Table 1. For each GPS location i, given the scalar values of deformation rate of the ascending p_i^{asc} and descending p_i^{desc} values having σ_i^{asc} and σ_i^{desc} (both as outputs of StaMPS) and the LOS vector of the UDc being u_i^{asc} and u_i^{desc}, respectively we have calculated the σ_i of the Table 1 using the equation 2.14.

$$\sigma_i = \frac{\sigma_i^{asc} \cdot p_i^{asc} \cdot U_i^{asc} + \sigma_i^{desc} \cdot p_i^{desc} \cdot u_i^{desc}}{p_i^{asc} \cdot U_i^{asc} + p_i^{desc} \cdot u_i^{desc}}, i = 1 \dots 25 \quad (2.14)$$

In all the calculation we have used the average value LOS vector for each PS patch.

GPS point	Longitude (°E)	Latitude (°N)	Diff. between Asc-Desc Up-Down component (mm year^{-1})	Average Up-Down component (mm year^{-1})	σ (mm year^{-1})
O000	22.1146	38.3931	5.9	2.9	1.4
TRIZ	22.0727	38.3654	-0.7	-0.3	1.5
UPAT	21.7905	38.2894	2.7	1.3	1.5
CG30	22.1519	38.4023	-2.2	-1.1	1.5
F000	22.07	38.15	5.1	2.5	1.5
C000	22.184	38.324	12.3	6.1	1.6
L000	21.8079	38.1046	1.6	0.8	1.6
RION	21.7827	38.3109	13.3	6.6	1.6
Q619	22	38.21	7.3	3.6	1.6
P226	22.0429	38.2613	7.2	3.6	1.6
D000	22.13	38.24	-1.3	-0.7	1.7
C075	22.24	38.355	2.1	1	1.7
PSAR	22.1843	38.3217	2.3	1.1	1.8
KOUN	22.0458	38.2095	-0.8	-0.4	1.8
LAMB	21.9731	38.3204	1.3	0.7	1.8
N730	21.9371	38.3017	0.7	0.3	1.8
CT00	22.39	38.38	-7.4	-3.7	1.9
K001	21.8894	38.257	3.7	1.9	1.9
RIOE	21.7816	38.3116	6.2	3.1	2
J000	21.8494	38.3389	-0.2	-0.1	2.1
T000	22.24	38.18	-11.5	-5.8	2.2
C499	22.27	38.385	-12.2	-6.1	2.3
N000	21.9391	38.3276	-7	-3.5	2.6
CG42	21.97	38.23	-8.5	-4.3	2.7
CG43	22.19	38.13	-1.7	-0.9	2.7

Table 1. Estimations of the UDc in the GPS locations and their σ.

So far we have constrained the patches of the LOS deformation rates of both tracks using a set of 25 EWc and NSc values and a set of 3 UDc of GPS measurements. Moreover we have assumed that the trend slope of the UDc deformations rate in the locations of the GPS points, along the longitude dimension is zero. Actually, we have no reason for this assumption but the shortage of a robust dataset of UDc deformation rate components from GPS data. In parallel to this procedure we have estimated the UDc deformation rates from the InSAR data surrounding each one of the GPS locations along with an estimation of σ.

The following procedure will constrain all the PSs.

For each descending PS a corresponding descending one has been selected lying within the range of d_g=~100m (5 pixels). For each pair of these PS (one descending and its corresponding ascending) the looking vector has been calculated. The LOS vector values (East-West, North-South, Up-Down) ranging between [-0.406 -0.340], [-0.100 -0.084] and [0.937 0.908] and [0.346 0.405], [-0.100 -0.086] and [0.909 0.934] for ascending and descending track respectively. Considering that the NSc is low it has been neglected. By solving the equation (2.15) we have calculated the UDc and EWc deformation rate values. The d_g has been selected so that the final combined number of PSs to be a little bit more maximum number of descending and ascending passes.

$$\left.\begin{aligned} V_{LOS}^{asc} &= \begin{bmatrix} V_{east} \\ V_{north} \\ V_{up} \end{bmatrix} \cdot \begin{bmatrix} U_{east}^{asc} & U_{north}^{asc} & U_{up}^{asc} \end{bmatrix} \\ V_{LOS}^{desc} &= \begin{bmatrix} V_{east} \\ V_{north} \\ V_{zen} \end{bmatrix} \cdot \begin{bmatrix} U_{east}^{desc} & U_{north}^{desc} & U_{up}^{desc} \end{bmatrix} \end{aligned}\right\} \xrightarrow[U_{north}^{desc} \approx 0]{U_{north}^{asc} \approx 0}$$

$$\left\{\begin{aligned} V_{LOS}^{asc} &= \begin{bmatrix} V_{east} \\ V_{up} \end{bmatrix} \cdot \begin{bmatrix} U_{east}^{asc} & U_{up}^{asc} \end{bmatrix} \\ V_{LOS}^{desc} &= \begin{bmatrix} V_{east} \\ V_{up} \end{bmatrix} \cdot \begin{bmatrix} U_{east}^{desc} & U_{up}^{desc} \end{bmatrix} \end{aligned}\right\} \quad (2.15)$$

Where:

V_{LOS}^{asc} : The deformation rate of ascending PS.

V_{LOS}^{desc} : The deformation rate of descending PS.

$\left.\begin{bmatrix} U_{east}^{asc} \\ U_{north}^{asc} \\ U_{up}^{asc} \end{bmatrix} \right.$
$\left. \begin{bmatrix} U_{east}^{desc} \\ U_{north}^{desc} \\ U_{up}^{desc} \end{bmatrix} \right\}$: The Line of Sight vectors from ascending and descending tracks.

The total number of PSs for the South Gulf of Corinth (SGoC) was for Ascending 64322 and Descending 71195. The σ of the PSs was ranging between [1.2 4.2] mm and [0.89 3.3] mm for ascending and descending track respectively. The total number of combined PS set was 82165. The σ_i for each combined PS *i* (Figure 2-27) has been calculated using equation 2.14. In its corresponding map we can see that the σ_i is biased according to the deformation. That is normal due to the equation used to calculate it.

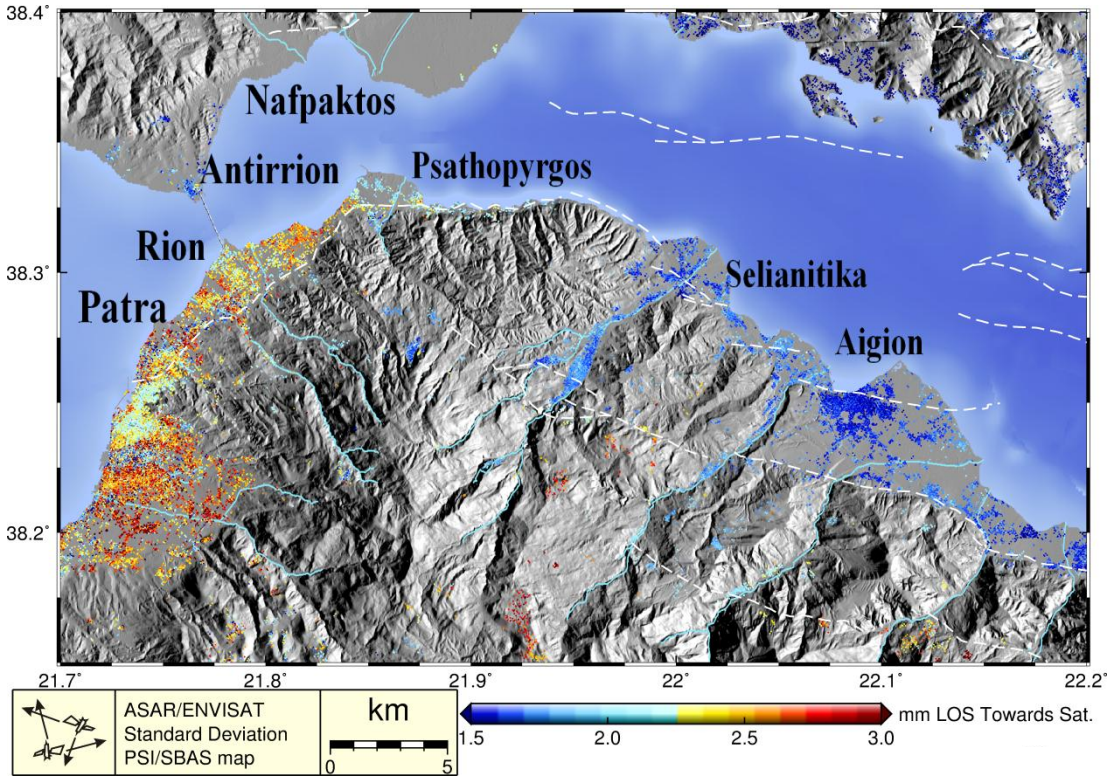

Figure 2-27. The σ for each combined PS using equation 1.14 for the South GoC.

Finally, we have produced the UDc (Figure 2-28) and EWc (Figure 2-29) maps for the South GoC. Their special features will be investigated in the following sections.

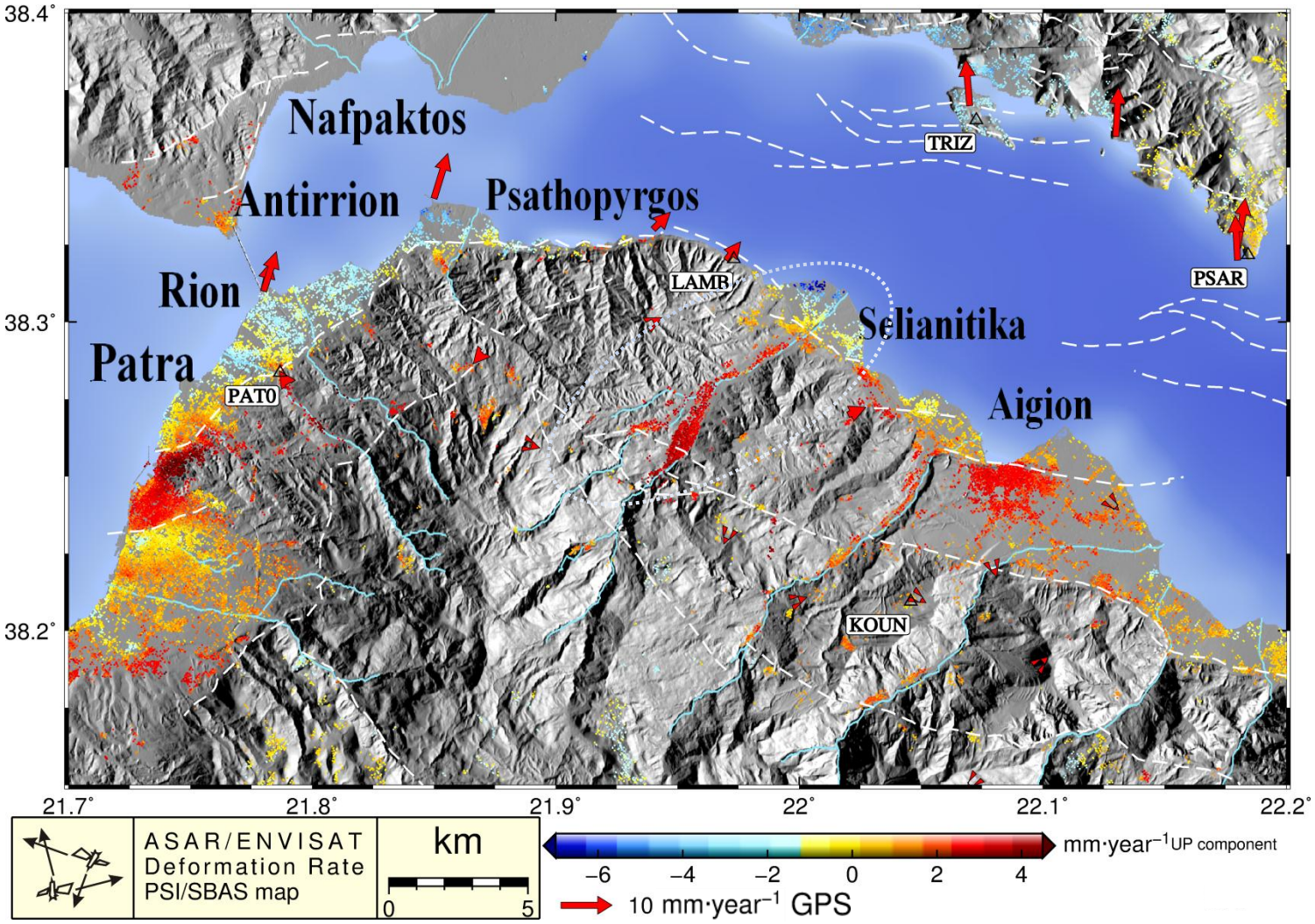

Figure 2-28. The UDc of the South GoC. With red arrows the planar GPS measurements are shown. White dashed lines indicate the faults. See §2.5.3 for the dot line.

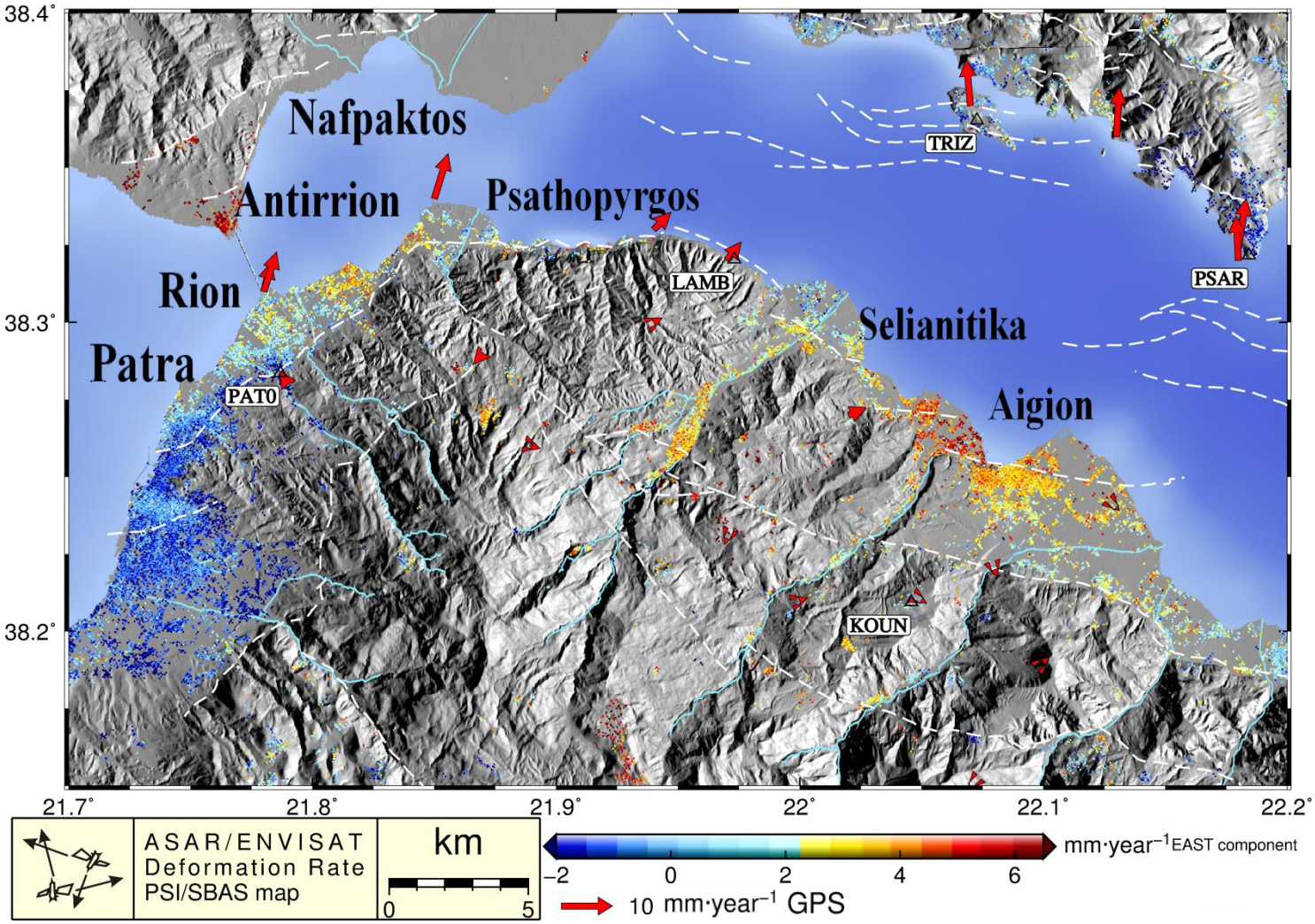

Figure 2-29. The EWc of the South GoC. With red arrows the planar GPS measurements are shown. White dashed lines indicate the faults.

2.5.2. North Gulf of Corinth

For both ascending and descending tracks we followed the same procedure as for the South GoC.

For each GPS point location we have calculated the median LOS values (of both tracks) of a formed patch containing the deformation rate values of the PS lying within a range of 400 m. close to the GPS location. By forcing each EWc and NSc values of each patch to match that of the GPS values , we have calculated the corresponding expected UDc values. For each patch as LOS value we have used the average of all PS LOS values inside it (Figure 2-30a and Figure 2-30b) for ascending and descending respectively. Then for each permanent GPS Station that lies inside the study area, we have calculated a linear fitting along the longitude dimension between the expected UDc values and the GPS ones (Figure 2-30c and Figure 2-23d). The permanent GPS stations that theirs UDc components have been used for both ascending and descending tracks was LIDO, PSAR and TRIZ. The linear trends (blue lines of Figure 2-30a and Figure 2-30b) are fitting well with the expected UDc values of descending but not so well with the ascending track.

From a total number of 139 GPS measurements we have used 24 (Table 2).

In the next step we have removed the linear trend between the expected and GPS UDc values, resulted to the Figure 2-30e and Figure 2-30f. In both tracks we can see a clear residual trend (shown with blue lines) that has opposite signs. This matching is a good indication that the red slope trend is possible but as the case of South GoC, since the volume of GPS UDc measurements is very small we cannot claim this.

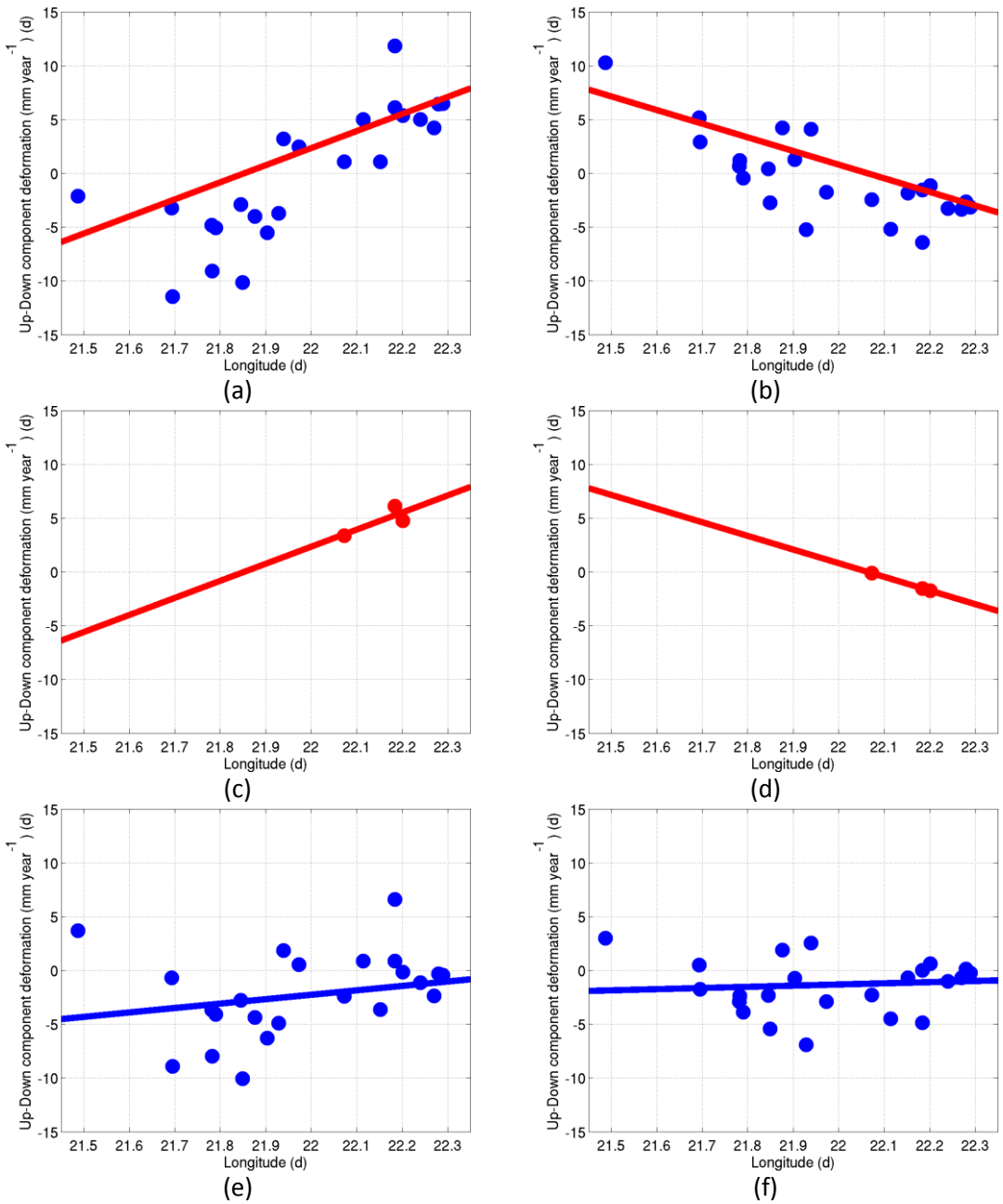

Figure 2-30. For the North GoC Q : (a) The Expected values along the longitude dimension of ascending track , with red line the trend from calculated from the UDc of the GPS is shown, (b) the Expected values of descending track , with red line the trend from calculated from the UDc of the GPS is shown, (c) the difference between the expected and the GPS UDc values and its trend line in red, (d) the difference between the expected and GPS UDc values and its trend line in red, (e) the expected UDc values after the linear trend correction of ascending track, with blue line the residual trend is shown and (f) the expected UDc values after the linear trend correction of descending track, with blue line the residual trend is shown.

Figure 2-31a shows the difference between the corrected expected ascending and descending UDc values along the longitude dimension. Again, using condition 1.13 we have calculated the difference between the corrected expected UDc values of ascending and descending tracks (Figure 2-31b). The trend slope along longitude dimension has been minimized for both tracks. The patterns of both tracks are pretty much the same (Figure 2-24c and Figure 2-24d). Their σ before the correction was 8.5 mm year^{-1} and after is 4.2 mm year^{-1}.

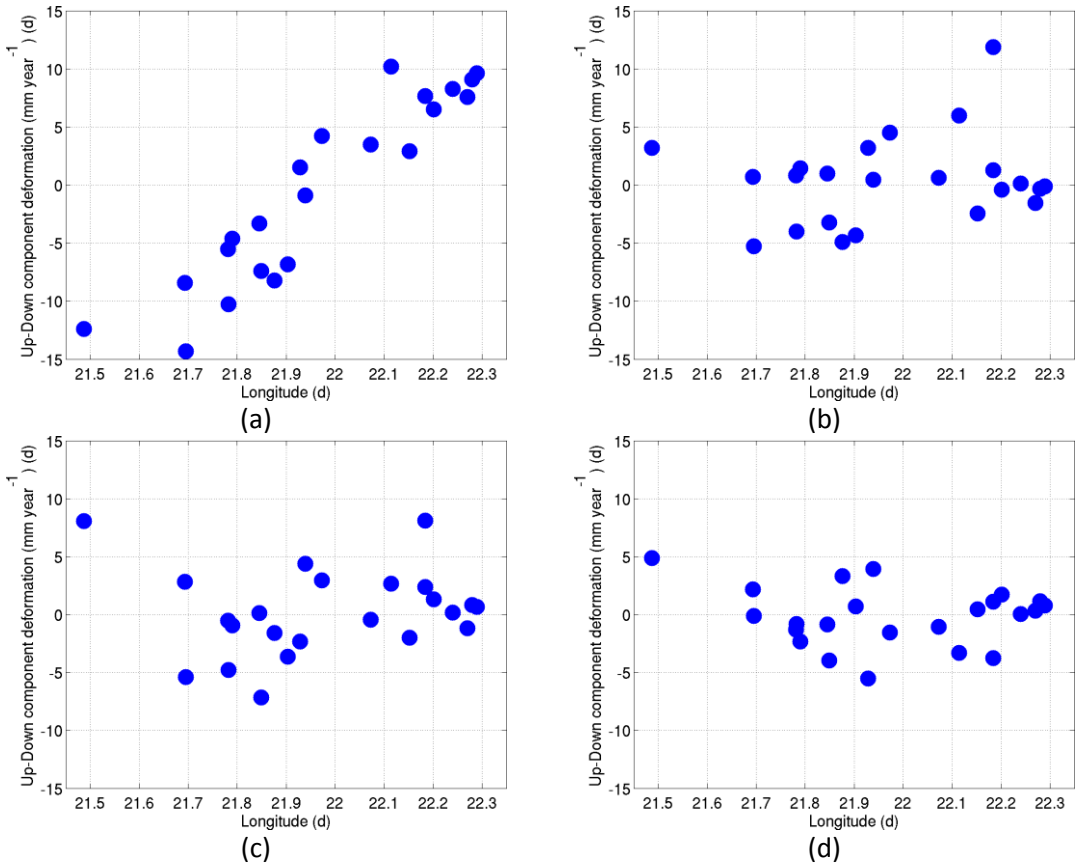

Figure 2-31. (a) The difference between the corrected expected ascending and descending UDc patch values along the longitude dimension, (b) the difference between the corrected expected ascending and descending UDc patch values after the residuals correction, (c) the expected UDc values after the residuals trend correction of ascending track and (d) the expected UDc values after the residuals trend correction of descending track.

The rms between the corrected expected and the GPS UDc value was 1.4 mm year^{-1} and 0.9 mm year^{-1} and after the correction is 0.9 mm year^{-1} and 0.1 mm year^{-1} for the ascending and descending track respectively.

In Figure 2-32a and Figure 2-32b the expected Up-Down patch component of both tracks versus the latitude dimension are shown. In Figure 2-32c and Figure 2-32d the expected values, but after the application of the correction, have been plotted. In the descending track there is an obvious shift of the values lying between latitude 38.2°N and 38.25°N, but there are not reversed slope trends between ascending and descending passes as it was the case in the longitude dimension. No correction has been applied along the latitude dimension.

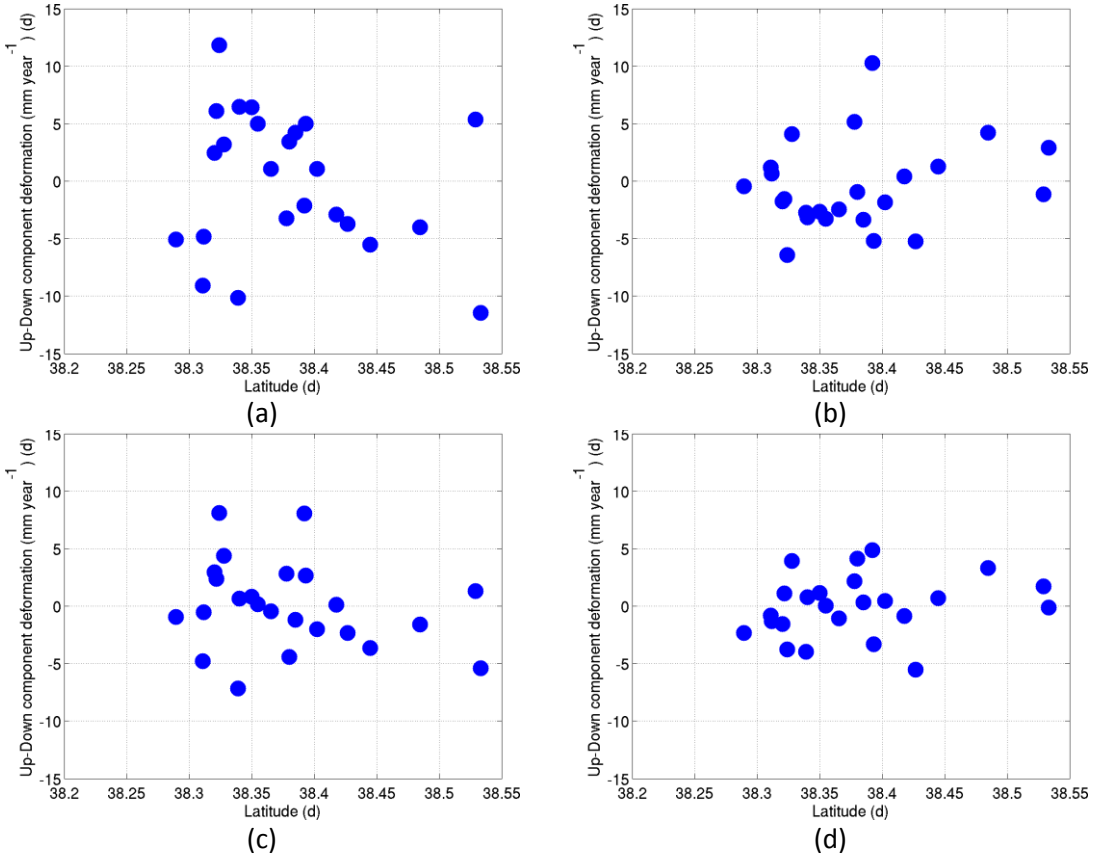

Figure 2-32. (a) The difference of the expected and the GPS UDc values of ascending track along the latitude dimension, (b) the difference of the expected and the GPS UDc values of descending track, (c) the difference of the expected and GPS UDc values after the residual trend correction of ascending track and (d) the difference of the expected and GPS UDc values after the residual trend correction of descending track.

In Figure 2-33a and Figure 2-33b the difference between expected and GPS UDc values of both tracks along the latitude dimension are shown. In Figure 2-33c and Figure 2-33d the difference between expected and GPS UDc values of both tracks along the latitude dimension after the correction are shown.

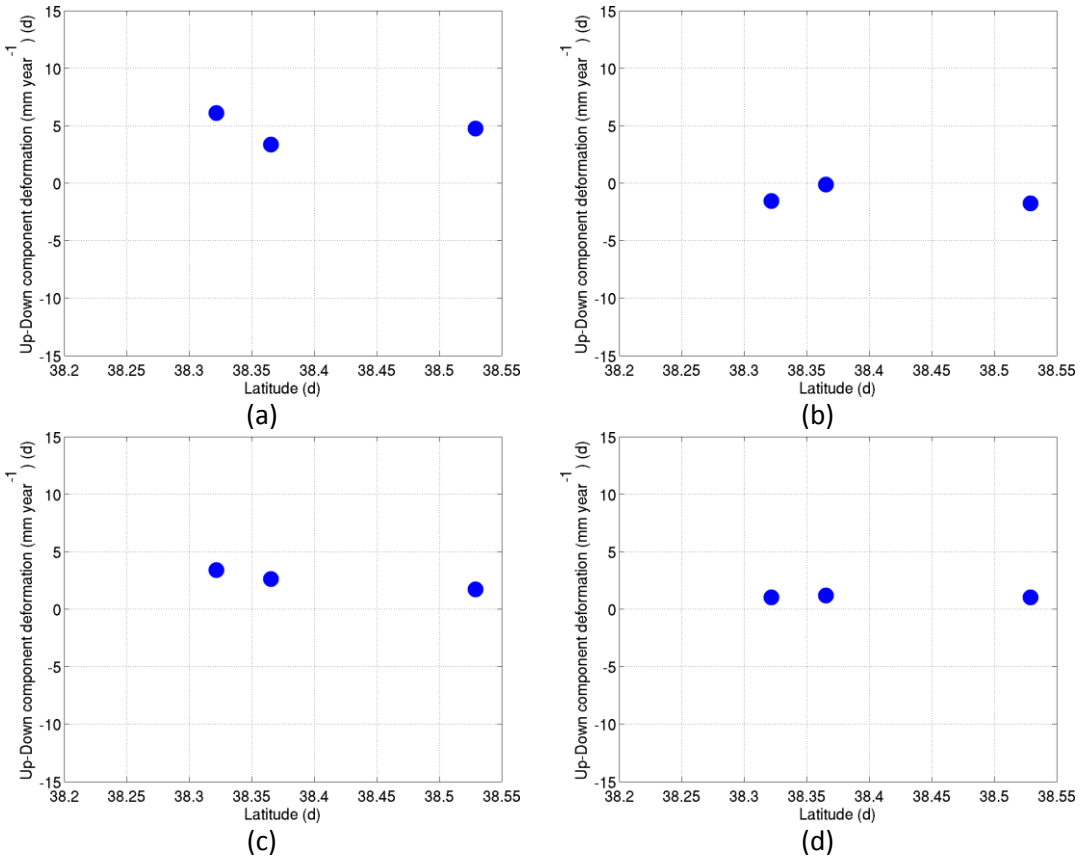

Figure 2-33. (a) difference between expected and GPS UDc values of ascending track along the latitude dimension, (b) difference between expected and GPS UDc values of descending track along the latitude dimension, (c) difference between expected and GPS UDc values of ascending track along the latitude dimension after the correction and (b) difference between expected and GPS UDc values of descending track along the latitude dimension after the correction.

Unfortunately, the volume of the GPS of which the UDc exists is very small and it can't form a statistically robust group.

Even if the volume of the GPS of which the Up-Down component exists is very small and it can't form a statistically robust group we have good matching of the slope trends calculated from the forth mentioned dataset and compared with the trend slope of the expected Up-Down components (Figure 2-30a and Figure 2-30b). Thus, after the trend slope correction the residual trend is small (Figure 2-30e and Figure 2-30f).

The corrected expected values of Figure 2-30e and Figure 2-30f (along longitude) and Figure 2-32c and Figure 2-32d (along latitude), provide estimates of the UDc in the GPS locations. Neglecting any real linear trends along the two dimensions the table of the estimations of the UDc in the GPS locations and their σ are shown in Table 2. The σ again has been calculated using the equation 1.14.

GPS point	Longitude (°E)	Latitude (°N)	Diff. between Asc-Desc Up-Down component (mm year^{-1})	Average Up-Down component (mm year^{-1})	σ (mm year^{-1})
I335	21.8456	38.4176	1	0.5	1.2
LIDO	22.201	38.529	-0.4	-0.2	1.3
TRIZ	22.0727	38.3654	0.6	0.3	1.3
CG30	22.1519	38.4023	-2.5	-1.2	1.3
EYPA	21.9284	38.4268	3.2	1.6	1.4
C000	22.184	38.324	11.9	5.9	1.4
O000	22.1146	38.3931	6	3	1.4
PSAR	22.1843	38.3217	1.3	0.6	1.5
THOM	21.4877	38.392	23.2	11.6	1.5
CT00	22.39	38.38	-8.5	-4.3	1.6
RION	21.7827	38.3109	14.5	7.3	1.6
H000	21.98	38.53	9.1	4.6	1.6
I000	21.9029	38.4447	-4.3	-2.2	1.7
K337	21.8694	38.2949	-4.9	-2.4	1.7
C075	22.24	38.355	1.5	0.7	1.7
UPAT	21.7905	38.2894	1.4	0.7	1.8
RC01	21.6933	38.3778	3.6	1.8	1.8
J000	21.8494	38.3389	-3.2	-1.6	2
K001	21.8894	38.257	2	1	2
LAMB	21.9731	38.3204	4.5	2.2	2.1
N000	21.9391	38.3276	-6.9	-3.4	2.3
RC02	21.8763	38.4848	-7	-3.5	2.3
AVAR	21.6951	38.5333	-5.3	-2.6	2.5
RIOE	21.7816	38.3116	-6.1	-3	2.7

Table 2. Estimations of the UDc in the GPS locations and their σ.

By following the same procedures to combine the ascending and descending tracks and solving the equation 2.15 we have calculated the UDc and EWc deformation rate values in the area of North Gulf of Corinth (NGoC). The d_g has been selected so that the final combined number of PSs to be a little bit more maximum number of descending and ascending passes.

The total number of PSs for the NGoC was for Ascending 105299 and Descending 85049. The σ of the PSs was ranging between [1.0 4.4] mm and [0.8 3.9] mm for ascending and descending track respectively. The Total number of combined PS set was 85439. The σ_i for each combined PS *i* (Figure 2-34) has been calculated using equation 2.14.

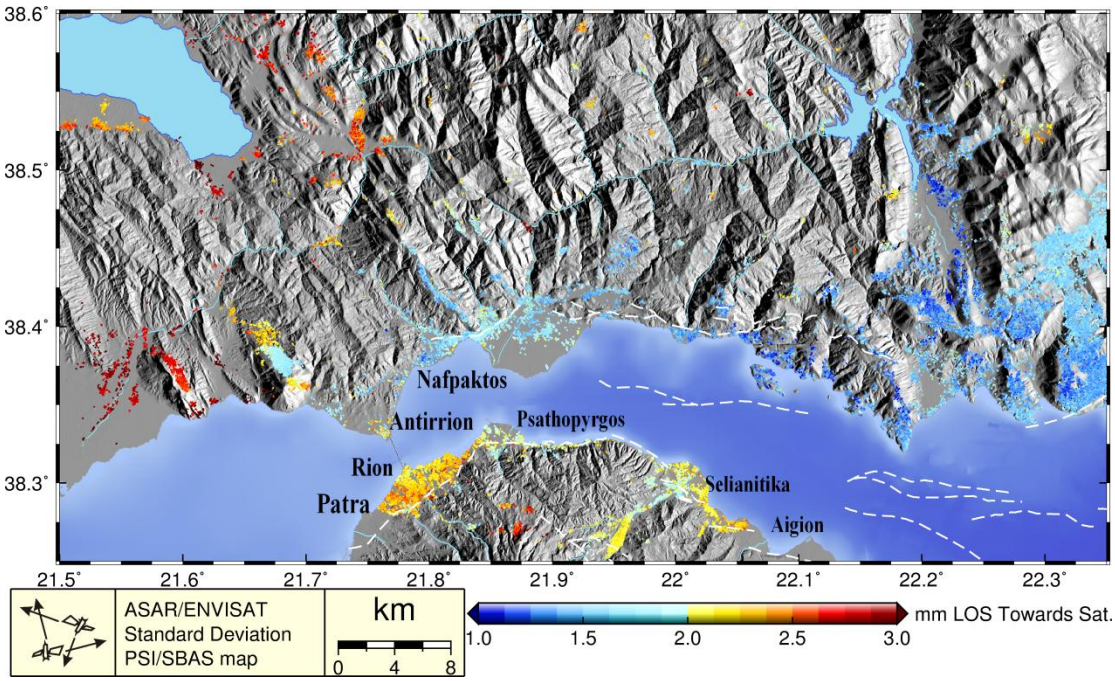

Figure 2-34. The σ for each combined PS using equation 1.14 for the North GoC.

Finally, we have produced the UDc (Figure 2-35) and EWc (Figure 2-36) maps for the North GoC.Their special features will be investigated in the following sections.

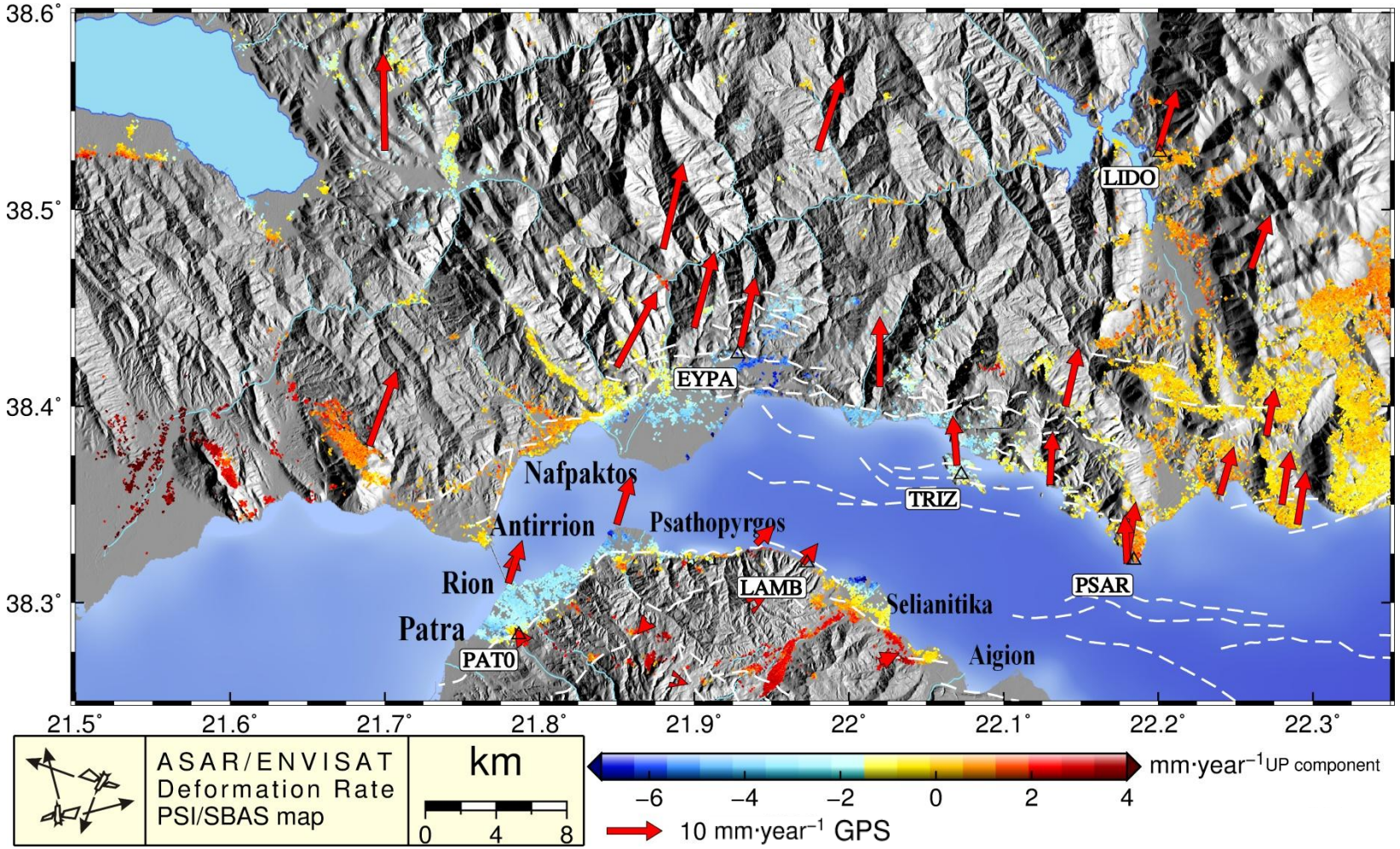

Figure 2-35. The UDc of the North GoC. With red arrows the planar GPS measurements are shown. White dashed lines indicate the faults.

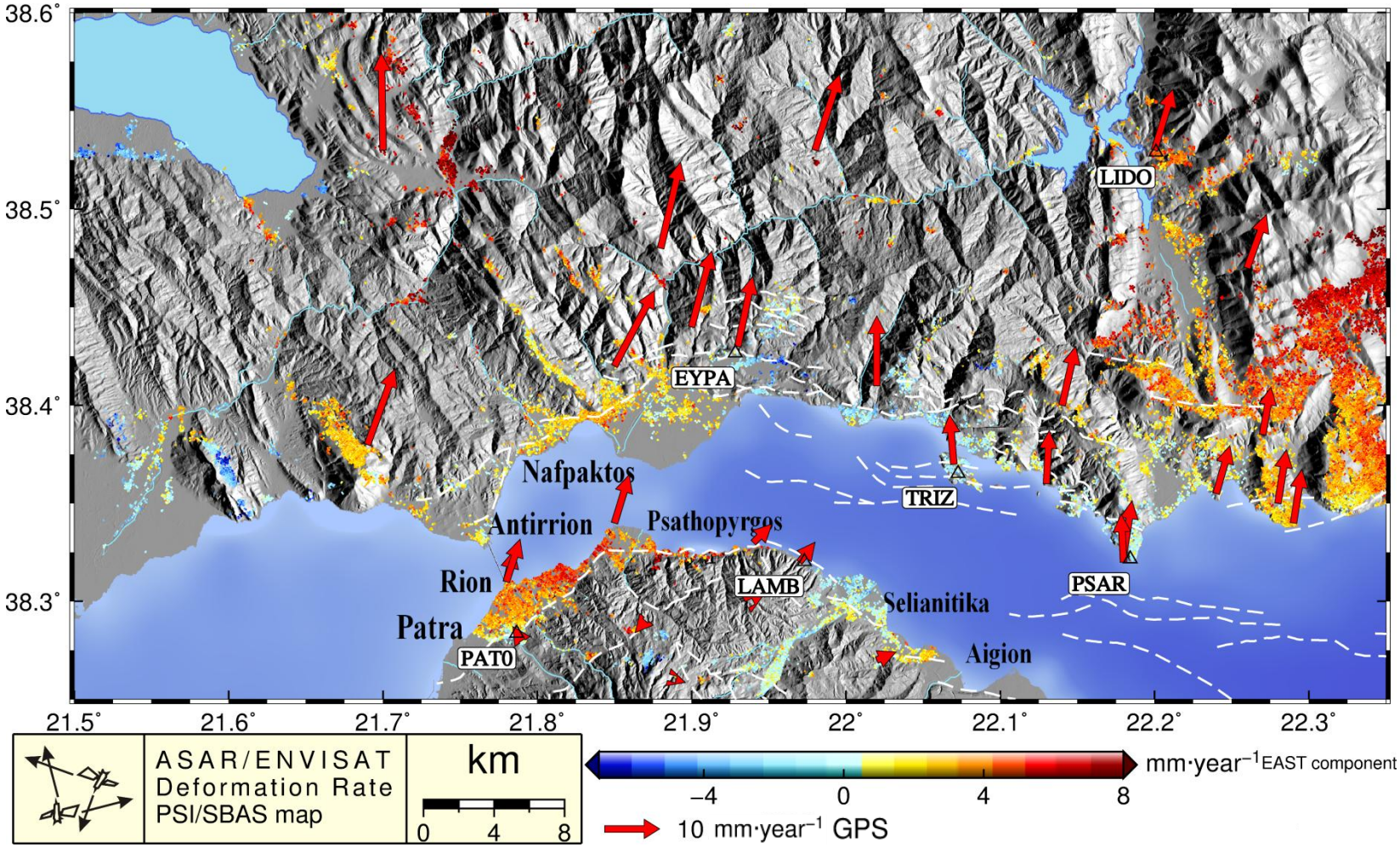

Figure 2-36. The EWc of the North GoC. With red arrows the planar GPS measurements are shown. White dashed lines indicate the faults.

2.5.3. Validation

A comparison of the available GPS data and the PS values will be performed in this chapter. Moreover the episodic event of Efpalio Earthquake (§3.2) will be investigated for its affect in the PSI/SBAS study.

Because of the large spatially water coverage between the NGoC and the SGoC we have partitioned the study areas in two different processing chain. The SBAS technique uses 3d unwrapping in 3D and in spatial dimension extended watered areas may cause artifacts. But by inspecting the common area of the two processed areas we can see the consistence between them. But we keep some concerns about this.

In the original PSI/SBAS maps (Figure 2-16, Figure 2-18, Figure 2-20 and Figure 2-22), we have in purpose leave some PS falling on the sea in order to demonstrate the use of the proper threshold of PS selection.

An artifact has been detected in the SBAS processing of the descending track 279. In the area marked with dotted line in Figure 2-28 the SBAS PSs have been overestimated (probably due to the phase slipping of the 3D unwrapping).

In Table 3 we can see the EWc of the GPS that have been used to constraint the PSI/SBAS data (§2.5.2) and the corresponding PS values as well as their uncertainties for the NGoC. These data are plotted in Figure 2-37.

GPS no.	Name	PS EWc (mm year^{-1})	GPS EWc (mm year^{-1})	Uncert. PS (mm)	Uncert. GPS (mm)
1	I335	-0.8	5.2	1.6	1.6
2	LIDO	0.5	3.3	1.3	0.3
3	TRIZ	-2	-0.8	1.3	0.3
4	CG30	-1.1	1.8	1.3	2.5
5	EYPA	-5.5	2.9	1.5	0.3
6	C000	0.9	-0.1	1.4	0.4
7	O000	0.8	4.4	1.1	6.3
8	PSAR	0.8	0.2	1.4	0.3
9	THOM	4.8	4	2.9	0.7
10	CT00	0	1	1.6	0.3
11	RION	-2.8	2.9	2.1	0.9
12	H000	-4	3.9	2.3	0.7
13	I000	-1.4	3.8	1.6	0.5
14	K337	1.7	2.1	2.4	3.2
15	C075	0.5	1.9	1.4	1.1
16	UPAT	-2	-0.8	1.3	0.3
17	RC01	1.3	4.4	1.7	0.7
18	J000	-6	2.3	1.9	0.5
19	K001	1.8	2.6	2.8	0.7

20	LAMB	0	2.8	2	0.5
21	N000	2.4	2.8	2.1	0.5
22	RC02	1.3	4.4	1.7	0.7
23	AVAR	-3.2	0.8	2.5	3.2
24	RIOE	-2.7	0	2.1	1.6

Table 3. The EWc of the GPS that have been used to constraint the PSI/SBAS data and the corresponding PS values as well as their uncertainties for the NGoC.

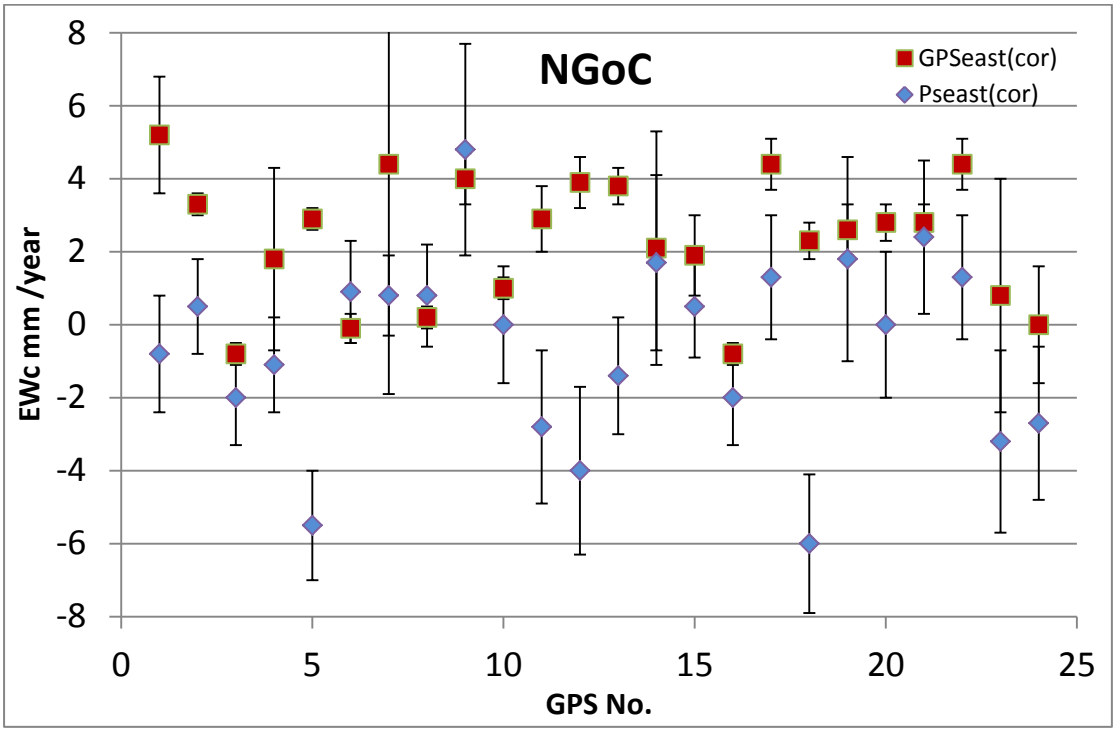

Figure 2-37. Diagram of the EWc of the GPS that have been used to constraint the PSI/SBAS data and the corresponding PS values as well as their uncertainties for the NGoC.

In Table 4 we can see the EWc of the GPS that have been used to constraint the PSI/SBAS data (§2.5.1) and the corresponding PS values as well as their uncertainties for the SGoC. These data are plotted in Figure 2-38.

GPS no.	Name	PS EWc (mm year^{-1})	GPS EWc (mm year^{-1})	Uncert. PS (mm)	Uncert. GPS (mm)
1	O000	1.5	2.8	2	0.5
2	TRIZ	-3	-0.8	1.4	0.3
3	UPAT	1.6	-1.1	3.4	4.5
4	CG30	-1.1	1.8	1.7	2.5
5	F000	1.6	-0.2	1.6	0.3
6	C000	0.3	-0.1	1.5	0.4
7	L000	0.7	1	1.8	0.3
8	RION	-1.3	2.9	2.2	0.9

9	Q619	1.5	-1.2	1.8	7.1
10	P226	2.2	4	1.8	0.6
11	D000	1.4	1.1	1.8	0.6
12	C075	-0.6	1.9	1.5	1.1
13	PSAR	0	0.2	1.5	0.3
14	KOUN	0.7	1	1.8	0.3
15	LAMB	-0.3	0.7	2.7	0.8
16	N730	1.5	2.8	2	0.5
17	CT00	-1.8	1	1.9	0.3
18	K001	1.3	2.6	1.9	0.7
19	RIOE	-1.7	0	2.5	1.6
20	J000	-4.9	2.3	2	0.5
21	T000	0.3	-1.7	1.6	0.6
22	C499	-1.1	0.9	1.6	0.4
23	N000	1.5	2.8	2	0.5
24	CG42	-0.7	2.5	1.5	1.5
25	CG43	0.3	1	2.6	1.5

Table 4. The EWc of the GPS that have been used to constraint the PSI/SBAS data and the corresponding PS values as well as their uncertainties for the SGoC.

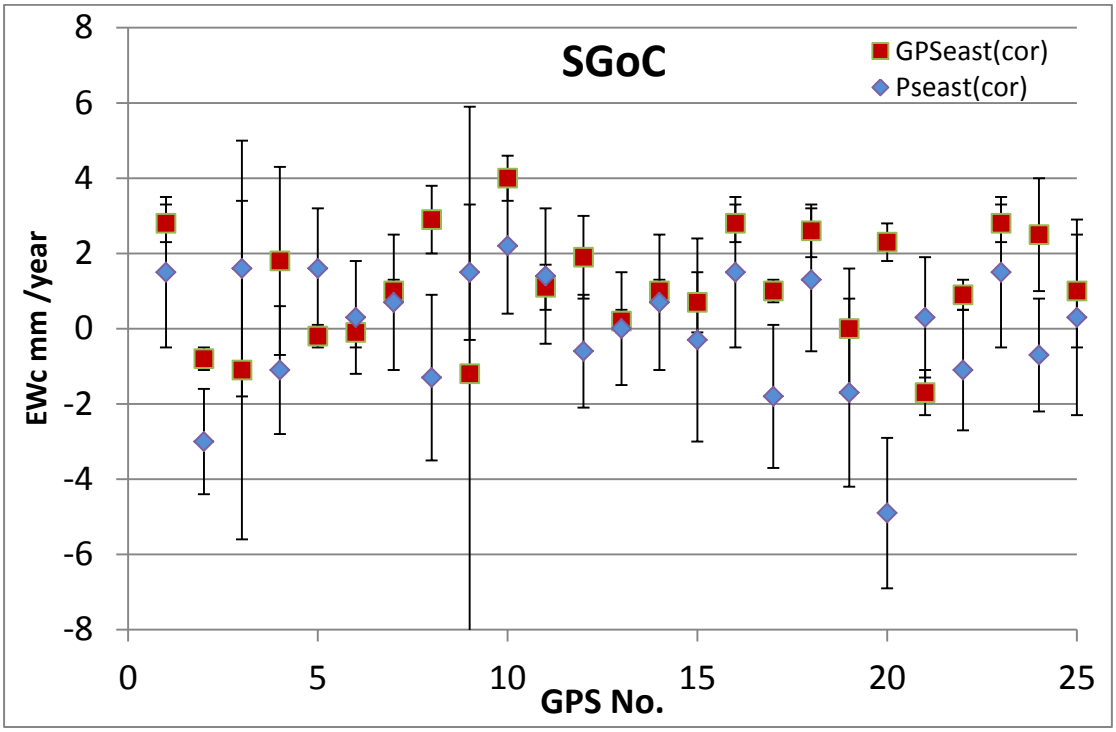

Figure 2-38. Diagram of the EWc of the GPS that have been used to constraint the PSI/SBAS data and the corresponding PS values as well as their uncertainties for the SGoC.

From these diagrams we can conclude that the correction we have applied worked well. In the SGoC the results are better than in the NGoC.

For validation using more GPS data for EWc we relaxed the maximum distance between the GPS and the PS used. Specifically the maximum distance in the correction phase was 0.004 (~400 m) and in the present phase is 0.01 (~1km).

In Table 5 we can see the EWc of the GPS and the corresponding PS values as well as their uncertainties for the NGoC. The volume of the GPS data used is 51. These data are plotted in Figure 2-39.

GPS no.	Name	PS EWc (mm year^{-1})	GPS EWc (mm year^{-1})	Uncert. PS (mm)	Uncert. GPS (mm)
1	3000	-1	1.7	1.4	0.4
2	3002	-1	2.5	1.4	0.9
3	3100	-0.1	0.9	1.4	0.5
4	ARI4	0.2	3.4	2.2	1
5	ARIO	-0.5	3.5	2.1	3.3
6	AVAR	-3.2	0.8	2.5	3.2
7	B000	-0.6	2.9	1.9	0.4
8	C000	0.9	-0.1	1.4	0.4
9	C075	0.5	1.9	1.4	1.1
10	C131	-0.1	-0.1	1.5	0.6
11	C216	-1.4	0	1.3	0.7
12	C499	-0.6	0.9	1.4	0.4
13	C711	-1.1	1.8	1.3	2.5
14	CG31	-0.1	2.5	1.4	1.5
15	CT00	0	1	1.6	0.3
16	CT30	-0.2	0.3	1.5	0.7
17	D004	-0.3	0.7	2.2	4.2
18	EYPA	-5.5	2.9	1.5	0.3
19	H000	-4	3.9	2.3	0.7
20	I000	-1.4	3.8	1.6	0.5
21	I335	-0.8	5.2	1.6	1.6
22	I682	-3	2.9	1.4	3.4
23	J000	-6	2.3	1.9	0.5
24	K000	1.8	0.8	2.8	0.6
25	K001	1.8	2.6	2.8	0.7
26	K337	1.7	2.1	2.4	3.2
27	KLLI	-1	3.3	1.4	1.3
28	LAMB	0	2.8	2	0.5
29	LIDO	0.5	3.3	1.3	0.3
30	M000	-3.3	0.1	1.5	0.7
31	MOL0	0.3	5.4	1.8	1.3
32	N000	2.4	2.8	2.1	0.5
33	N200	0.8	4.4	1.1	6.3
34	O002	-1.1	1.7	1.2	1.9
35	O003	-1.1	1.5	1.2	1.8

36	O005	-1.1	1.9	1.2	0.6
37	O106	-2.3	0.6	1.3	1.1
38	P226	2.7	4	2.1	0.6
39	PAT0	1.4	-1.6	2.2	1.3
40	PSAR	0.8	0.2	1.4	0.3
41	RC01	1.3	4.4	1.7	0.7
42	RCS2	-2.7	3	2.2	1.5
43	RCS3	-2.6	2.6	2.1	1.2
44	RESV	0.3	4.6	1.8	1.4
45	RIO2	-2.6	0.8	2.2	1.9
46	RIO4	-2.7	0	2.1	1.6
47	RION	-2.8	2.9	2.1	0.9
48	THOM	4.8	4	2.9	0.7
49	TR41	-0.5	5.3	2.2	1.9
50	TR4A	-0.4	5.1	2.2	3
51	TRIZ	-2	-0.8	1.3	0.3

Table 5. The EWc of the GPS and the corresponding PS values as well as their uncertainties for the NGoC in the validation phase.

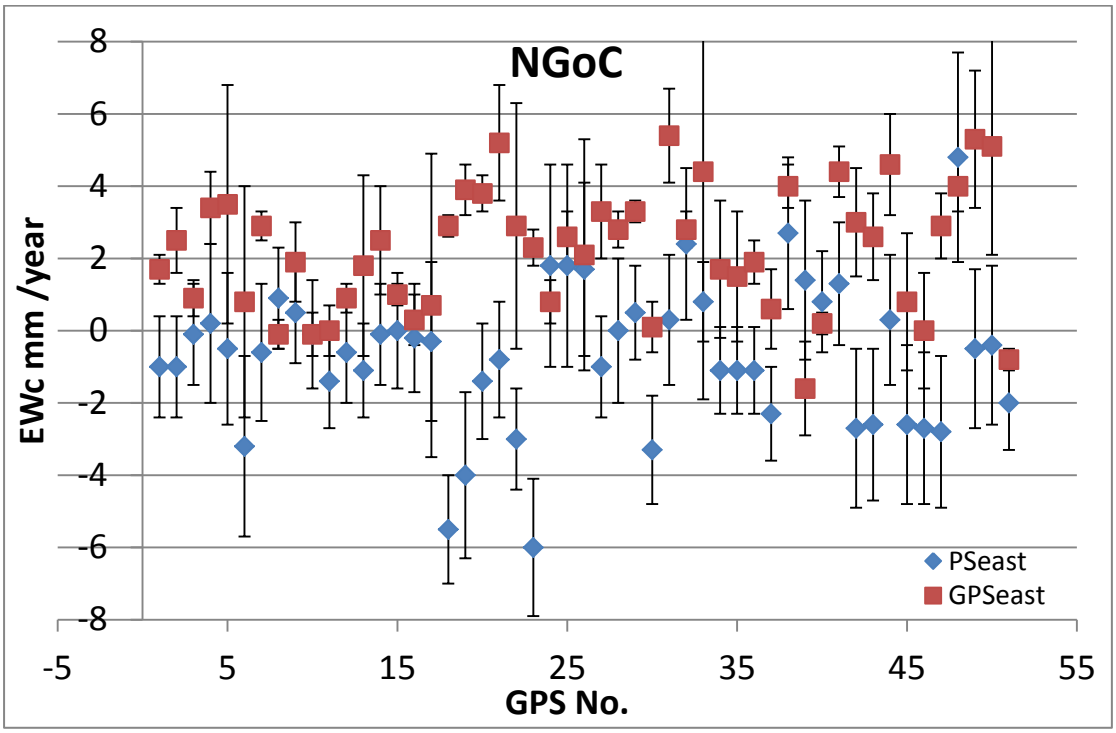

Figure 2-39. Diagram of the EWc of the GPS and the corresponding PS values as well as their uncertainties for the NGoC.

In Table 6 we can see the EWc of the GPS and the corresponding PS values as well as their uncertainties for the SGoC. The volume of the GPS data used is 55. These data are plotted in Figure 2-39.

GPS no.	Name	PS EWc (mm year^{-1})	GPS EWc (mm year^{-1})	Uncert. PS (mm)	Uncert. GPS (mm)
1	1130	-0.3	-0.3	2.7	0.7
2	3000	-1.3	1.7	1.6	0.4
3	3002	-1.3	2.5	1.6	0.9
4	3100	-0.7	0.9	1.5	0.5
5	4200	-0.3	0.8	2.7	1.6
6	4202	-0.3	1.7	2.7	0.5
7	4203	-0.3	0.4	2.7	1.1
8	ARI4	2.5	3.4	1.6	1
9	ARIO	1.4	3.5	1.6	3.3
10	C000	0.3	-0.1	1.5	0.4
11	C075	-0.6	1.9	1.5	1.1
12	C131	-0.8	-0.1	1.7	0.6
13	C216	-2	0	1.5	0.7
14	C499	-1.1	0.9	1.6	0.4
15	C711	-1.1	1.8	1.7	2.5
16	CG31	-0.7	2.5	1.5	1.5
17	CG43	0.3	1	2.6	1.5
18	CT00	-1.8	1	1.9	0.3
19	CT30	-1.7	0.3	1.9	0.7
20	D000	1.4	1.1	1.8	0.6
21	D004	-0.6	0.7	1.7	4.2
22	D005	1.5	0.3	1.7	0.9
23	DIAK	0.5	-2.3	1.6	1.3
24	E412	1.6	-0.2	1.6	0.3
25	J000	-4.9	2.3	2	0.5
26	K000	1.3	0.8	1.9	0.6
27	K001	1.3	2.6	1.9	0.7
28	K337	1.9	2.1	1.8	3.2
29	KLLI	-1.3	3.3	1.6	1.3
30	KOUN	0.7	1	1.8	0.3
31	LAKA	-0.3	0.7	2.7	0.8
32	MOL0	1.7	5.4	1.7	1.3
33	N000	1.5	2.8	2	0.5
34	O002	-2.3	1.7	1.3	1.9
35	O003	-2.3	1.5	1.3	1.8
36	O005	-2.3	1.9	1.3	0.6
37	O106	-3.4	0.6	1.3	1.1
38	P226	2.2	4	1.8	0.6

39	PAT0	2.7	-1.6	2.4	1.3
40	PSAR	0	0.2	1.5	0.3
41	Q619	1.5	-1.2	1.8	7.1
42	R000	-1.3	1.2	2.6	2.2
43	R001	-1.3	1.6	2.6	0.6
44	RCS2	-1.2	3	2.2	1.5
45	RCS3	-1.3	2.6	2.2	1.2
46	RESV	2.3	4.6	1.5	1.4
47	RIO2	-1.6	0.8	2.2	1.9
48	RIO4	-1.7	0	2.5	1.6
49	RION	-1.3	2.9	2.2	0.9
50	T000	0.3	-1.7	1.6	0.6
51	TR41	1.4	5.3	1.7	1.9
52	TR4A	1.4	5.1	1.7	3
53	TRIZ	-3	-0.8	1.4	0.3
54	U000	0.3	-0.1	2.6	0.4
55	U815	1.6	-1.1	3.4	4.5

Table 6. The EWc of the GPS and the corresponding PS values as well as their uncertainties for the SGoC in the validation phase.

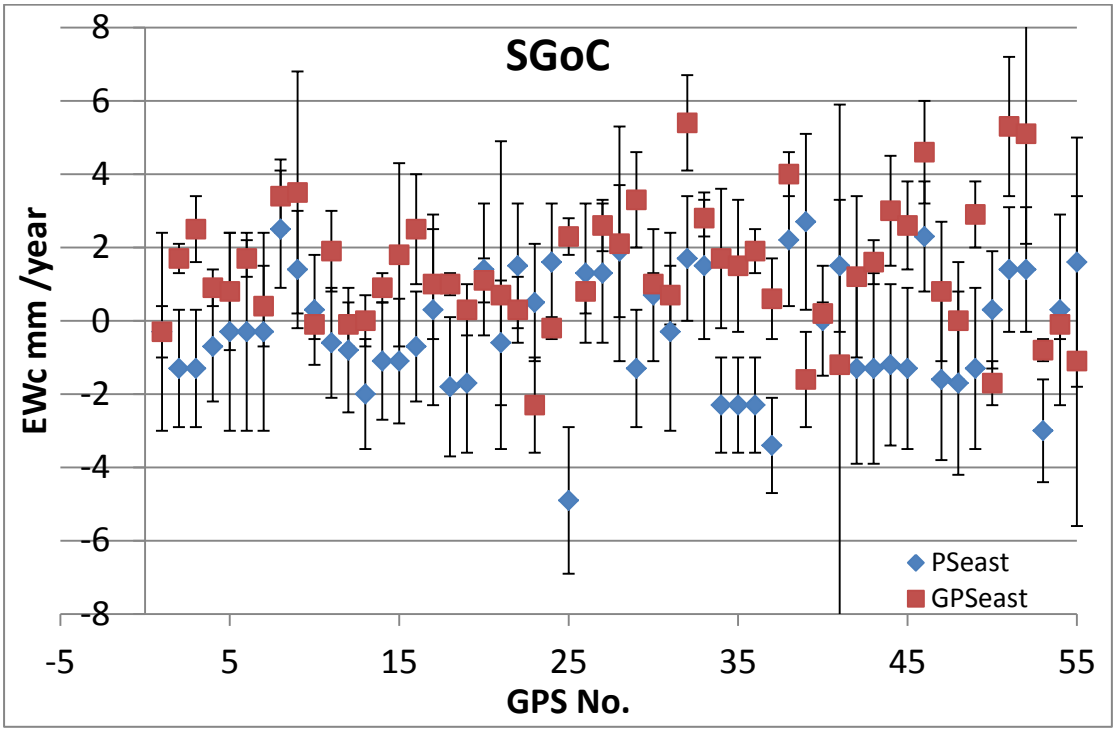

Figure 2-40. Diagram of the EWc of the GPS and the corresponding PS values as well as their uncertainties for the SGoC.

From these diagrams we can conclude that again we have better results in the SGoC. In this case and because we increased the maximum distance between the PS and the GPS we have increased the volume of the locations for comparison. Nevertheless we have induced noise in these additional PS values in the additional to the correction phase.

Finally, we validate by using the UDc of the permanent GPS stations. In Table 7 we can see the UDc of the GPS and the corresponding PS values as well as their uncertainties for the NGoC. These data are plotted in Figure 2-41. It is interesting to mention here that even though only the horizontal deformation rate components have been used to correcte the PSI/SBAS maps the Vertical components of it and with GPS have a very good accordance. Especially the GPS point KOUN has an ITRF2008 vertical rate of almost 0 mm year^{-1} the corrected PSI/SBAS corresponding rate is 0.8 mm year^{-1} (Table 8, Figure 2-42).

Name	PS UDc (mm year^{-1})	GPS UDc (mm year^{-1})	Uncert. PS (mm)	Uncert. GPS (mm)
LIDO	4.6	0.6	1.3	8.2
PSAR	-1	0	1.4	7.9
TRIZ	-0.6	-2.3	1.3	6.8
EYPA	-1.1	-1.6	1.4	9.5

Table 7. The UDc of the GPS and the corresponding PS values as well as their uncertainties for the NGoC.

.

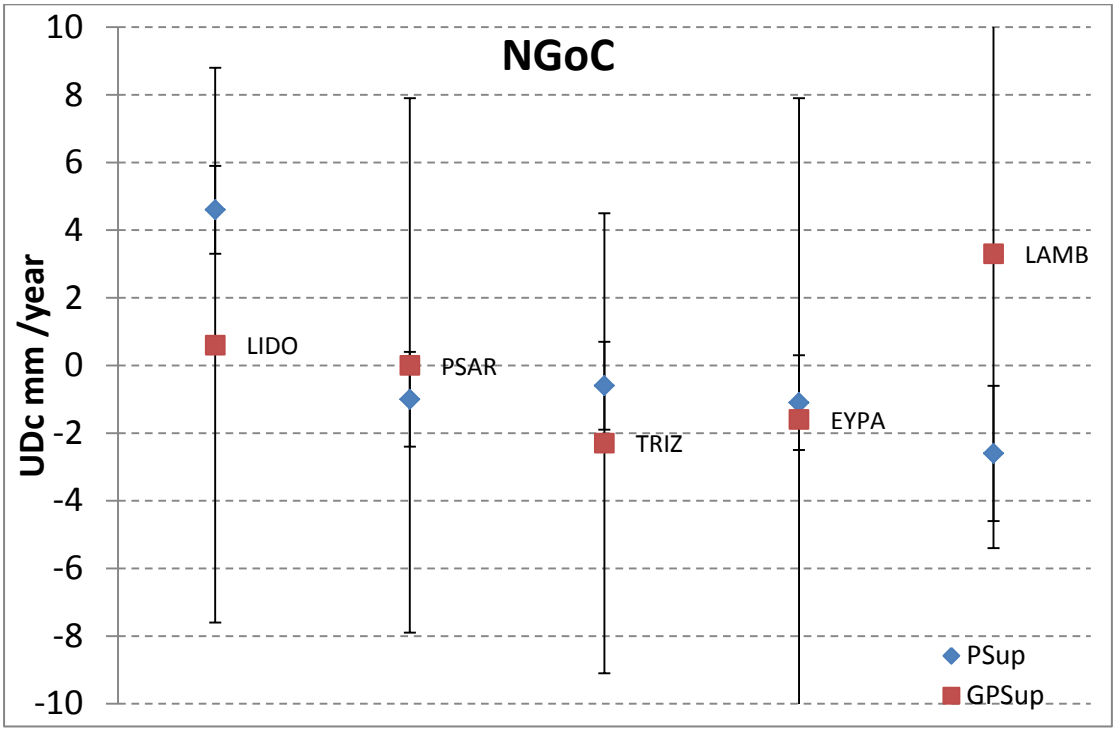

Figure 2-41. Diagram of the UDc of the GPS and the corresponding PS values as well as their uncertainties for the NGoC.

In Table 8 we can see the UDc of the GPS and the corresponding PS values as well as their uncertainties for the NGoC. These data are plotted in Figure 2-42.

Name	PS UDc (mm year^{-1})	GPS UDc (mm year^{-1})	Uncert. PS (mm)	Uncert. GPS (mm)
PSAR	-2	0.0	1.5	7.9
TRIZ	-0.8	-2.3	1.4	6.8
KOUN	0.8	0.0	1.8	7.5
LAMB	0.9	3.3	1.7	8.7

Table 8. The UDc of the GPS and the corresponding PS values as well as their uncertainties for the SGoC

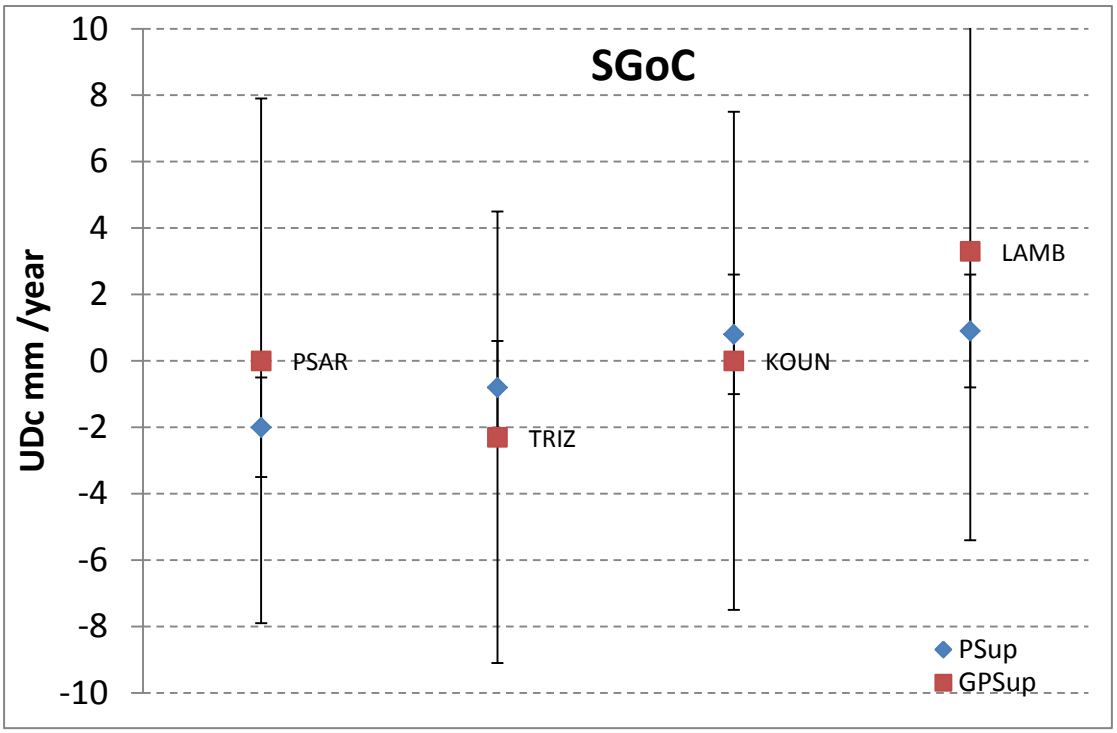

Figure 2-42. Diagram of the UDc of the GPS and the corresponding PS values as well as their uncertainties for the SGoC.

From the investigating of the UDc between the GPS and PS measurements we validate the good quality of the final PSI/SBAS map. The SGoC set has higher accuracy than the NGoC one.

3. Earthquakes

3.1. Movri 2008

3.1.1. Introduction

On 2008 June 8, a strong crustal earthquake struck NW Peloponnese, Greece (Figure 3-4). The event is reported as a moment magnitude M_W=6.4 strike-slip earthquake by the global centroid moment tensor (gCMT) catalogue [Ekstrom et al. 2005], making it the largest such event instrumentally recorded in this area. The enhanced shaking of this earthquake was felt throughout mainland Greece. It triggered a number of landslides and rockfalls, toppled old buildings and poorly reinforced houses and cracked reinforced concrete building in nearby communities. No evidence of surface rupture or significant surface deformation linked direct with the fault was observed [Briole et al. 2008; Ganas et al. 2009]. The most important spots of liquefaction caused by the earthquake were observed in the Kato Achaia Beach [Papadopoulos et al., 2010]

[Feng et al., 2010] assuming the fault length of 25km and allowing a generous bottom depth of 25 km, considers a burial depth to 10 km as unlikely. They estimate the burial (upper fault egde) as 5km more likehood and claim that such predicted displacements should be readily observable from InSAR. The burial depth and downdip extent of the fault within a homogeneous elastic earth cannot explain the observed small surface deformation. Therefore, they argue that the compositionally weak, ~3km thick flysch layer acts as a near-surface decoupling agent that isolates subsurface deformation from the surface.

[Papadopoulos et al., 2010] propose a rectangular planar seismic fault with mainshock rupture of 20 km and seismic fault depth ranging from 5 km to 20 km thus a down-dip width of 15 km. No co-seismic movement was detected by DInSAR analysis with the exception of the Kato Achaia area where again vertical ground displacement ranging from 3.0 cm to 6.0 cm was calculated.

[Ilieva, 2011] proposes rectangular fault parameters of length of 40km and depth of around 20-25km.

All the works considering that the fault plane covers a large part of the seismicity.

3.1.2. Constraining for the GPS and seismicity

Assuming for the earthquake a dislocation of a rectangular fault in homogeneous elastic half-space with average shear modulus μ=30 GPa we have performed a number of inversions of the deformation source. The forward algorithm used is that developed by [Okada 1985]. The inverse algorithm is that developed by [Briole et al. 1986] using a least squares approach proposed by [Tarantola and Valette 1982]. The inversion cost function is the rms scatter between the GPS planar measurements and the ones estimated from the model.

According to the fault plane solutions determined from various institutes, the earthquake ruptured a nearly vertical, strike-slip fault [Ganas et al. 2009]. Thus the strike slip angle has been set to 0 for pure strike slip fault and the dip angle at 89°. (Figure 3-1)

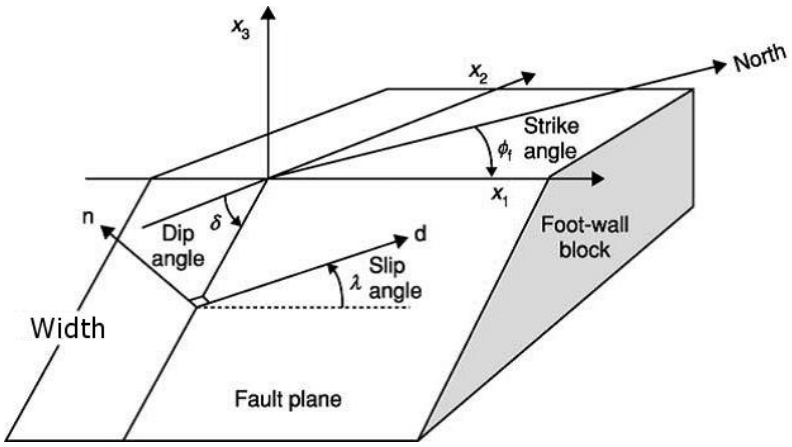

Figure 3-1. The geometrical parameters of the modeled fault [Stein and Wysession 2003].

The fault center is constrained by the seismicity of the yellow cluster (as will explain later) at the initial inversions. The strike azimuth is aligned with the seismicity at 25°.

For a range of the fault length between [8 28] km and upper fault depth between [6 21] km, with a strike azimuth at 25° we performed a number of inversions leaving the width and the slip free. Three fault center locations (i.e. C_1: 21.5235°E / 37.9374°N, C_2: 21.5462°E / 37.9379°N and C_3: 21.5690°E / 37.9385°N) have been tested according to the following procedure. The location C_1 presented the best fitting (as will explain later) and will be demonstrated.

The Mo has been calculated according to equation 1.

$$M_O = \mu \cdot L \cdot W \cdot D \quad (1)$$

Where: μ shear modulus
L length of the fault
W width of the fault and
D the slip

The Mo used to constrained the solution was the gCMT (http://www.globalcmt.org): $M_O^{gCMT} = 4.6 \cdot 10^{18}$ Nm. In Figure 3-2 the solutions of each inversion are plotted. These that satisfy the condition $M_O \cong M_O^{gCMT} \pm 0.15 \cdot 10^{18}$ Nm are listed in Table 9.

From Figure 3-2 we can see that in depth around 16.5 km both constrains (i.e. the rms is minimized and condition of M_O is satisfied) are met.

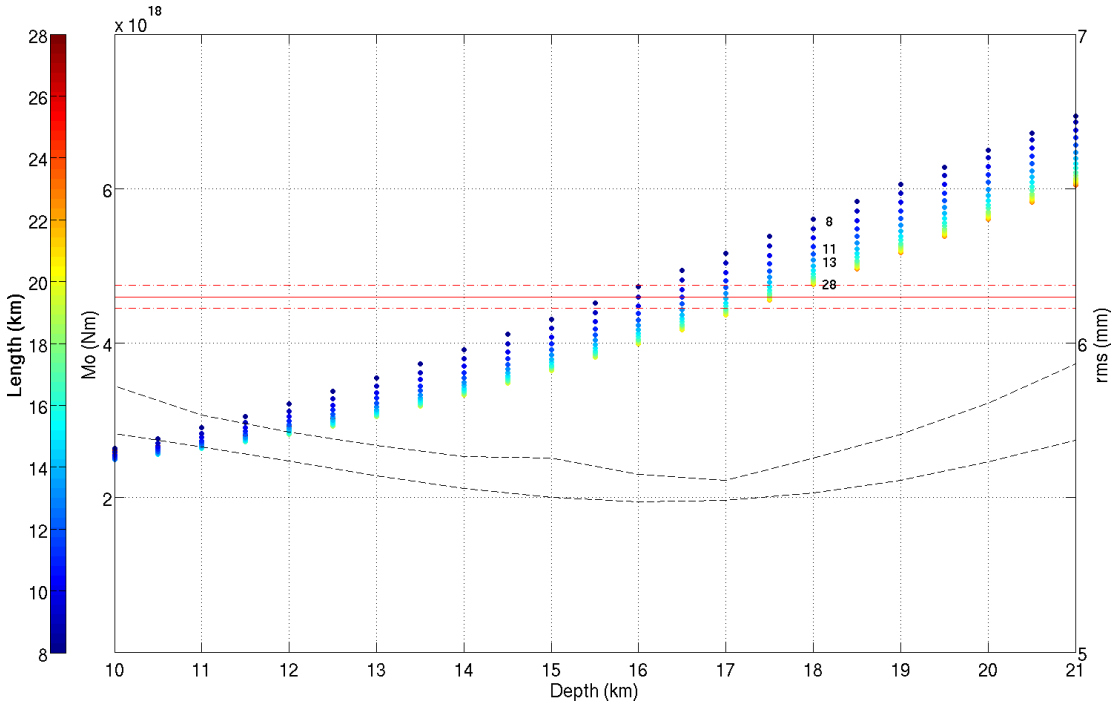

Figure 3-2. Plot of the Depth versus the M_O of the inversions for center fault location at C_1. The length of the fault is presented in color and in text within the diagram. The black dashed lines represent the upper and lower limits of the GPS rms error for the solutions of different length, its values are on the right vertical axe. The red line marks the M_O of gCMT value and the red dashed line the range of gCMT ±0.15 10^{18} Nm.

No.	Depth (km)	Length (km)	M_O (10^{18} Nm)	rms (mm)	Slip (m)	Width (km)	Lower Depth (km)
1	16.0	10.0	4.48	5.50	1.27	11.8	27.8
2	17.0	16.0	4.48	5.49	1.16	8.0	25.0
3	16.5	12.0	4.51	5.50	1.22	10.2	26.7
4	15.5	8.0	4.52	5.51	1.35	13.9	29.4
5	**17.0**	**15.0**	**4.52**	**5.50**	**1.18**	**8.5**	**25.5**
6	17.5	21.0	4.56	5.51	1.14	6.4	23.9
7	17.5	22.0	4.56	5.5	1.13	6.1	23.6
8	17.5	23.0	4.56	5.52	1.12	5.9	23.4
9	17.5	24.0	4.56	5.54	1.12	5.7	23.2
10	17.5	25.0	4.56	5.54	1.11	5.5	23.0
11	**17.0**	**14.0**	**4.57**	**5.50**	**1.20**	**9.1**	**26.1**
12	17.5	26.0	4.57	5.53	1.11	5.3	22.8
13	17.5	20.0	4.58	5.52	1.14	6.7	24.2
14	17.5	27.0	4.58	5.54	1.10	5.1	22.6
15	16.5	11.0	4.59	5.50	1.26	11.1	27.6

16	17.5	19.0	4.59	5.50	1.15	7.0	24.5
17	16.0	9.0	4.60	5.51	1.32	12.9	28.9
18	17.5	28.0	4.60	5.55	1.10	5.0	22.5
19	17.5	18.0	4.61	5.50	1.16	7.4	24.9
20	**17.0**	**13.0**	**4.64**	**5.50**	**1.22**	**9.7**	**26.7**
21	**17.5**	**17.0**	**4.64**	**5.51**	**1.18**	**7.8**	**25.3**
22	**17.5**	**16.0**	**4.68**	**5.50**	**1.19**	**8.2**	**25.7**
23	16.5	10.0	4.70	5.51	1.30	12.0	28.5
24	17.0	12.0	4.72	5.51	1.25	10.5	27.5
25	16.0	8.0	4.73	5.52	1.39	14.2	30.2
26	**17.5**	**15.0**	**4.73**	**5.51**	**1.20**	**8.7**	**26.2**

Table 9. The solutions on the inversions lying between the M_O of gCMT ±0.15 10^{18} Nm for the fault center location at C_1. The *Lower Depth* isn't a direct inverted parameter but the addition of (Upper) *Depth* and *Width*. In bold the most likehood solution.

Among these the solutions 5, 11, 20, 22 and 26 are the most likehood since their lower depth (ranging between [25.3 26.7] km) reaching the lower depth of seismicity. All of their rms are the lowest. The depth is ~17 km, the length ranging between [13 17] km, the width between [7.8 9.7] km and the slip between [1.18 1.22] m. Due to the extension of the seismicity related with the fault the most likehood length is 15 km. Finally the larger depth (i.e. 17.5 km) is the most preferable as it was provided by the DInSAR study. The validity of these hypotheses will be demonstrated right after. The seismicity projected on the fault plane, as well as the fault sides are displayed at Figure 3-3. The seismicity is colored according to the cluster that each earthquake belongs to. The clustering of the earthquakes has been realized according to their location in 3D space and the time of their occurrence.

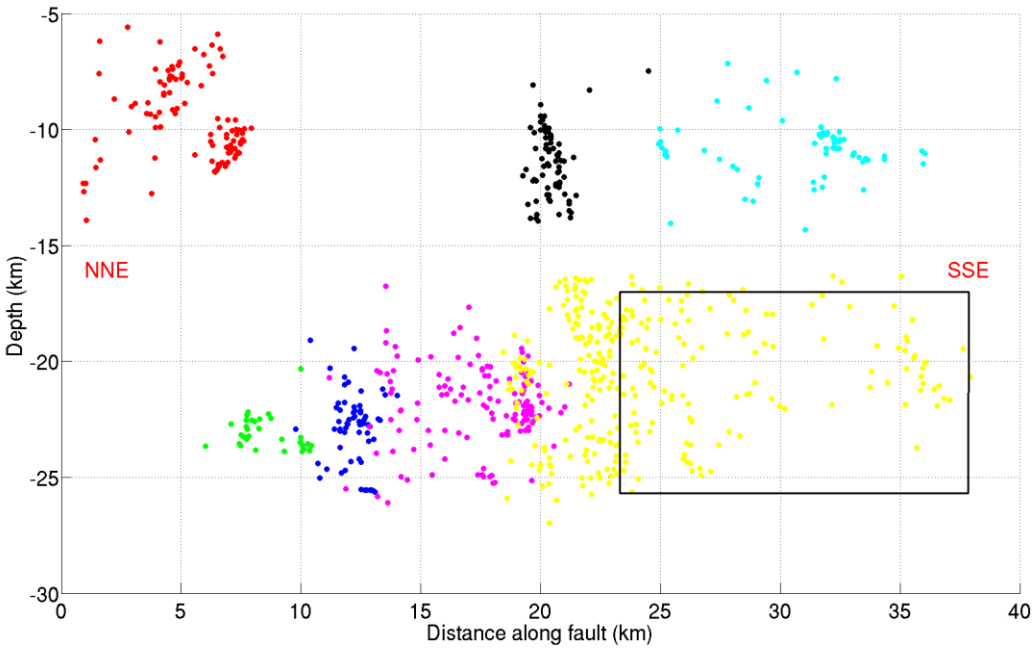

Figure 3-3. The seismicity projected on the fault plane. The orientation the *Distance along fault* is from NNE towards SSE. The rectangle is the proposed fault representation at location C_1. The seismicity is colored according to the cluster that each earthquake belongs to.

In Figure 3-4 the GPS deformation vectors, the modeled vectors and the seismicity (with the cluster information) are presented. We can notice that even in the far field (i.e. in the eastern stations of the permanent CRL GPS network) the deformation was measurable from

GPS observations. Moreover the matching between the GPS and the modeled deformations vectors is high in most of the locations.

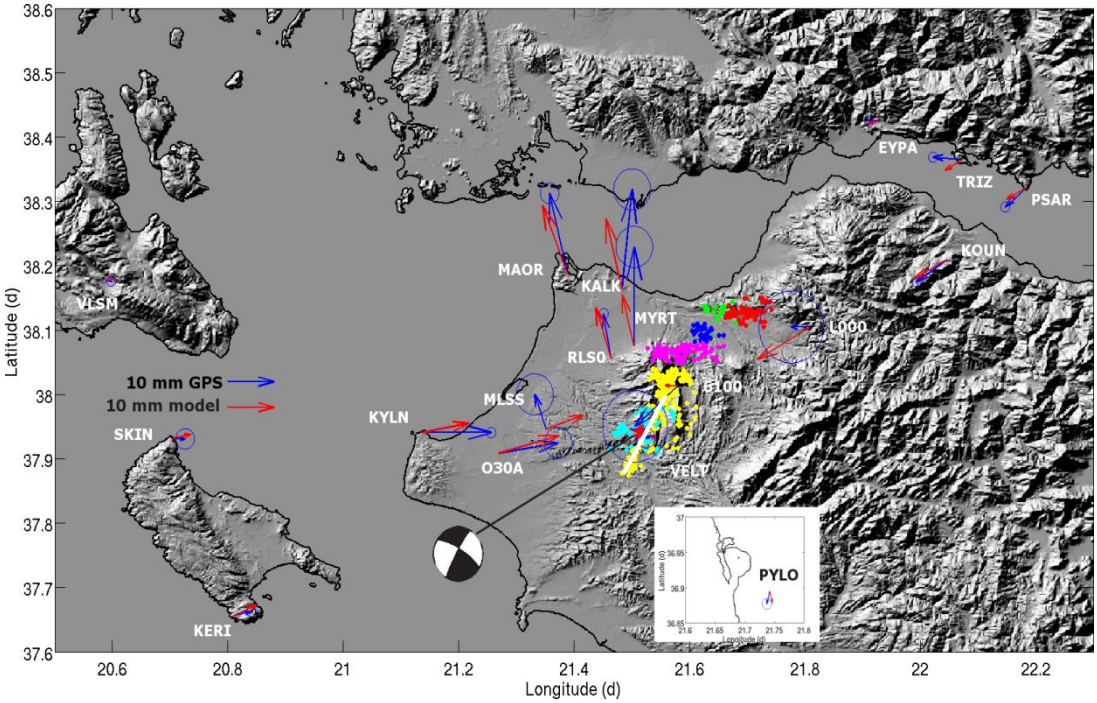

Figure 3-4. Shaded relief of the study area. The GPS vectors (along with their names) in blue along with their errors, the modeled vectors in red and the seismicity (with the cluster information). White line represents the proposed fault at location C_1. In the inset the PYLO vectors which are located south of the main image, is show,

In Figure 3-5 we focus in the area where the seismicity is concentrated.

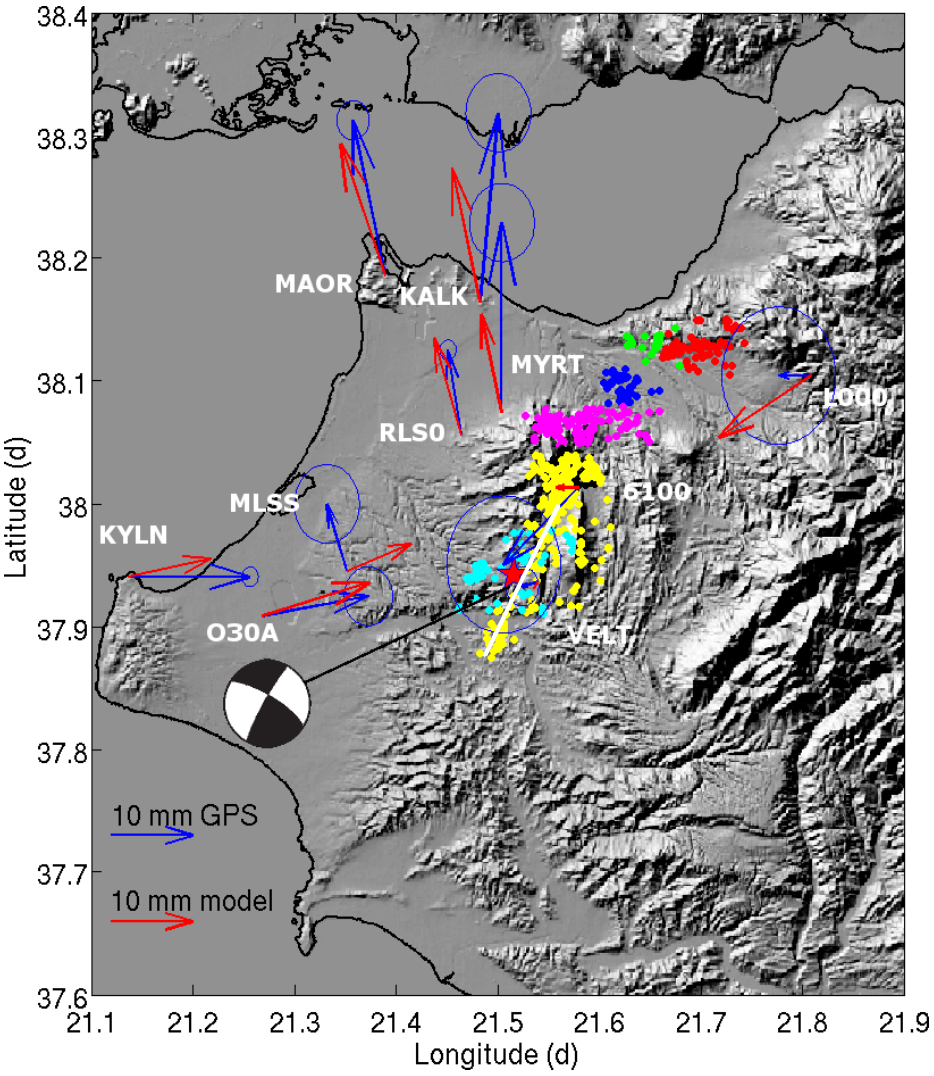

Figure 3-5. Focused in the earthquake area of the Figure 3-4.

In Table 10 we present the name in the network that it belongs to, the measured deformation in East (d_{East}) and North (d_{North}) components, along with its uncertainty values (sig d_{East}, sig d_{North}, respectively) and the corresponding model no. 26 (M_{East}, M_{North}) of Table 9.

No	Name	Network	Longitude	Latitude	d_{East} (mm)	sig d_{East} (mm)	d_{North} (mm)	sig d_{North} (mm)	M_{East} (mm)	M_{North} (mm)
1	6100	CRL-net	21.5796	38.0138	-9.2	7.0	-2.8	7.0	-7.9	0.0
2	MLSS	CRL-net	21.3520	37.9456	-2.5	4.0	8.0	4.0	6.8	2.8
3	MAOR	CRL-net	21.3897	38.1862	-4.0	2.0	-5.6	2.0	15.8	13.7
4	KALK	CRL-net	21.4831	38.1641	2.2	4.0	-3.5	4.0	19.3	13.9
5	MYRT	CRL-net	21.5043	38.0747	0.0	4.0	-2.6	4.0	19.3	10.1
6	KYLN	CRL-net	21.1364	37.9406	23.0	4.0	10.4	4.0	13.5	1.9
7	L000	CRL-net	21.8079	38.1047	-3.9	7.0	-11.5	7.0	0.0	-6.4
8	VELT	CRL-net	21.5396	37.9368	-1.9	4.0	-0.5	4.0	-0.5	-0.7
9	EYPA	CRL-perm	21.9285	38.4268	-2.1	1.0	-2.3	1.0	-0.4	-0.8
10	KOUN	CRL-perm	22.0459	38.2095	-6.5	1.0	-7.1	1.0	-4.3	-3.7
11	PYLO	CRL-perm	21.7420	36.8956	-0.6	1.0	0.6	1.0	-2.3	-2.2
12	PSAR	CRL-perm	22.1843	38.3218	-4.6	1.0	-4.4	1.0	-3.8	-2.3
13	RLS0	NOA-perm	21.4648	38.0559	-1.7	1.0	-3.4	1.0	8.7	10.1
14	TRIZ	CRL-perm	22.0727	38.3654	-6.3	1.0	-3.8	1.0	0.4	-2.2
15	VLSM	NOA-perm	20.5887	38.1768	1.2	1.0	1.3	1.0	-0.1	0.6
16	KERI	ETHZ-perm	20.8080	37.6551	4.0	1.0	5.3	1.0	1.0	2.3
17	SKIN	ETHZ-perm	20.7020	37.9310	3.0	2.0	4.4	1.0	0.0	0.9
18	030A	HEPOS-net	21.2687	37.9088	13.0	3.0	13.4	3.0	2.0	3.5

Table 10. The GPS measurements used in the present study. Where the measured deformation in East (d_{East}) and North (d_{North}) components, along with its significance values (sig d_{East}, sig d_{North}, respectively) and the corresponding model no. 26 (M_{East}, M_{North}) of Table 9. For CRL see [Briole et al., in prep ; Avallone 2003 ; https://gpscope.dt.insu.cnrs.fr/chantiers/corinthe/] , for NOA see [http://www.gein.noa.gr/services/GPS/noa_gps.html], ETHZ see [Muller et al., 2011] and [http://www.sgc.ethz.ch] and for HEPOS see [Gianniou 2011].

From the seismicity (Figure 3-3 and Figure 3-5) we observed that the NNE part of the 'yellow' cluster is constraining the fault SSE edge. To support this hypothesis we have prepared two more groups of inversions moving the epicenter C_1 at 2km and at 4km towards NNE at locations C_1 and C_2 respectively, as stated before. In Figure 3-6 and Figure 3-7 the solutions of each inversion for the two locations (NNE the C_1) are plotted.

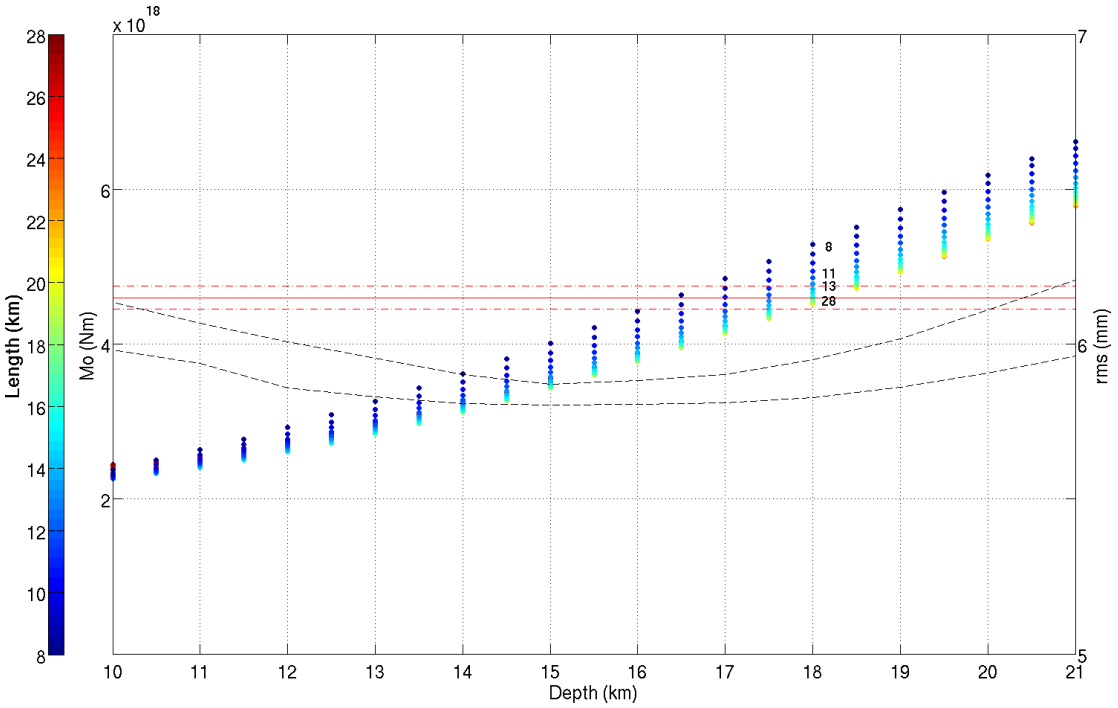

Figure 3-6. Plot of the Depth versus the M_O of the inversions for center fault location at C_2.

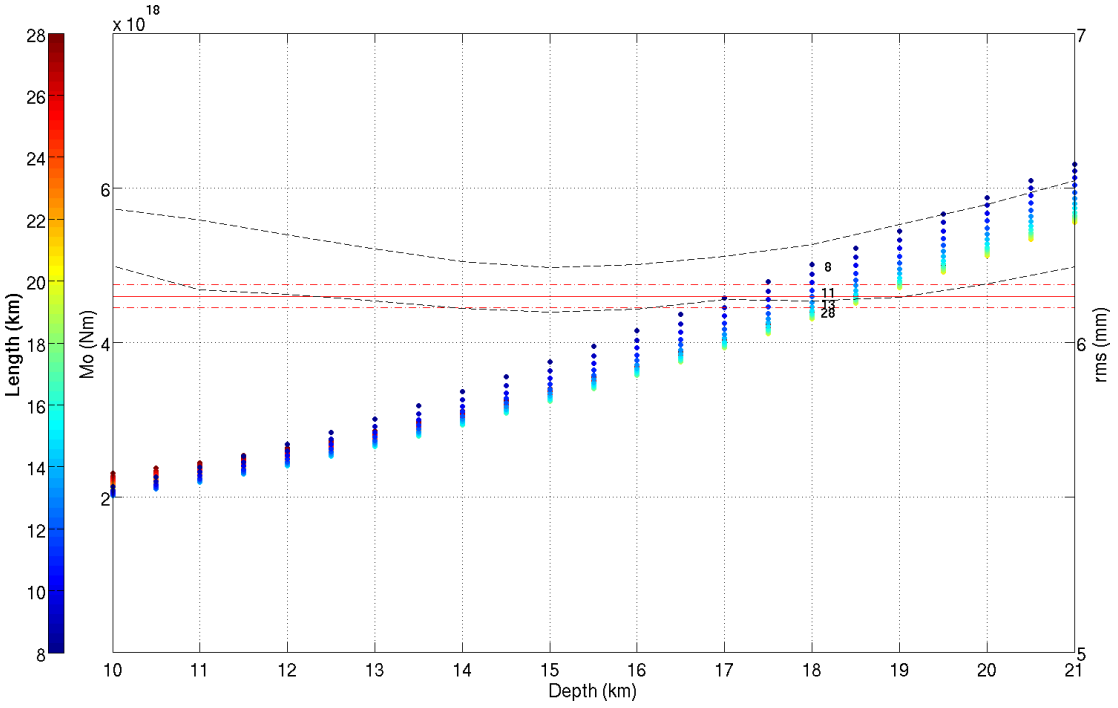

Figure 3-7. Plot of the Depth versus the M_O of the inversions for center fault location at C_3.

In these plots we can see that the range of rms error along the depth dimension of the inversions (black dashed lines) of the two groups corresponding to the location of epicenters C_2 and C_3 are significantly larger in comparison with the one of the epicenter that located in C_1 (Figure 3-7).

Moreover, if we kept the same geometry with that of the fault in question and move only the epicenter locations to C_2 and C_3 we will measure an rms error of 5.9 mm and 6.3 mm, respectively in contrast with 5.5 mm where the epicenter located at C_1. The seismicity

projected on the fault plane along with a representation of it, have been plotted in Figure 3-8 and Figure 3-9, for the fault center located at C_2 and C_3, respectively.

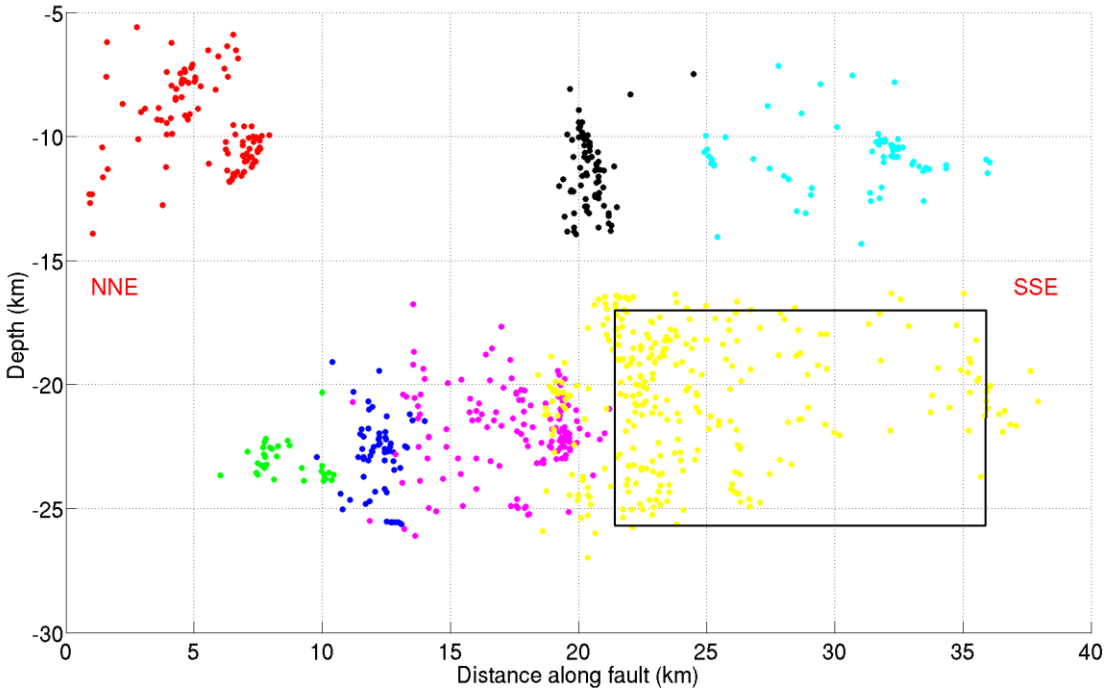

Figure 3-8. The seismicity projected on the fault plane. The orientation of the *Distance along fault* is from NNE towards SSE. The rectangle is the proposed fault representation at location C_2. The seismicity is colored according to the cluster that each earthquake belongs to.

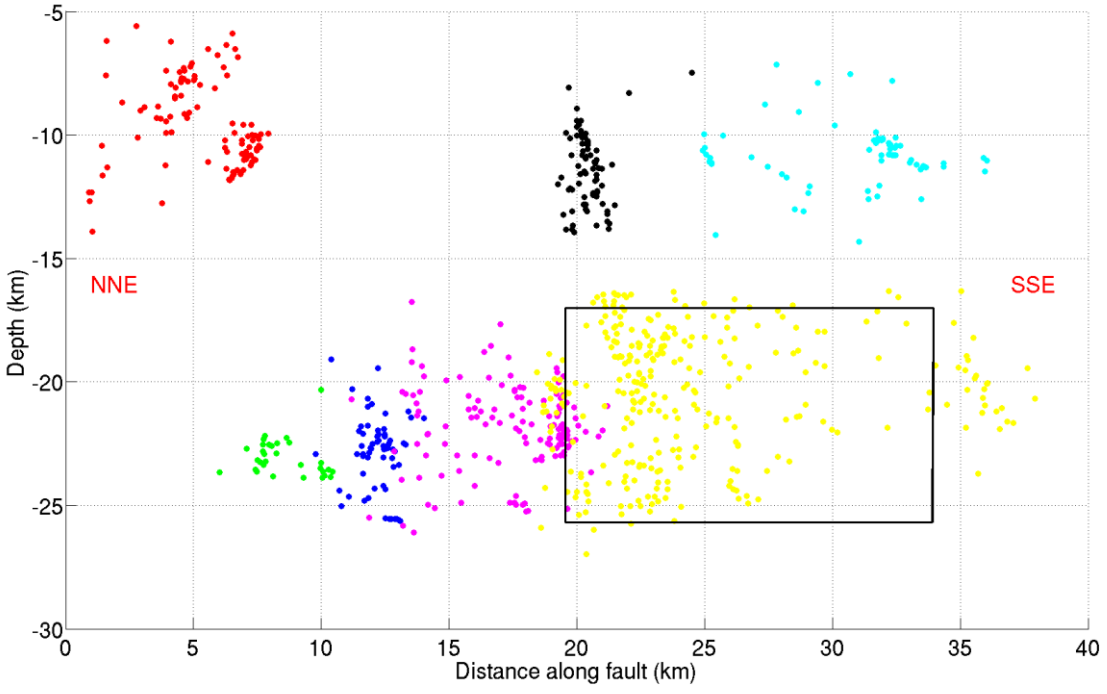

Figure 3-9. The seismicity projected on the fault plane. The direction of the *Distance along fault* is from NNE towards SSE. The rectangle is the proposed fault representation at location C_3. The seismicity is colored according to the cluster that each earthquake belongs to.

The seismicity linked to the fault in question was blocked to ~26km as we have discussed earlier and includes only the 'yellow' cluster. We can see that mitigating the epicenter location NNE the fault plane overcomes this blocking limit.

3.1.3. Constraining for the DInSAR

No obvious deformation was visible from single interferograms either from ASAR/ENVISAT or PALSAR/ALOS. Following the methodology of interferogram stacking (e.g. averaging each pixel of all single interferograms spanning the date of the earthquake), we proceeded to the investigation for the existence of a small deformation pattern. Accordingly thirty co-seismic ASAR/ENVISAT descending interferograms of Track 279, have been created by multilooking of 4x20 with ROI-PAC software [Rosen et al. 2004]. Its topography effect has been eliminated by using Ktimatologio DTM reprojected from traverse Mercator projection of GGCS87 Datum with cell size of 5mx5m to geographic projection of WGS84 datum with cell size 0.0002°N x 0.0002°E. Nineteen interferograms has been selected by visual inspection presenting relatively good coherence. In Figure 3-10 the dates versus the baselines is plotted.

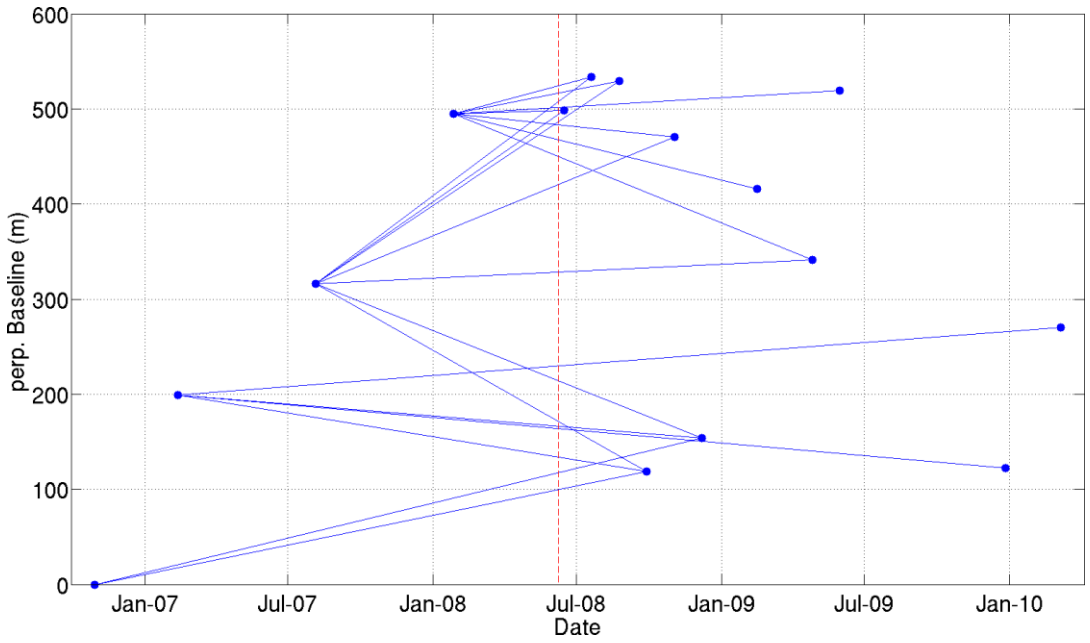

Figure 3-10. Plot of the dates of the participating ASAR/ENVISAT acquisitions versus the baselines of the interferograms used in the study. With red dotted line the date of the earthquake is indicated.

The selected differential interferograms have been unwrapped by SNAPHU software [Chen et Zebker 2002]. From all the interferograms we have excluded from any posterior calculations the pixels falling into the sea, the areas without the existence of deformation information and the areas where the absolute modeled deformation value is above 10mm. In order to minimize any linear orbital and low frequency tropospheric effect we have followed the following procedure. We partitioned each interferogram in 65 horizontal and

44 vertical zones of 50 pixels, each. Then for all the interferograms we applied a linear least square fitting to remove any N-S trend slope of the average values of the horizontal zones. The same procedure has been followed for the E-W trend with the vertical zones. Simultaneously the mean value of each interferograms has been set to zero (Figure 3-11).

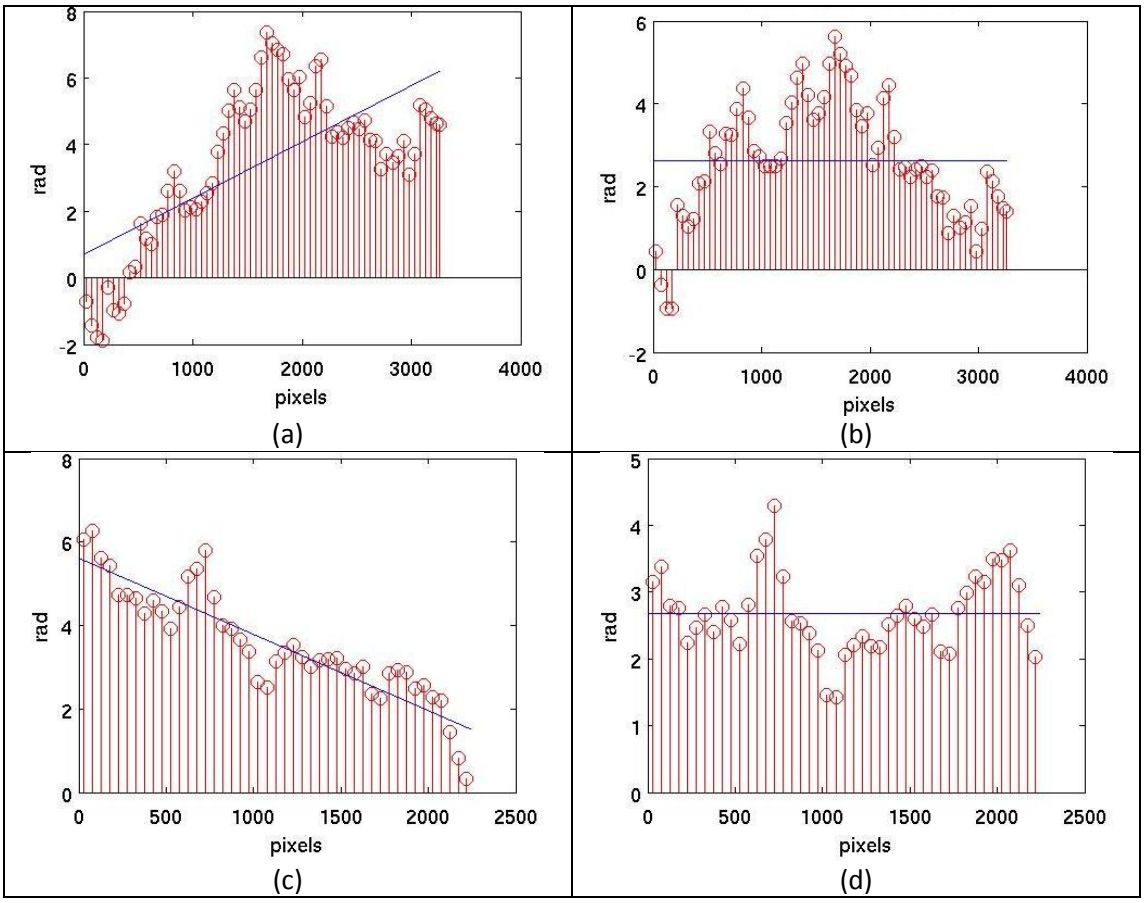

Figure 3-11. An example of the trend slope linear correction of the interferogram spanning the dates 29/10/06 and 28/9/08 is presented. (a) Average values of the horizontal zones before and (b) after the linear correction for the N-S trend. (c) Average values of the vertical zones before and (d) after the linear correction for the E-W trend. Blue lines indicate the corresponding linear trends.

By using the 19 corrected unwrapped differential interferograms we have calculated their mean values in order to amplify the common mode deformation signal and decrease the uncorrelated noise. Finally we produced the filtered (by an average filter of size 1km x 1km) mean stacked interferogram to minimize any high-to-medium frequency common mode noise signal and we have converted it to mm (Figure 3-12). The small deformation field predicted by the model (amplitude less than one fringe) didn't permitted us to correct for unwrapping phase cycle slip errors as we have done in the case of Athens earthquake of 1999 [Elias et al. 2006].

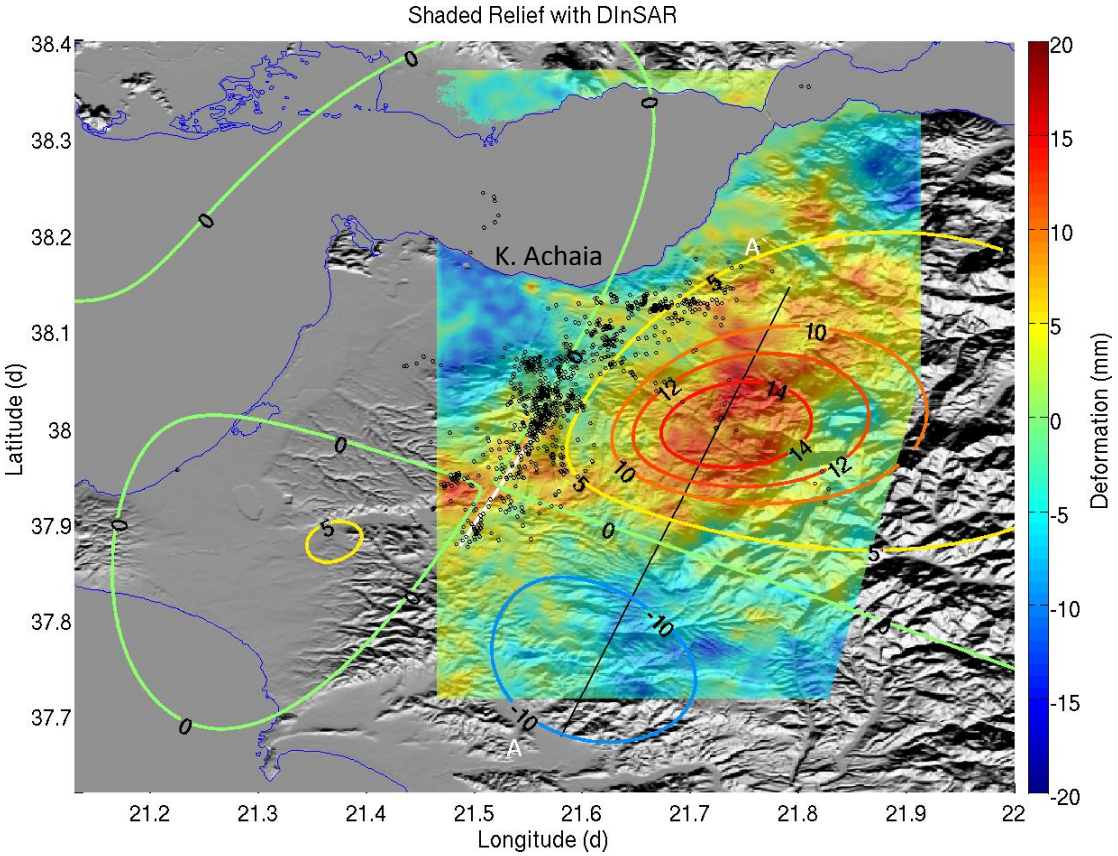

Figure 3-12. The filtered mean stacked interferogram superimposed over shade relief. In contour lines the modeled deformation is drawn. The seismicity is plotted with black circles. The fault is drawn with white line. The color representation is common in both, the interferogram and the contours. The black line A-A' corresponds to the trace of the cross section discussed in the study.

In Figure 3-12 the modeled deformation has been plotted in contour lines. The color representation of the contours and the filtered mean stacked interferogram is the same. The positive values represent deformation in LOS away the satellite. We can observe a coincidence of the area of the maximum deformation lobe with the maximum area of the mean differential interferogram, especially in contour having a value of 14mm. This maximum deformation area of the filtered mean stacked interferogram is not linked to the topography since in the E and SE areas the relief is more steep and mountainous but the observed deformation isn't. The model seems to be overestimated in comparison with the filtered mean stacked interferogram but this is expected since the noise component is very high and the average filter decreases the magnitude of the measurements. Furthermore in Figure 3-13 where we see the cross section A-A' (Figure 3-11 and Figure 3-12) of the model and the filtered mean stacked interferogram, the yellow lines (which is the unfiltered mean stacked interferogram) locally overcomes the amplitude of the model. The red line is the filtered mean stacked interferogram and the green lines are single interferograms. The model variance is almost one fringe or half the ASAR/ENVISAT wavelength.

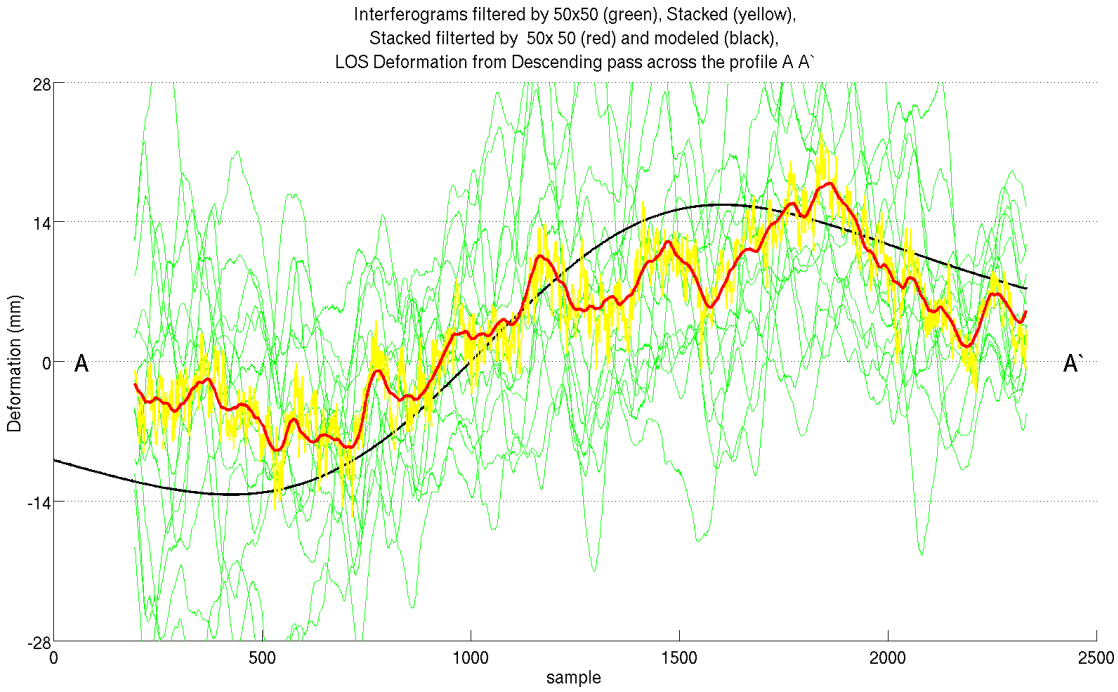

Figure 3-13. The cross section A-A' (Figure 3-19 and Figure 3-12) of the model in black and the filtered mean stacked interferogram in red. The yellow line represents the unfiltered mean stacked interferogram and the green lines single (linear N-S and E-W trends corrected) unwrapped interferograms.

This cross section passes through the maximum modeled deformation lobes. Here also we can see the coincidence of the DInSAR and the model. We can observe the common mode of all the interferograms that tends to the model.

The single interferograms are quite noisy. The high vegetated land cover, the increased abrupt slopes, the heavy precipitation rate and the increased moisture levels of the area away the coast as well are unwrapping phase slip errors are sources of the increased noise levels. For this reason in the PSI/SBAS maps we have quite few Persistent Scatterers left.

In Figure 3-14 the filtered mean stacked interferogram with the modeled deformation subtracted is presented.

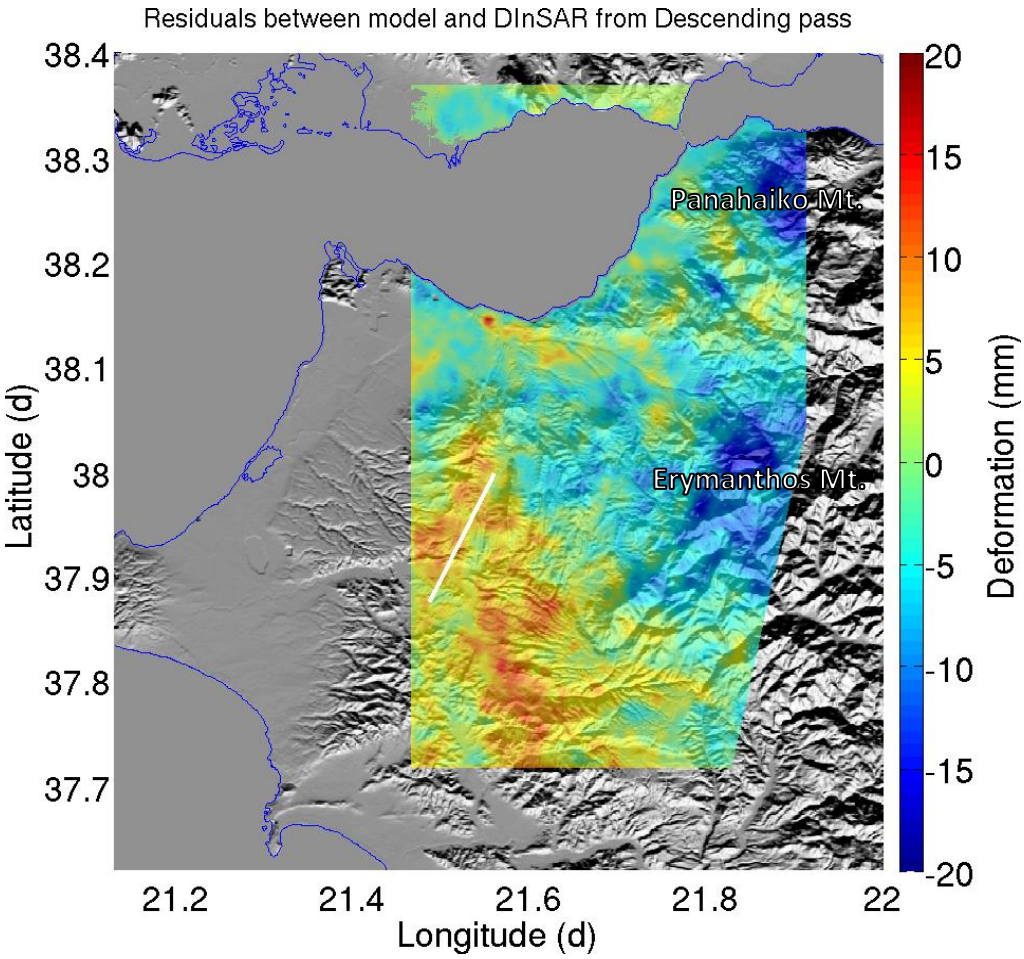

Figure 3-14. The residuals of the filtered stacked mean interferogram and the model are presented.

We can see a clear correlation of the residual deformation with the topography especially in the Panahaiko (1928 m) and Erymanthos (2224 m) mountains. By investigating the correlation between the topography and the deformation (Figure 3-15) a clear trend is being revealed. It is almost 10 mm per 2km height.

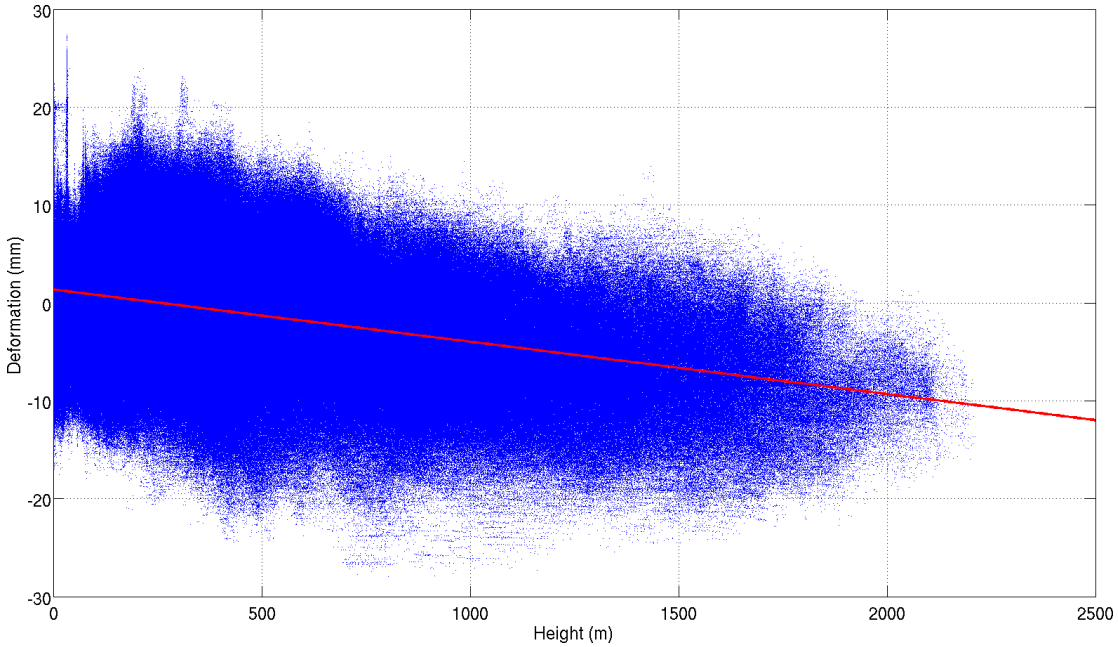

Figure 3-15. Plot between the height and the deformation values of the mean stacked interferogram. The red line corresponds to the least squares linear fit of the data.

We have removed this trend from the filtered mean stacked interferogram resulting to that of the Figure 3-16.

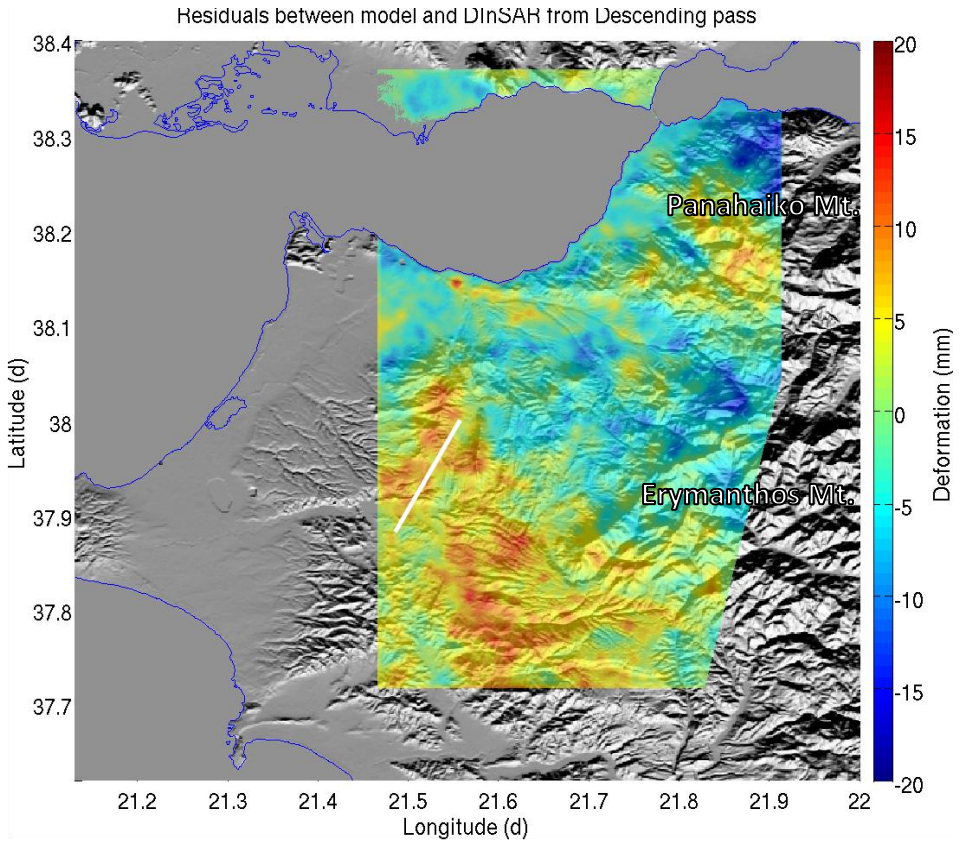

Figure 3-16. The residuals of the filtered stacked mean interferogram after the linear trend correction of Figure 3-15 and the model are presented. White line indicates the proposed fault.

The improvements are small in comparison with Figure 3-14. There are improvements in Erymanthos and North Panahaiko. Mts, but there is also deterioration in the South Panahaiko Mt. By applying this correction to the initial filtered mean stacked interferogram we resulted to the Figure 3-17. Its cross section A-A' is plotted in Figure 3-18.

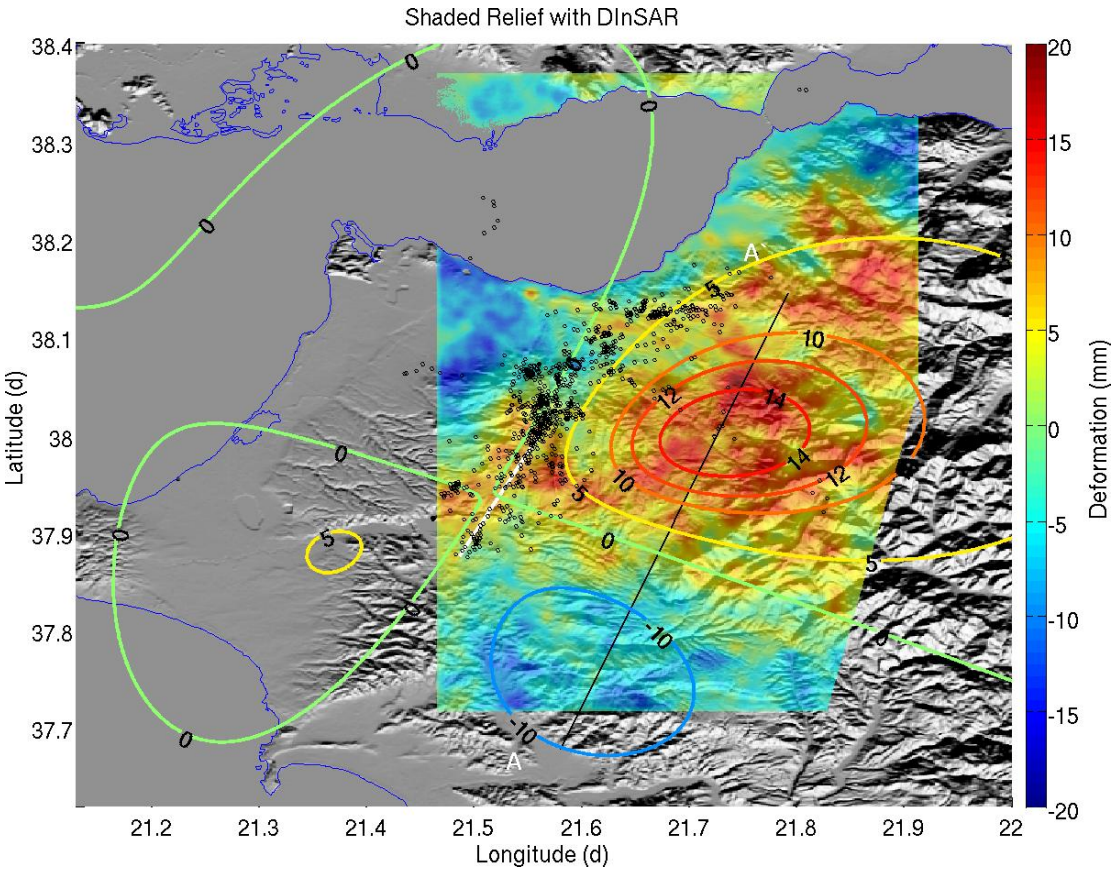

Figure 3-17. The filtered mean stacked interferogram after the linear trend correction of Figure 3-15, superimposed over shaded relief. White line indicates the proposed fault.

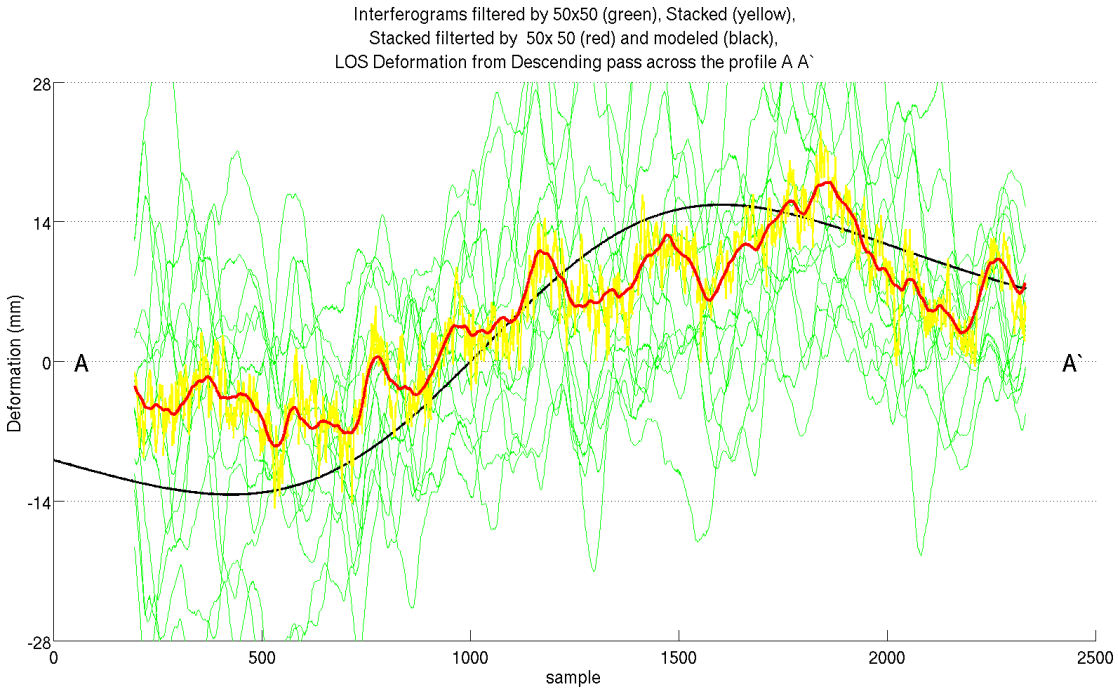

Figure 3-18. All curves of Figure 3-13 after the linear trend of height versus deformation correction of Figure 3-15.

Once more the improvement is also small but present in comparison with Figure 3-13.

In Figure 3-19 the modeled interferogram for descending mode, fault location at C_1 and preferred fault geometry (model no. 26 of Table 9) is presented.

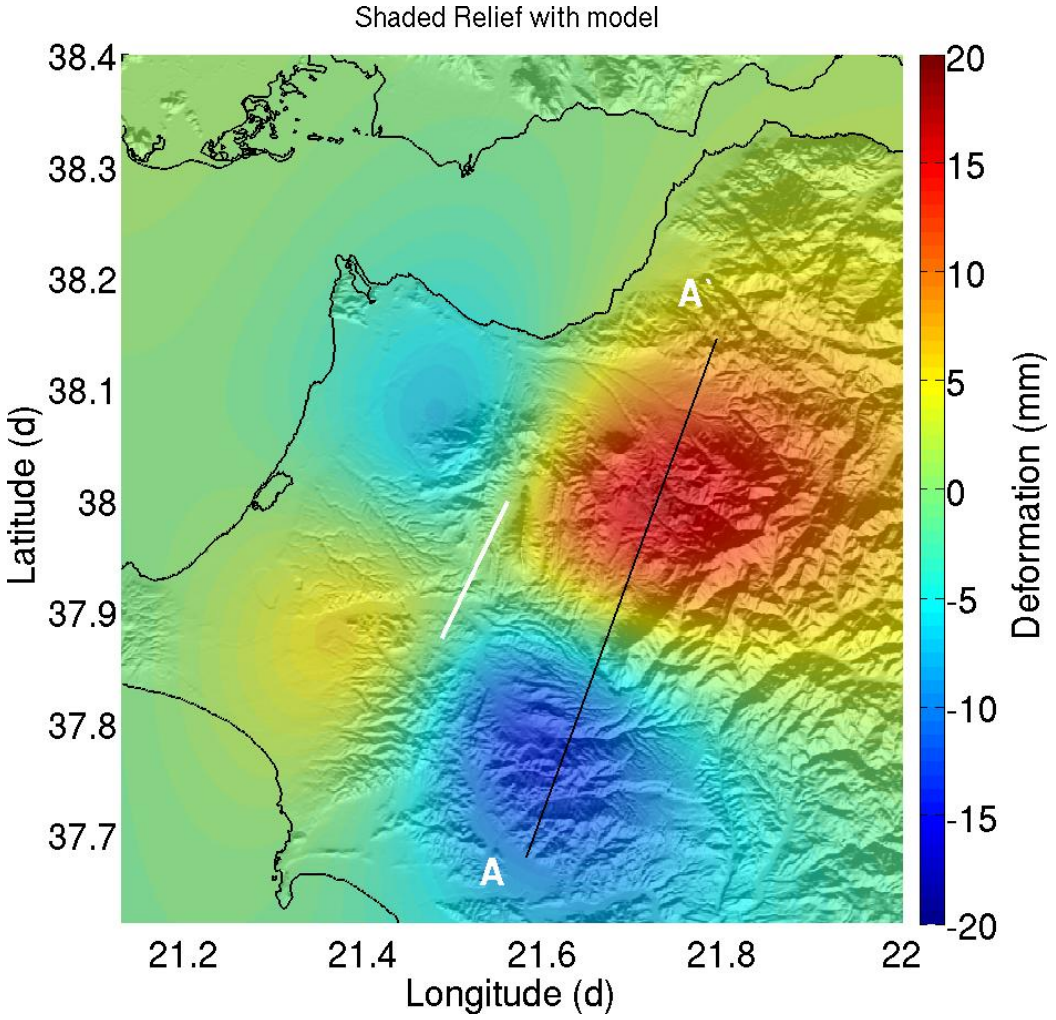

Figure 3-19. Modeled unwrapped interferogram for descending track of the proposed geometry and fault center location at C_1 superimposed over shaded relief of the study area. Positive values represent deformation in mm along the LOS away the satellite. The black line A-A' corresponds to the trace of the cross section discussed in the study. White line indicates the proposed fault.

3.1.4. Detection from multitemporal InSAR

In Figure 3-20 the deformation history of a PSI Persistent Scatterer of descending track 279 located at 38.2834°N, 21.7593°E, ~40km NE of the epicenter is plotted. We can clearly discriminate a discontinuity at the date of the event of about 10mm. This observation is a validation of the ability of the InSAR to detect this earthquake.

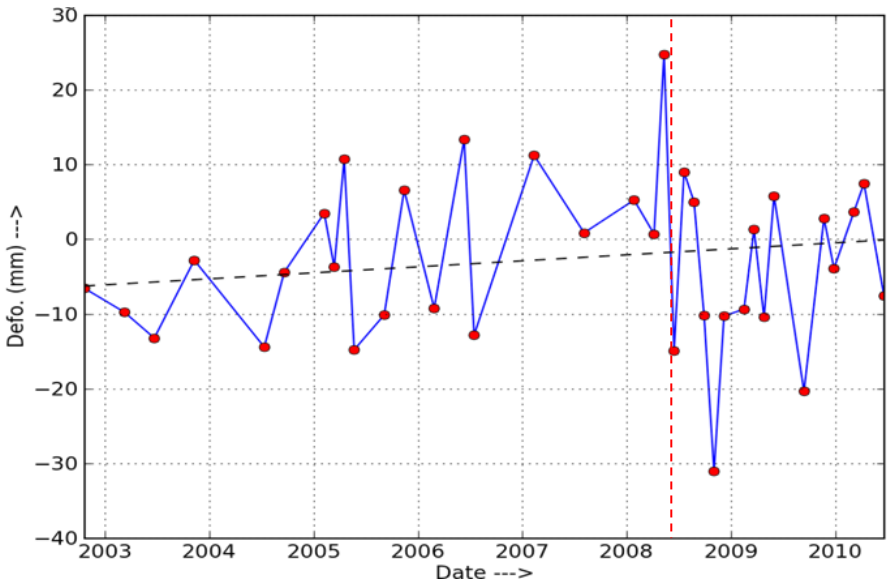

Figure 3-20. Deformation history of a PSI Persistent Scatterer of descending track 279 located at 38.2834°N, 21.7593°E, ~40km NE of the epicenter. With black dashed line the PS deformation rate is plotted. With red dashed line the date of the main seismic event is noted.

3.1.5. Conclusions

The model has to be constrained by the planar GPS measurements, the seismicity, the seismic moment and the DInSAR observations. We investigated the inversions of a set of models by setting and locking a range of lengths and depths leaving the width and the slip free. By limiting their volume according to their M_O we concluded in a group of 26 solutions from which 6 of them presenting the maximum likehood. The depth is ~17 km, the length ranging between [13 17] km, the width between [7.8 9.7] km and the slip between [1.18 1.22] m. By selecting the one that indicated by the seismic cluster location and the DInSAR study we proceeded to further investigation. Finally we have concluded to depth of 17.5 km, length of 15 km, width of 8.7 km and slip of 1.20 m as the moth likehood. We have realized two more investigations as the previous one by sliding the epicenter NNE along the seismic trace leading to their rejection because of high GPS measurements error and of the mismatching with the related seismicity cluster location. Finally we confirmed the coherence of the modeled deformation field with a set of ASAR/ENVISAT descending acquisitions, by following the stacking methodology of DInSAR descending acquisitions.

The Movri earthquake was detected by many remote GPS due to its depth, its Mw and its mechanism (strike-slip) but it has also detected by InSAR from a large distance. For this

reason the multitemporal geodetic observations investigating for the rate of continuous deformation have to be corrected for even distant earthquakes.

The Movri earthquake was hardly detected by InSAR but the depth was very well defined form it.

We have demonstrated that the fault covers only a small portion of the aftershocks.

This earthquake demonstrate the complementarity of InSAR and GPS observations.

3.2. Efpalio 2010

3.2.1. Introduction

On January 18, 2010 an earthquake of Mw=5.3 occurred near the town of Efpalio on the northern coast of the western Corinth Gulf. Almost immediately the seismic activity expanded ~5 km towards north-east where four days later another Mw=5.2 event occurred on January 22 (Figure 3-21).

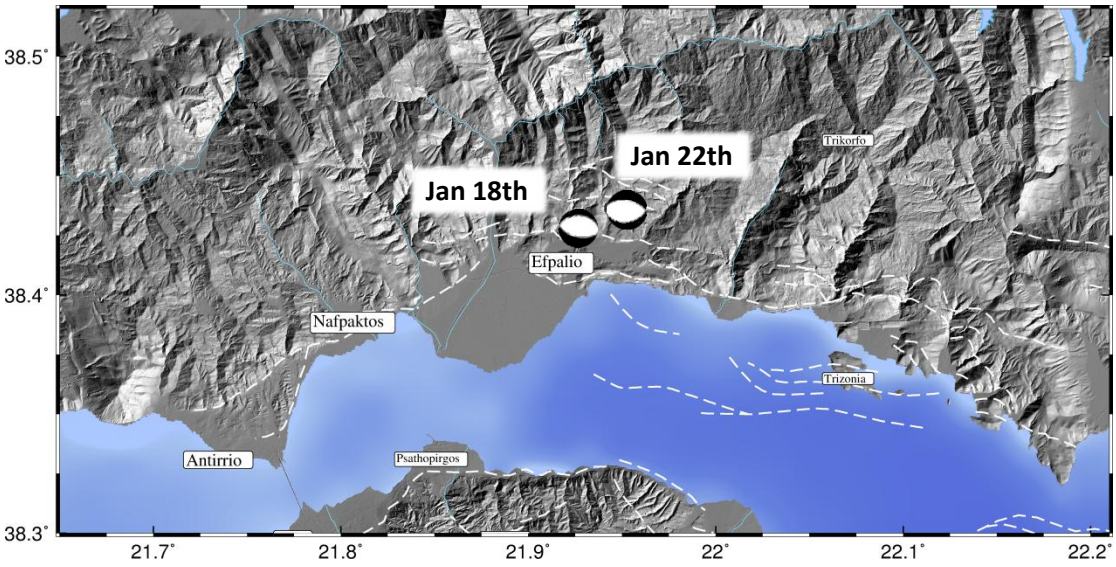

Figure 3-21. The epicenter and the two mechanisms along with the dates of the two events of the Efpalio earthquake.

[Sokos et al., 2012] discriminate the two events and propose a two fault solution of event 1) depth 4.5 km striking 102°, dipping 55° and 2) depth 6km, striking 282° and dipping 52°, based on seismological observations. In Figure 3-22 the aftershocks of the two events along with its mechanisms are plotted.

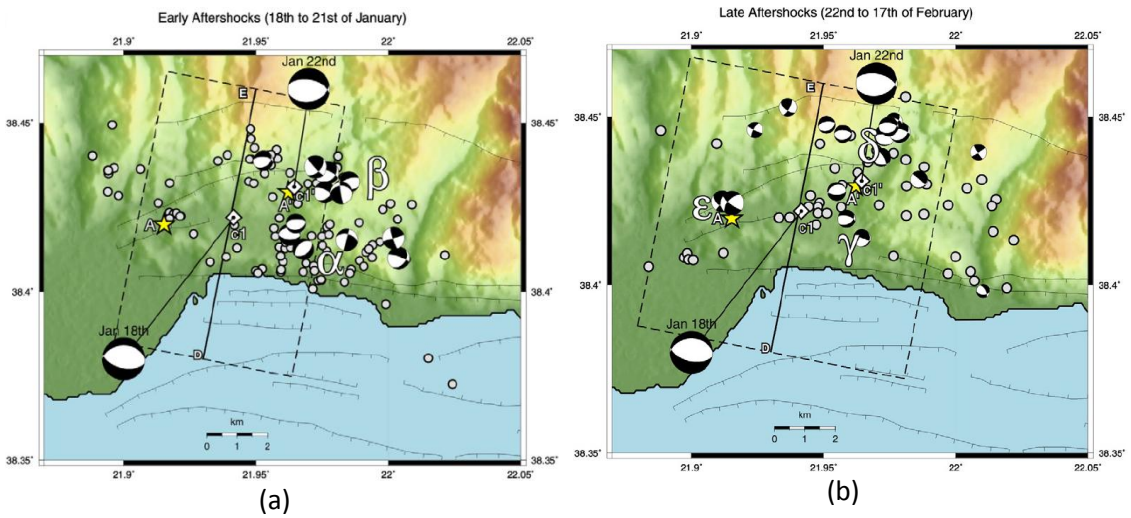

Figure 3-22. Courtesy of [Sokos et al., 2012]. Aftershocks and (selected) focal mechanisms a) of early aftershocks, denoted α and β (between the occurrence of the two events and b) of later aftershocks, denoted γ, δ and ε (after the occurrence of the second event and up to February 17).

3.2.2. Modeling

We have used the same hypothesis of a rectangular fault in homogeneous elastic half-space and the following methodology as described in §0 for the modeling of the Efpalio earthquake.

3.2.3. GPS data

One of the CRL permanent GPS station, EYPA, is located at 21.928E, 38.427N close to the epicenters area. Information, data and coordinate time series are available on the GPSCOPE web portal at https://gpscope.dt.insu.cnrs.fr/chantiers/corinthe. We post-processed the GPSCOPE solution as follows: (a) we estimated the absolute velocity of the station for the period 2001-2009 (11.2, 2.2 and -2.2 mm/yr in E,N and U components) and a sinusoidal annual oscillation (amplitude 0.7, 2.6 and -2.5 mm in E,N and U components with phase offset of -82.5 days). Figure 3-23 shows the residual coordinate time series after removing those trends. An offset is clearly visible in correspondence of the January 2010 seismic swarm.

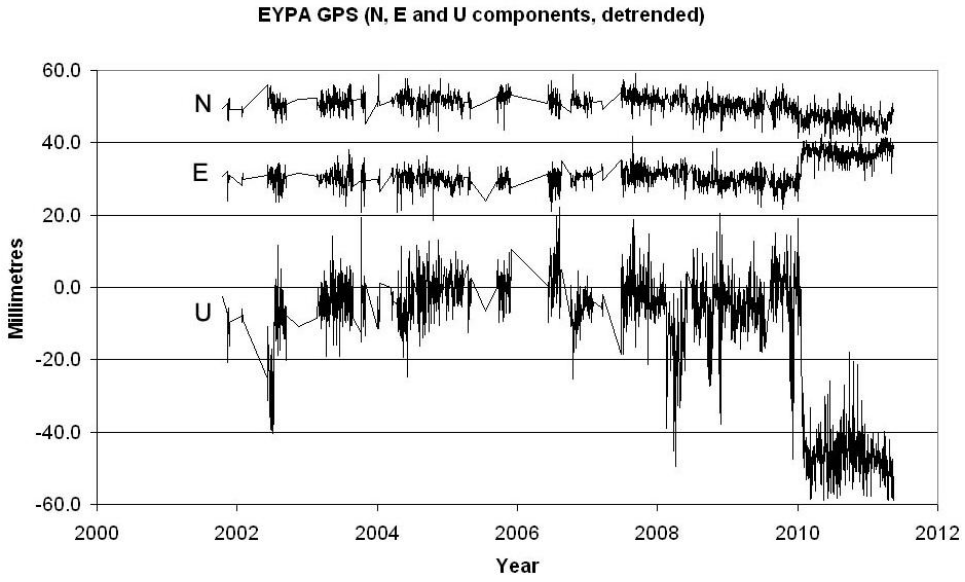

Figure 3-23. Coordinate change at EYPA GPS station after removing a long term geodynamic component and a term of annual oscillation. The co-seismic signal of the January 2010 sequence is clearly visible in the E and U components and a small negative offset is also present in the N component.

Averaging one year of data before the swarm (from January 1, 2009 to January 1, 2010) and one year of data after the swarm (February 1, 2010 to February 1, 2011) leads to offsets of 7.5±0.3, -3.3±0.3 and -41.7±1.2 mm in the E, N and U components. Although the post-swarm period is short compared to the pre-swarm, we see to evidence of change in the long term trend at the stations, thus no significant post-swarm deformation. Figure 3-24 shows a two months zooming into the time series. The E and N offsets cannot be quantified anymore nor precisely dated, while two ~2cm step appear relatively clearly in the U component on 18 and 22/01.

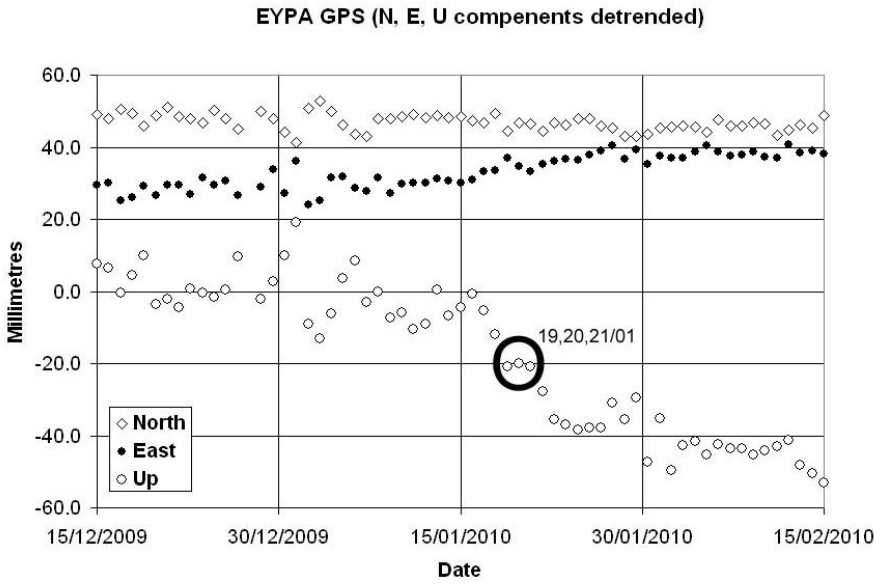

Figure 3-24. Two months of coordinates at the EYPA GPS stations. Over such a short period the daily GPSCOPE solutions is too noisy for E and N offset to appear clearly at the time of the 18/01 and 22/01 events. The offset is seen more clearly in the vertical component which signature of the two main events with almost similar amplitude of ~2cm for each

In order to better constrain the offset produced by each of the two main events we processed in differential mode the EYPA data together with the other CRL GPS stations. Daily solutions did not lead to better results that the GPSCOPE solution. Stacking the results of a static differential processing between EYPA and the other stations with only one hour of data before the event and one hour after (which is enough to fix the phase ambiguities provided the size of the network) lead to the following offsets: 1±4, 5±11, -38±9 mm for the 18/01 event and 9±2, 9±15 and -21±6 mm for the 22/01 event in E, N and U components. The uncertainties in N are too large to be compared with the long term offset. In the E component, this result suggests that the second event produced a larger displacement, while in the U component the first event has a larger signature of perhaps twice that of the second. Finally we analyzed the RINEX data files in order to detect the carrier phase offsets directly in the raw data. We were able to successfully detect the co-seismic offsets in the 30seconds sample rate raw data files (Figure 3-25 and Figure 3-26) and the signature of the first event appears to be somewhat larger than that of the second one, which again suggests a somewhat larger subsidence during the first event.

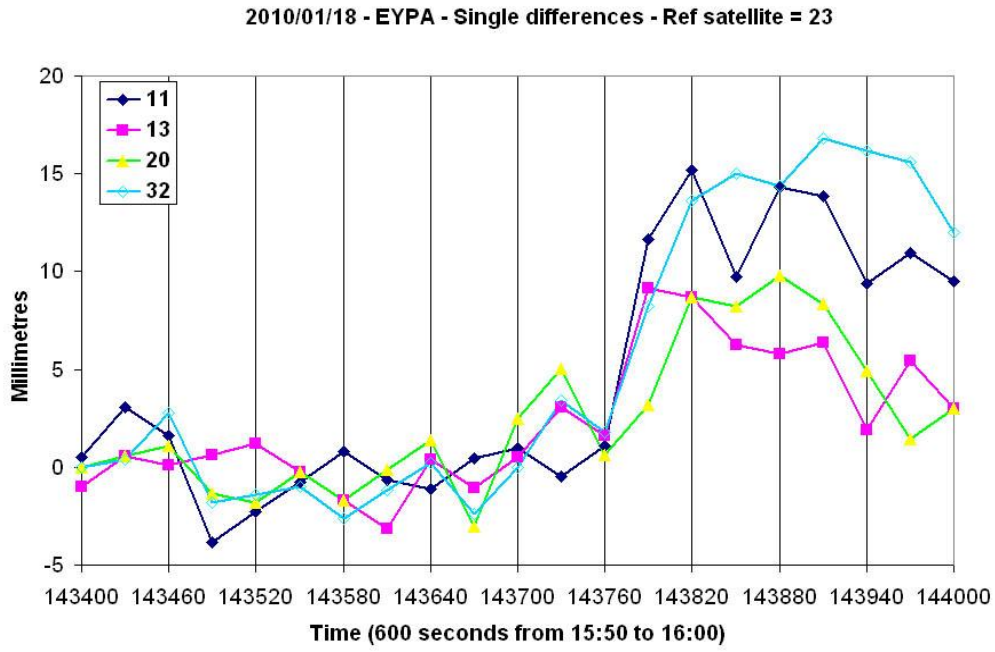

Figure 3-25. The co-seismic signal of the 18 January earthquake seen at EYPA in the raw differential GPS phases acquired at 30s rate.

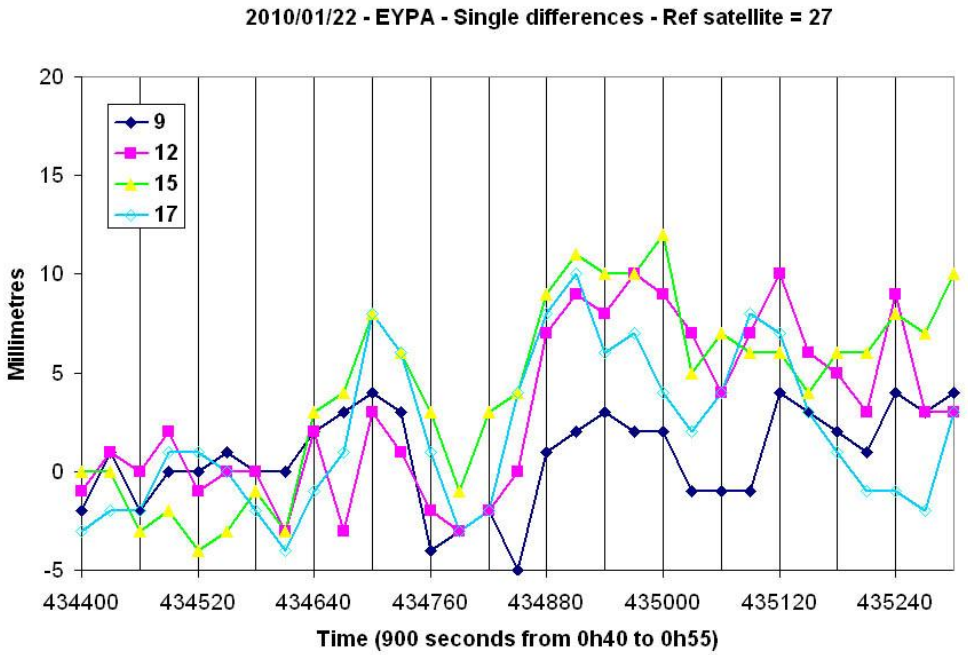

Figure 3-26. The co-seismic signal of the 22 January earthquake seen at EYPA in the raw differential GPS phases acquired at 30s rate.

Taking into account those various analysis of the GPS data our best a priori estimate for the co-seismic signal induced by both events is as follows: (a) 18/01 event 0, -2, -28 mm, (b) 22/01 event: 7, -1, -14 mm in E, N and U components.

3.2.4. DInSAR data

Following the methodology of interferogram stacking (e.g. averaging each pixel of all single interferograms spanning the date of the earthquake), we proceeded to the production of a clear deformation pattern. Accordingly forty co-seismic ASAR/ENVISAT, acquired from 2008-2011, descending interferograms of Track 279, have been created by a multilooking of 4x16, with ROI-PAC software [Rosen et al. 2004]. Its topography effect has been eliminated by using a 20m grid DEM derived from SPOT differential imagery cell size of 0.0002°N x 0.0002°E. Eight differential interferograms has been selected by visual inspection presenting relatively good coherence. In Figure 3-27 the dates versus the baselines has been plotted.

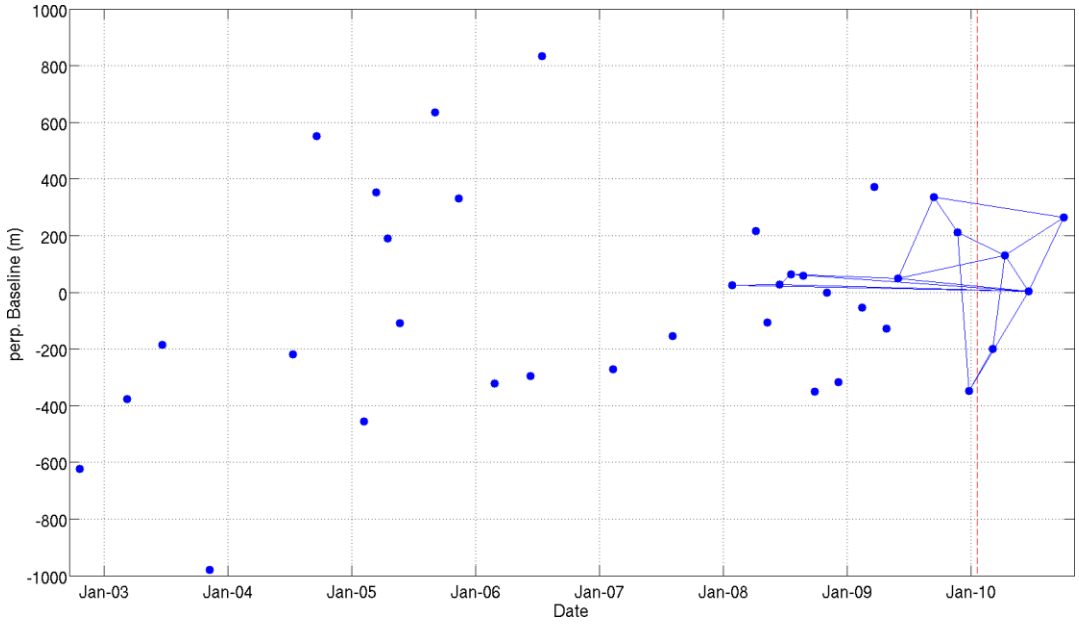

Figure 3-27. Plot of the dates of the participating ASAR/ENVISAT acquisitions versus the baselines of the co-seismic interferograms used in the study. With red dashed line the date of the earthquake is indicated.

The selected differential interferograms have been unwrapped by SNAPHU software [Chen et Zebker 2002]. Following the same procedure as for Movri earthquake (section) we produced eight single unwrapped corrected for N-S and E-W linear trends differential interferograms (Figure 3-28) and mean stacked interferogram to minimize any high-to-medium frequency common mode noise signal (Figure 3-29). We haven't corrected for unwrapping phase cycle slip errors as we have done in the case of Athens earthquake of 1999 [Elias et al. 2006].

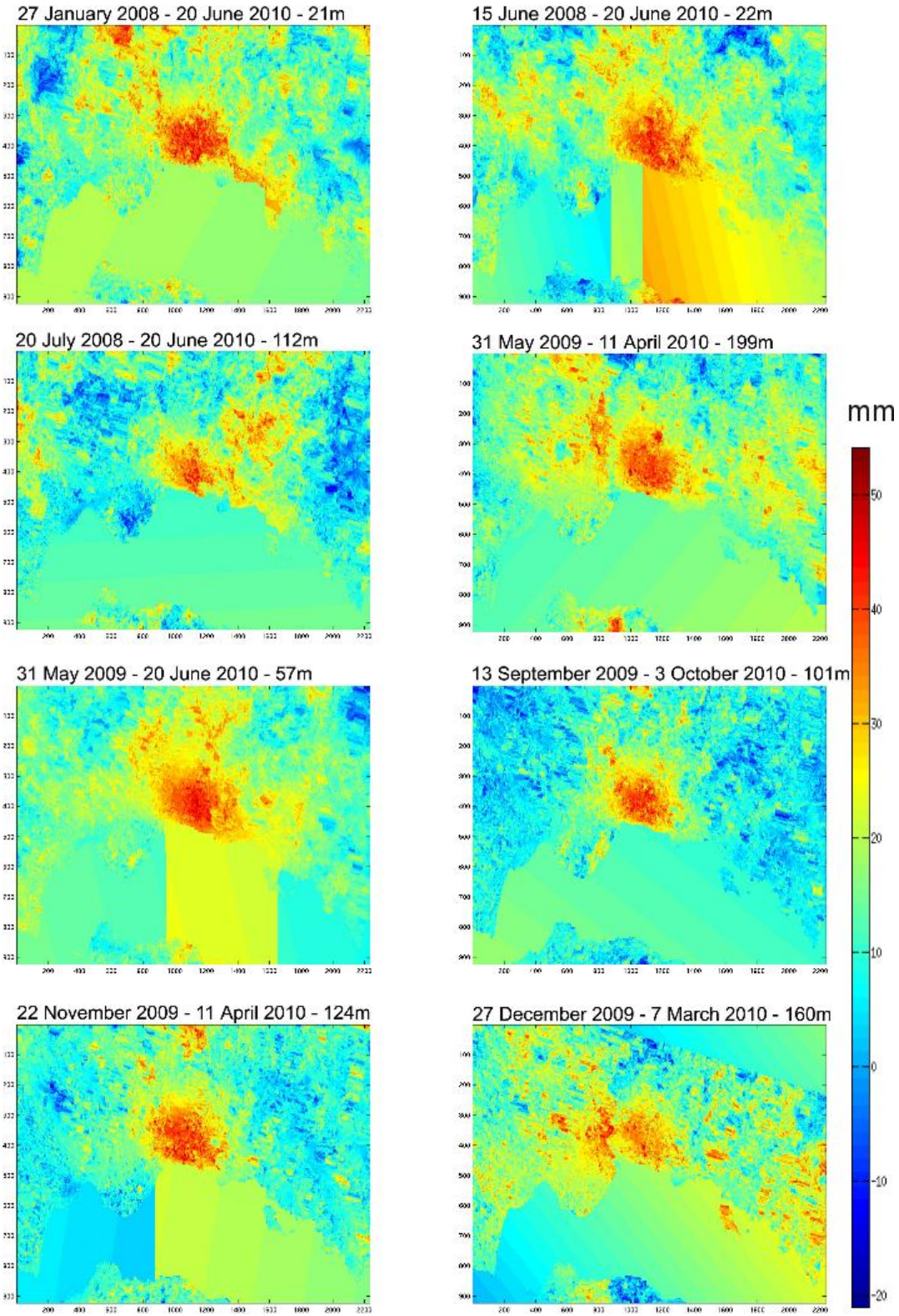

Figure 3-28. The eight unwrapped, corrected for N-S and E-W and converted to mm single differential co-seismic interferograms. The presence of deformation in the sea demonstrates the zero coherence induced in the unwrapping procedure, for the sea cover.

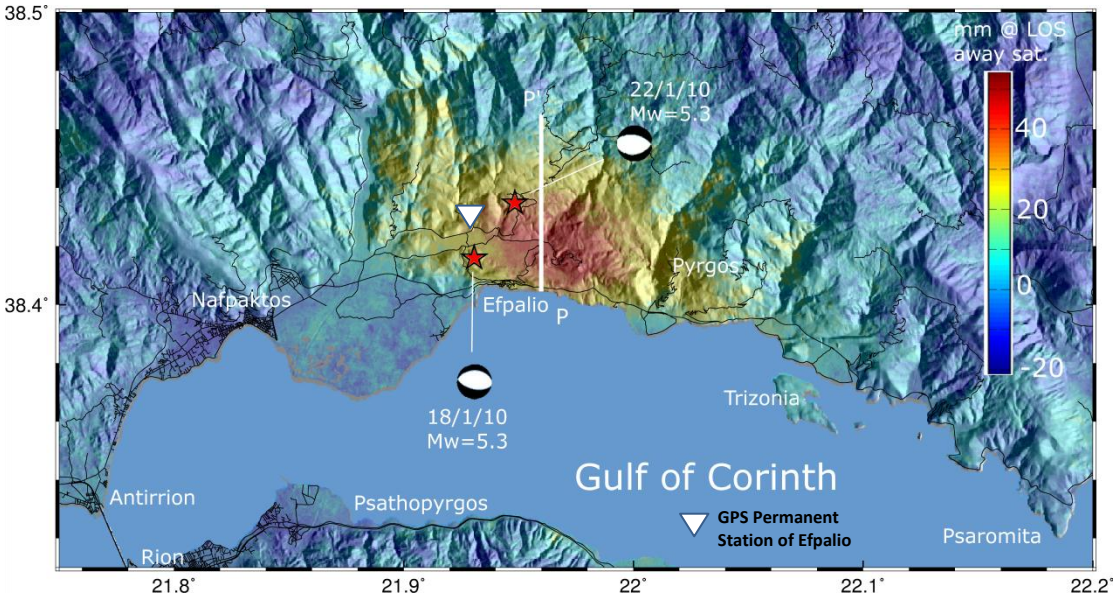

Figure 3-29.The mean stack interferogram (at LOS with positive values away the satellite) that have been used in the modeling. Line P-P' represents the cross section trace. The permanent GPS location EYPA is marked with reverse white triangle.

For the modeling we filtered (by an average filter of size 700m x 700m) and a number of 428 points (one sample kept on a grid of 620 m east x 0.77 m north) selected in the main deformed area (Figure 3-30).

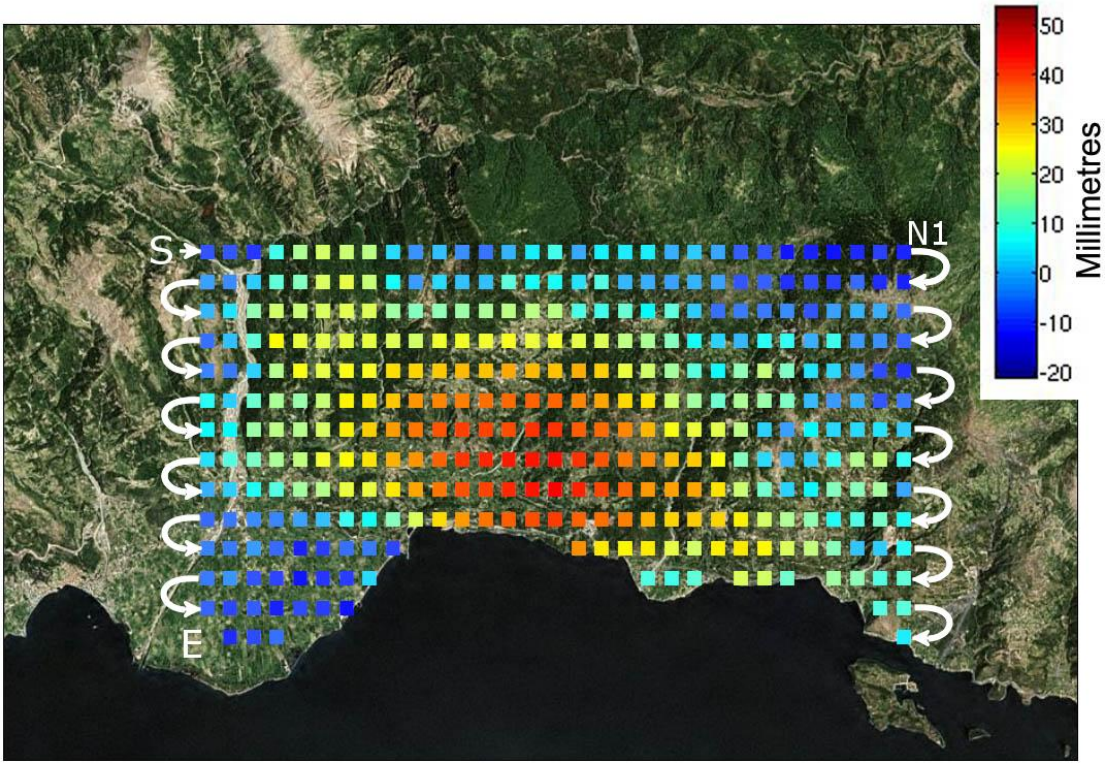

Figure 3-30. LOS deformation (positive values away the satellite) of the 428 selected samples of the filtered mean stack interferogram that have been used to the modeling. White arrows and text indicate the path to sampling for the creation of the diagram of Figure 3-34.

In order to have an estimation of the noise component we have selected 8 interferograms not spanning the earthquake with similar temporal and spatial baselines as the eight co-seismic. In Figure 3-31 the dates versus the perpendicular baselines of the eight interferogram not containing the earthquake are presented.

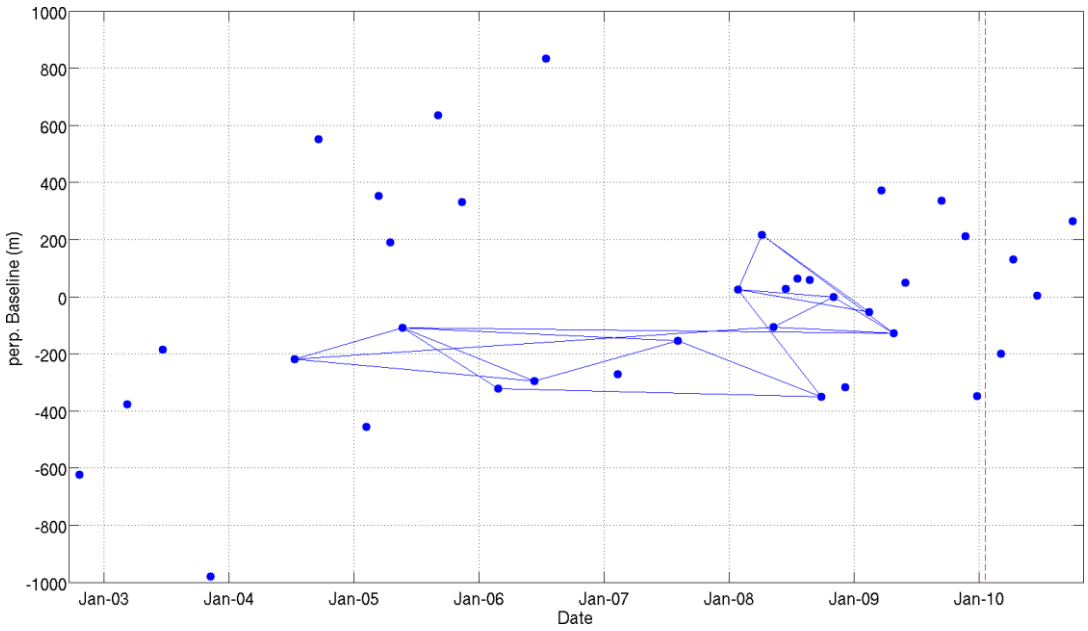

Figure 3-31. Plot of the dates of the participating ASAR/ENVISAT acquisitions versus the baselines of the interferograms not containing the deformation due to the earthquake and have been used to estimate the level of noise. With red dashed line the date of the earthquake is indicated.

From the corresponding aseismic filtered mean stack interferogram (Figure 3-32) and the coseismic (Figure 3-29) one we can conclude that the S/N ratio is satisfactory high in the main deformed area.

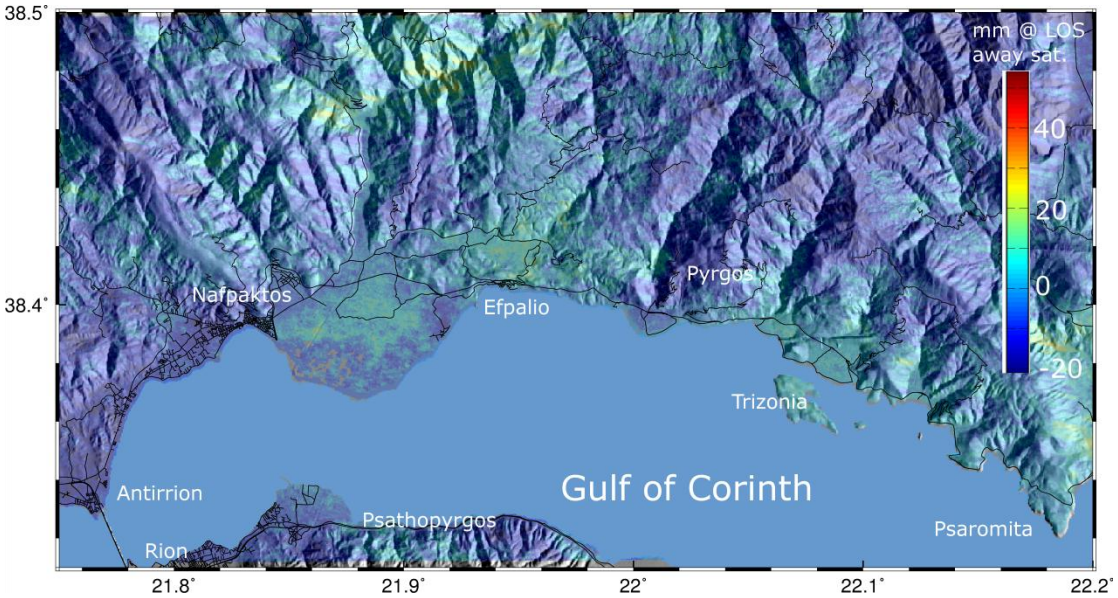

Figure 3-32. The filtered mean stack interferogram that have been produced to estimate the level of noise component.

Summarizing we kept the eight more coherent interferograms (Figure 3-28). Each of the eight interferograms was then tilted and shifted so as to set to zero the value of the pixels out of the box comprised between long 21.74°-22.20° and lat 38.31°-38.5° (only the coherent pixels at land were used for this operation). Figure 3-29 shows the averaged stack of the eight tilted and shifted interferograms. This average stack vas then low pass filtered using a 33 x 33 window and one sample kept on a grid of 0.62 (east) x 0.77 (north) km as shown in Figure 3-30. Further data inversion is performed using those 428 data.

3.2.5. Consistency between GPS, DInSAR and seismicity

The closest pixel to EYPA GPS station is at 580.92E – 4253.77N with LOS change -28mm. while the LOS change at EYPA deduced from the GPS displacement is -35.5mm, there is therefore a 7.5mm difference between the two estimates of LOS change at EYPA. As the sample period for both estimates is the same (two years window) and given the procedure used to tilt and shift the interferograms and the stack of eight of them, we do not expect the 428 LOS data to have an offset (and this is confirmed by the results of the modeling, seen below), therefore the cause of the difference most probably comes from the GPS, perhaps because of a small local amplification of the displacement at EYPA which is located on the slope of a hill facing south. In the following models we used the LOS values deduced from the DInSAR analysis. We made some trials with increasing the LOS values by 3mm and we found no major changes in the modeled faults and a 5% increase of the modeled geodetic seismic moment.

Figure 8 shows a good fit between the localization of the aftershocks and the localization of the deformed area.

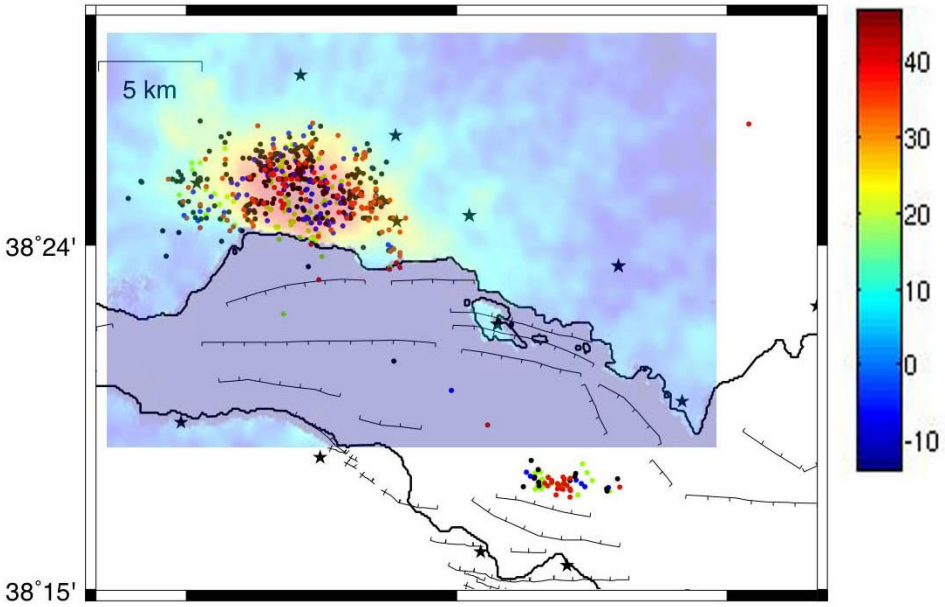

Figure 3-33. Comparison of the location of the interferogram and the aftershocks

3.2.6. Single fault model

The shape of the interferogram is smooth and as the two earthquakes are not extremely shallow (according to the centroid depths inferred from the seismic data analysis) we started with a single fault model. Table 11 shows the parameters of the four models tested, two of them with azimuth and dip angle fixed and two with those angles free. Figure 3-34 and Figure 3-35 show the fit between the LOS changes and the observations. Table 11 also contains the prediction of displacement at EYPA for the four models. The "geodetic" seismic moment appears to be stable in all models, with a value of 2.3±0.1 10^{16} Nm, which is not surprising as this number is primarily a function of the global surface displacement and not very sensitive to the fault parameters. Figure 3-34 plots the 428 DINSAR the modeled deformation values sampled form the point *'S'* (Figure 3-30) and continue to the end of the first row at node *'N1'* and carry on as the white arrows indicates to the second row and so on until point *'E'*.

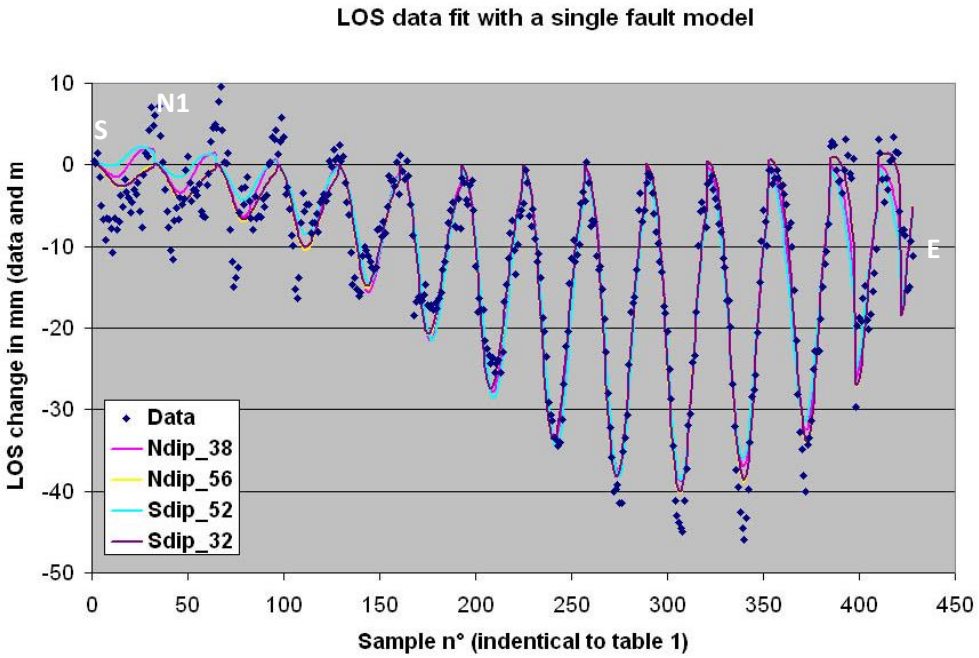

Figure 3-34. Fit of the DInSAR LOS (positive values away the satellite) with the four models presented in Table 11. Fault parameters deduced from the inversion for a single fault plane. The two first models are for a north dipping fault, one with the azimuth and dip angle kept close to the preferred values from seismology, the other leaving free those angle. When the dip angle is left free it has the tendency to increase and the fault width and slip to decrease. The two next models are for a south dipping fault, again one with angle fixed and the other with free angles. Here the dip angle tends to decrease when left free. The with text corresponds to the samples ordering of Figure 3-30.

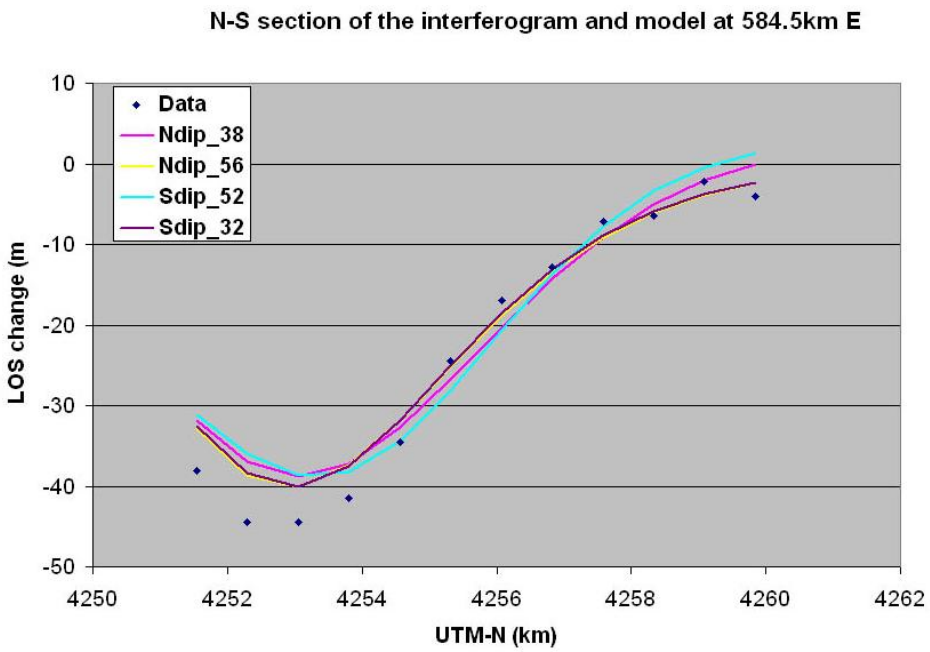

Figure 3-35. Fit of the DInSAR data along the cross section P-P' of Figure 3-29.

	Model 1 Ndip_38	Model 2 Ndip_56	Model 3 Sdip_52	Model 4 Sdip_32
Centre of upper fault edge (UTM-E, km)	583.33	583.16	583.83	583.56
Centre of upper fault edge (UTM-N, km)	4252.38	4252.11	4254.55	4253.29
Fault azimuth (°)	-75 (fixed)	-72	100 (fixed)	108
Depth of upper fault edge (km)	4.1	4.3	5.2	4.5
Half length of the fault (km)	4.4	4.7	3.9	4.7
Fault width (km)	5	2.3	2.5	2.3
Dip angle (°)	38 (fixed)	56	52 (fixed)	32
Normal slip (mm)	182	338	418	341
"DInSAR" Mo (x 10^{16})	2.4	2.19	2.45	2.21
"DInSAR" centroid depth (km)	5.6	5.3	6.2	5.1
Predicted motion at EYPA-GPS (E, mm)	9.7	6.9	10	6.7
Predicted motion at EYPA-GPS (N, mm)	3.1	-3.7	2.3	-5.2
Predicted motion at EYPA-GPS (U, mm)	-35	-36	-34	-36.6

Table 11. Fault parameters deduced from the inversion for a single fault plane. The two first models are for a north dipping fault, one with the azimuth and dip angle kept close to the preferred values from seismology, the other leaving free those angle. When the dip angle is left free it has the tendency to increase and the fault width and slip to decrease. The two next models are for a south dipping fault, again one with angle fixed and the other with free angles. Here the dip angle tends to decrease when left free.

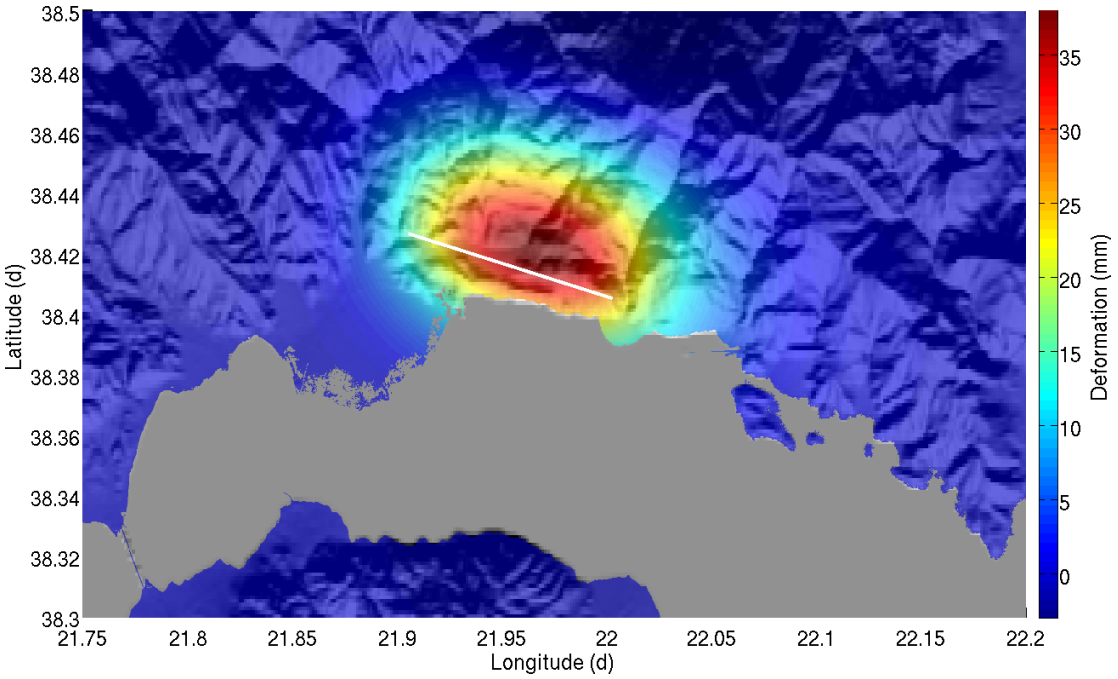

Figure 3-36. The synthetic modeled interferogram of the Model 1 Ndip_38. With white line the fault trace in shown.

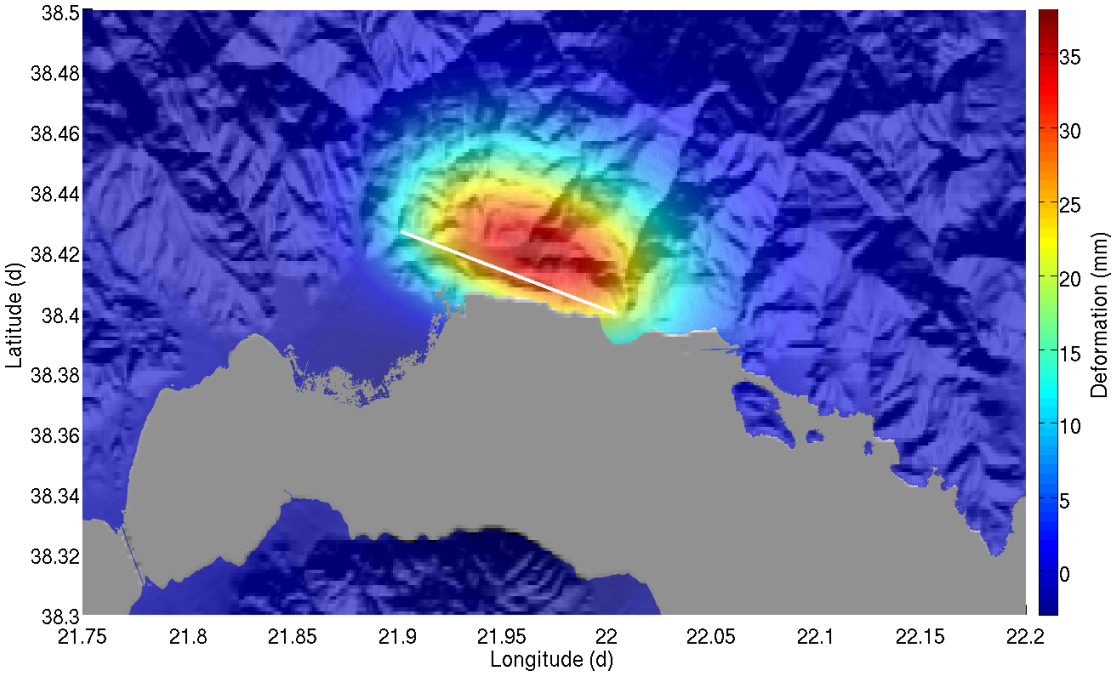

Figure 3-37. The synthetic modeled interferogram of the Model 2 Ndip_56. With white line the fault trace in shown.

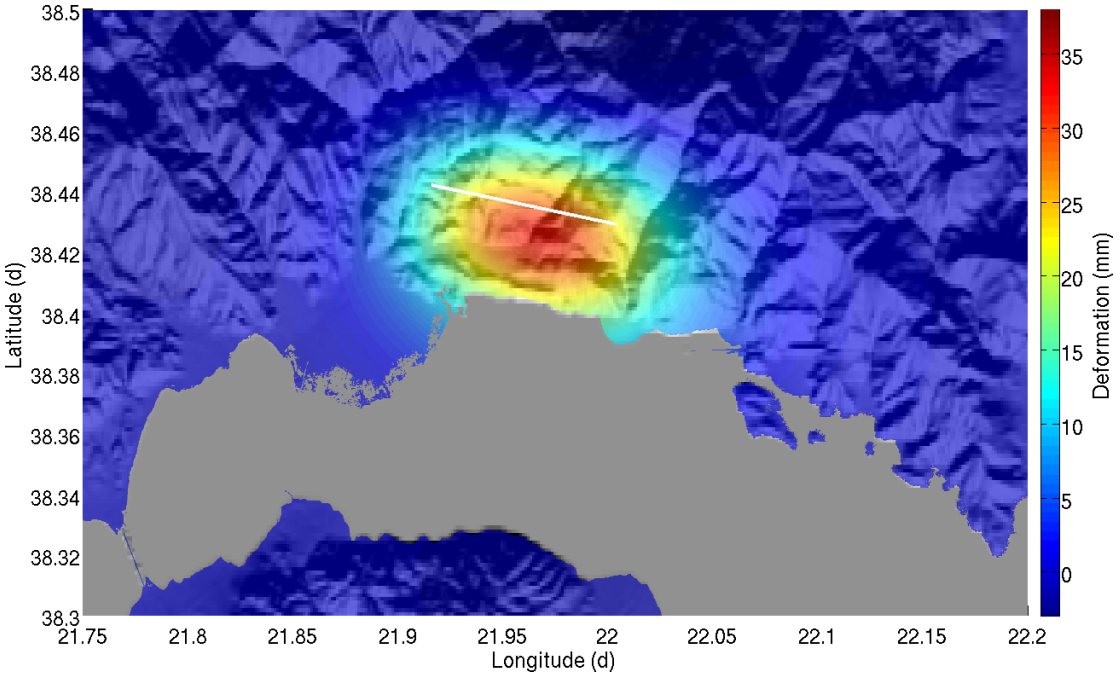

Figure 3-38. The synthetic modeled interferogram of the Model 3 Ndip_52. With white line the fault trace in shown.

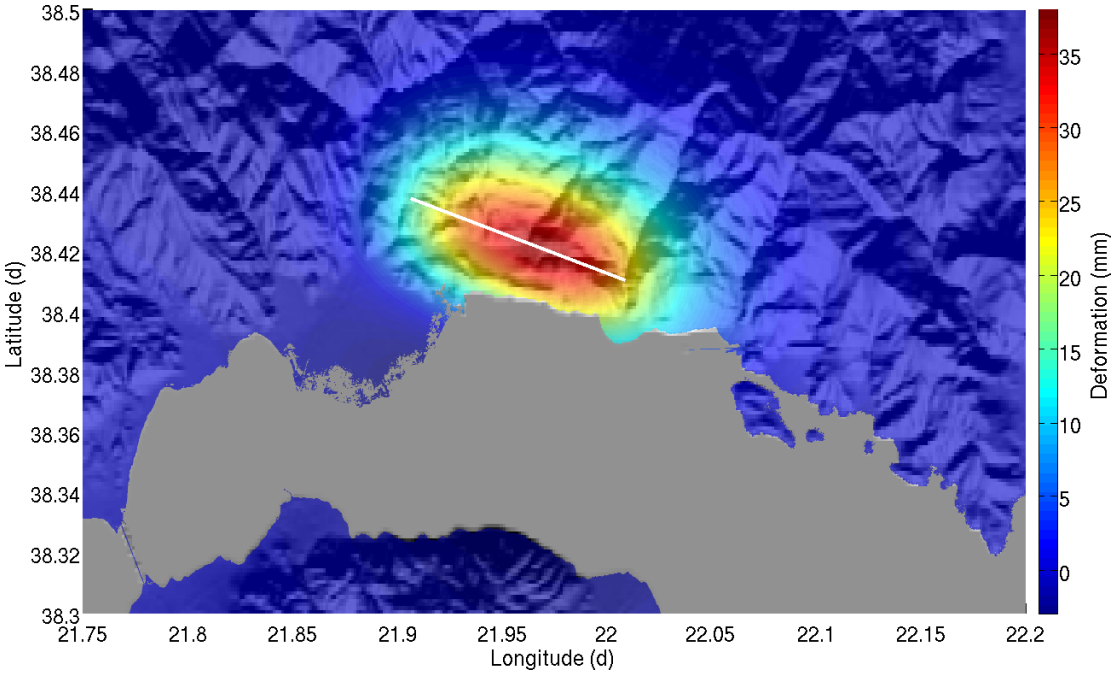

Figure 3-39. The synthetic modeled interferogram of the Model 4 Sdip_32. With white line the fault trace in shown.

In Figure 3-40 the InSAR measurements and the models of SDip 52 and [Sokos et al., 2012] are plotted. The SDip 52 model is approximating better the measurements as a mean values but it is following the model less than [Sokos et al., 2012]. The fact that we have considered a single fault doesn't permit the higher order fitting.

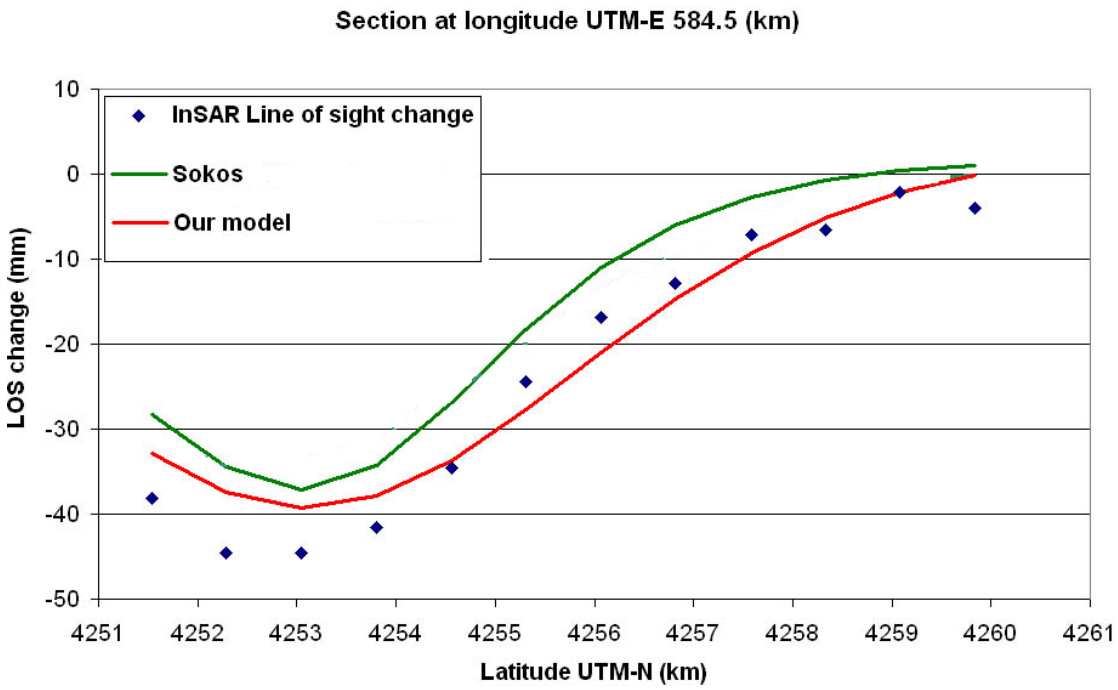

Figure 3-40. Cross section along the P-P' line of Figure 3-29. Blue diamonds represents the InSAR LOS measurements. With red line the Sdip 52 model is plotted and with green line the model using the [Sokos et al., 2012] two faults dipping North and South.

3.2.7. Detection from multitemporal InSAR

In §3.2 we have presented and modeled the Efpalio earthquakes of 2010. The dates of the earthquake are included in the date range of the two main descending and ascending tracks that have been use in the current study. The subsidence rate we have measured in the villages most deformed from the earthquakes (Figure 3-29 and Figure 5-30), e.g. Efpalio and Monastiraki with the PSI/SBAS are high. Thus we have investigated the effect of these earthquakes in the PSI/SBAS products. By first approximation we can discriminate the pattern of the earthquake Figure 3-29 in Figure 5-30. In Figure 3-41 the effect of the Efpalio earthquake is obvious. It has contaminated all the time series after the event.

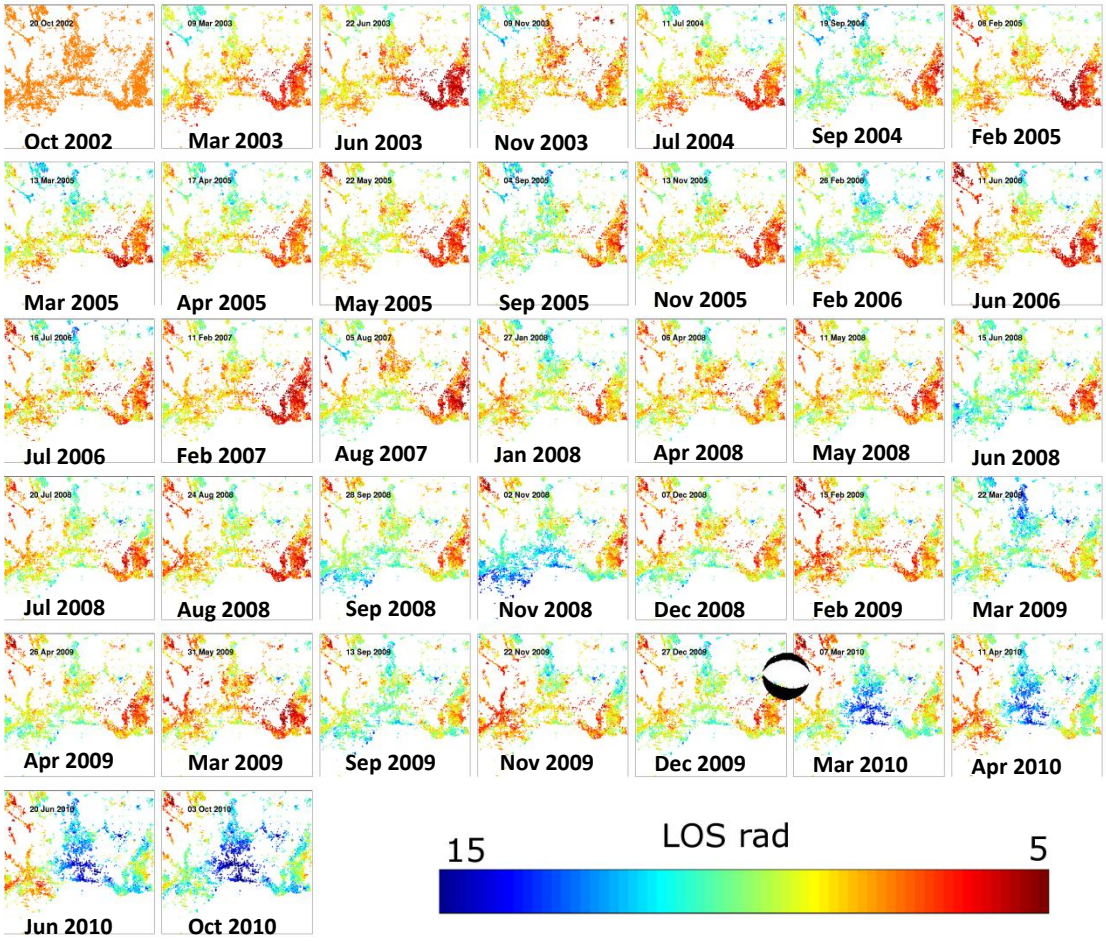

Figure 3-41. Temporal evolution of the area of Efpalio 2010 Earthquakes. The values are in radians in the descending LOS referenced to the first image. Positive values are towards satellite. The date of the earthquakes marked with one (of the two) focal mechanisms.

In Figure 3-42 we can see some temporal evolution of SBAS PS in the LOS of descend track 279, which located to the subsidence field of the Efpalio earthquakes. The subsidence after 2010 and how it is affected the rate is obvious.

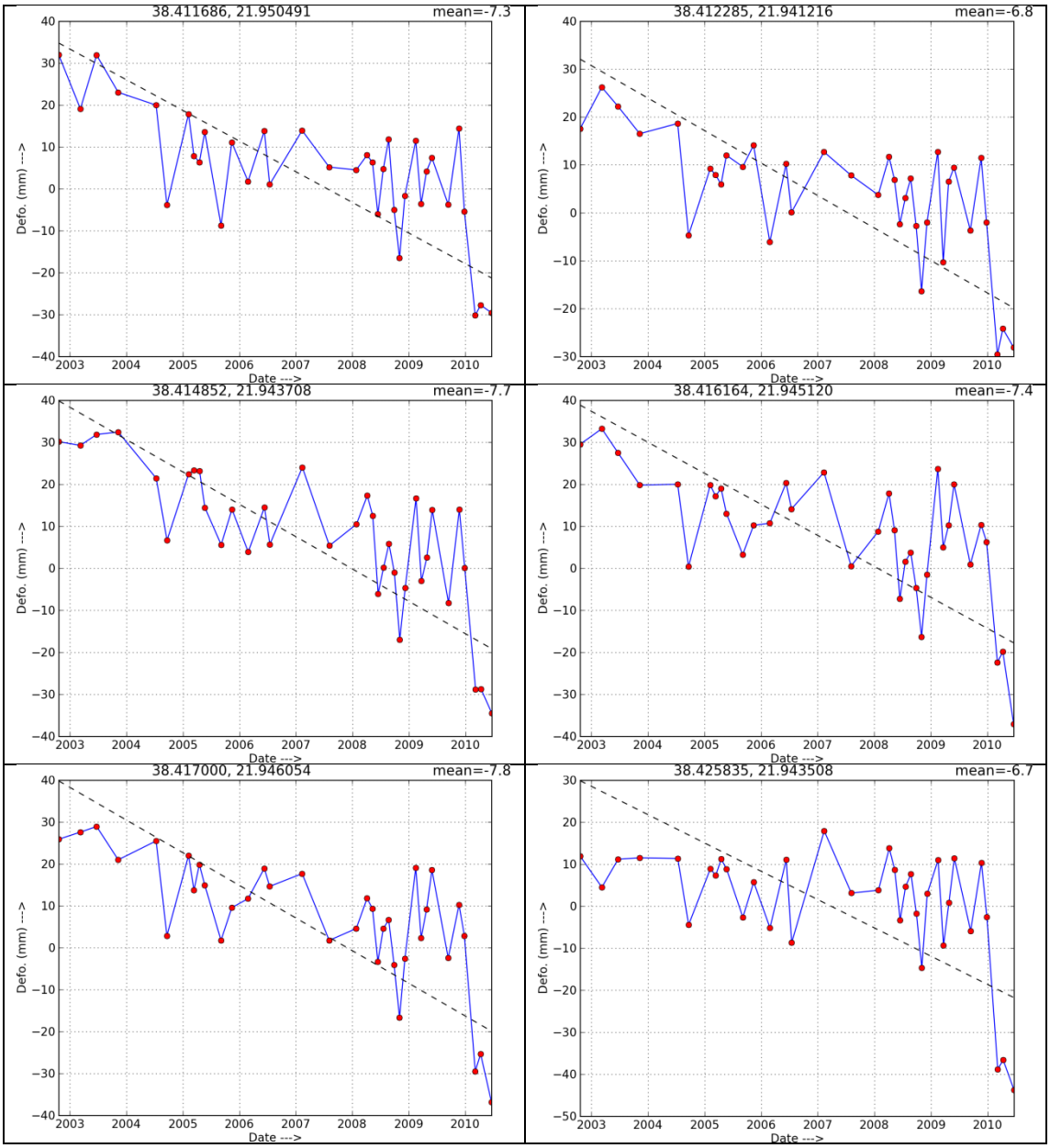

Figure 3-42. Selected SBAS PS of the descending track 279 which affected heavily from the Efpalio 2010 earthquake. Positive values represents descending LOS deformation towards the satellite.

Concluding we declare that the deformation rates that we have measured in Efpalio and Monastiraki (§5.2 and §5.6) are contaminated by the Efpalio earthquakes of 2010 and cannot be considered valid.

3.2.8. Conclusions

The earthquake ground deformation field was easily detected easily, with a clear deformation pattern by InSAR. On the contrary it was detected only by one close permanent GPS station. The InSAR alone could not constrain the fault parameters very well (in contrary of e.g. Athens 1999 earthquake) because of the mixed double shock event, since there was not an acquisition between the two events. In a single fault case we have concluded to depth of ~4.5 km, length of 8.5±1 km, width of ~2.5 km (~5 km being more compatible with initial seismological findings) and a slip of ~25 cm.

In order to constrain the earthquake better and examine the two fault case (separating the deformation of the two events) the contribution of seismology is needed.

3.3. Discussion

The two earthquakes investigated herein, demonstrate the variety of geophysical events occurring in the extended area of the Gulf of Corinth and thus the need of multidiciplinarity of the observations in different spatial and temporal scales. Specifically the complementarity of InSAR and GPS observations are crucial for constrain the fault parameters. These observations are very promising and valuable, especially with the arrival of new SAR satellites with higher spatial resolution, smaller revisit time and generally improved reception characteristics.

In case of time series of deformation where we are interested in estimating the rate we should pay attention to the 'contamination' of even distant earthquakes. We have demonstrated that even these earthquakes have been detected from remote locations from InSAR and GPS even from a distance of ~780km.

Concluding, it is interesting to compare the two earthquakes in terms of their characteristics and their detection, summarizing in Table 12.

Efpalio	Movri
Normal mechanism	Strike slip mechanism
Lower Mw=5.2, 5.3	Higher Mw=6.4
Shallow	Deeper
Clear deformation pattern from InSAR	Hardly detected by InSAR (only with stacking)
One permanent GPS point (horizontal & vertical components)	Many GPS points (horizontal component)
Detectable deformation at near field	Detectable deformation at far field from permanent GPS and multitemporal InSAR
Fault parameters constrained from InSAR	Fault parameters constrained (mainly) from GPS

Table 12. Summarizing of the two investigated earthquakes

4. Main Observed Discontinuities

From the corrected PSI/SBAS maps herein we will investigate the city of Patras and Rio-Patra discontinuities (Figure 4-2).

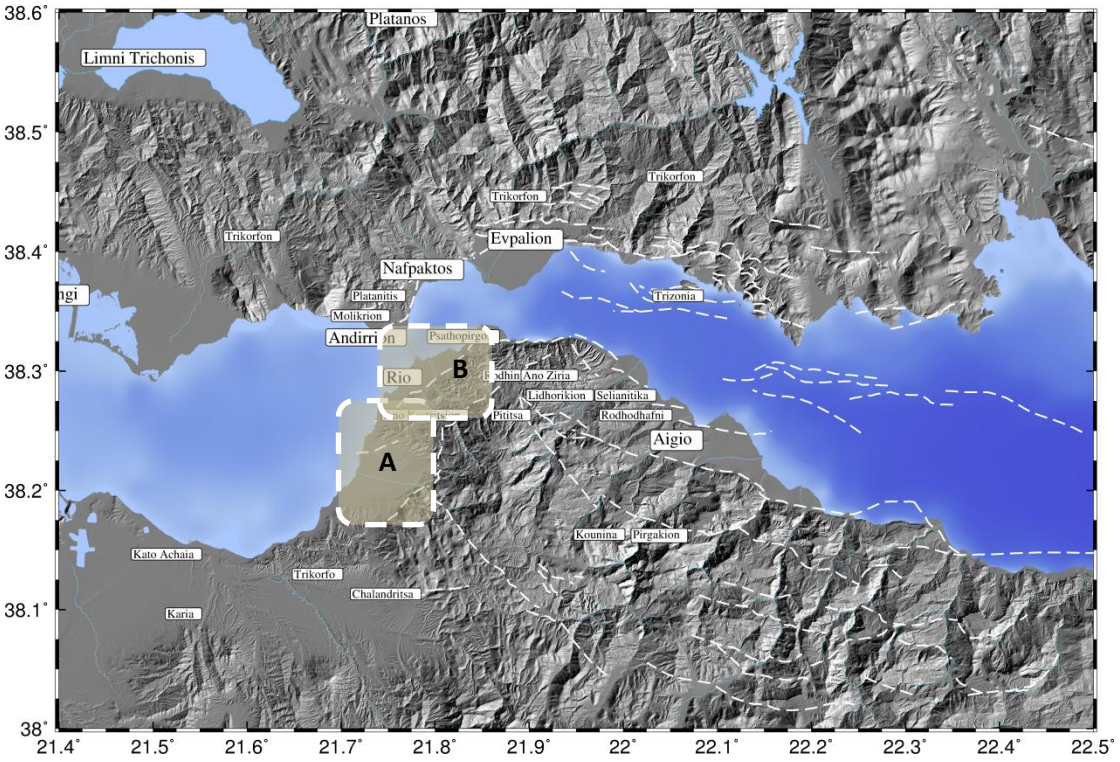

Figure 4-1. The study areas of Patras (A) and Rio-Patra (B).

4.1. City of Patras

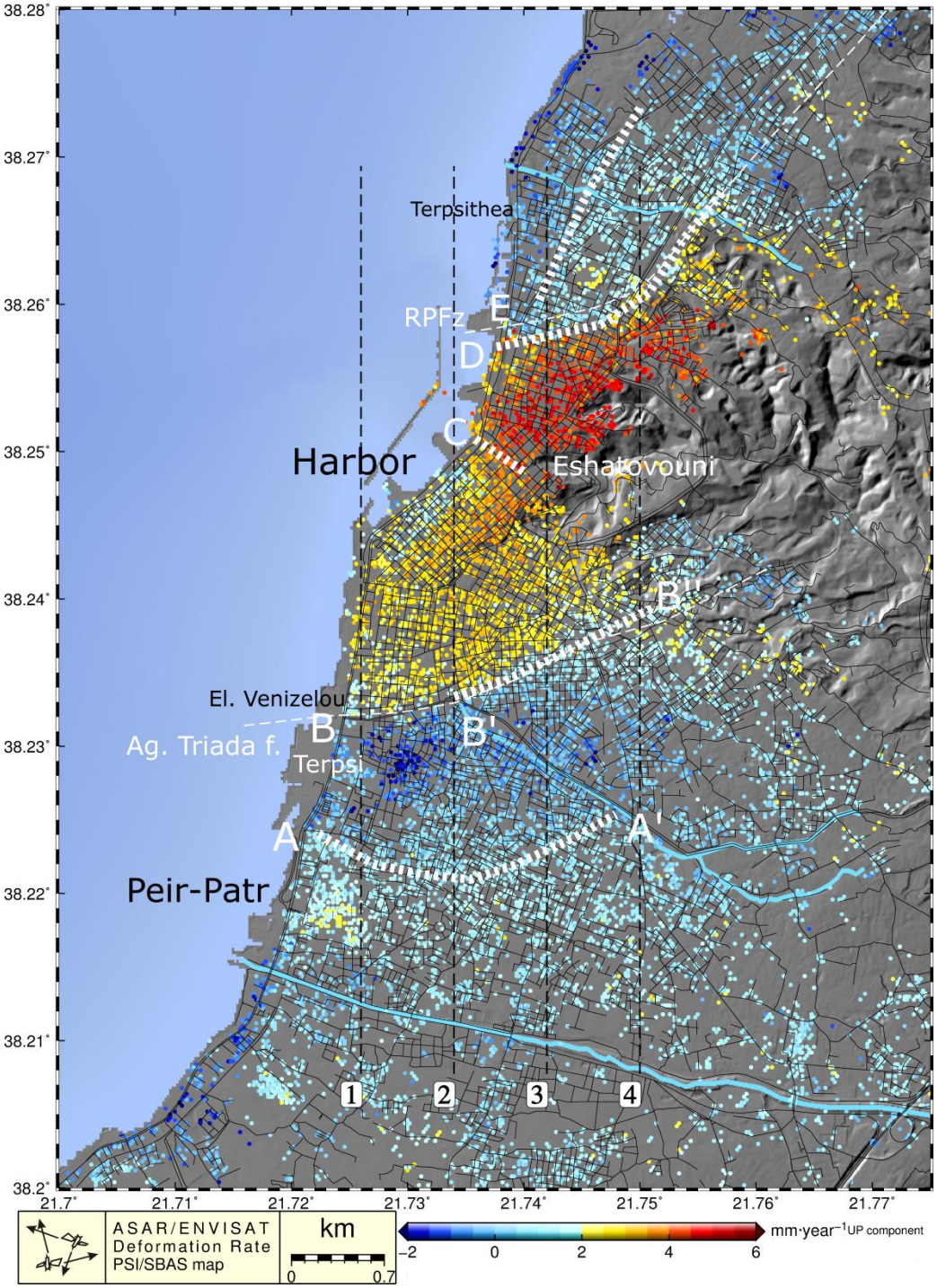

Figure 4-2. PSI/SBAS map of the UDc rate of the city of Patras. The black dotted lines correspond to the cross sections of Figure 4-3, Figure 4-4, Figure 4-5, Figure 4-6. In the map we can discriminate the main discontinuities of A-A', in Terspi, along El. Venizelou street at B until B' and after to B", at C, D, E to Ekso Agia until F and North or Peiraiki-Patraiki. In thin white dotted line represents the fault traces of Ag. Triada and RPFz (Rion-Patras fault zone).

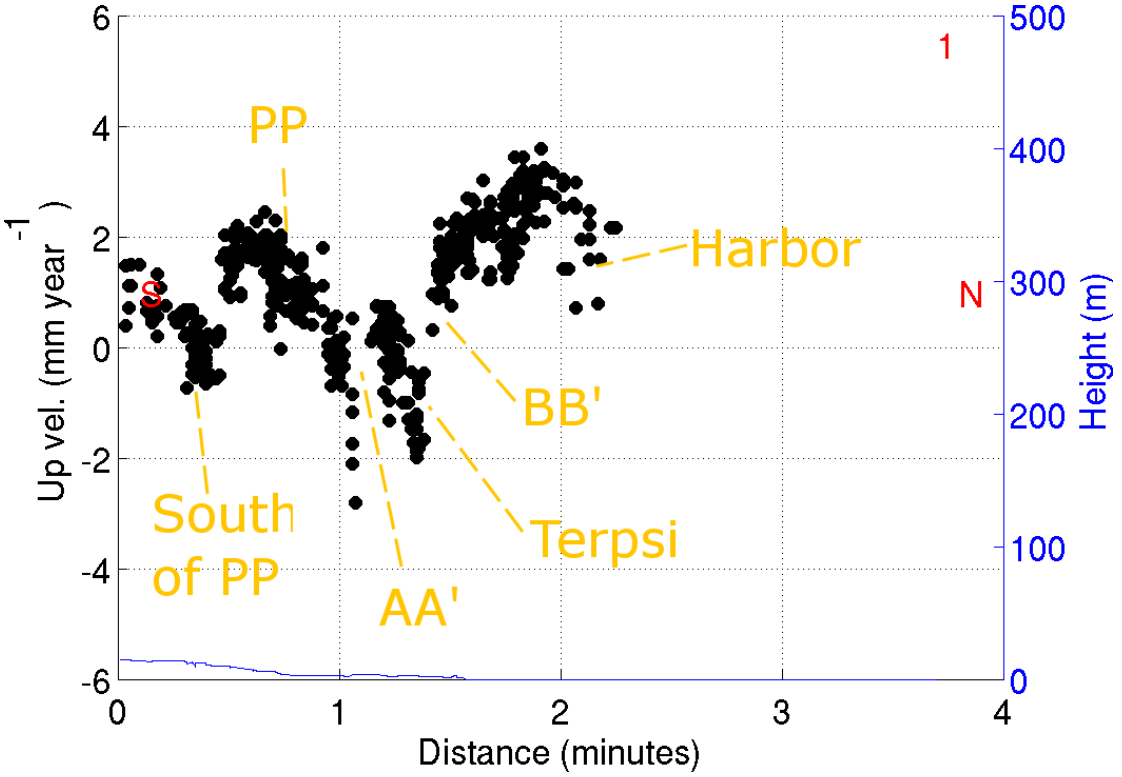

Figure 4-3. Cross section no. 1 (Figure 4-2) of the UDc of the city of Patras. In orange letters the features that we have discriminated are marked. *PP* stands for Peiraiki-Patraiki.

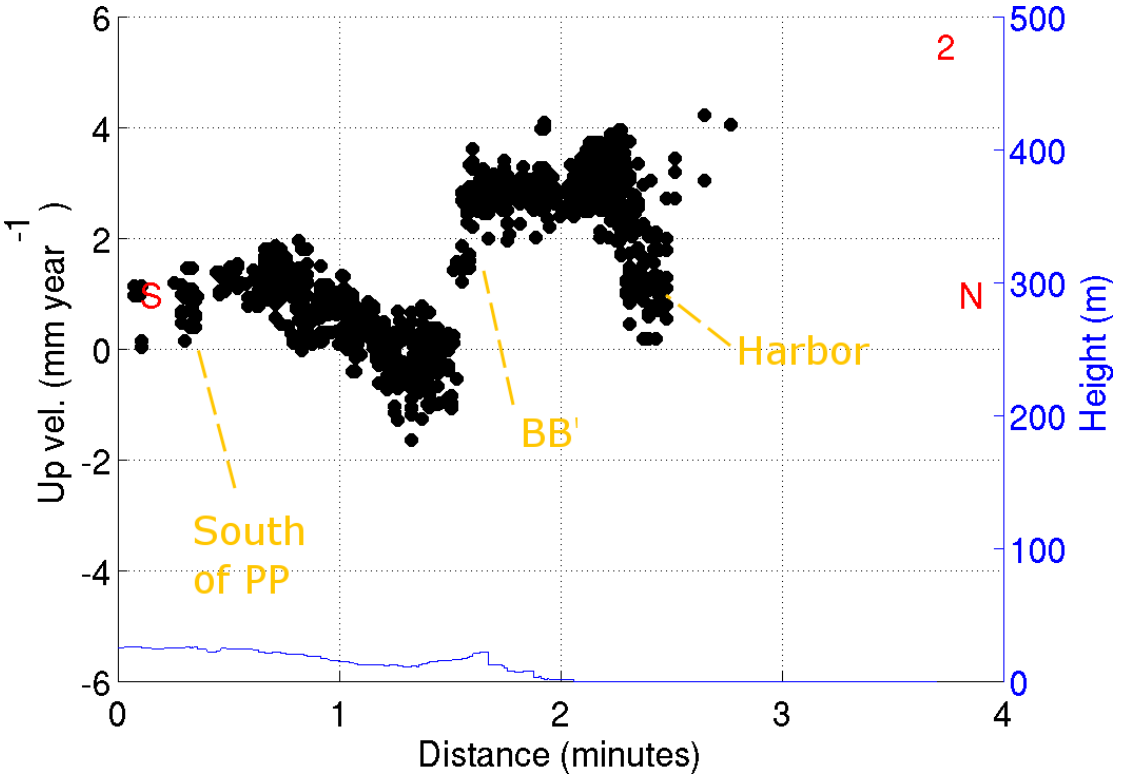

Figure 4-4. Cross section no. 2 (Figure 4-2) of the UDc of the city of Patras. In orange letters the features that we have discriminated are marked. *PP* stands for Peiraiki-Patraiki.

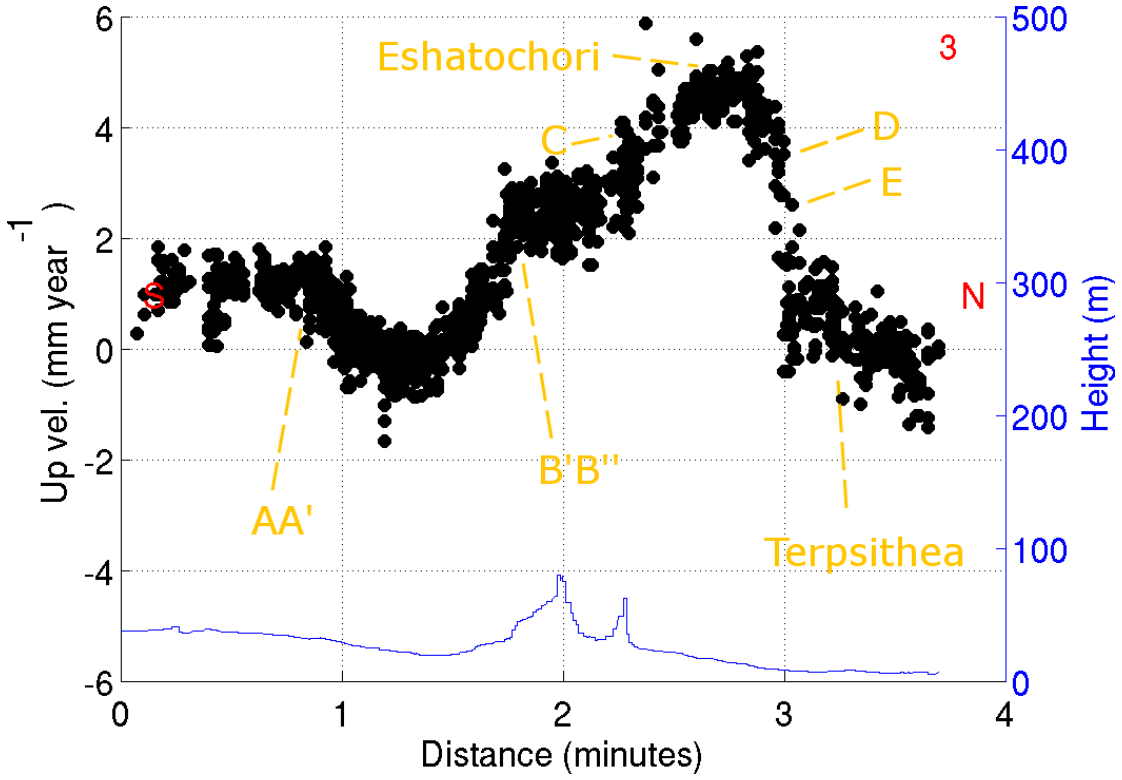

Figure 4-5. Cross section no. 3 (Figure 4-2) of the UDc of the city of Patras. In orange letters the features that we have discriminated are marked.

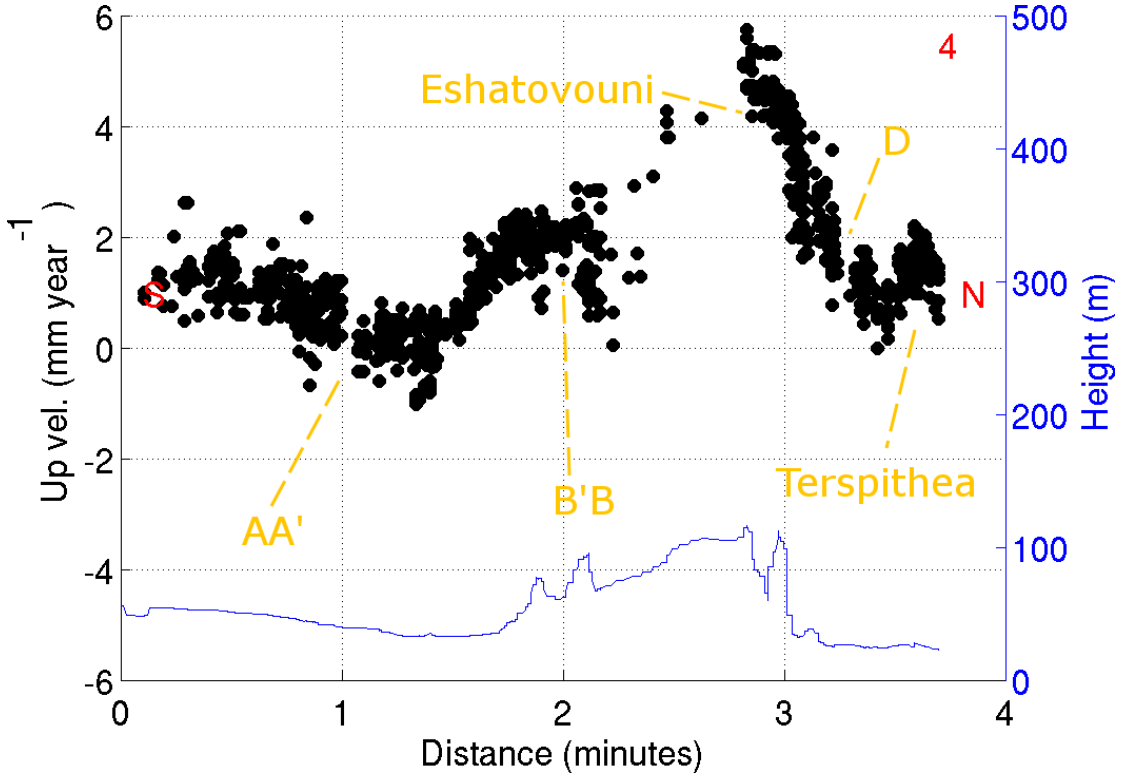

Figure 4-6. Cross section no. 4 (Figure 4-2) of the UDc of the city of Patras. In orange letters the features that we have discriminated are marked.

The city of Patras seems to uplifting relatively to our reference, except South of Peiraiki-Patraiki, near Terpsi and in Terpsithea which subsides with a rate of up to 2mmyear-1.

The cross section no. 3 is the most representative for the overall deformation of the city (Figure 4-5). We can discriminate 4 bending points along the cross section. The first two are at points A-A' and B-B'. They form two mirror faults the first one dipping North and the second dipping South and collapsing in the middle forming a subsiding basin. The third point is at C. There seems to be the hanging wall of the third (minor) fault. The fourth point D is located in the RPfz.

In the city of Patras and in the UDc (Figure 4-2) we can discriminate the main discontinuities of :

- Downlift South of Peiraiki –Patraiki.
- Uplift in Peiraiki-Patraiki.
- The patch between A-A' and B-B'-B" seems to form a subsiding basin. Inside through it passes the old Diakoniaris river . In the center of it almost -1.8 mm $year^{-1}$. In the eastern part of it deformation is descreased.
- B-B'-B" : In the profiles 1 and 2 the discontinuity is steep but in the diagrams 2-3 it is smoothed. It is ranged 2-3.5 mm $year^{-1}$. On 31st of August 1989 a shallow earthquake of M_S=4.8 occurred in the city of Patras [Kalteziotis et al., 1991]. The author stated that the most important feature connected with the seismic activity is the longitutional surface rupture (Figure 4-7) along Ag. Triada fault, that in the present study concides with the B-B'-B" feature. He is considering it a normal fault but without vefirying that this fault is directly related with the earthquake
- The harbor is slightly subsiding (no. 2, Figure 4-4) in relation with its surrounding at about 1-2 mm year and uplifting at 1 mm $year^{-1}$ in absolute.
- Along C we see an abrupt discontinuity of almost 1 mm $year^{-1}$.
- Footwall between C and D is uplifting with the higher rate of almost 5 mm $year^{-1}$, ~3.5 mm $year^{-1}$ relative to its northern and ~4 relative to its southern footwalls.
- D line coinsides with the Rion-Patras fault zone.
- Across E there is a downlift in the area of Terpsithea.

[Koukis et al., 2005] proposed a map of certain and probable faults based on systematic fieldwork and aerial photo interpretation (Figure 4-8). We can relate some of these features, i.e. *A* striking EES, *B* striking EEN, along harbor, striking NE, *C* and *D* striking E and *F* striking NE (Figure 4-2). According to the author Agia Triada fault is a normal fault which was reactivated during the 1989 Patras earthquake.

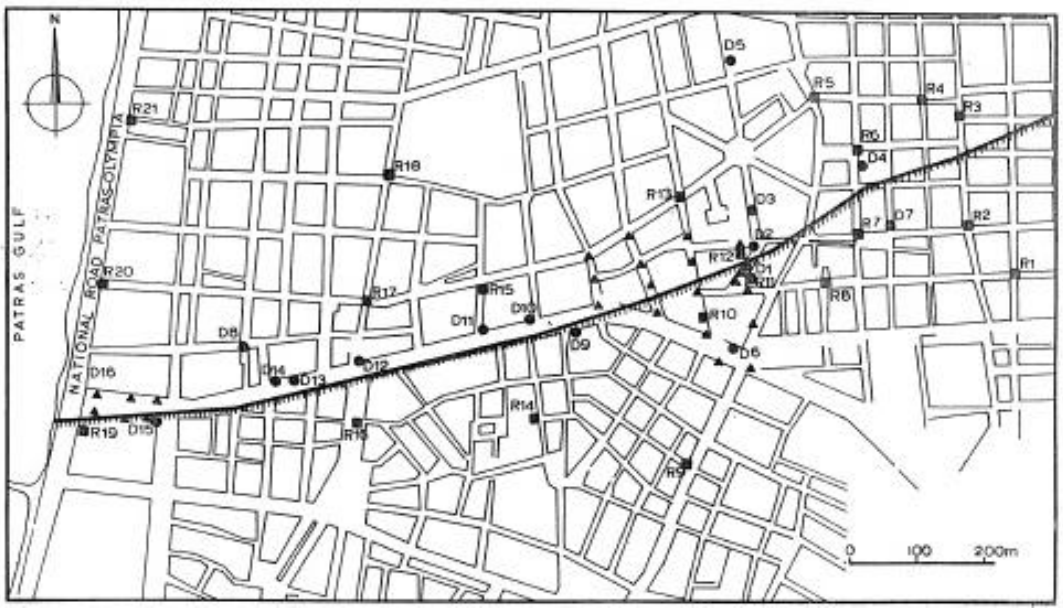

Figure 4-7. Courtesy of [Kalteziotis et al., 1991]. The most important feature connected with the seismic activity of Patra 1989 earthquake, according to the author.

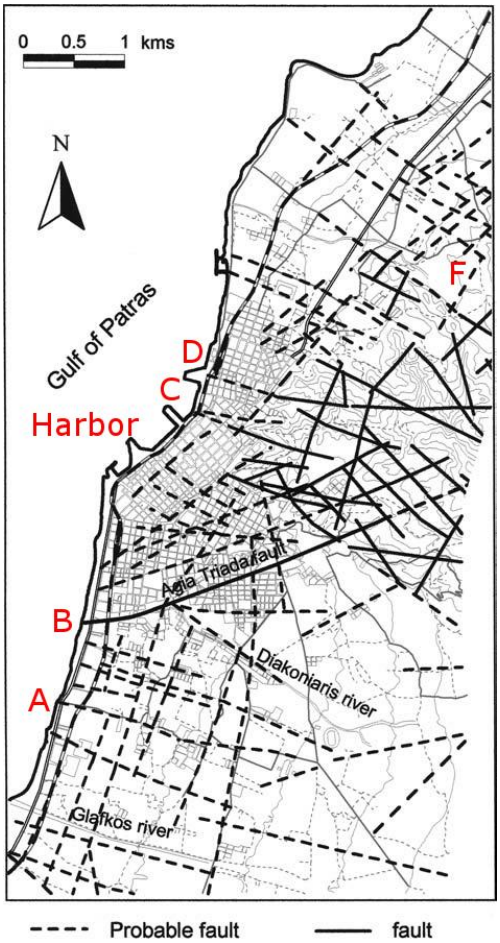

Figure 4-8. courtesy of [Koukis et al., 2005]. Fault trace map of the city of Patras. The red letters corresponds to the discriminated features of Figure 4-2.

[Parcharidis et al., 2009] has performed a study in the city of Patras using 42 AMI/ERS1&2 SAR scenes acquired between 1992 and 2000 along descending track 279. The processing was performed on the IPTA processing scheme. Author's detected discontinuities coincide with the present study ones for the B-B'-B" and D (Rion-Patras Fault Zone) features (Figure 4-2, Figure 4-9). The Author's cross-section trace is coincided with the number 3 (Figure 4-5) cross sections of the present. As we can see both cross sections coincide very well. Since the sensitivity vector of the UDc of LOS of AMI/ERS1&2 and ASAR/ENVISAT mode I2 prevails over the two others we can compare these two profiles mostly qualitatively and less quantitatively. The Author's point for the reference of the rate values is indicated by a star. Thus the common detected discontinuities seem to be persistent for at least 20 years (1992-2010).

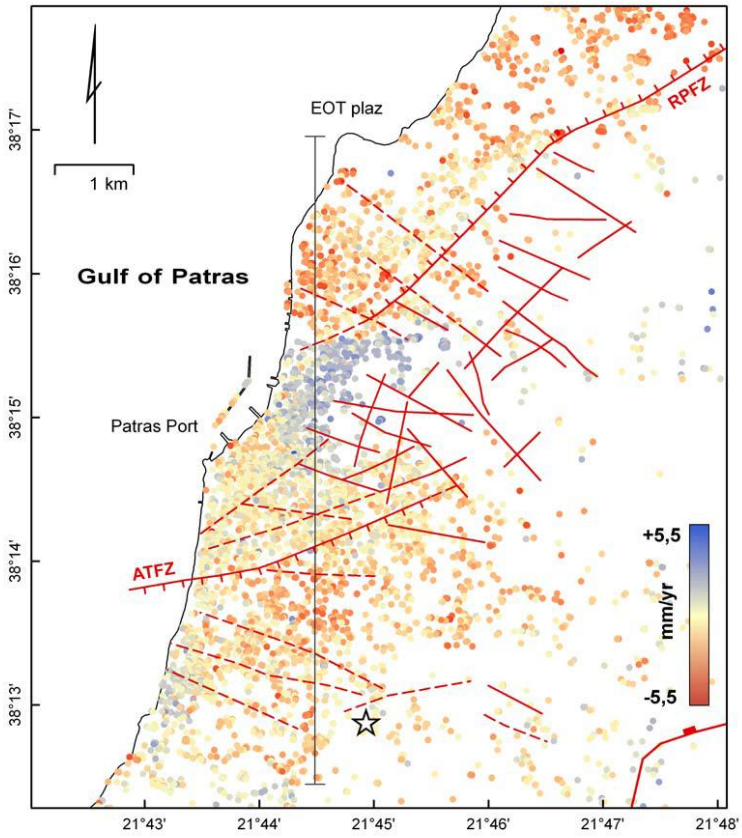

Figure 4-9. Courtesy of [Parcharidis et al., 2009]. Point targets plotted over the fault map for Patras area (ATFZ: Ag. Triada Fault Zone), solid line corresponds to the section of Figure 4-10, fault pattern modified from [Koukis et al. 2007].

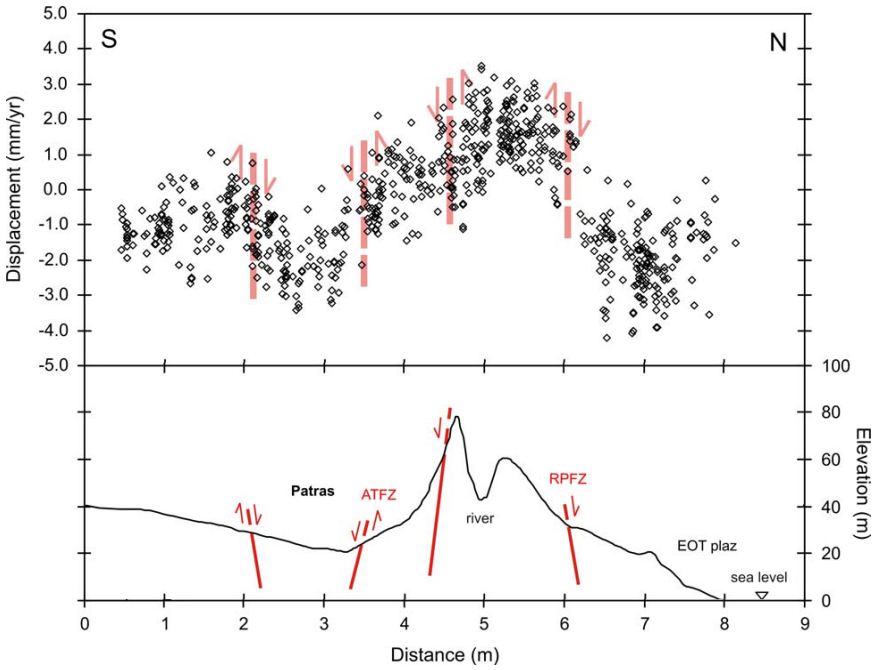

Figure 4-10. Modified from [Parcharidis et al., 2009]. Spatial profile showing the displacement field as observed by IPTA and plotting targets within 150 meters in both sides of the profile (upper), and the related topography (down), red lines correspond to the faults.

For the EWc (Figure 4-12) we have superimposed the features we have found from UDc. From Figure 4-12 and Figure 4-11 we can discriminate the deformed patch F-B-B"-G (moving eastwards about 2-3 mm year^{-1} relative to the clutter) and Terpsithea (moving eastwards about 2mm). The first area coincides in great degree with the corresponding upsiding patch of Figure 4-2, but not exactly. A question that can be imposed here is *does this increased EWc biased by the increased UDc?* Considering that the situation in the Eshatovouni and Terpsithea patch is the opposite we can conclude negatively. In Anthoupoli and NE of Terpsithea we can discriminate the beginning of the Rion-Patra fault zone.

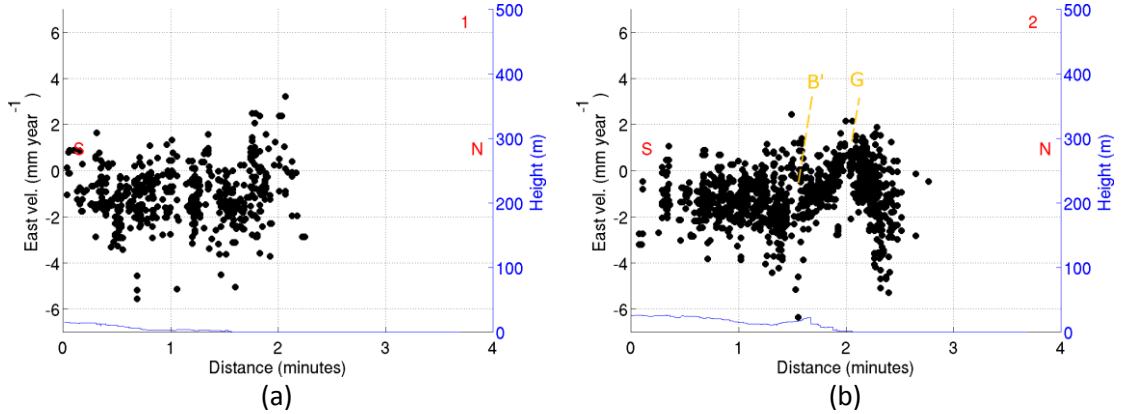

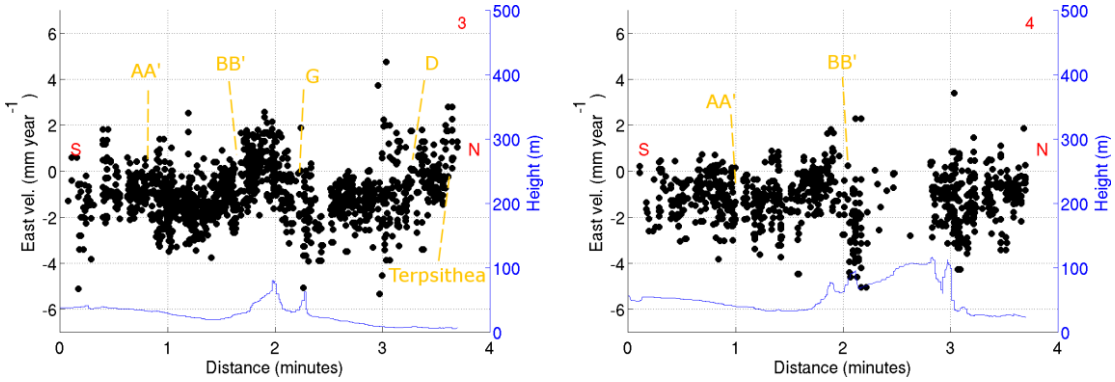

Figure 4-11. Cross sections 1,2,3 and 4 (Figure 4-12) of the EWc of the city of Patras.

Concluding the horn bordered by B-B'-B''-Anthoupoli-D is uplifting due probably to pressure accommodated from the North and South. The RPfz (as will see in the next paragraph) is an oblique deformed fault, with its strike component to be right lateral. Its continuation after Rio is offshore and along the Patras coastline. Probably this NNE-SSW is producing this uplift in the upper layers of the crust. It shouldn't be a deep but mostly a shallow feature. In Figure 4-12 the block deformed in the EWc is limited to F-B'-B''-G.

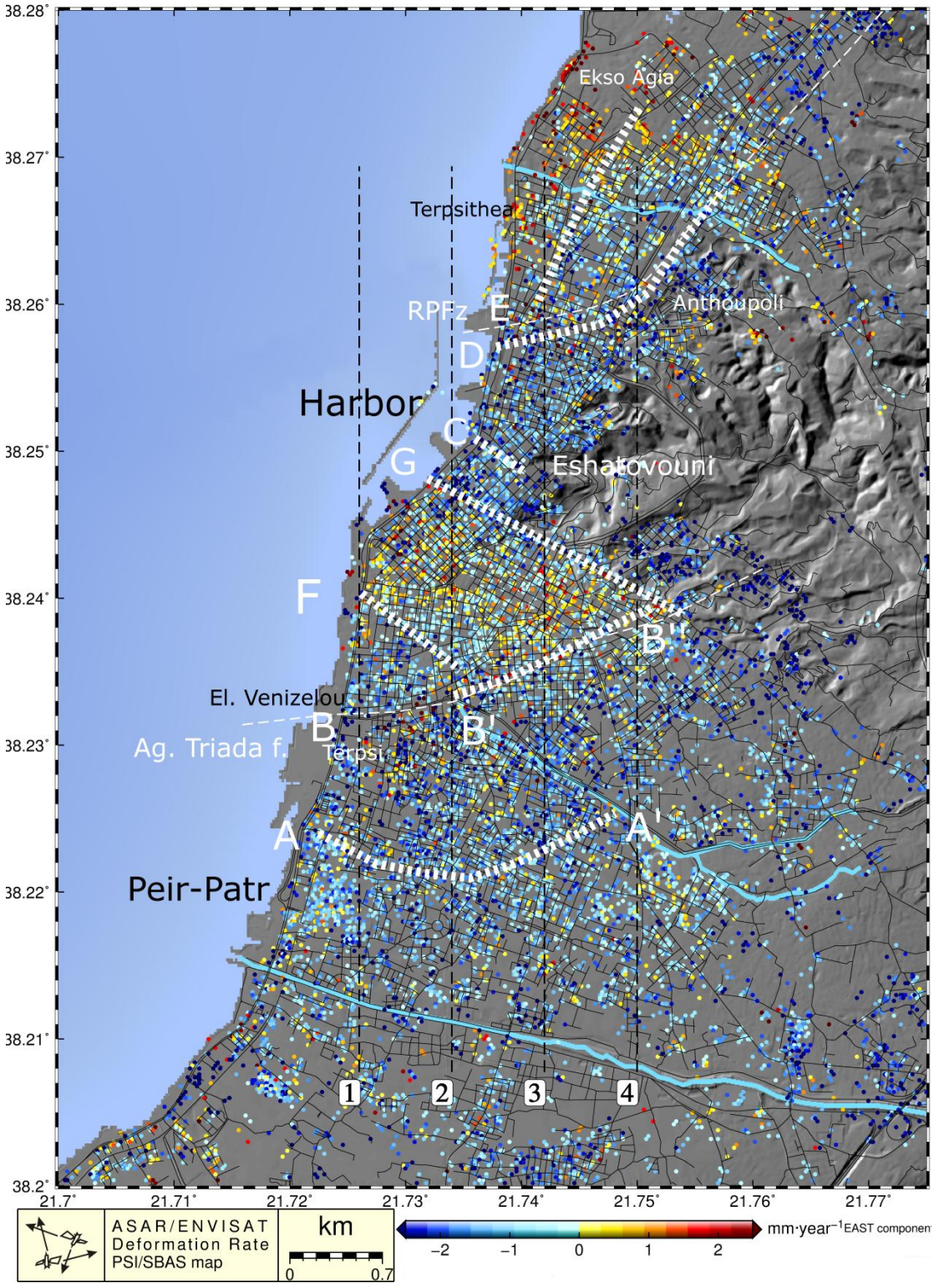

Figure 4-12. PSI/SBAS map of the EWc rate of the city of Patras. The black dotted lines correspond to the cross sections of Figure 4-3, Figure 4-4, Figure 4-5, Figure 4-6. In the map we superimposed the main discontinuities of UDc. Moreover we have marked two more existing in the present EWc map, i.e. *F* and *G*. In thin white dotted line represents the fault traces of Ag. Triada and RPFz (Rion-Patras fault zone).

4.2. Rion-Patras fault zone

The PSI/SBAS UDc of the Rion-Patras fault zone if shown in Figure 4-13.

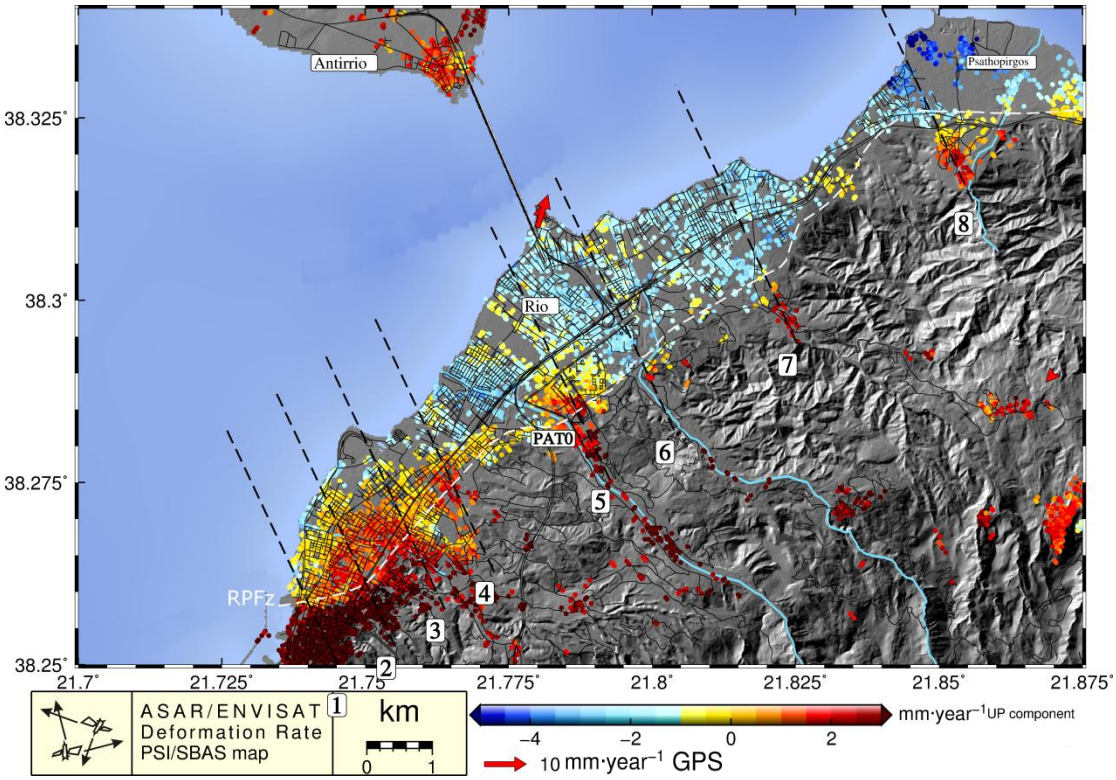

Figure 4-13. The PSI/SBAS UDc of the Rion-Patras fault zone. The cross section traces are marked with black dotted lines and its values are plotted in Figure 4-14. The fault trace of RPfz is marked with white dashed line.

In the Figure 4-13 we can discriminate many discontinuities striking NNW and NW that their origin is unknown. We will focus in the RPfz (Figure 4-14).

The Rion-Patras fault zone has a NE-SW general direction and extends along the rangefront that is found behind the large alluvial fans of the Rion-Patras coastal plain [Stamatopoulos et al., 2004; Flotte et al. 2005]. In Figure 4-14 the cross sections marked in Figure 4-13 are plotted. Their length is almost 1.9° and they don't cover the full length of 4° of the diagrams. We kept the deformation and the distance the same for all the cross sections of the study in order to have the same reference. We noted that in cross sections 1 and 3 (Figure 4-14a and Figure 4-14c) the gradient of the discontinuity is very high and highly localized. Moreover this very high gradient localized very close to the fault trace. In the profiles no. 2,3,7 and 8 the gradient is high ranging up to ~5 mm year^{-1} per distance of a minute (~1.9 km) The UDc across the RPfz is ranging between 0.5 and 4 mm year^{-1}. In the map we are detected also a rate difference of ~1.5 mm year^{-1} between Rion and Antirrion.

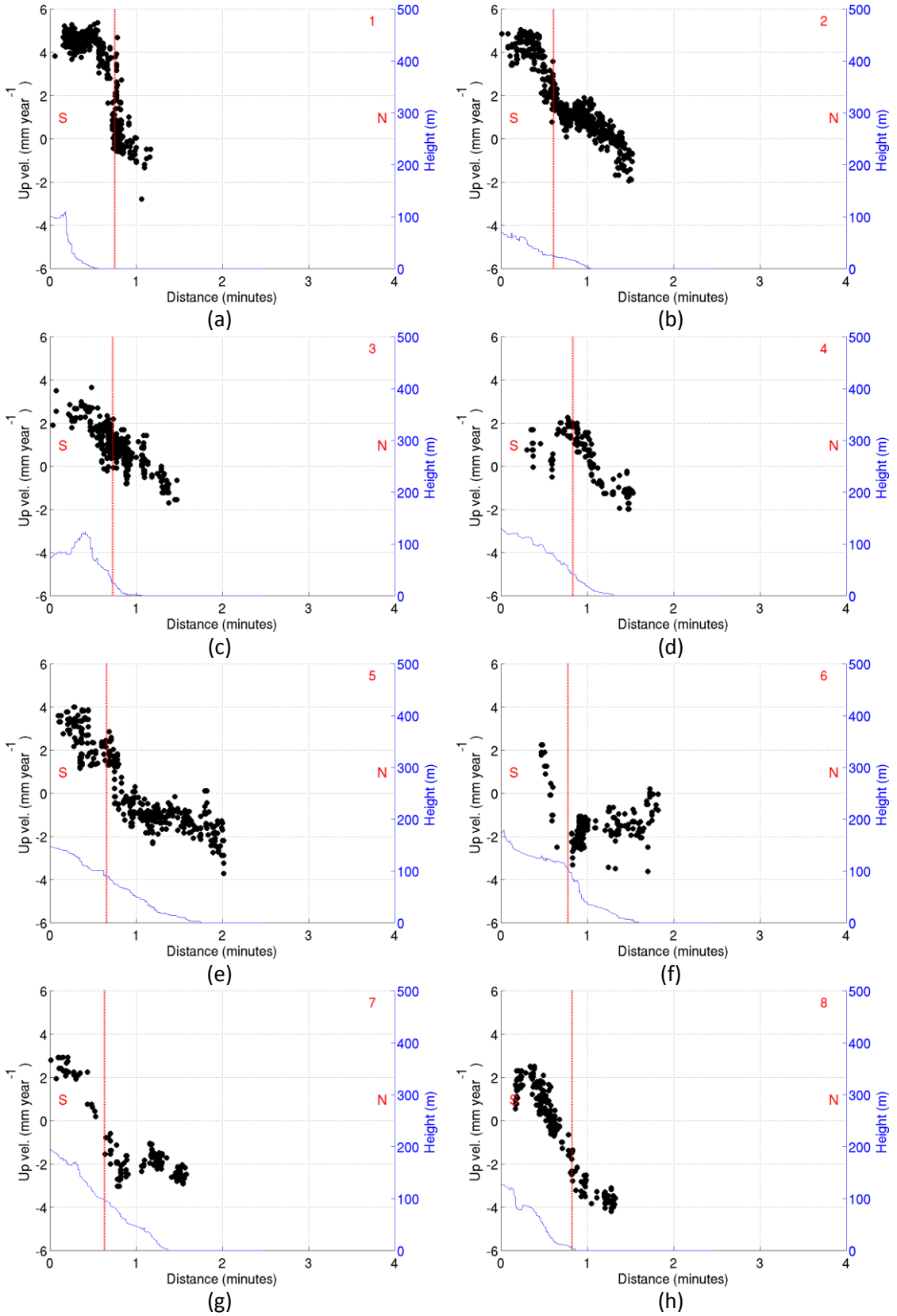

Figure 4-14. Cross sections no 1-8 (Figure 4-13) of the UDc of the Rion-Patra fault zone. Red line indicates the RPfz as marked in Figure 4-13.

The PSI/SBAS EWc of the Rion-Patras fault zone if shown in Figure 4-15.

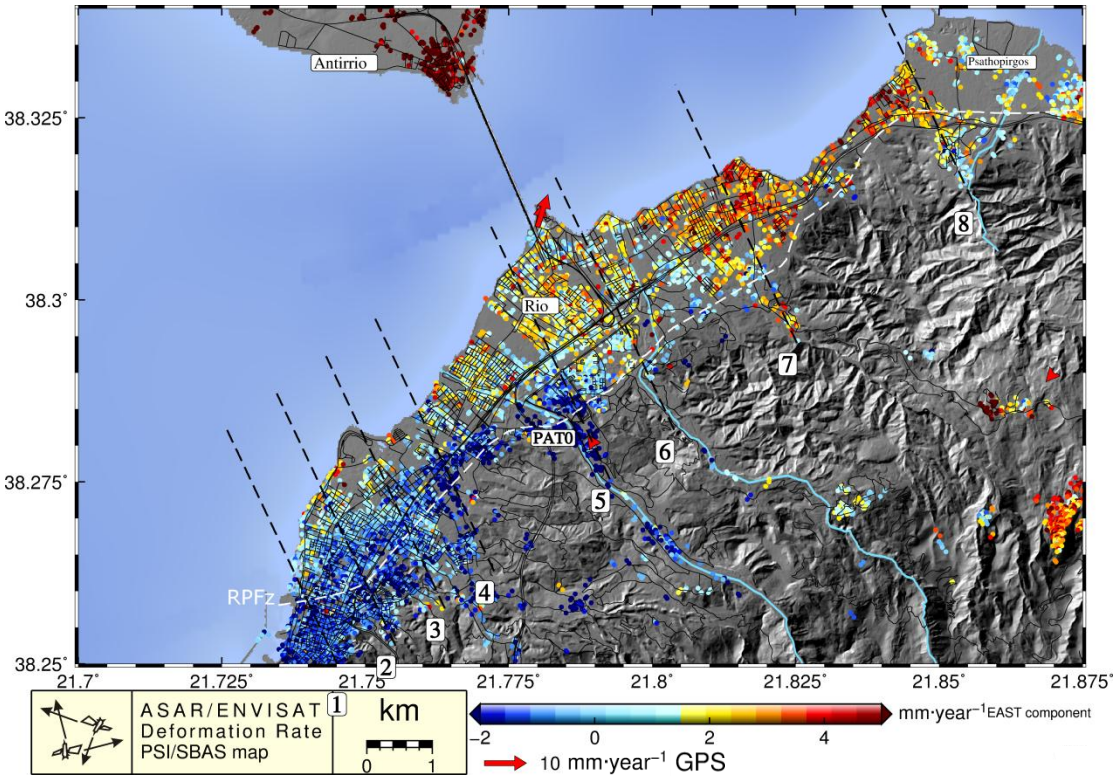

Figure 4-15. The PSI/SBAS EWc of the Rion-Patras fault zone. The cross section traces are marked with black dotted lines and its values are plotted in Figure 4-16. The fault trace of RPfz is marked with white dashed line.

In the Figure 4-15 the main feature that we can discriminate is the RPfz.

In Figure 4-16 the cross sections marked in Figure 4-15 are plotted. We noted that in all the cross sections, except no. 8 the gradient of the EWc high and towards East ranging between 0.5 to 4 mm year^{-1} per minute of distance (~1.9 km). Its maximum is located in profile no 5. In the map we are detected also a rate difference of more than 1.5 mm year^{-1} between Rion and Antirrion. In the case of EWc we don't have the very high gradients as of the case of UDc.

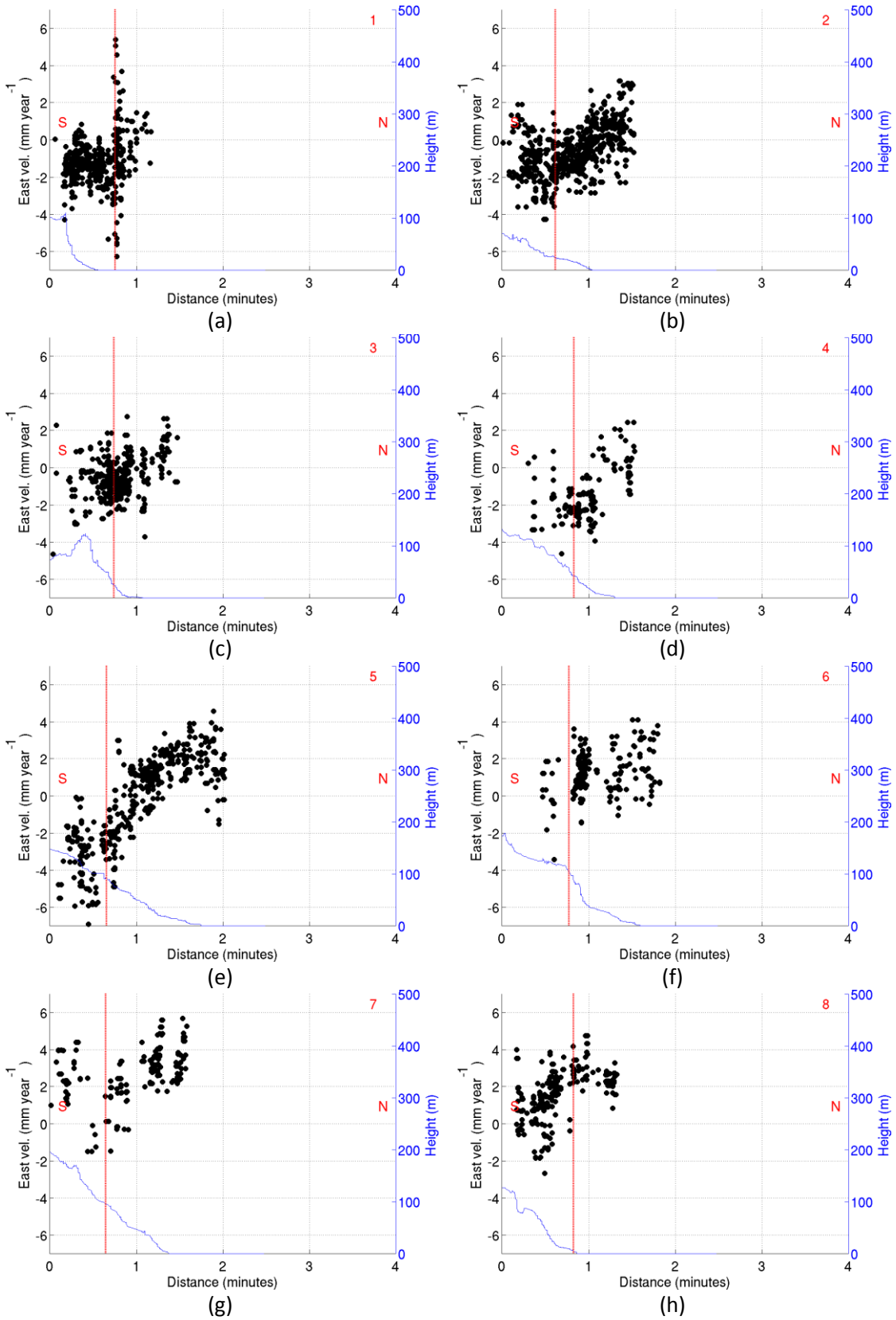

Figure 4-16. Cross sections no 1-8 (Figure 4-13) of the EWc of the Rion-Patra fault zone. Red line indicates the RPfz as marked in Figure 4-13.

In order to investigate the relation between the UDc and EWc for each cross section we have calculate the *Oblique Index* as in equation 2.1.

$$\forall\ cross\ section\ \ p, ObliqueIndex = \frac{UDc_i^p - EWc_i^p}{UDc_i^p + EWc_i^p}, \tag{4.1}$$

$$i = 1 \dots N, number\ of\ point\ in\ the\ cross\ section\ p.$$

The UDc_i^p and EWc_i^p has been shifted so that their minima and maxima for each cross-section to be equal and opposite. This way we transform the reference frame of the two components to be relative to the area of each cross section.

In Figure 4-17 the histogram of the *ObliqueIndex* for each cross section are plotted. Large population being after *ObliqueIndex*=.5 means bigger UDc and large population being before *ObliqueIndex*=.5 means bigger EWc. More the population gathered to the edges means that the difference of the two components is big. From the histograms we can conclude that the EWc of the deformation rate across the zone defined by the RPfz zone prevails over the UDc.

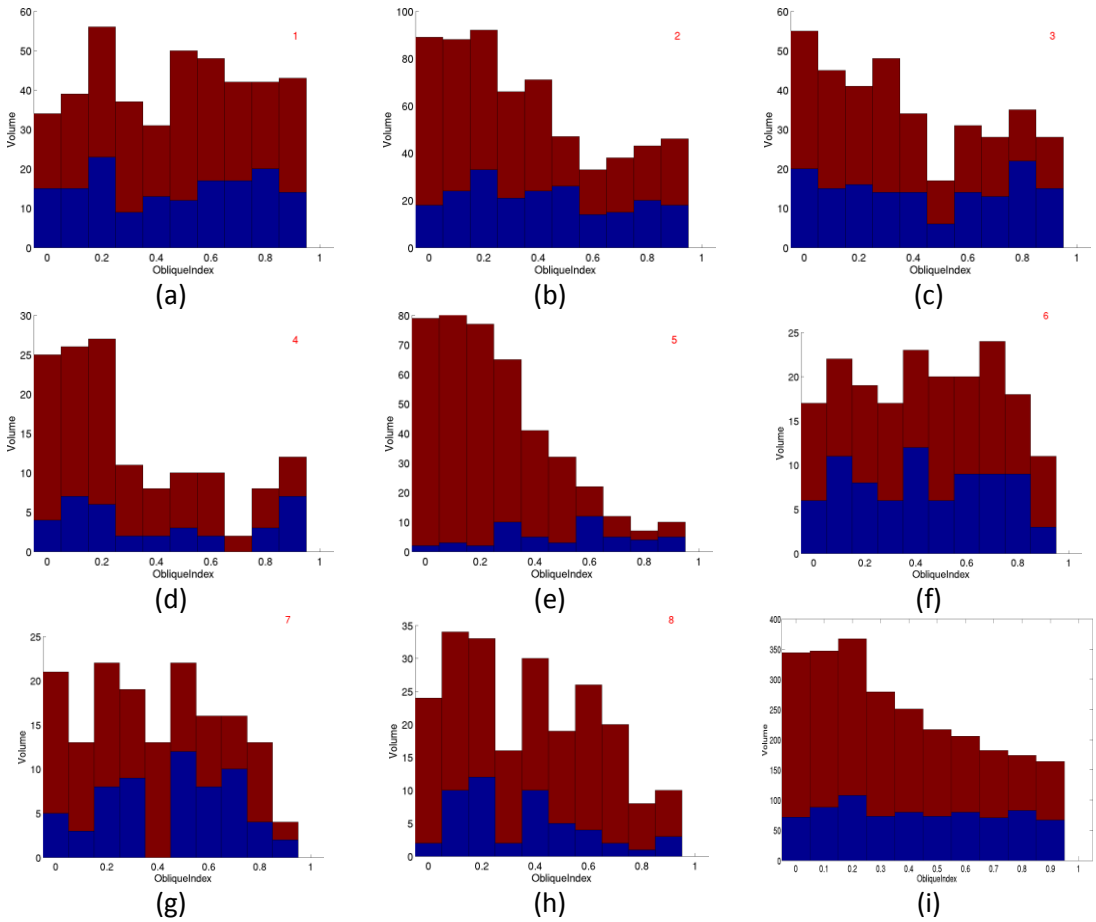

Figure 4-17. (a) to (h) histograms of the *ObliqueIndex* of the cross sections of RPfz area. (j) histogram the *ObliqueIndex* taking into account all the cross sections. With blue color marked the points having the same sign (i.e. moving Upwards and Eastwards, or Downwards and Westwards) and with red color the points having opposite sign (i.e. moving Upwards and Westwards, or Downwards and Eastwards).

In the Figure 4-18 and Figure 4-19 the UDc and the EWc of PSI/SBAS map of the area of the University of Patras, is shown.

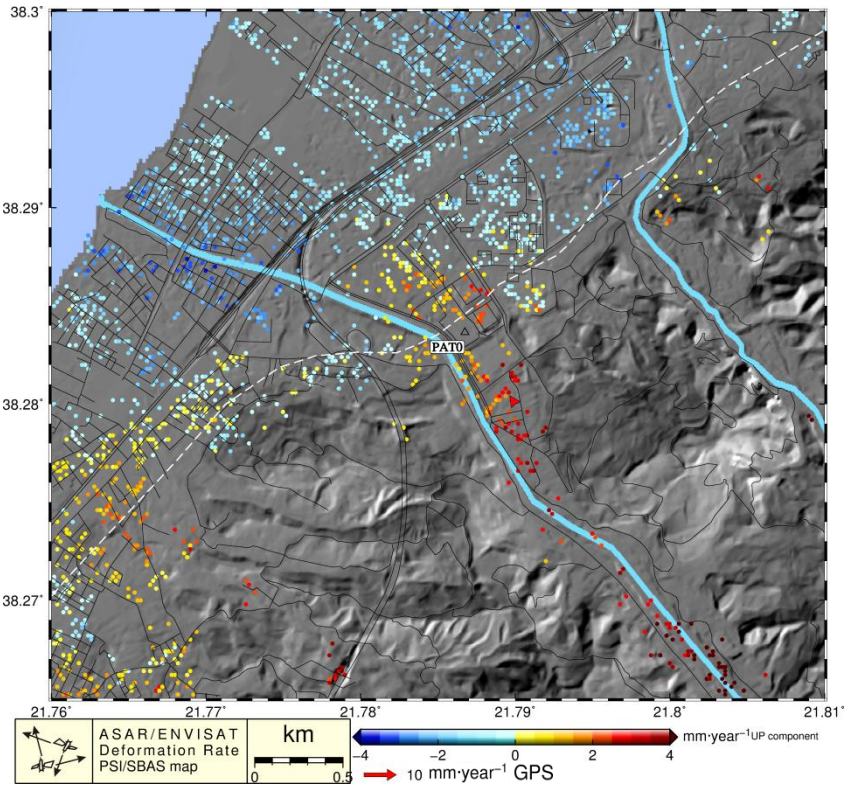

Figure 4-18. The PSI/SBAS UDc of the area of University or Patras, superimposed over shaded relief. The RPfz is marked with dashed white line.

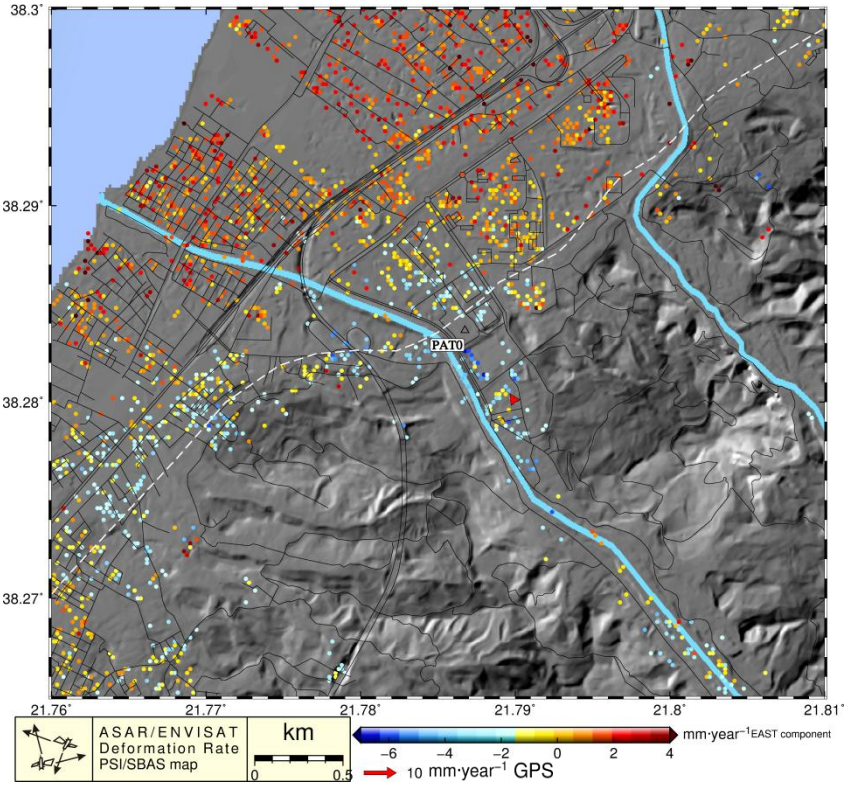

Figure 4-19. The PSI/SBAS EWc of the area of University or Patras, superimposed over shaded relief. The RPfz is marked with dashed white line.

5. Secondary Observed Discontinuities

From the corrected and initial PSI/SBAS maps herein we will investigate the Aigion, Nafpaktos-Mornos Delta, Akrata Delta-Platanos, Sellianitika and Rododafni Delta, Psathopyrgos Delta, Efpalio-Marathias, Trizonia-Psaromita, Profitis Ilias, Souli, Panagopoula and some the interested features , its location shown in Figure 5-1.

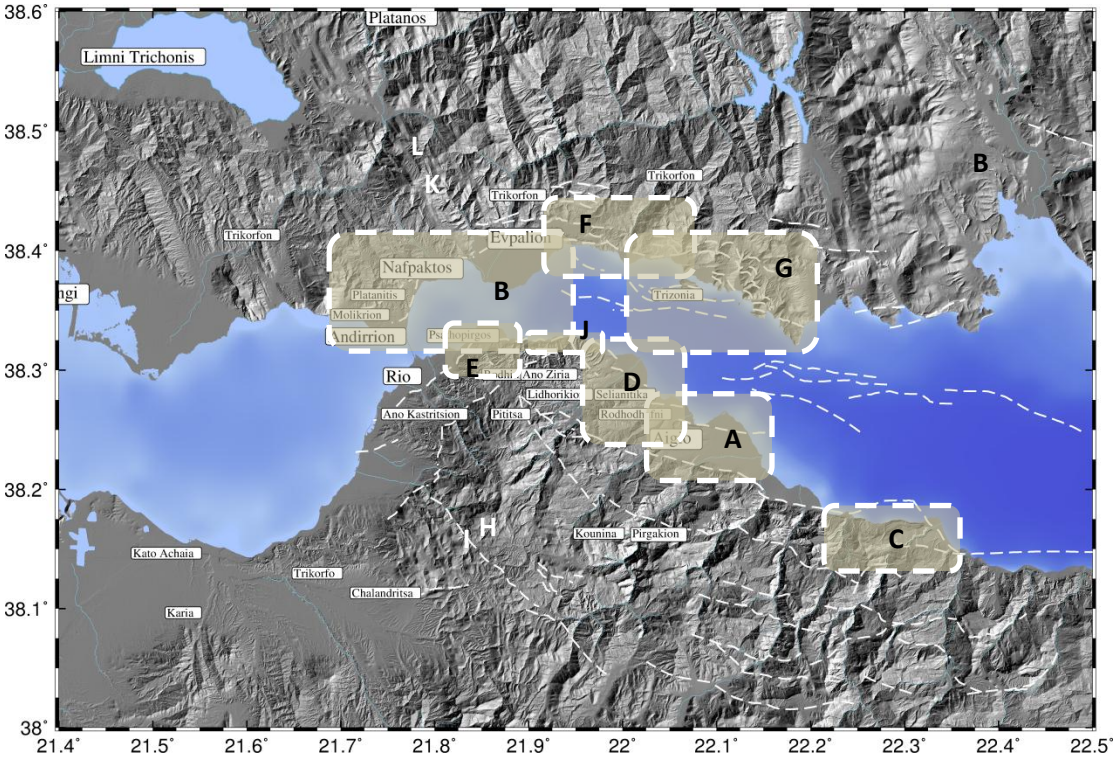

Figure 5-1 The study areas of Aigion (A), Nafpaktos-Mornos Delta (B), Akrata Delta-Platanos (C), Sellianitika and Rododafni Delta (D), Psathopyrgos Delta (E), Efpalio-Marathias (F), Trizonia-Psaromita (G), Profitis Ilias (H), Souli (I), Panagopoula (J) and the interested features (K) and (L).

5.1. Aigion

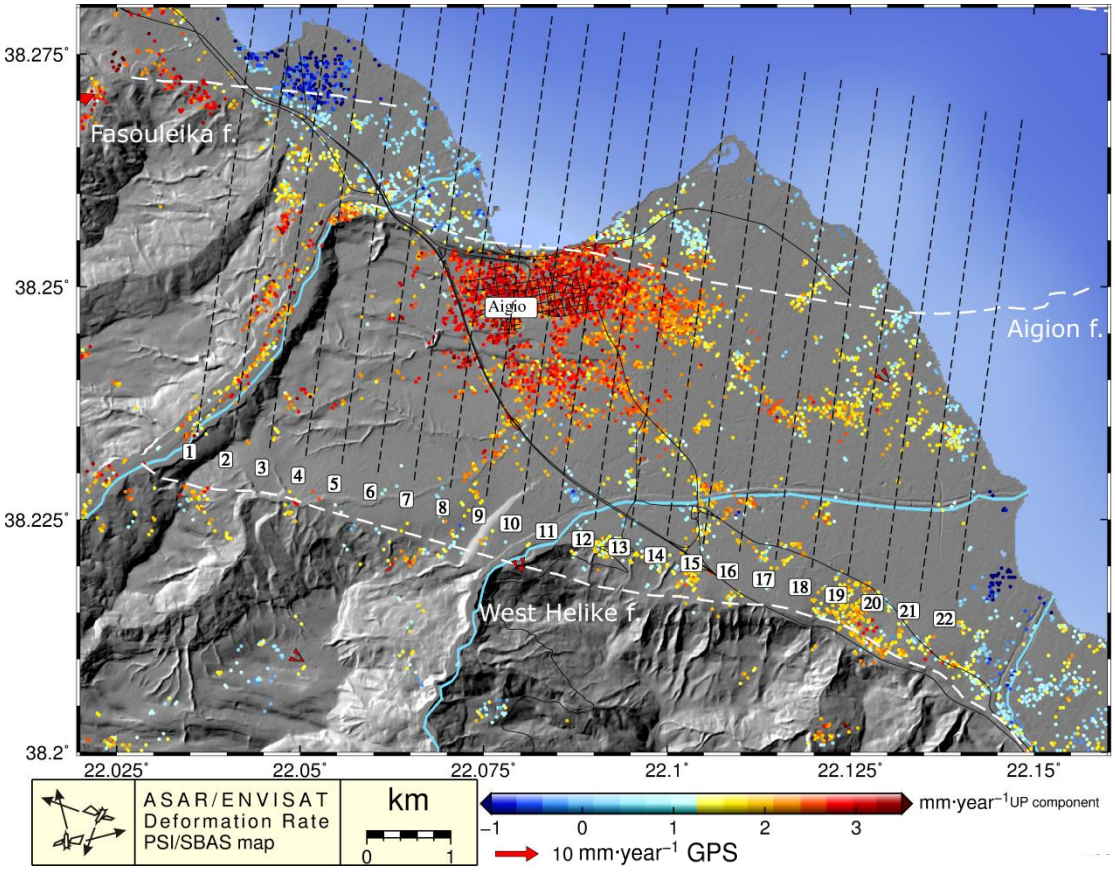

Figure 5-2. The PSI/SBAS UDc of the Aigion fault area. The cross section traces are marked with black dashed lines and its values are plotted in Figure 5-4. The fault traces of Aigion, West Helike and Fasouleika are marked with white dashed line.

In the cross sections no. 8, 11 and 12 (Figure 5-4) we can see an abrupt discontinuity, with almost 2 mm year^{-1}. The maximum gradient is detected at no. 3 and is reaching the 6 mm year^{-1} per minute of distance (~1.9 km).

In [De Martini et al., 2003] individual terraces were tentatively correlated with the eustatic sea-level curve, constrained by some direct dating of the deposits blanketing the terraces. They obtained long-term cumulative uplift rates over the past 200–300 kyr (using U series dating) for the East Eliki,West Helike and Aigion Fault footwalls. The Authors declare that the terraces of Stage 5 (Figure 5-3) have clearly emerged more rapidly (1.2 mm year^{-1}) with respect to those of Stage 7 (1.05 mm year^{-1}). This discrepancy can be attributed to different factors: (a) changing uplift rate through time, with a recent acceleration; (b) different distance from the fault, Stage 7 terraces being at a distance of 2–4 km, whereas those of Stage 5 are much; (c) activity of the West Helike segment, which could negatively influence the coeval Aigion Fault footwall uplift, especially the Stage 7 terraces that are the closest to the West Helike Fault trace.

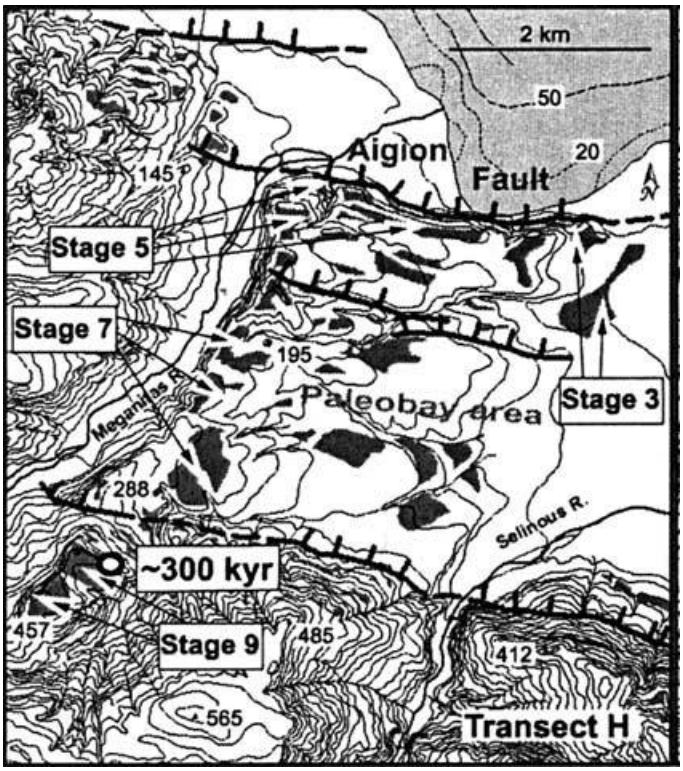

Figure 5-3. Courtesy of [De Martini et al., 2003]. Map of marine terraces and fluvial surfaces in the transects on Aigion Fault footwalls. Contour interval is 20 m.

Indeed in Figure 5-4, in the cross sections no. 8-14 (but in the rest of them until no. 18, also) where there are good distribution of PSs across them, we can see the decrease of the UDc as moving towards the W. Helike fault. Neglecting the cross sections below no. 6 which falling into the Fasouleika fault and by considering the reference to be the at the sea level, thus our PSs falling into the coastal areas, we have an uplift rate of the Aigion footwall ranging between 1.5 mm year^{-1} and 2.5 mm year^{-1} which is bigger than proposed by the Authors. A cause of the observed discrepancy is that almost all the extension of the footwall lie upon deltas, which simultaneously are being compacted, increasing the rate in relation with the hangingwall. Moreover part of this discrepancy is the fact that with their method they have measured the uplift of the terraces caused by the mechanisms of both the creeping faulting and the erosion procedures, but the PSI/SBAS technique, based mostly in stable scatterers, (i.e. rocks, infrastructures, buildings etc.) which are not being affected by the procedures of erosion in time scales as decades, especially in the footwalls.

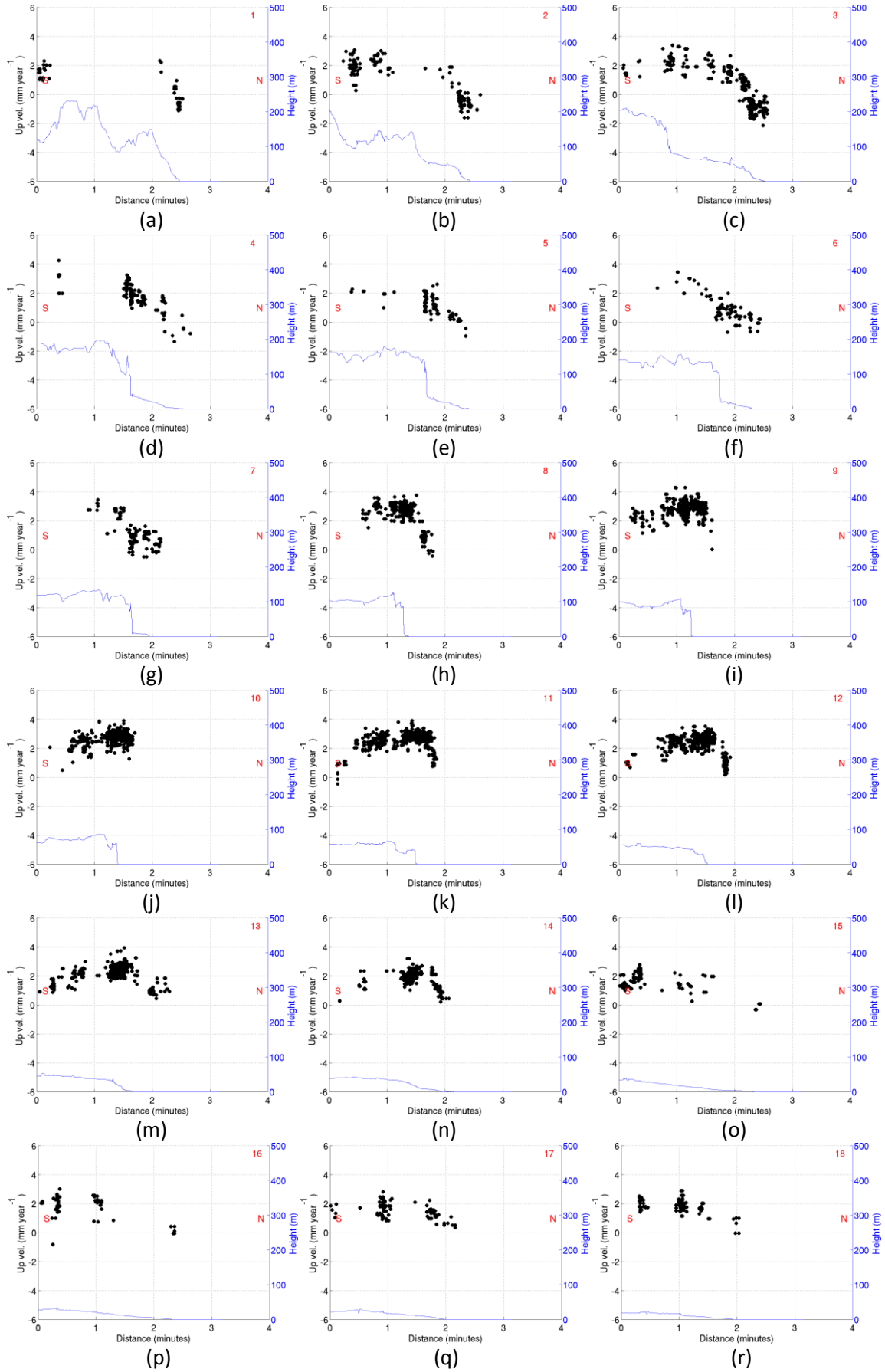

Figure 5-4. Cross sections across Aigion fault, no 1-18, of the UDc of the Figure 5-2.

In Figure 5-5 and in the cross sections no. 6-18 (Figure 5-6) we can discriminated a EWc along them with a constant gradient of almost 2 mm year^{-1} per distance of a minute (~1.9 km).

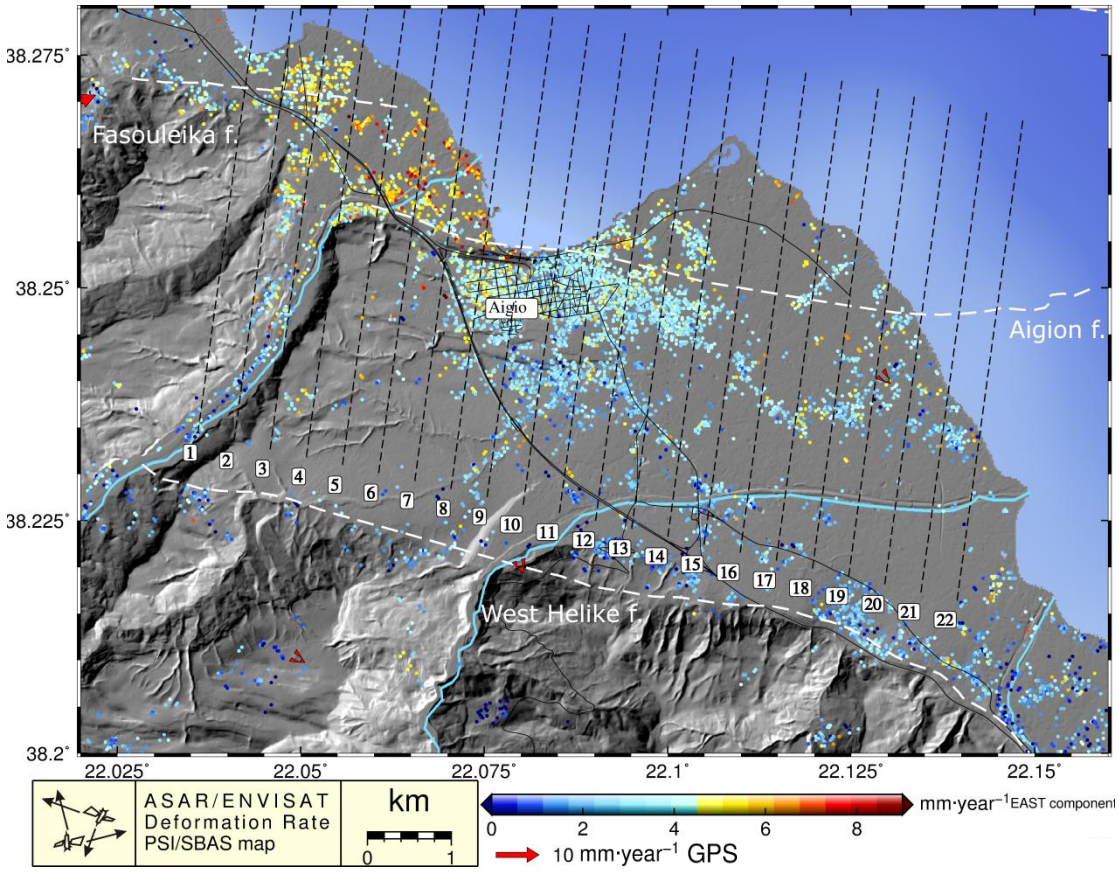

Figure 5-5. The PSI/SBAS EWc of the Aigion fault area. The cross section traces are marked with black dotted lines and its values are plotted in Figure 5-6. The fault traces of Aigion, West Helike and Fasouleika are marked with white dashed line.

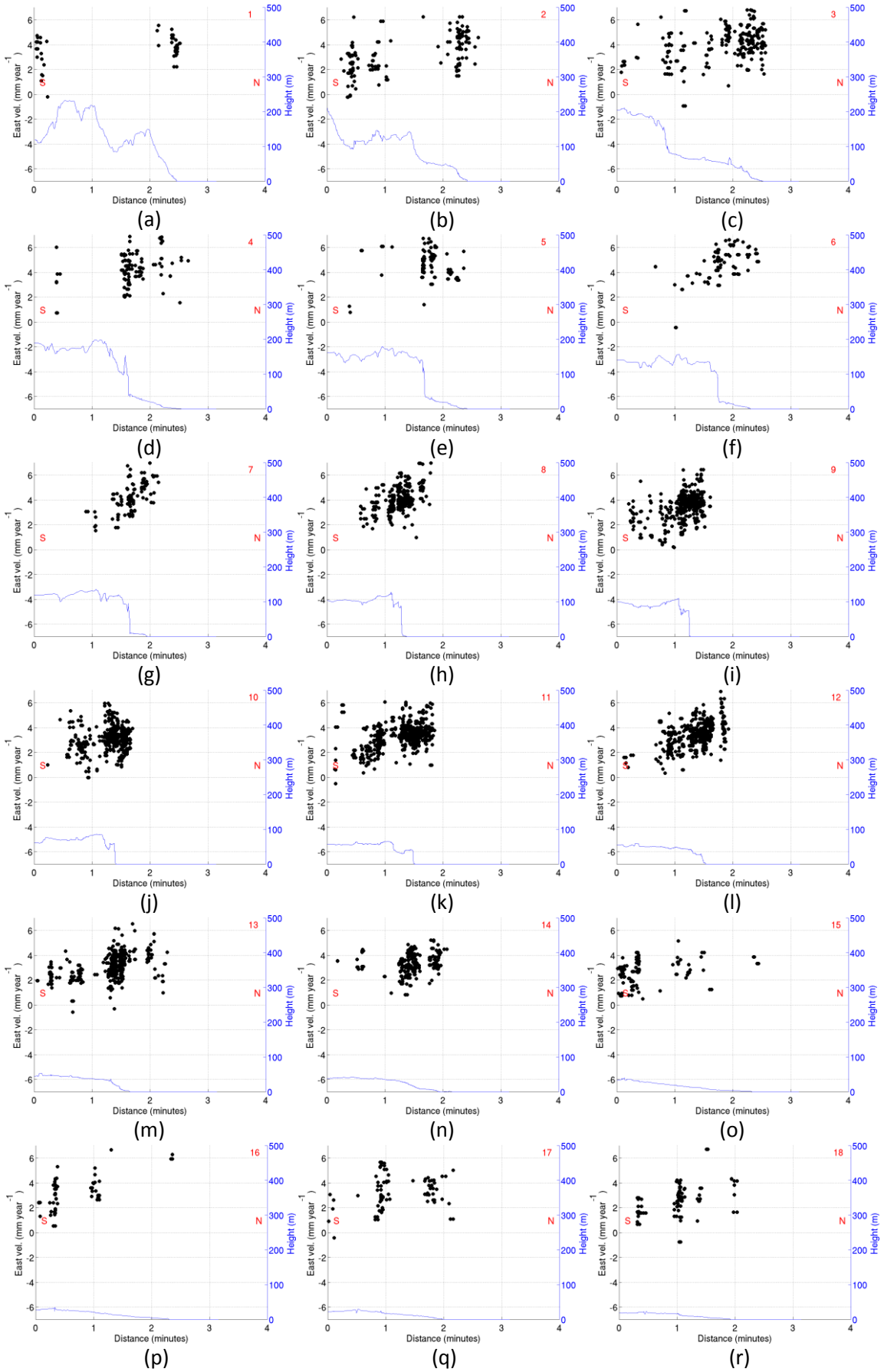

Figure 5-6. Cross sections across Aigion fault, no 1-18, of the EWc of the Figure 5-5.

In Figure 5-7 we can see the temporal evolution of the Aigion fault in the LOS. All the images are referenced to the first one. We can notice some nonlinear behavior and perhaps some failure of the unwrapping (phase slipping) is some samples (i.e. 15/6/03). These samples could be detected as outliers and a cycle of phase (i.e. ±λ/2) to be added in order to fit better with the other samples. Until now we haven't tried to separate the artifact caused by the PS processing and the real motion. In the temporal InSAR maps (i.e. PSI/SBAS) we have used the rate thus suspending the presented outliers

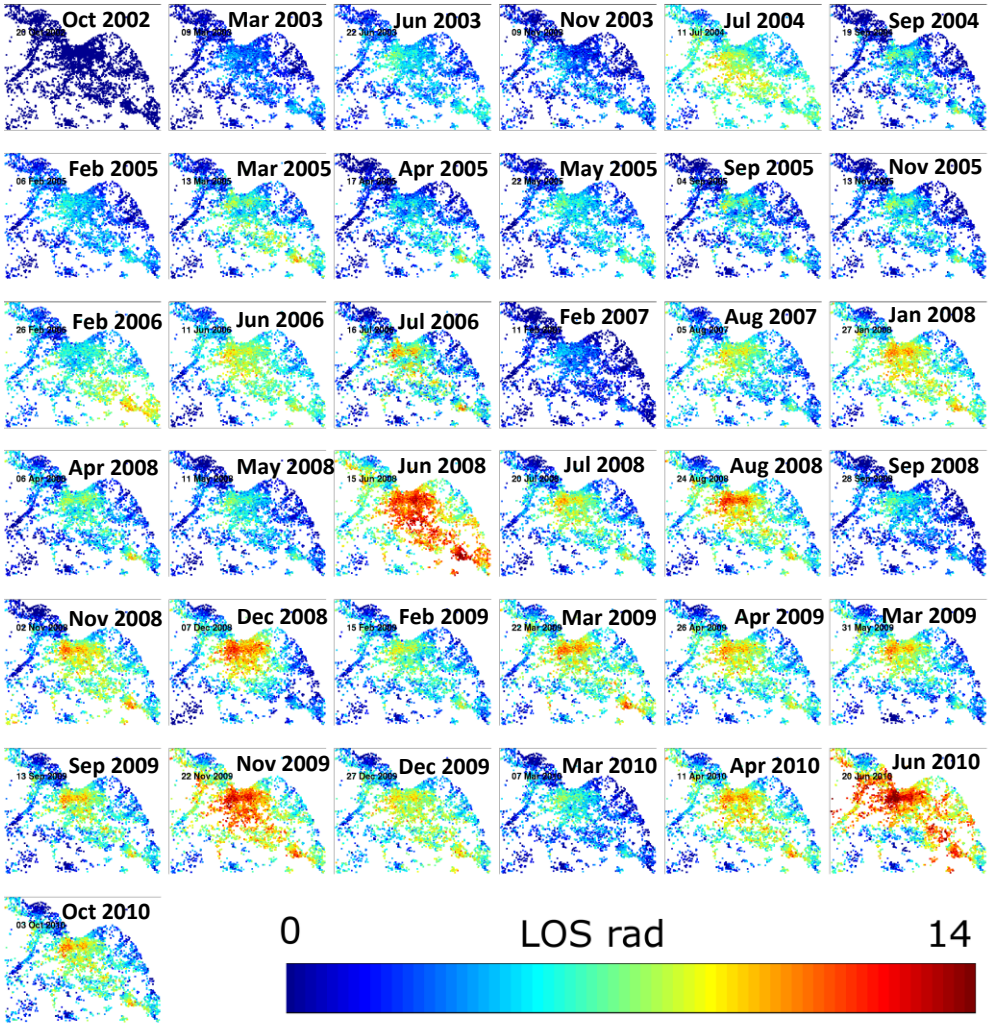

Figure 5-7. Temporal evolution of Aigion fault using PSI/SBAS values. The values are in radians in the descending LOS referenced to the first image. Positive values are towards satellite. One fringe corresponds to 6.28 radians.

For certain outliers (i.e. 15 Jun, 2008 and 7 March, 2010) we can consider the fact that these acquisitions was right after the earthquakes of Movri (8/6/2008) and Efpalio (19 and 22 January 2010). And indeed we can discriminate the effect of the two earthquake in PSI (Figure 5-8) map and in PSI/SBAS (Figure 5-9) one. The effect is stronger in PSI map.

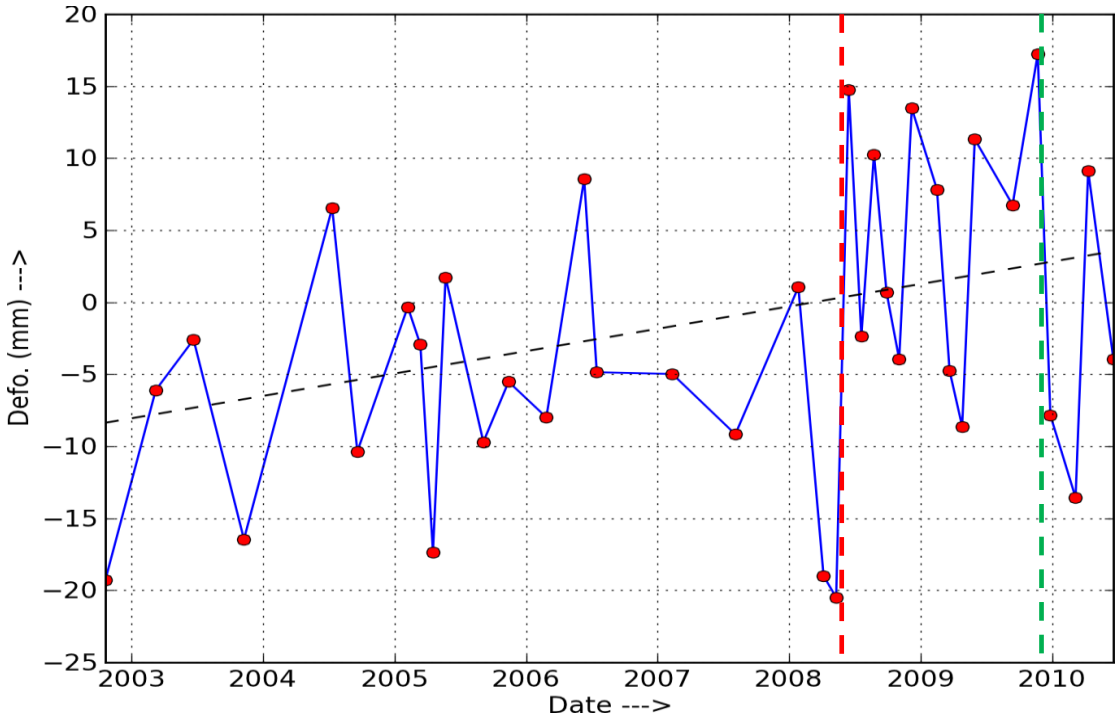

Figure 5-8. Temporal evolution of a PSI Persistent Scatterer located at the hangingwall of the Aigion fault at the LOS direction of the descending track 279. With red and green line the earthquake of Movri 2008 and Efpalio are indicated respectively.

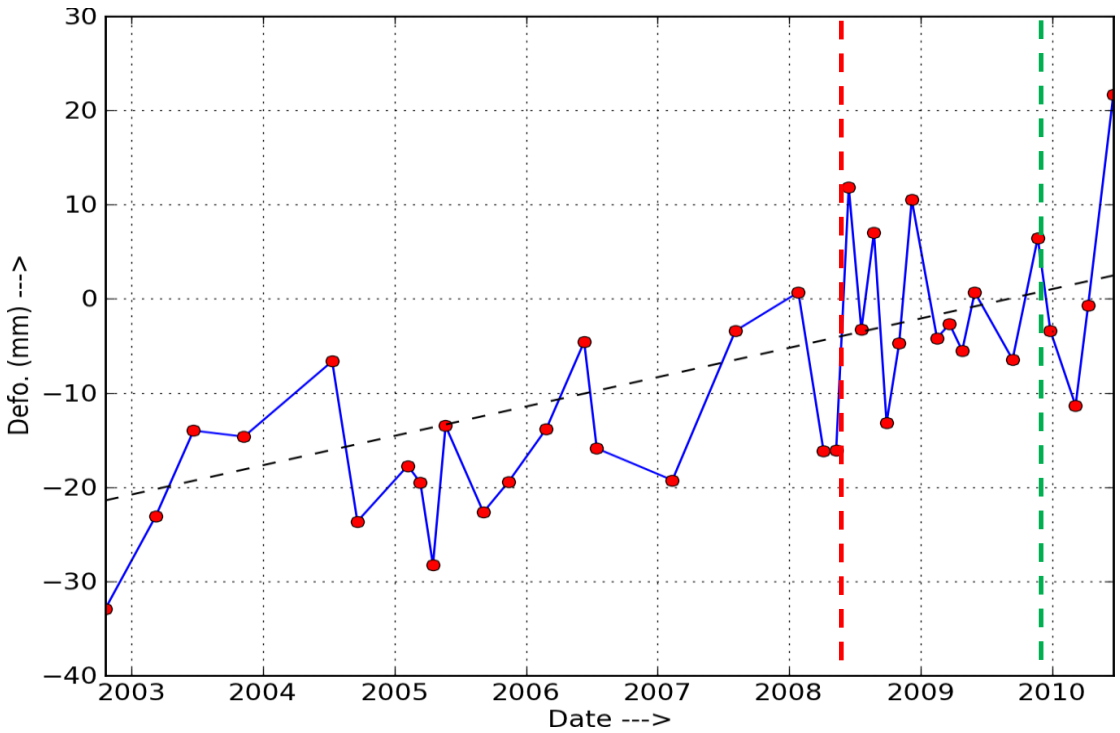

Figure 5-9. Temporal evolution of a PSI/SBAS Persistent Scatterer located at the hangingwall of the Aigion fault at the LOS direction of the descending track 279. With red and green line the earthquake of Movri 2008 and Efpalio are indicated respectively.

5.2. Nafpaktos – Mornos Delta

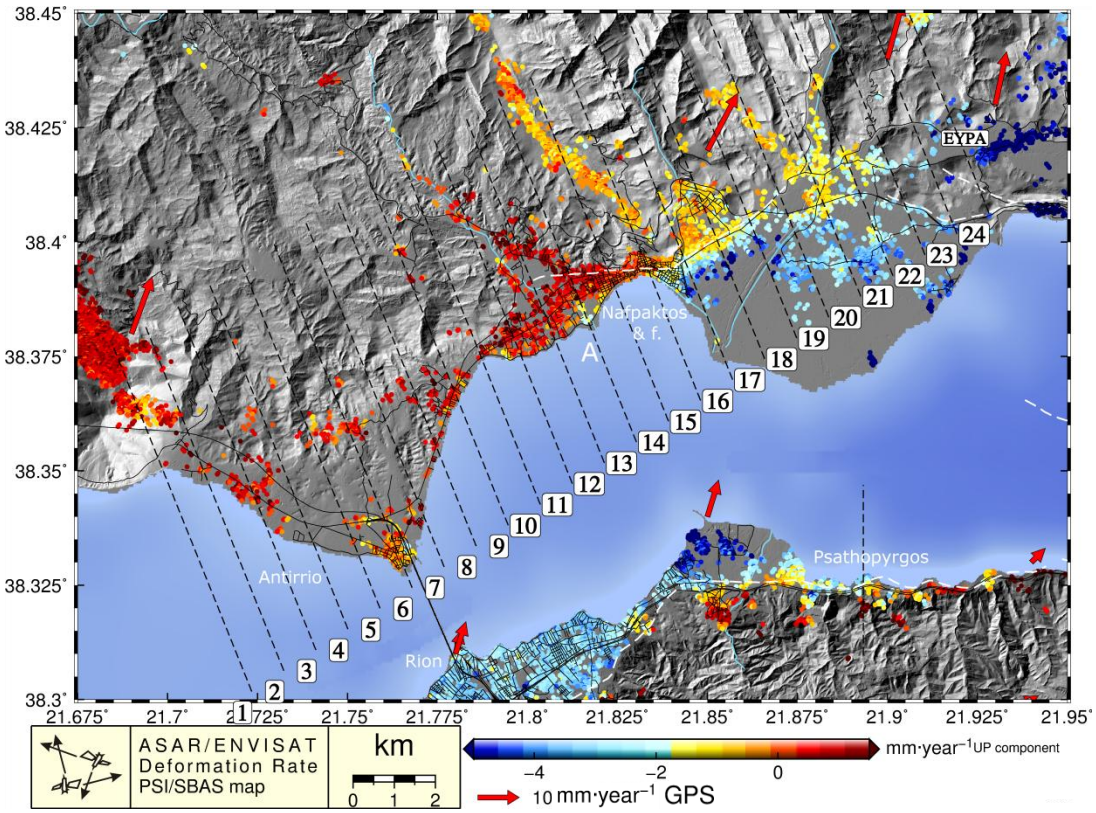

Figure 5-10. The PSI/SBAS UDc of the Nafpaktos fault and Delta of Mornos area. The cross section traces are marked with black dotted lines and its values are plotted in Figure 5-12. The traces of Nafpaktos and Rion-Patras faults are plotted in white dashed lines.

From Figure 5-10 we can detect a clear discontinuity along Nafpaktos fault, subsidence in the Delta and subsidence of Antirrio relative to its North as we can see in profiles no. 6 (Figure 5-12) of almost 1.5 mm year^{-1} but uplift relative to Rion. We can also spot a subsidence in Efpalio.

From Figure 5-13 we can detect small differentiation of EWc rate in the Delta and near Efpalio. As we will see later the areas of Efpalio and Monastiraki are contaminated with the deformation produced by the earthquakes of Efpalio 2010

Profiles no 12-16 (Figure 5-12) for Nafpaktos reveals a UDc discontinuity of almost ranging between 2 and -4 mm year^{-1}. In profile no 17 it is reaching -6 mm year^{-1} where it is the border for the Delta. In the EWc (Figure 5-14) we don't have clear discontinuities. The EWc ranging between 0 and 4 mm year^{-1}. Most of the Nafpaktos city is uplifting. In point '*A*' (Figure 5-10) there is a local subsidence. This could be the location of the continuation of the Nafpaktos fault and not as drawn passing by the South of Nafpaktos (close to point '*A*'), thus most of the extension of the city lies on the footwall.

In Figure 5-15 the coincidence of eastern part of Nafpaktos fault and the observed discontinuity in UDc is obvious. From Figure 5-15 and Figure 5-16, another features that we can discriminate is the deformation of Kastraki (-1.5 to -2.5 mm year^{-1} in UDc and ~1 in EWc), Malamata (-3 to -5 mm year^{-1} in UDc and ~1 in EWc), Managouli (-3 to -5 mm year^{-1} in UDc

and ~2 in EWc), Chiliadou (-3.5 to -5 mm year^{-1} in UDc and ~1 in EWc) , Monastiraki(-6 to -8 mm year^{-1} in UDc and ~0 in EWc), Efpalio (-5.5 to -7.5 mm year^{-1} in UDc and ~0 in EWc). Finally we can spot two areas near the SSE coast of the Delta at locations 'A' and 'B' where the deformation is reaching at -9 mm year^{-1} in UDc.

We can propose the existence of the mechanisms of the UDc (i.e. the Delta compaction due to old sediments, possible submarine landslides underneath and the effect of the faulting). As we can see in the cross sections 14 and 15 (passing by the Nafpaktos) the uplift is maximizing in the edge of the footwall in Nafpaktos but in its North and south is less. This is an indication of tectonics activity and in its South is the mixture of two mechanisms. We know that uplift is known to decrease with distance from a normal fault [Wend et al., 1989]. Similar cases with that of Psathopyrgos (§5.5) and Sellianitika (§5.4).

For the EWc (Figure 5-13) and the cross sections we can see that through the profiles 14-17 Nafpaktos is mitigating slightly earthwards relative to its North. Moreover from the map we can discriminate a differentiation in the EWc between Rio, Nafpaktos, Delta and hangingwall of RPfz (§4.2).

[Parcharidis et al., 2013] have used 42 AMI/ERS1&2 covering the time period 1992–2001 and 29 ASAR/ENVISAT acquisitions covering the time period 2002–2009 of descending track 279 and the IPTA PS methodology to extract deformation rates in the Delta of Mornos. The Authors' observations are along the descending LOS direction towards satellite, they are referenced to a point which our UDc value is ~1 mm year^{-1} and are shown in Figure 5-11.

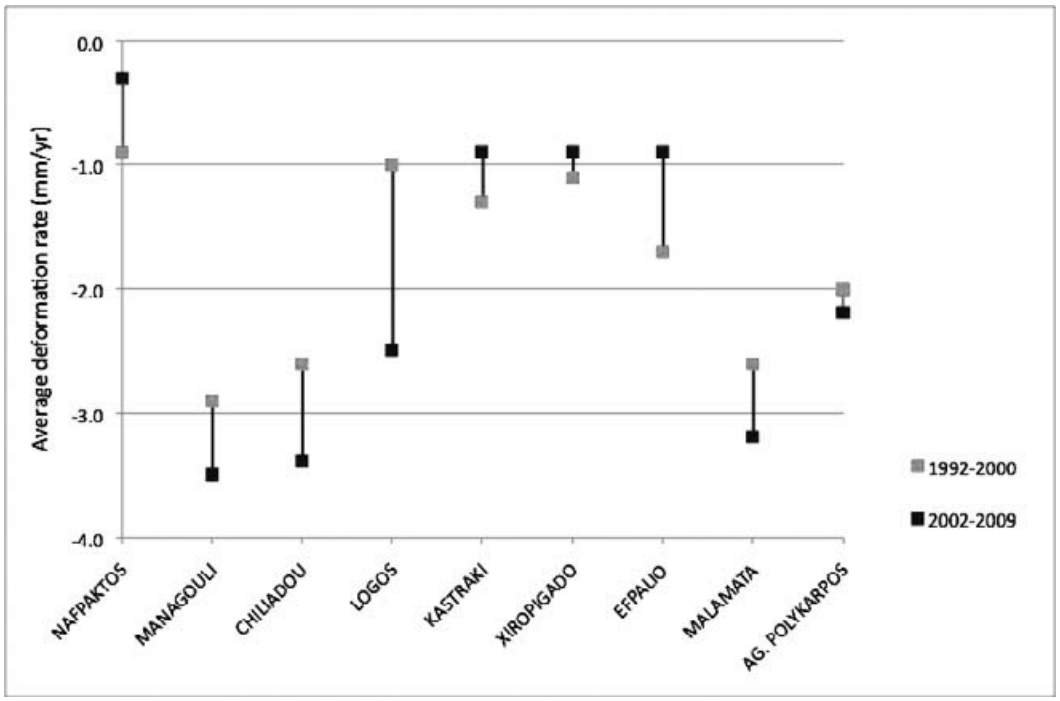

Figure 5-11. Courtesy of [Parcharidis et al., 2013], average deformation rate for each village located in the Mornos delta covering the time span between 1992 and 2009.

Concerning the Authors' reference point their observations have been shifted at -1 mm year^{-1} and are shown with our observation in UDc in Table 13.

Location	[Parcharidis et al., 2013] average descending LOS rate away satellite, shifted during 2002-2009 (mm year^{-1})	Present study average UDc rate During 2002-2010 (mm year^{-1})
Nafpaktos	-1	-1
Managouli	-4.5	-4.5
Chiliadou	-4.5	-4
Kastraki	-2	-2
Efpalio	-2	-6.5
Malamata	-4	-4

Table 13. comparison between our observations and [Parcharidis et al., 2013] ones, which have been shifted at -1 mm year^{-1}.

The two datasets are in good accordance. To be noted that Authors' observations are in the descending LOS direction away satellite that even in many cases its values are close to the UDc, when there is EWc this approximation is relaxing. In the case of Efpalio we have a discrepancy. In our datasets the date of the earthquakes of Efpalio (18/1/10 and 22/1/10) are included. The rest of the small discrepancies are due to the additional process we have performed after the original PSI/SBAS rate values.

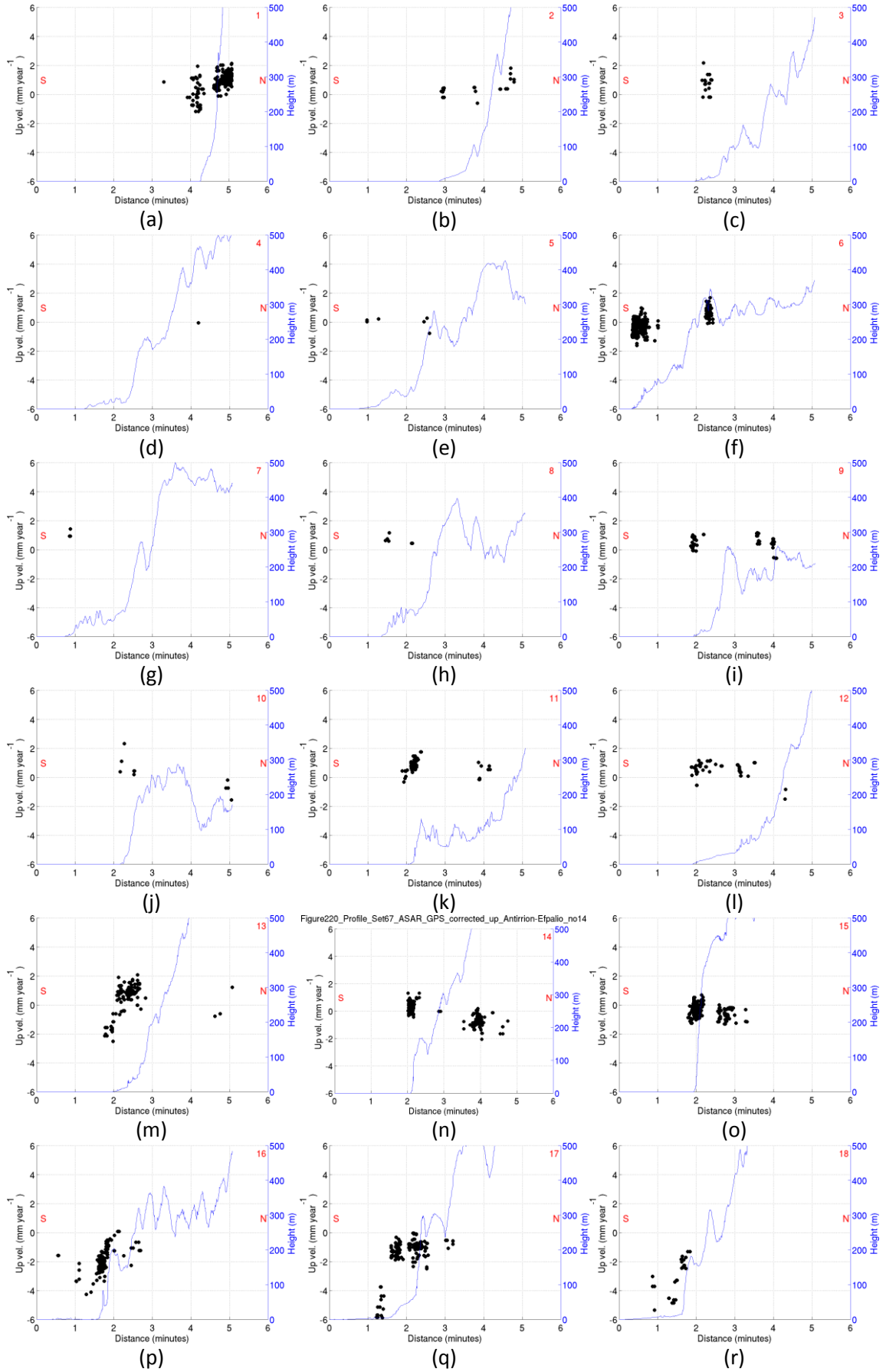
Figure220_Profile_Set67_ASAR_GPS_corrected_up_Antirrion-Efpalio_no14
Up vel. (mm year -1)
Height (m)
Distance (minutes)
S
N
(a)
(b)
(c)
(d)
(e)
(f)
(g)
(h)
(i)
(j)
(k)
(l)
(m)
(n)
(o)
(p)
(q)
(r)

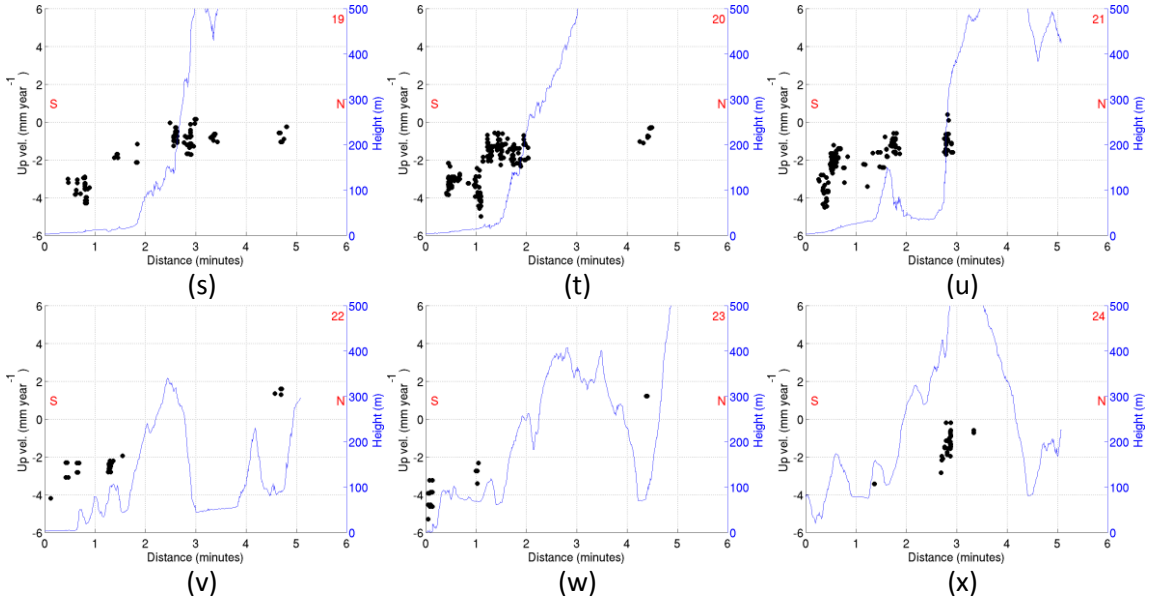

Figure 5-12. Cross sections no 1-24 (Figure 5-10) of the UDc of the Nafpaktos and Delta of Mornos area.

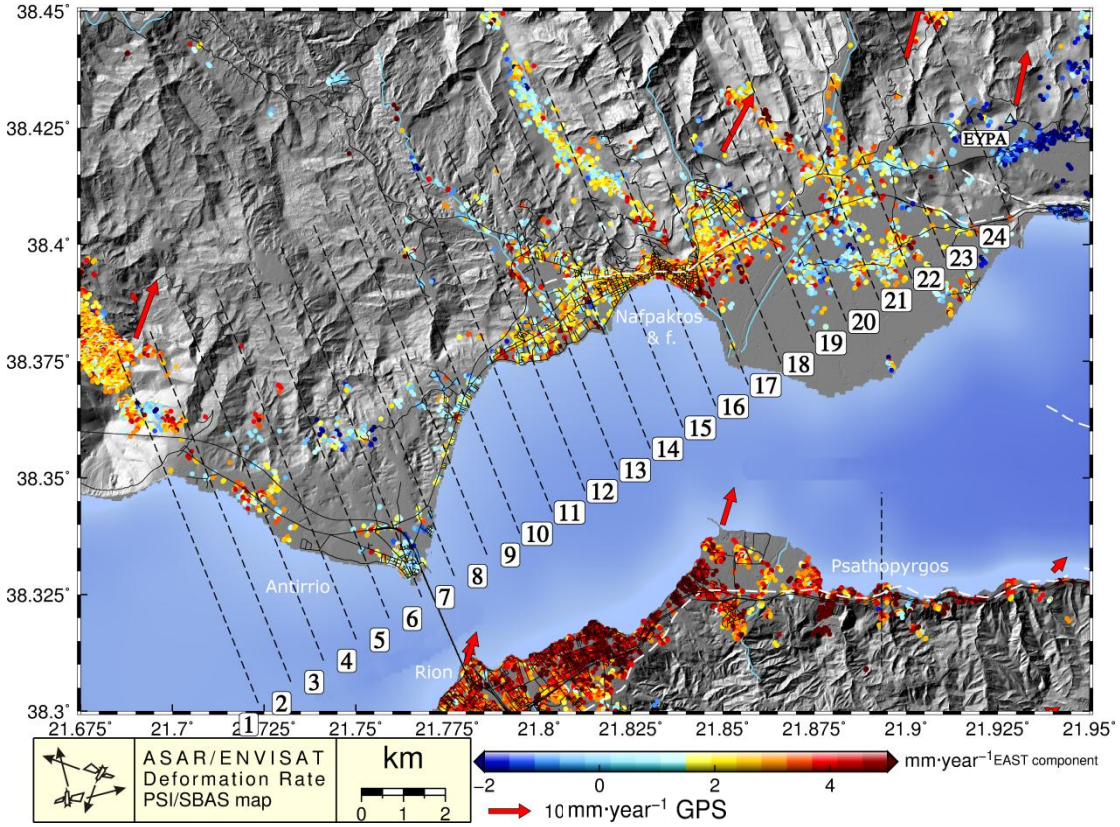

Figure 5-13. The PSI/SBAS EWc of the Nafpaktos fault and Delta of Mornos area. The cross section traces are marked with black dotted lines and its values are plotted in Figure 5-14. The traces of Nafpaktos and Rion-Patras faults are plotted with white dashed lines.

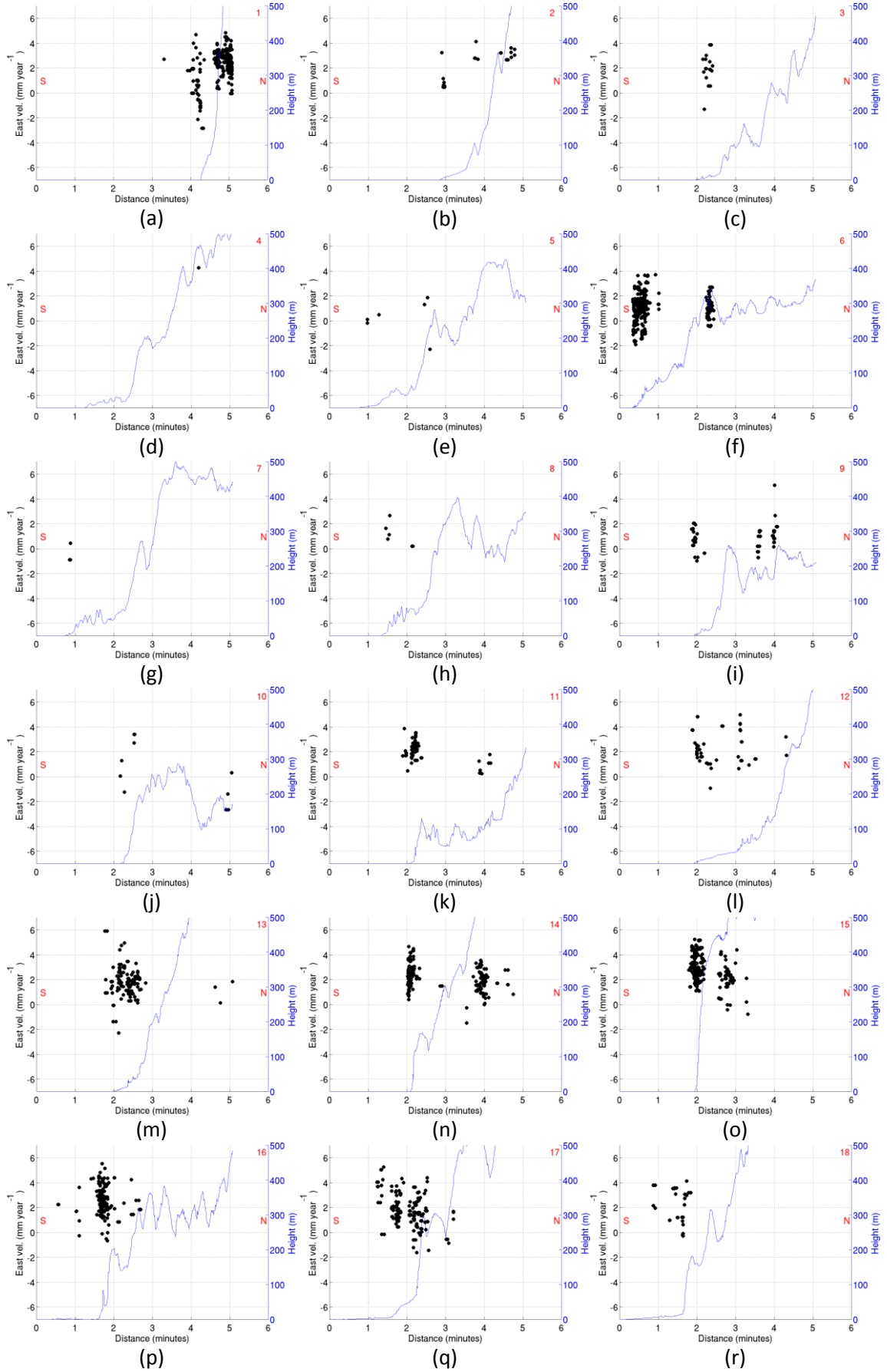
East vel. (mm year⁻¹)
Height (m)
Distance (minutes)
S
N
(a)
(b)
(c)
(d)
(e)
(f)
(g)
(h)
(i)
(j)
(k)
(l)
(m)
(n)
(o)
(p)
(q)
(r)

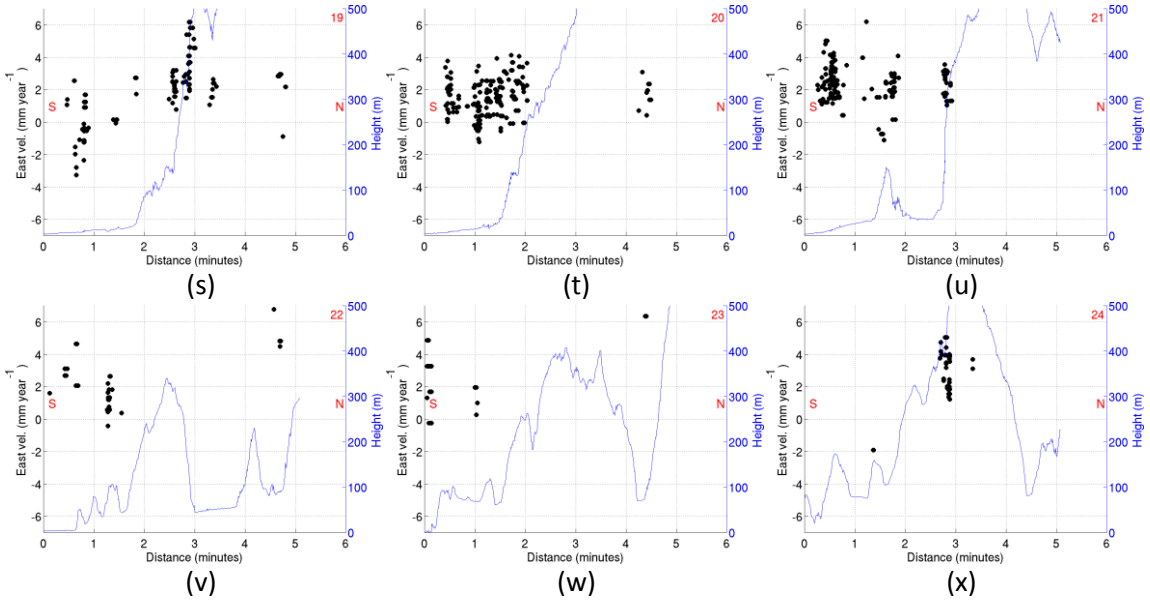

Figure 5-14. Cross sections no 1-24 (Figure 5-13) of the EWc of the Nafpaktos and Mornos area.

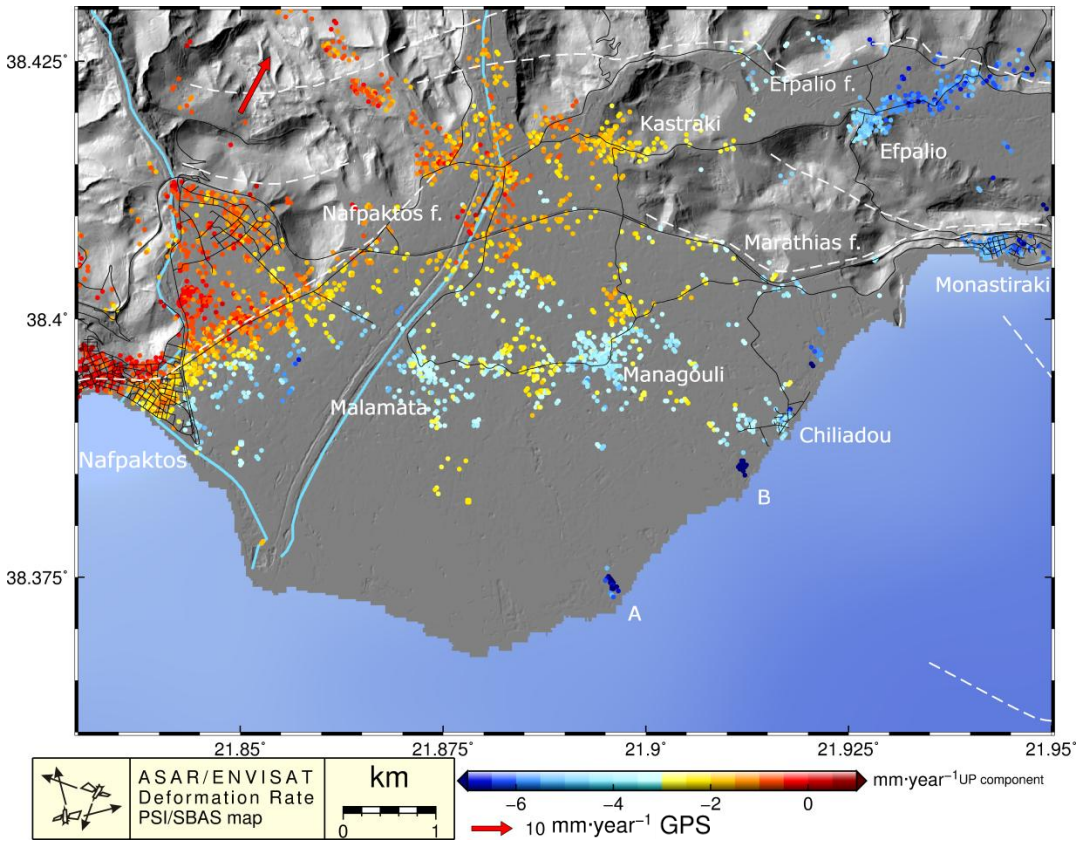

Figure 5-15. Focus on Delta of Mornos for the UDc. The fault traces of Nafpaktos, Efpalio, Marathias are plotted in white dashed lines.

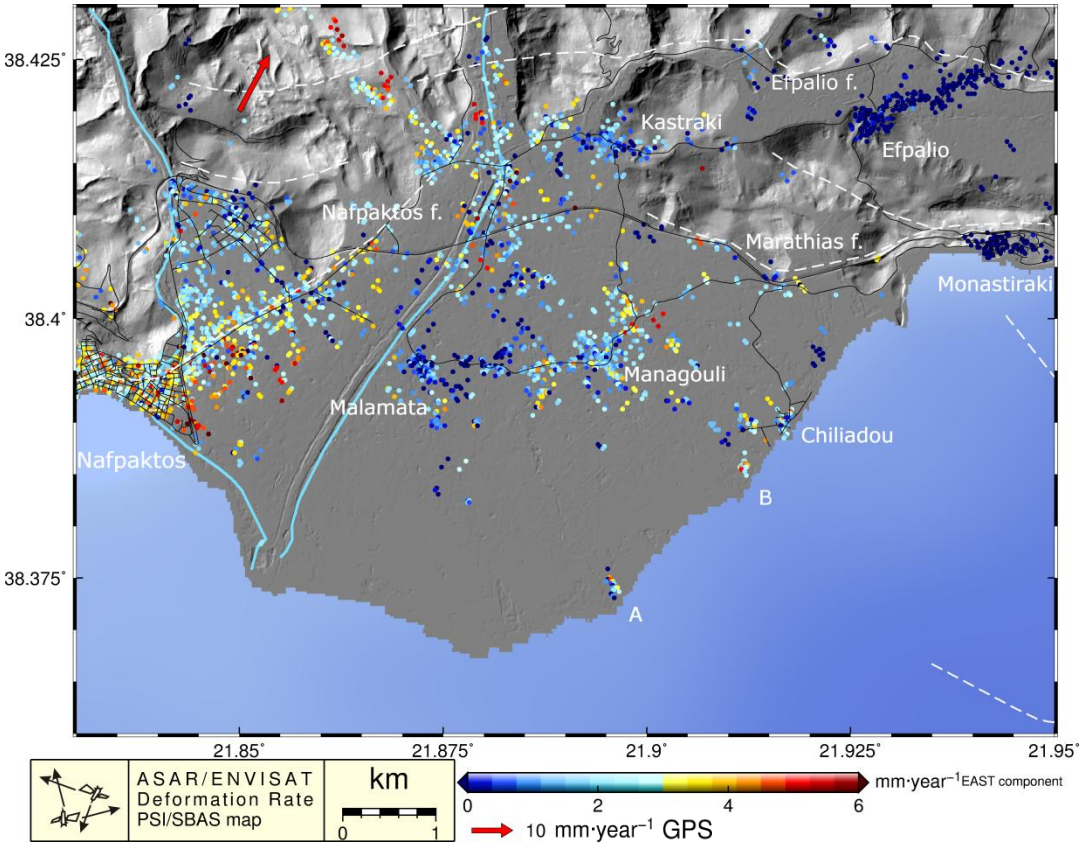

Figure 5-16 Focus on Delta of Mornos for the EWc. The fault traces of Nafpaktos, Efpalio, Marathias are plotted in white dashed lines.

5.3. Akrata Delta – Krathis fault – Landslide or Platanos

In Figure 5-17we can discriminate the block having similar UDc of Platanos/Paralia Platanou (ranging between -4.5 and -2.5 mm year^{-1}), Trazepa (-2 to 0 mm year^{-1}), Akrata/Siliveniotika(-5 to -3.5 mm year^{-1}), Paralia Akratas (south -5 to -4 mm year^{-1}, North -6 to -5 mm year^{-1}) and Delta (South -7.5 mm year^{-1} to -6.5 mm year^{-1}, North -7 mm year^{-1} to -5.5 mm year^{-1}).

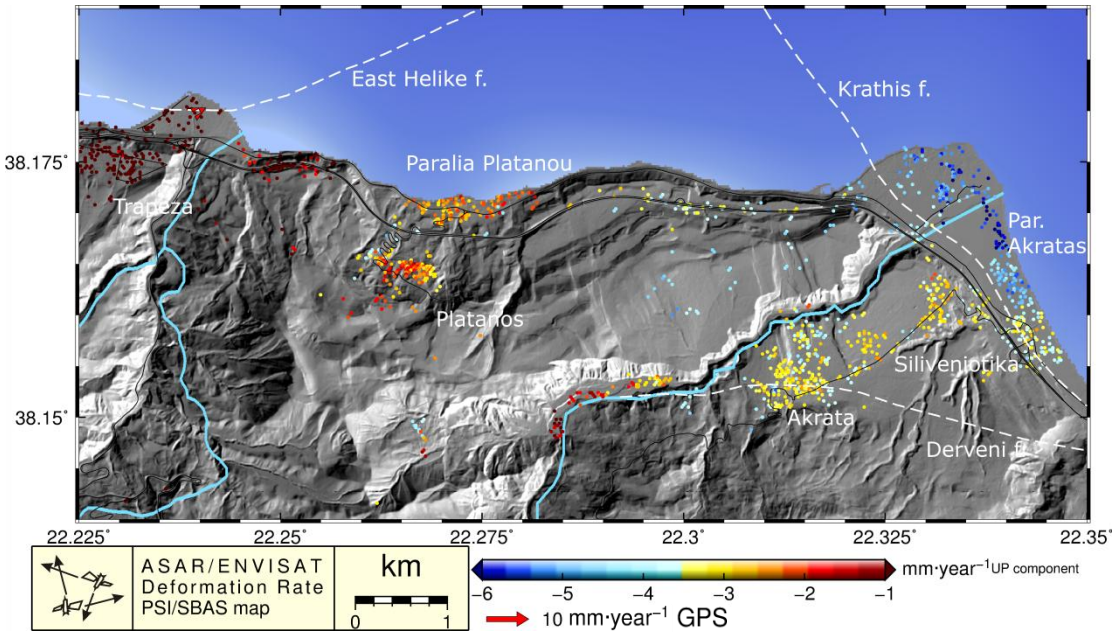

Figure 5-17. The PSI/SBAS UDc of the Platanos, Krathis fault and Delta of Aktata area. The traces of East Helike Krathis and Derveni faults are plotted with white dashed lines.

In Figure 5-18 the main blocks is the Platatos/Paralia Platanou. This block is landsliding. Its slope in oriented to NNE, It is the only concrete block moving Eastwords.

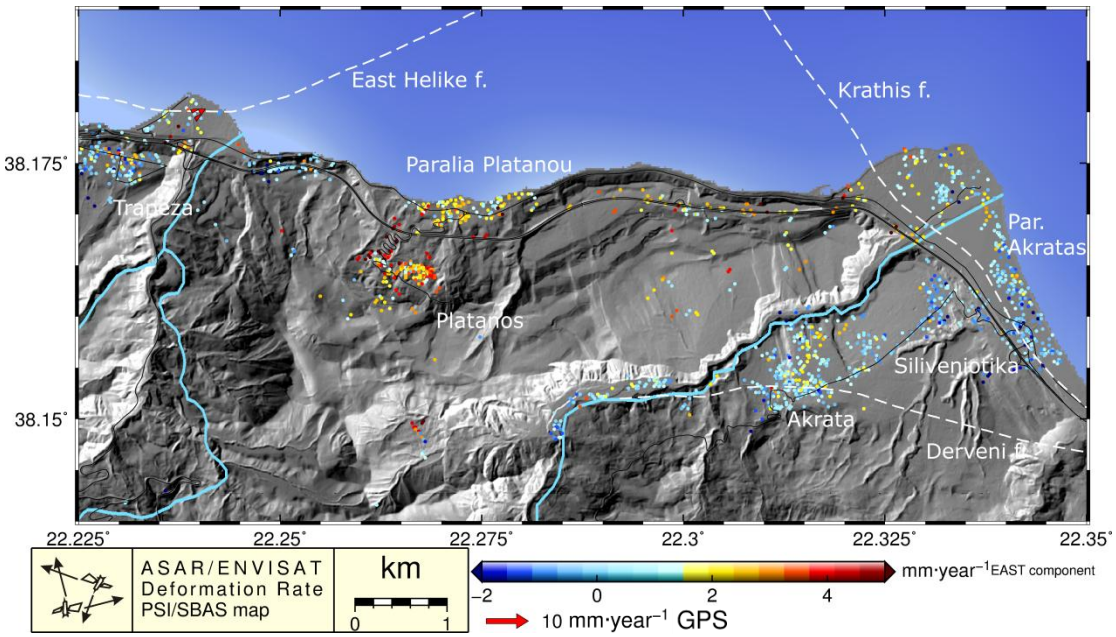

Figure 5-18. The PSI/SBAS EWc of the Platanos, Krathis fault and Delta of Akrata area. The traces of East Helike Krathis and Derveni faults are plotted with white dashed lines.

In Figure 5-19 and Figure 5-20 the same areas but in the LOS direction of descending and ascending track are shown respectively. We detect that in the area of Kalamias there are quite a few PSs in the descending but a big volume exists in the ascending track. In Figure 5-17 and Figure 5-18 only a few UDc and EWc PSs exist because our processing using simultaneously the PSs from both tracks. In LOS we can detect a discontinuity in Kalamias village which may be caused by a landslide.

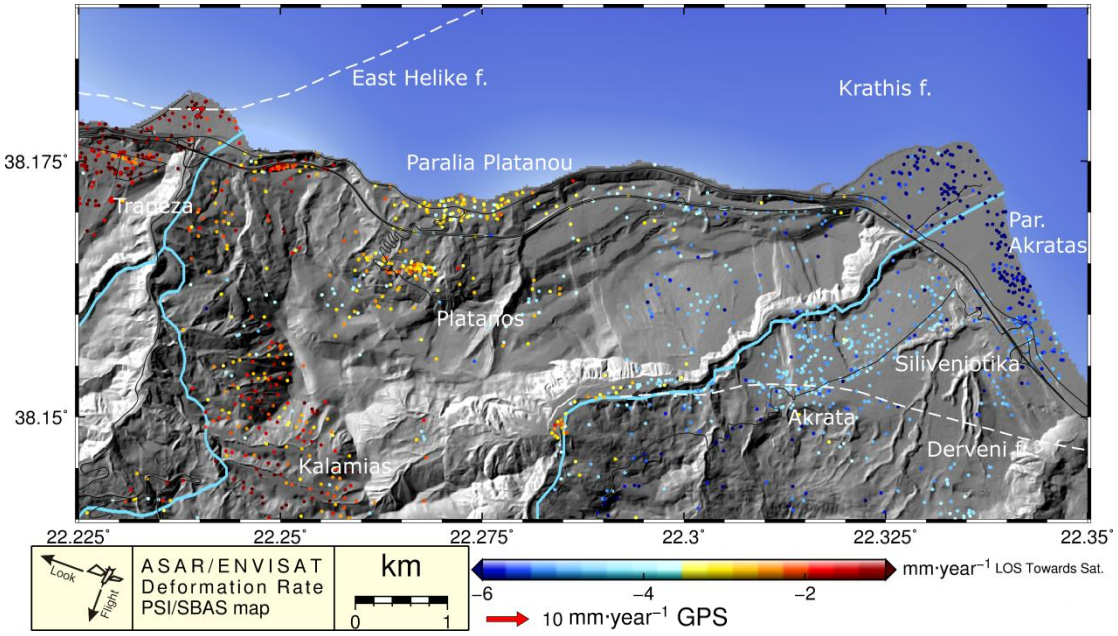

Figure 5-19. The descending PSI/SBAS of the Platanos, Krathis fault and Delta of Akrata area.

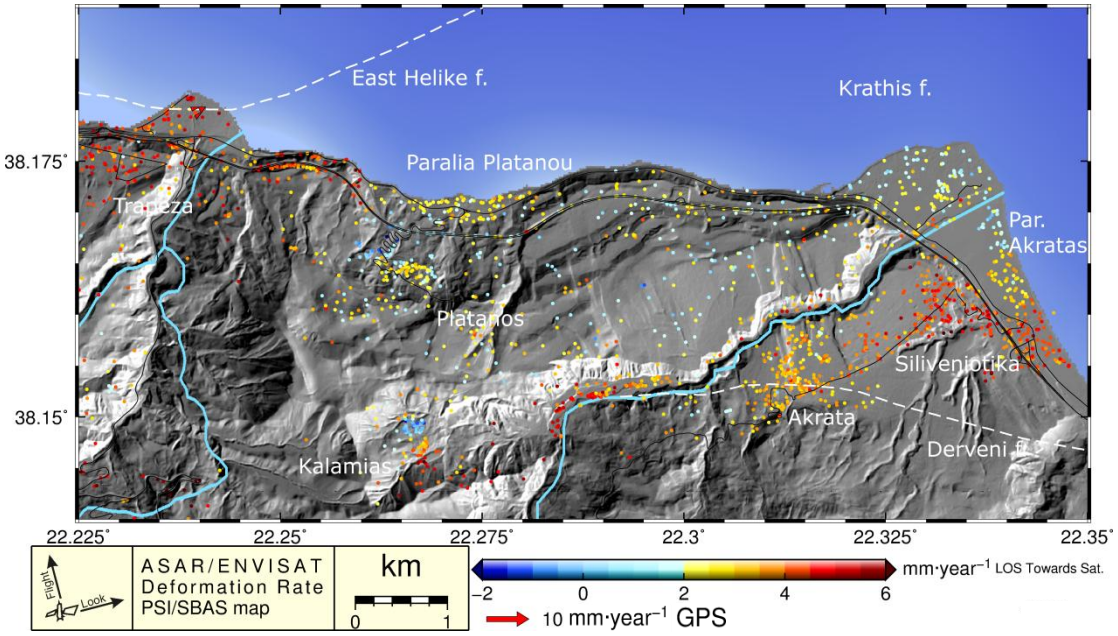

Figure 5-20. The ascending PSI/SBAS of the Platanos, Krathis fault and Delta of Akrata area.

5.4. Sellianitika and Rothodafni Delta

In Figure 5-21 the subsidence of Delta is obvious. In the cross section 3-6 of the UDc (Figure 5-22) Sellianitika fault we can see the gradient of the subsidence. It reaches 7 mm year^{-1} per distance of a minute (~1.9 km). Thus the Delta is tilting. In no. 5 we can see a small uplift before the subsidence. This bend is in the location of the Sellianitika fault. We can see this feature in no. 6 but we can't see it in no. 4. This seems the case of deformation due to two components: the fault and the Delta subsidence, similar case with the Deltas of Mornos (§5.2) and Psathopyrgos (§5.5).

We can also discriminate a subsidence to the Rothodafni Delta ranging between -1 to 2 mm year^{-1}.

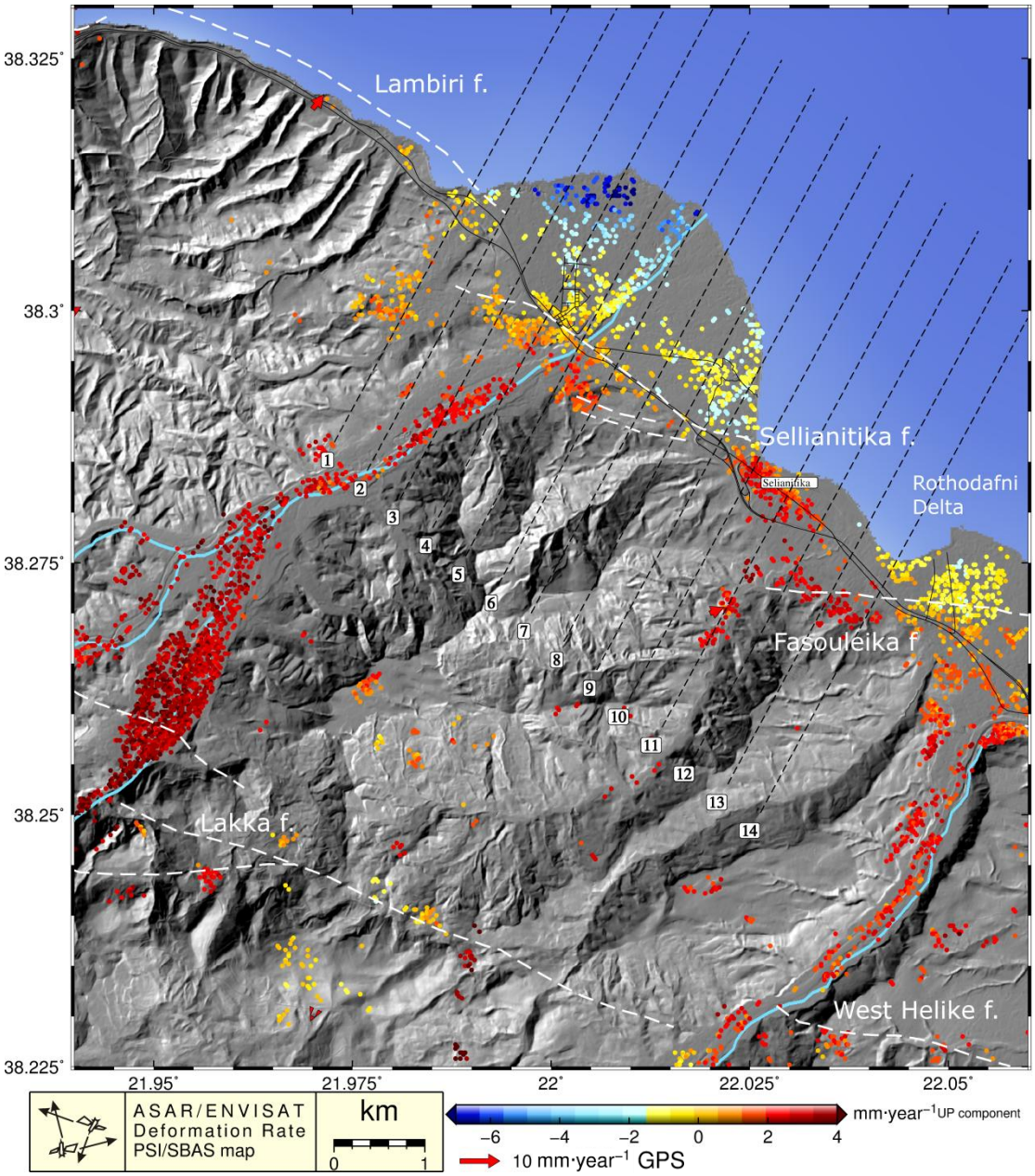

Figure 5-21. The PSI/SBAS UDc of the Sellianitika fault and its Delta area. The cross section traces are marked with black dotted lines and its values are plotted in Figure 5-22. The fault traces of West Helike, Lakka, Lambiri, Sellianitika and Fasouleika are plotted with white dashed lines.

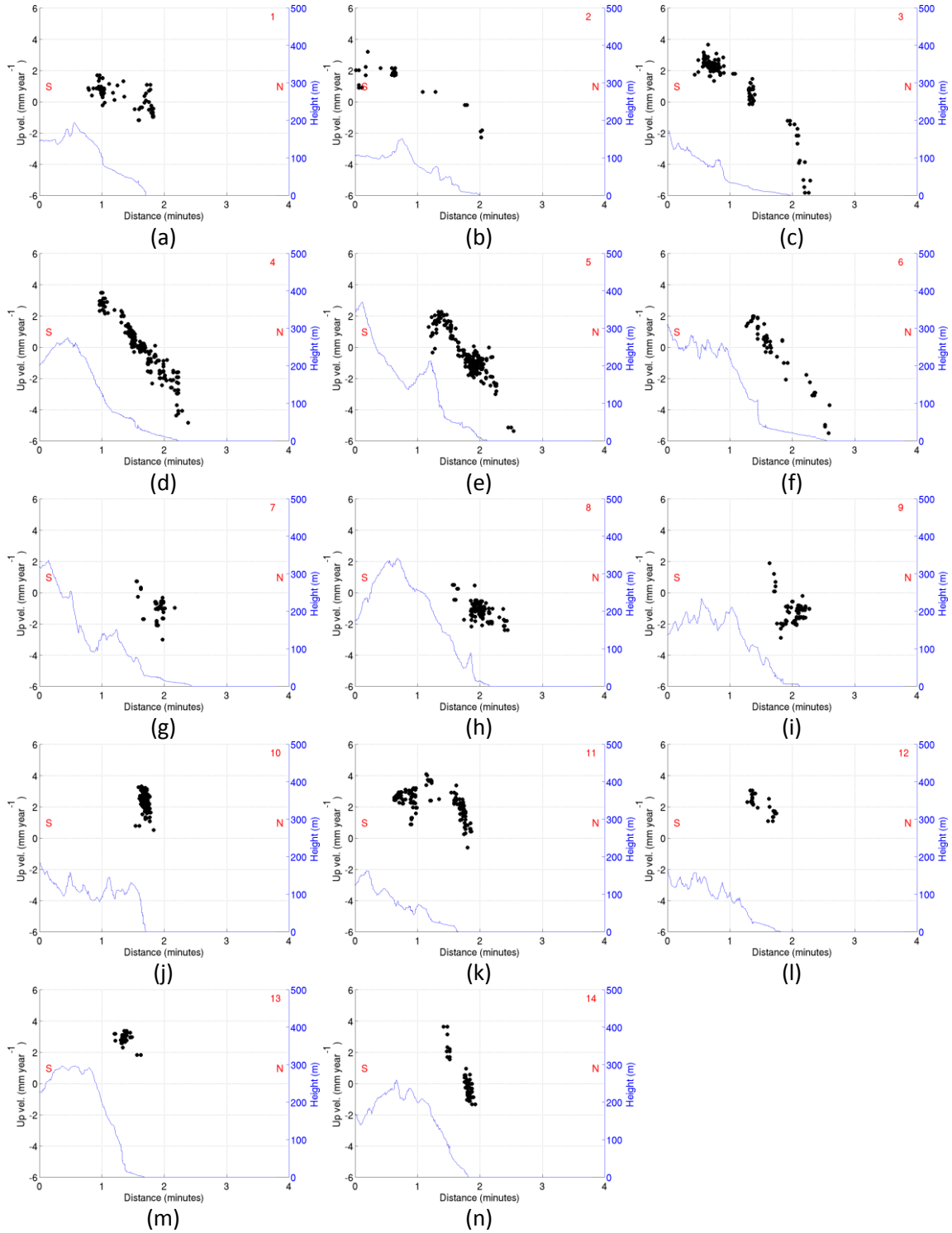

Figure 5-22. Cross sections no 1-14 (Figure 5-21) of the UDc of the Sellianitika area.

In Figure 5-23 we can discriminate a slope of the EWc in the Delta from cross sections no 3-6 (Figure 5-24). A higher EWc in Rothodafni Delta can also be seen.

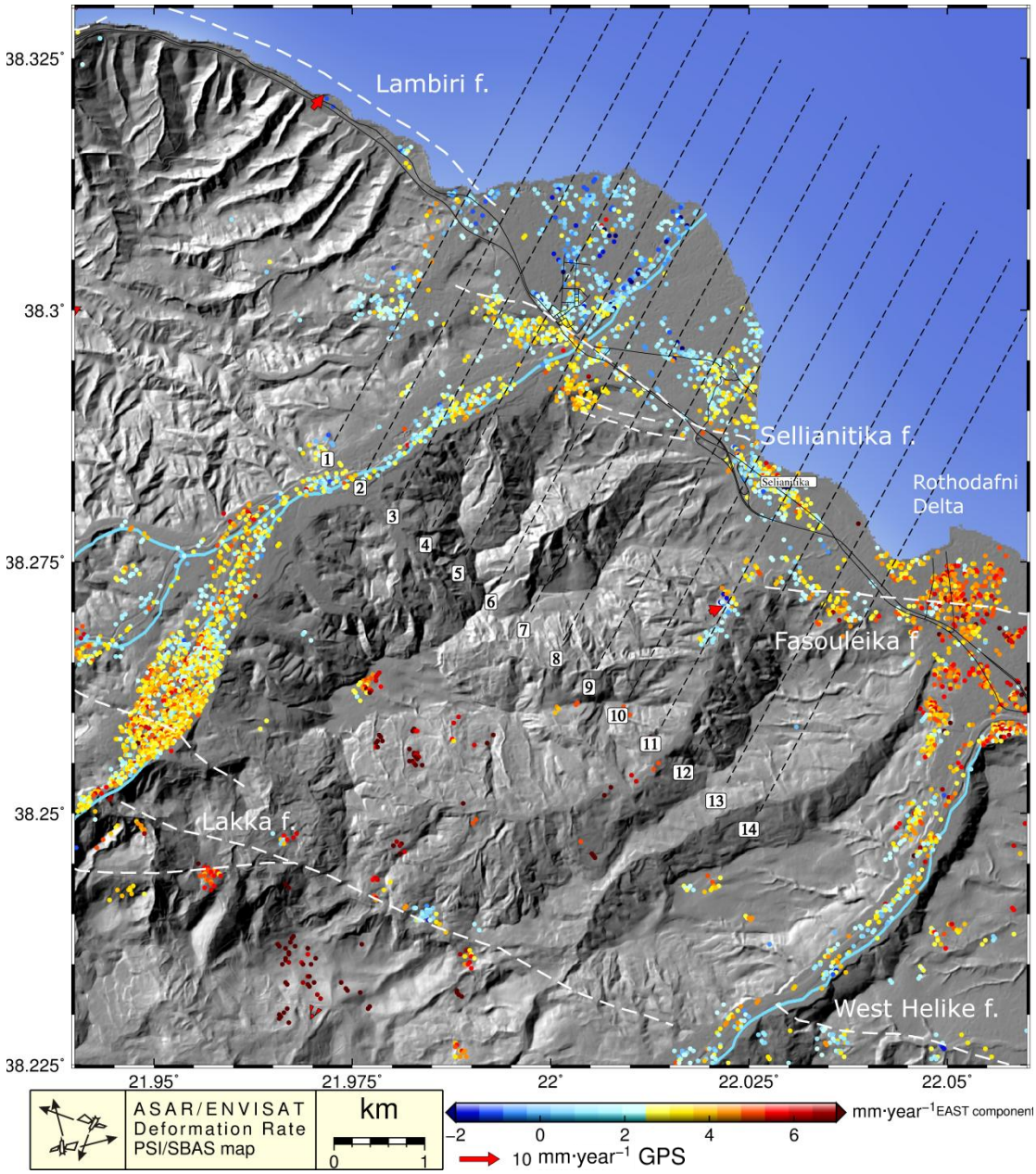

Figure 5-23. The PSI/SBAS EWc of the Sellianitika fault and its Delta area. The cross section traces are marked with black dotted lines and its values are plotted in Figure 5-24. The fault traces of West Helike, Lakka, Lambiri, Sellianitika and Fasouleika are plotted with white dashed lines.

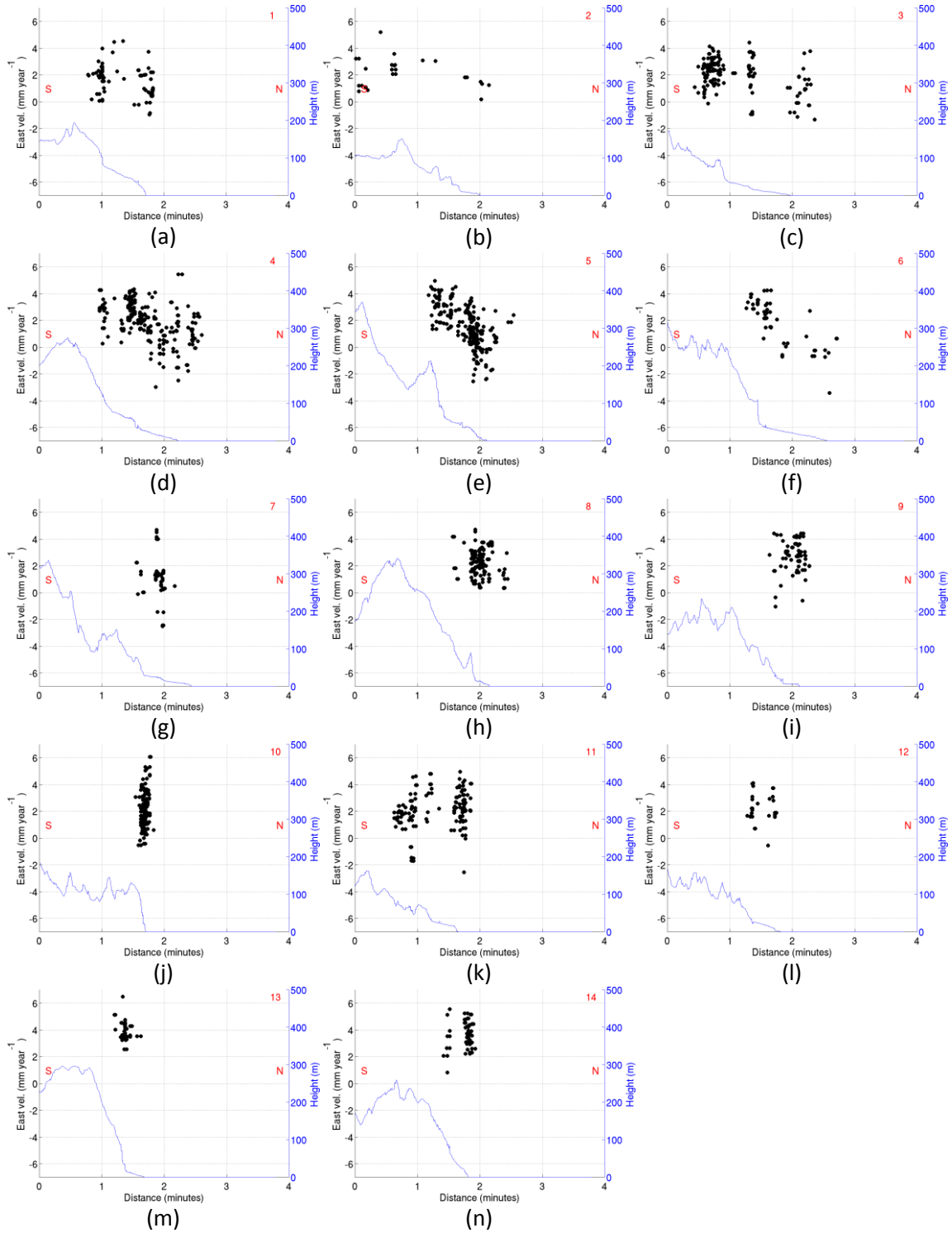

Figure 5-24. Cross sections no 1-14 (Figure 5-23) of the EWc of the Sellianitika area.

5.5. Psathopyrgos Delta and fault

In Figure 5-25 as well as in the cross-sections of Figure 5-26 we can discriminate the gradient of Delta due to its compaction. In cross section no 3 we can see an uplift and then a sudden downlift in the location where the Psathopyrgos fault is drawn. Thus the observed downlift seems to be the result of two components: the fault and the Delta subsidence. This looks similar to the cause of Sellianitika fault (Figure 5-21). We also spotted some discontinuities in Kato Arahovitika. More discontinuities observed in South of Psathopyrgos and in the two small Deltas at Kato Rodini. All these seem to be deformed due to the same two components.

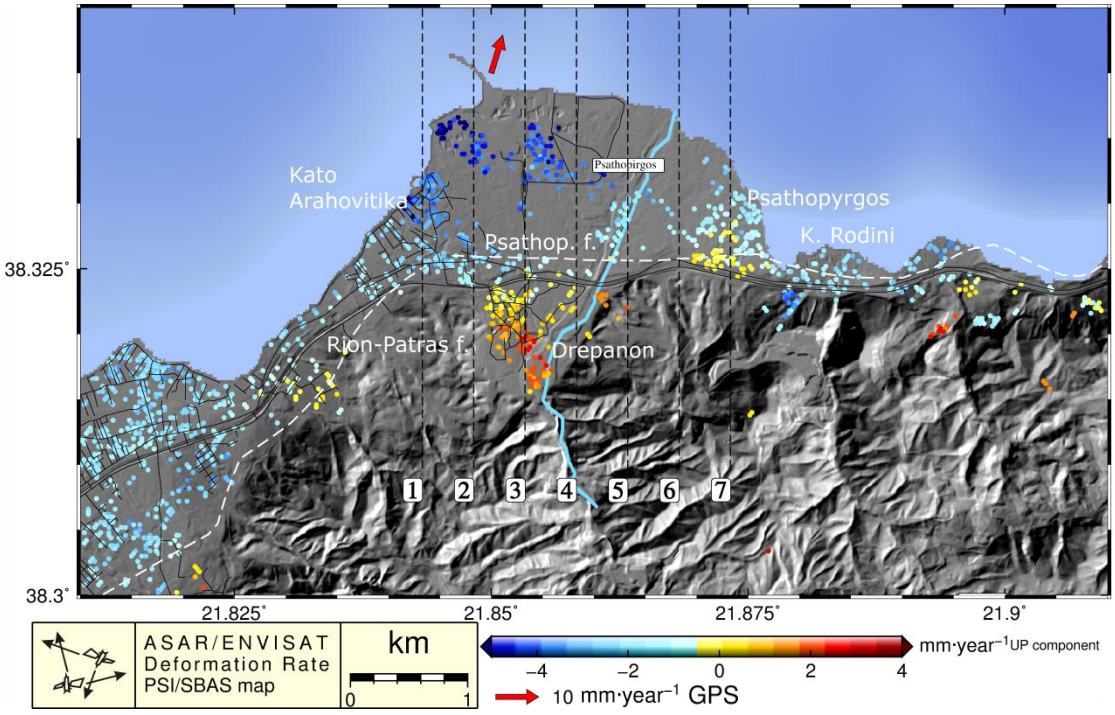

Figure 5-25. The PSI/SBAS UDc of the Psathopyrgos Delta area. The cross section traces are marked with black dotted lines and its values are plotted in Figure 5-26. The fault traces of RPF and Psathopyrgos faults are marked with dashed white lines.

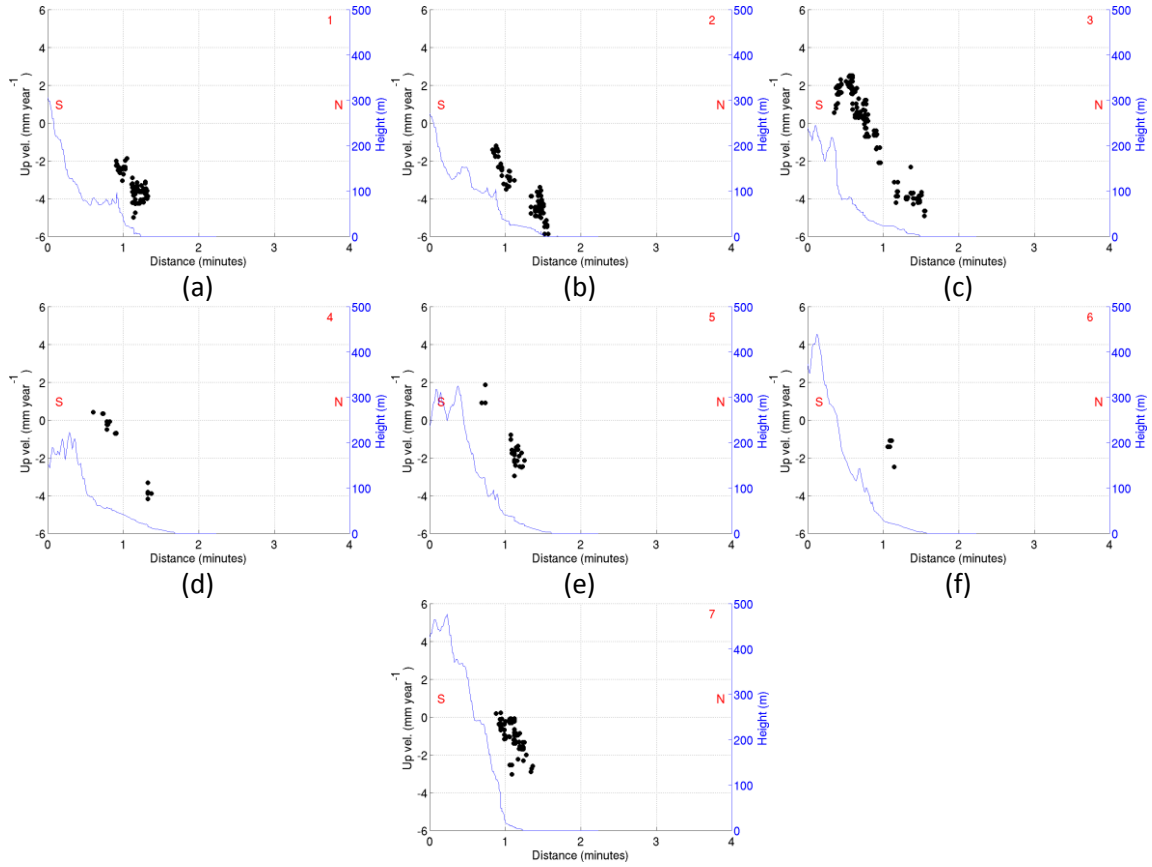

Figure 5-26. Cross sections no 1-7 (Figure 5-25) of the UDc of the Psathopyrgos Delta area.

In Figure 5-27 we can see the EWc of the Psathopyrgos Delta area. We can discriminate some discontinuities within the city of Psathopyrgos and around Delta. Moreover South of K. Rodini (South of the highway) we can discriminate a patch with different rate than the village itself. Actually the misfitting of the faults (plotted in dashed white lines) is obvious in many places including the present one. In Figure 5-28 we can see the cross-sections of the same area. In the profiles no. 2 and 3 we can observe a change of the sign of the deformation rate gradient.

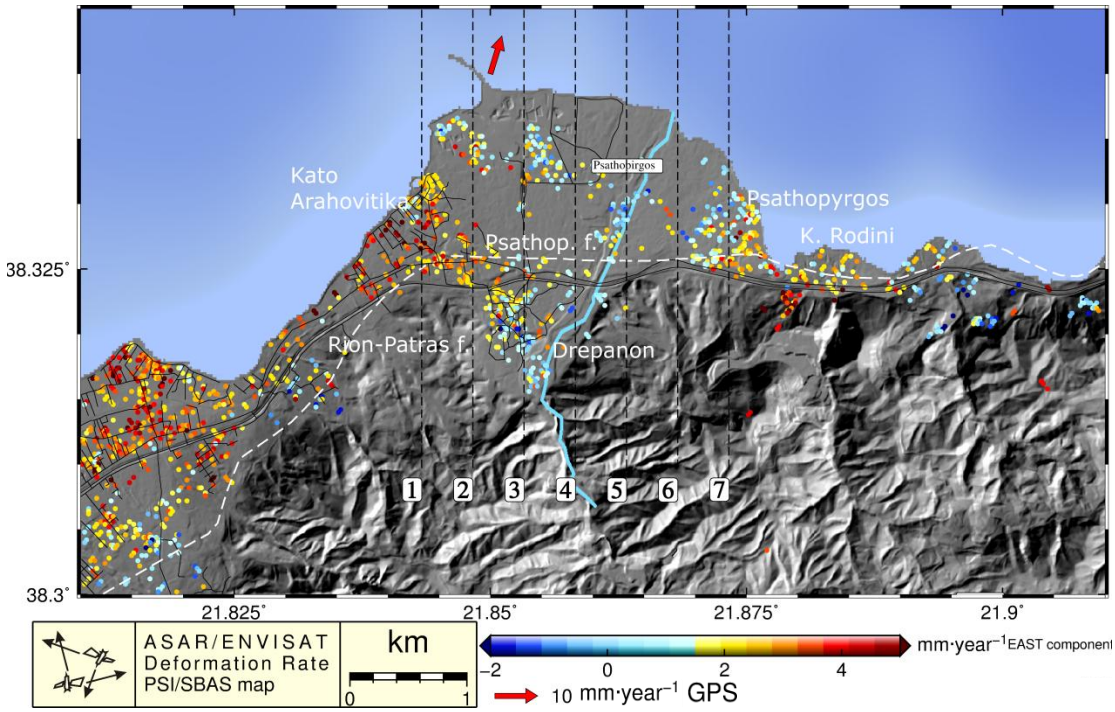

Figure 5-27. The PSI/SBAS EWc of the Psathopyrgos Delta area. The cross section traces are marked with black dotted lines and its values are plotted in Figure 5-28.The fault traces of RPF and Psathopyrgos faults are marked with dashed white lines.

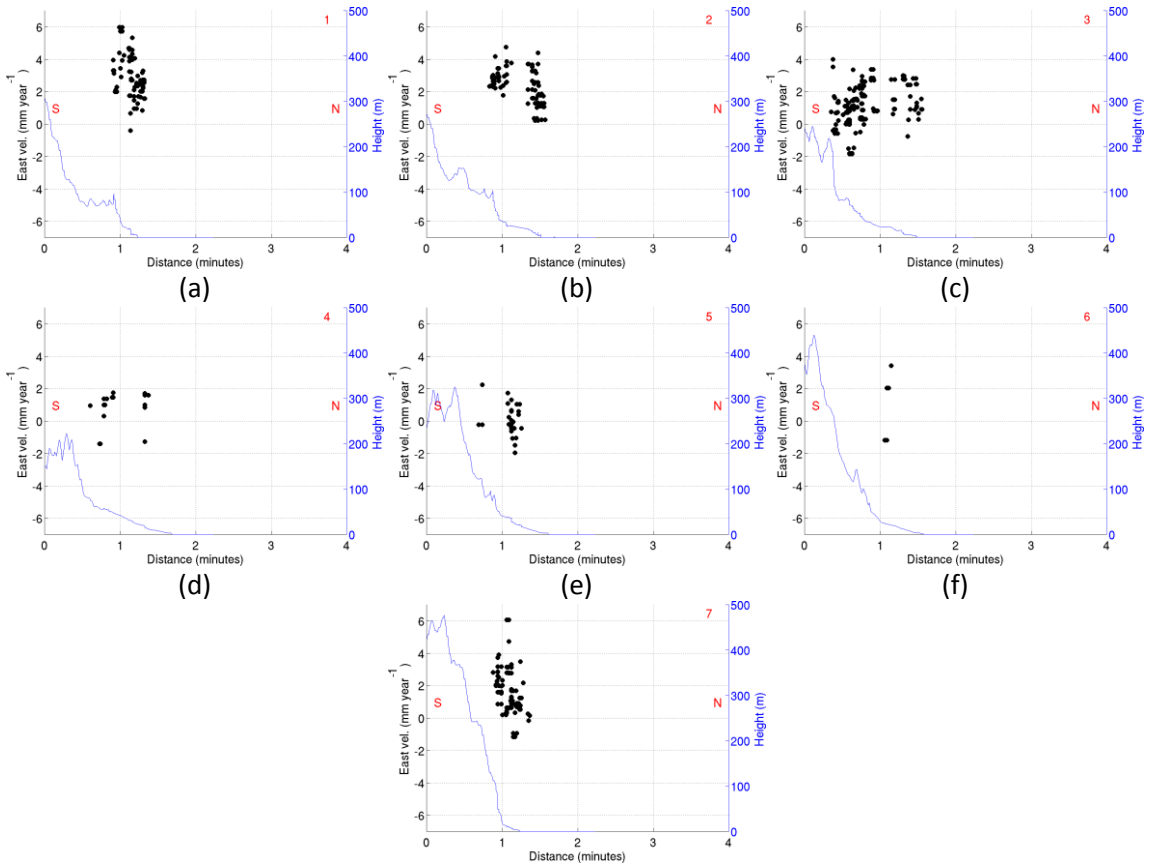

Figure 5-28. Cross sections no 1-7 (Figure 5-27) of the EWc of the Psathopyrgos Delta area.

In Figure 5-29 we can see the continuation of the Psathopyrgos fault, east of Figure 5-25. The density of PS point is not enough to discriminate the limits of Psathopyrgos fault. LOS maps will be also presented for the investigation on Panagopoula landslide in §5.8.3.

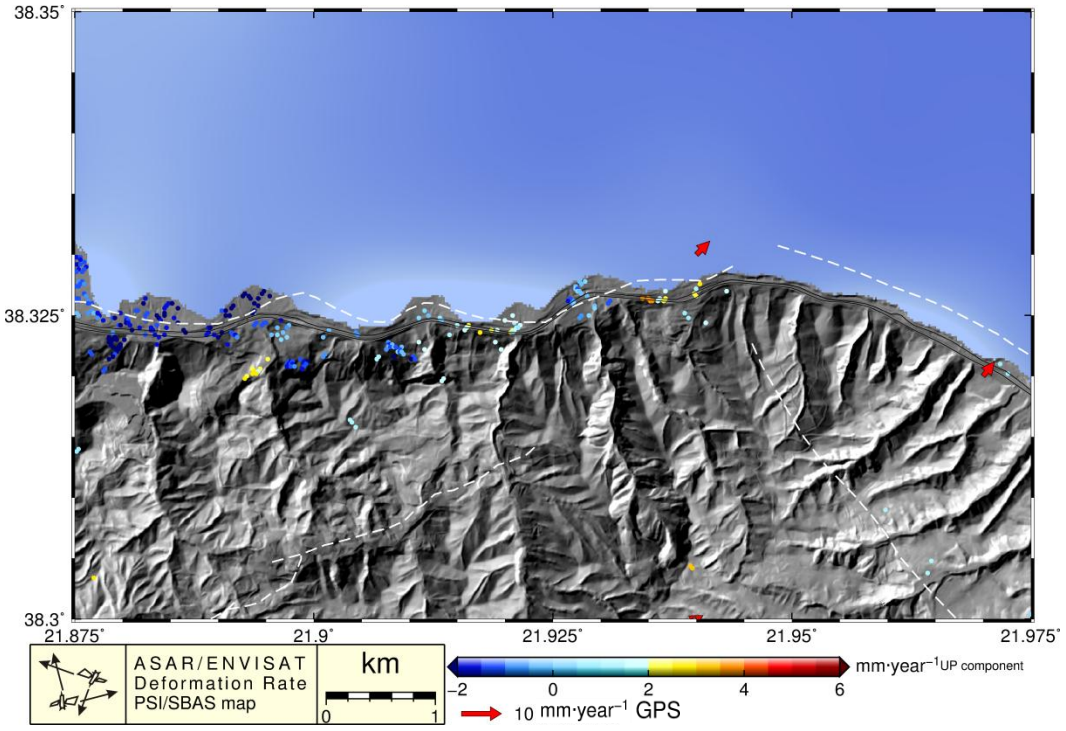

Figure 5-29. The PSI/SBAS UDc of the Psathopyrgos Fault, east of Figure 5-25.

5.6. Efpalio – Marathias

In Figure 5-30 first of all we have to indicate that the high value of subsidence of the Efpalio and Monastiraki is due to the Efpalio 2010 Earthquake (§0). We can clearly observe the subsiding of Marathias Delta and the rest of the coastal areas.

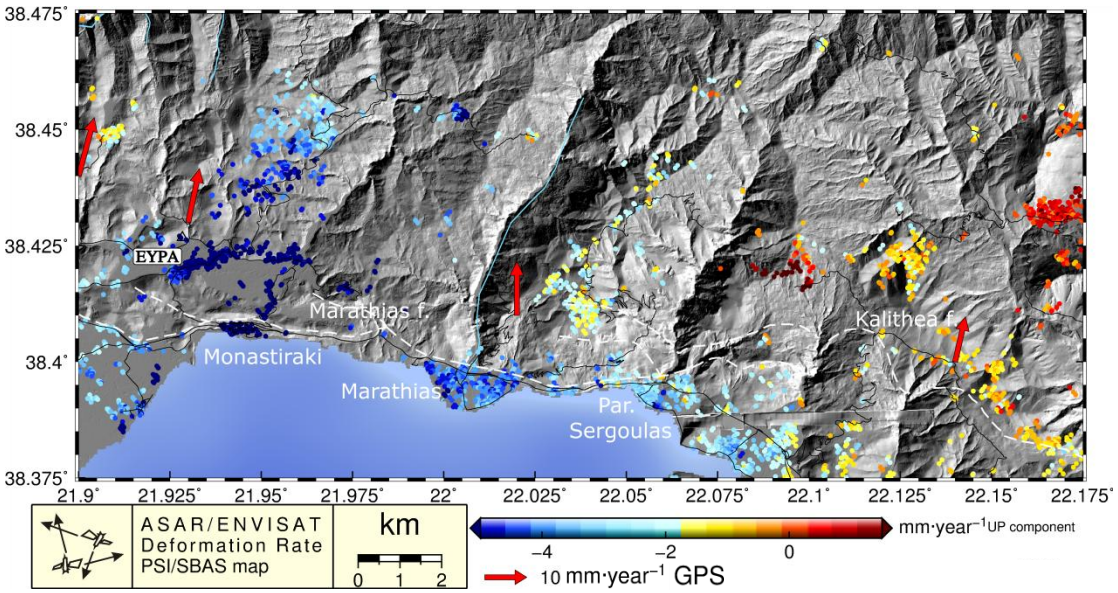

Figure 5-30. The PSI/SBAS UDc of the Efpalio-Marathias Delta area. The fault traces of RPF Marathias and Kalithea are marked with dashed white lines.

In Figure 5-31 we can see again the effect of the Efpalio earthquake (§0) and some discontinuities in the Marathias Delta.

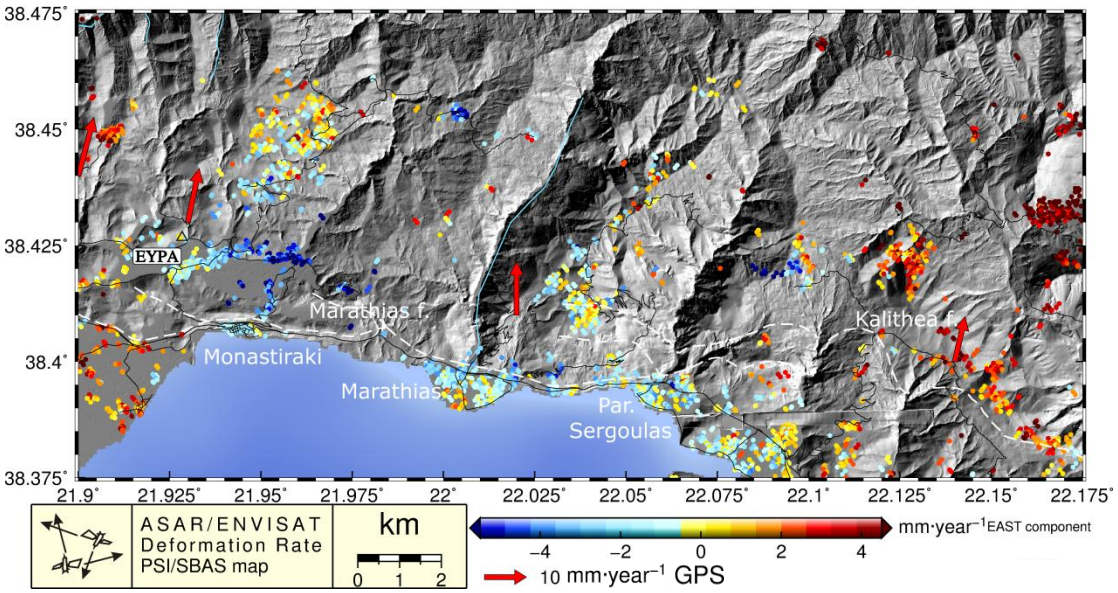

Figure 5-31. The PSI/SBAS EWc of the Efpalio-Marathias Delta area. The fault traces of RPF Marathias and Kalithea are marked with dashed white lines.

5.7. Trizonia – Psaromita

In Figure 5-32 we can discriminate a subsidence slope in Trizonia ranging between -1 to -3 mm year^{-1} at the direction NW, with Psaromita value to be almost 0.5 mm year^{-1}. We calculated the inclination of the Trizonia island, along the line A-A', where part A uplifting compared with the A' part, to be ~1 μrad year^{-1}.

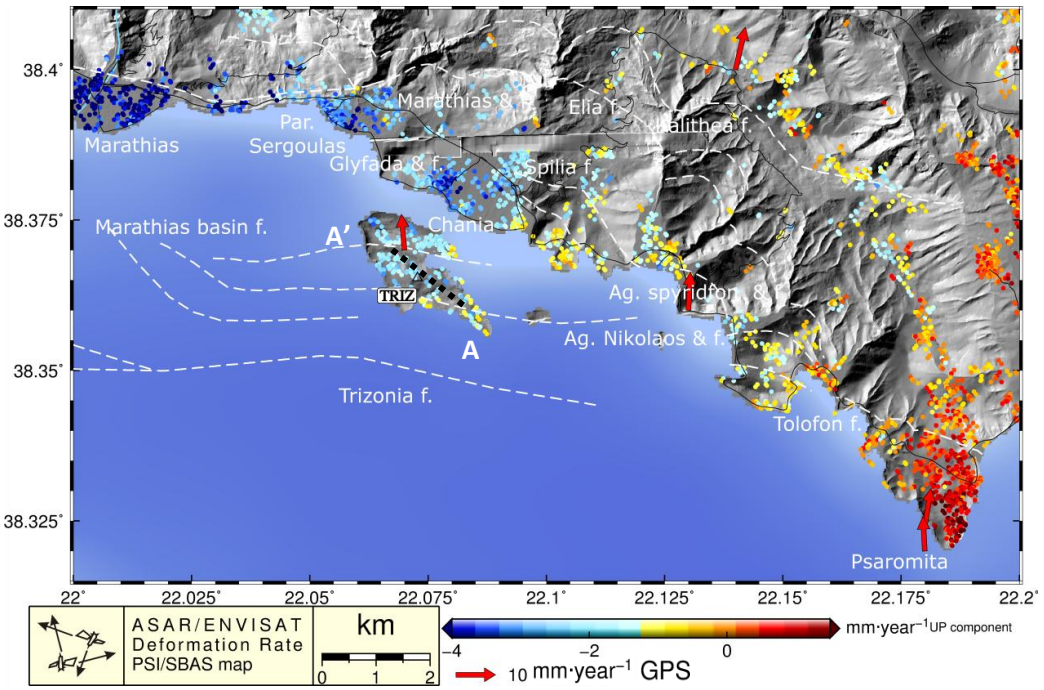

Figure 5-32. The PSI/SBAS UDc of the Trizonia and Psaromita area. A number of fault traces are marked with dashed white lines.

In Figure 5-33 we can discriminate a localized discontinuity inside Chania village in the EWc.

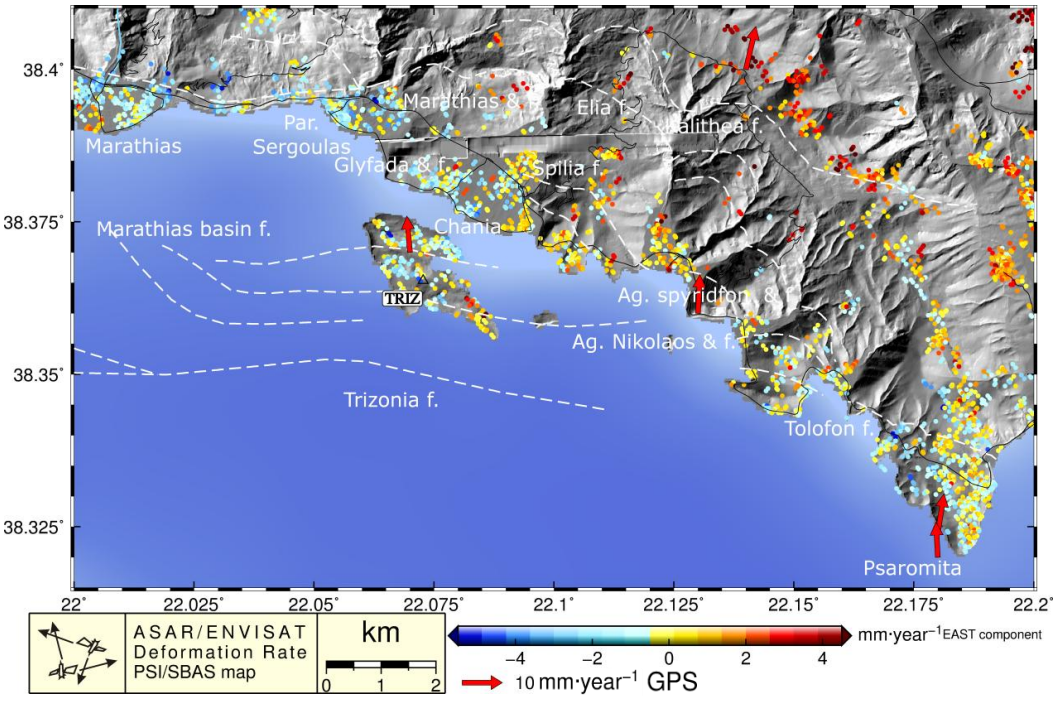

Figure 5-33. The PSI/SBAS EWc of the Trizonia and Psaromita area. A number of fault traces are marked with dashed white lines.

5.8. Landslides

Some Landslides was visible even if they were limited to a small spatial extent. Very high resolution data and retrospective analysis of their deformation history need to be performed for the full exploitation of SAR data. Landslide monitoring are not within our objectives for the current study but we are presenting some of them for the sake of completeness. In the case of landslide the ones which their slopes face westwards are detectable by the ascending track and vice versa. The ones which their slopes face northwards or southwards are detectable by both tracks but with smaller component dominating the LOS vector, thus being less measurable. Some limitations of landslide detection and monitoring could be seen in Table 14. Note that the incidence angle of ERS1&2 is ~23° matching the image mode I2 of ASAR/ENVISAT acquisitions used in the present study.

Slope aspect	Ascending ERS passes	Descending ERS passes	Notes
Slope facing East	Enhanced range resolution if α <67° Shadow if α > 67°	Foreshortening if α <23° Layover if α >23°	Only ascending data suitable for SAR interferometry and feature extraction by means of image interpretation. Slopes exceeding 67° are not covered. ID LOS deformation data.
Slope facing West	Foreshortening if α <23° Layover if α >23°	Enhanced range resolution if α <67° Shadow if α > 67°	Only descending data suitable for SAR interferometry and feature extraction by means of image interpretation. Slopes exceeding 67° are not covered. ID LOS deformation data.
Slope facing North or South	-	-	Both ascending and descending data are suitable for interferometry and feature extraction by means of image interpretation. 2D deformation analysis feasible. Low system sensitivity with respect to translational displacements along the North-South direction.

Table 14. Courtesy of [Colesanti and Wasowski 2006]. Assessment of suitability of ERS data for recognition of geological features through SAR image interpretation and for ground displacement monitoring via SAR interferometry, with reference to slope aspect and inclination (given the average incidence angle, or both the near and far range incidence angles, it is straightforward to adapt the table also to different radar sensors)

A number of possible landsliding areas have been detected. In §5.3 we have presented the known landslide of Platanos. Due to the processing of combing the ascending and descending tracks we have excluded some PS from one or the other track. Thus we are using the LOS view also.

5.8.1. Profitis Ilias

South-East of Patras we have detected a slope in some patches deformed similarly. In Figure 5-34 we can discriminate the patches *A*, *B* and *C*. In Figure 5-35 and Figure 5-36 we can see the aspect and slope map respectively of the same area. The patch A is located in an area with local slope ranging between 10° - 50° facing SW. The patch C is located in an area with local slope ranging between 20° - 50° facing E. The patch B is located in an area with local slope ranging between 30° - 40° facing SE. All of them are moving towards the platform

relative to the background values. This presents discrepancy the topography. The most probable explanation is that these landslides are moving faster than the measuring ability the ASAR platform exceeding often the one fringe (λ/2=28mm) per acquisition slot. The quantitative observations of the landslides in question are meaningless, but the detection could be followed by in-situ observations or by a study with very high resolution SAR sensors with better measuring capabilities. For example a more oblique incidence angle, with high resolution TERRASAR-X (X-band) acquisitions is more proper. In this case although the wavelength is shorter (λ=31mm), leading to easier cycle slipping, the revisit time can be as short as is 11 days (in contrast with ASAR which is 35 days), exploiting a constellation of such satellites. In X-band one fringe (λ/2) over 11 days corresponds to ~41 mm mo^{-1} and for C-band one fringe over 35 days corresponds to ~24 mm mo^{-1}. Thus the TERRSAR-X platform is able to monitor deformations twice as faster as ASAR does. This fact along with the higher resolution of TERRASAR-X makes this SAR platform more promising than the ASAR one.

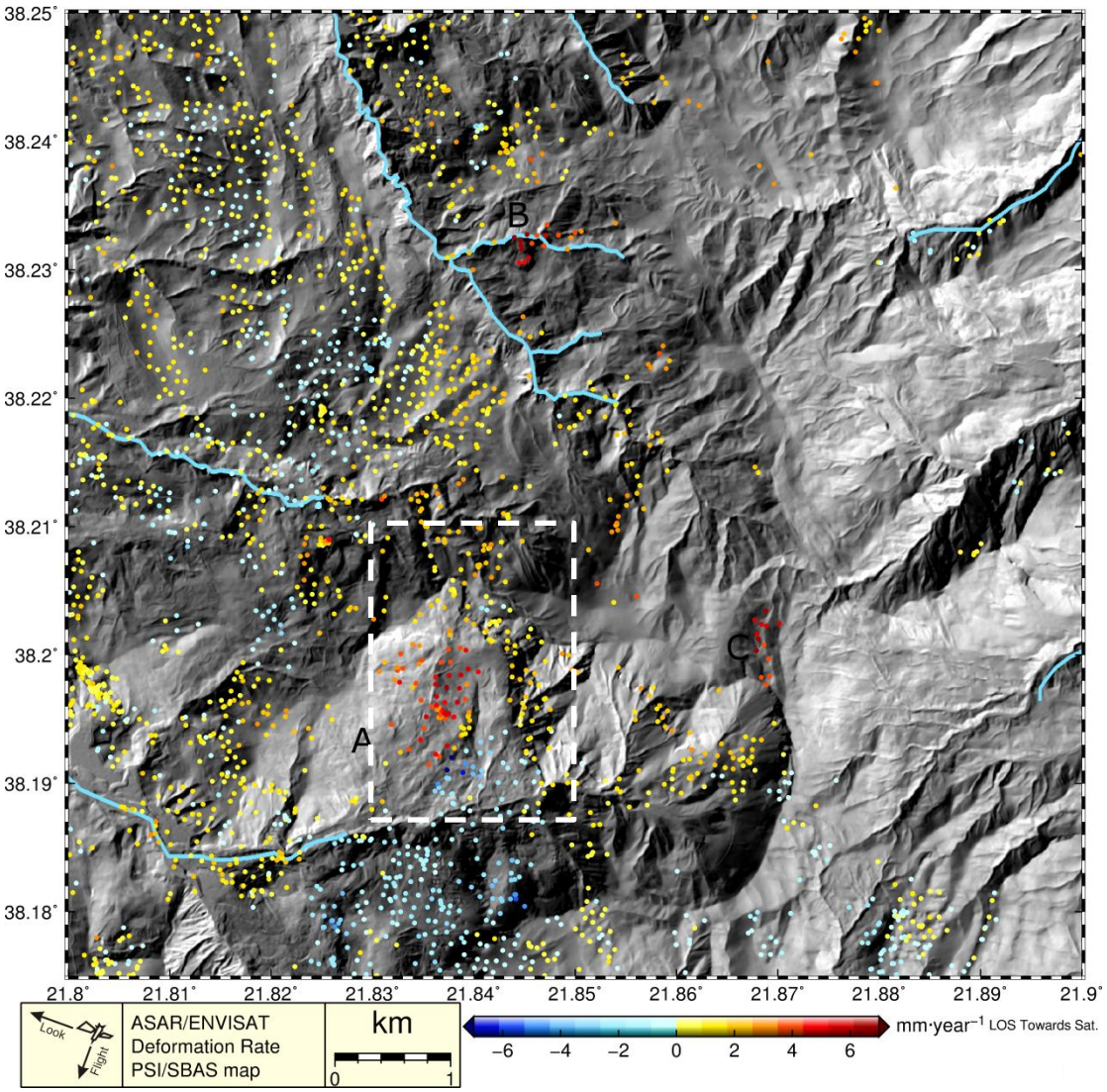

Figure 5-34. The PSI/SBAS map South-East of Patras in which there is a probable landslide. The white dotted rectangle with coordinates [21.83 21.85] °E, [38.175 38.21] °N, defines the area that has been investigated temporarily.

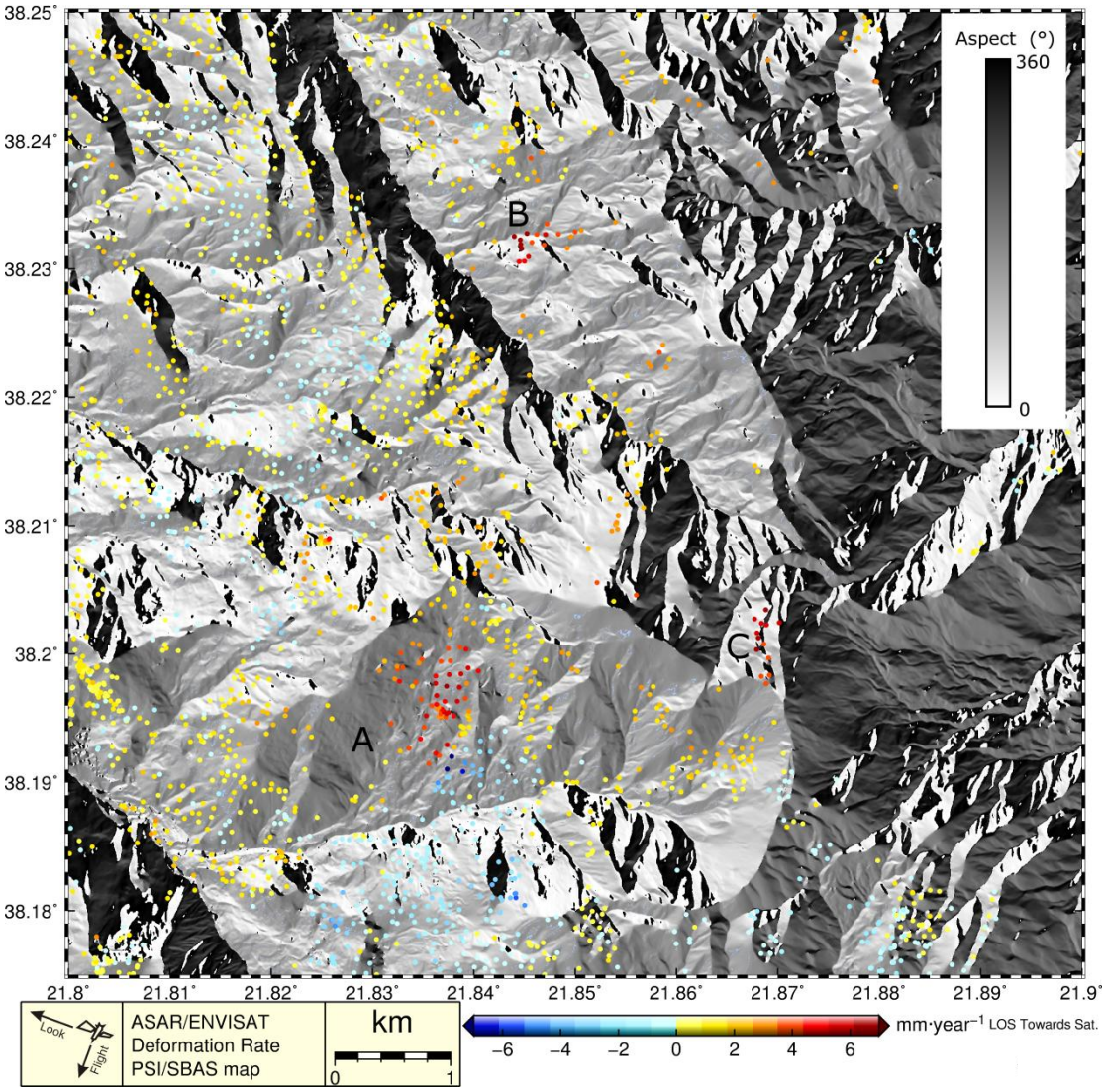

Figure 5-35. The PSI/SBAS map of the area of Figure 5-34, superimposed over aspect map calculated from the DEM.

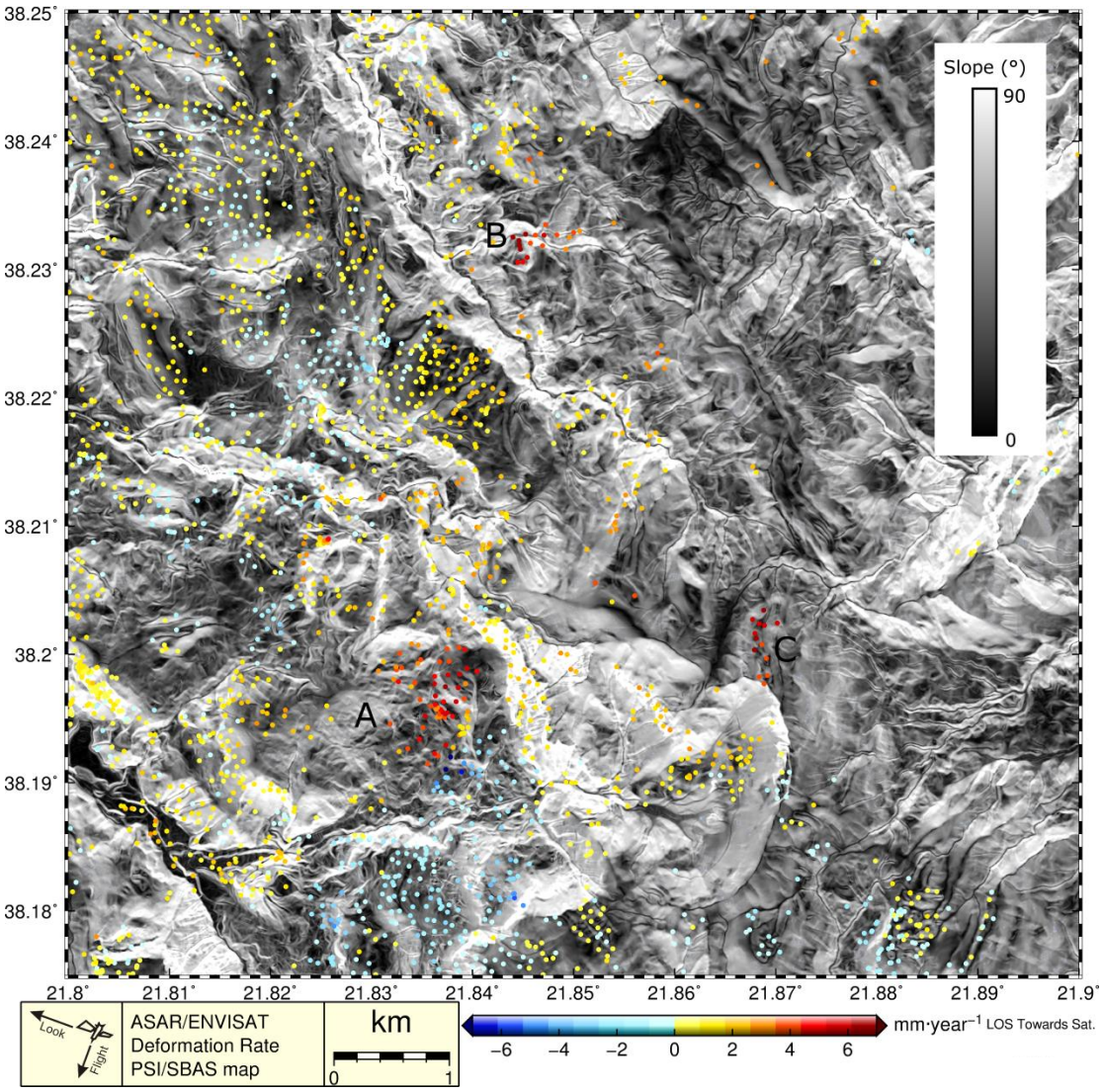

Figure 5-36. The PSI/SBAS map of the area of Figure 5-34, superimposed over slope map calculated from the DEM.

In Figure 5-37 we can see the evolution of the deformation of the PSI/SBAS PSs of the descending track 279 (§2.3.2) in the LOS direction ('red' represents deformation towards the Satellite). The area is bounded in the rectangle marked in Figure 5-34.

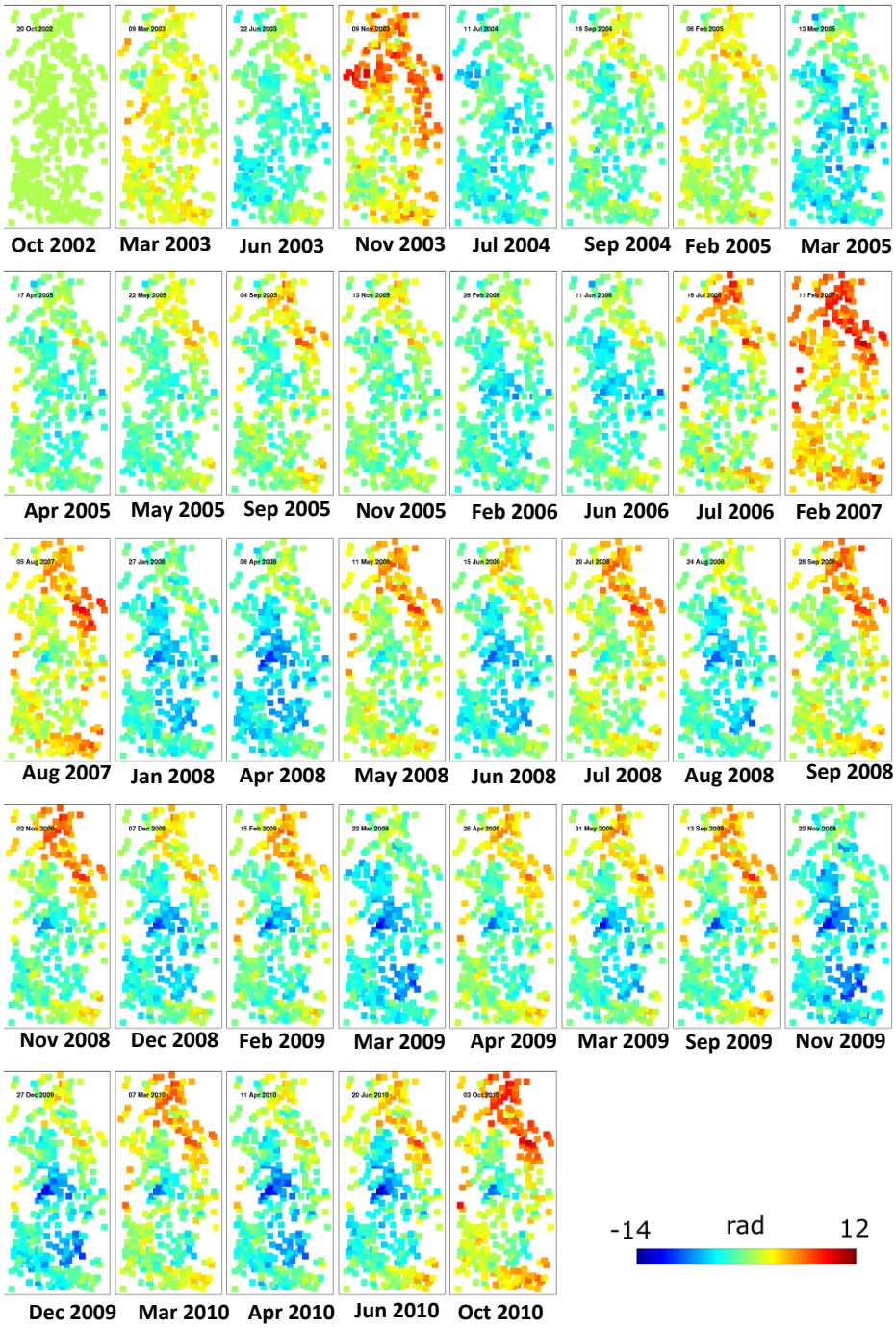

Figure 5-37. Deformation history of patch A inside the rectangle marked in Figure 5-34 at the LOS (red color declare deformation towards satellite) deformation of the Track 279 (§2.3.2). One fringe corresponds to 6.28 radians.

In Figure 5-38 the PSs of Figure 5-34 are shown in google-earth. The 'red' areas are located in a slope. Their deformation rate is meaning full due to the abnormal deformation behavior as seen in Figure 5-37. In the area of Kefalovriso the 'blue' PSs mean deformation away the satellite. In Figure 5-39 we see the same PSs but the viewpoint is from the satellite position.

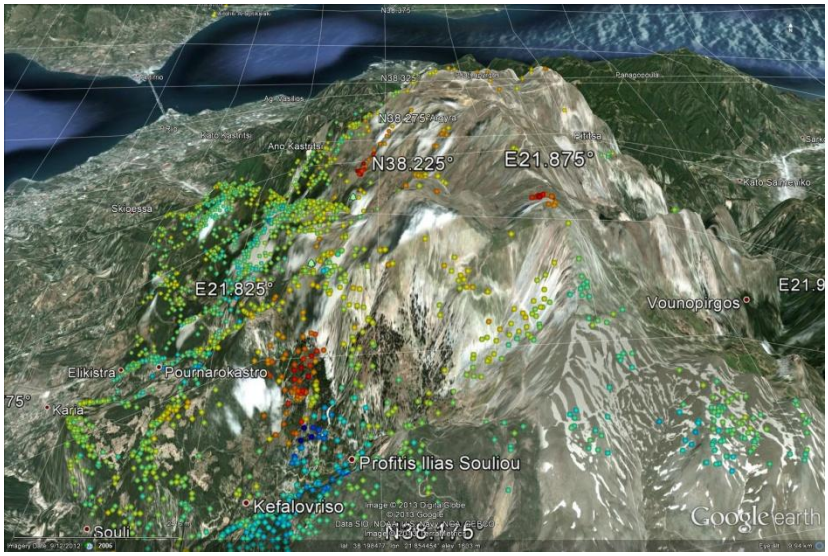

Figure 5-38. 3D view from South of the PSs at the area of Profitis Ilias.

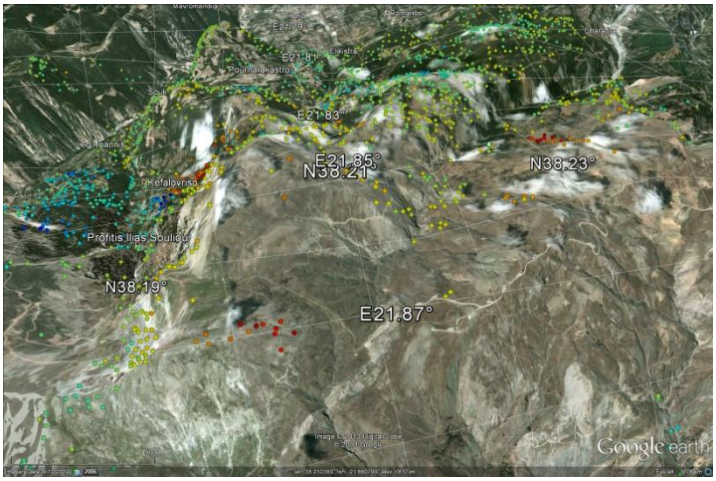

Figure 5-39. 3D view from the position of the satellite (LOS descending track 279 from an azimuth of almost 105° and incidence angle of 23°) of the PSs at the area of Profitis Ilias.

5.8.2. Souli

In Figure 5-40, we can spot 'blue' moving away PSs at the LOS of ascending track laid in a slope at the area of Souli, South-East of Patra.

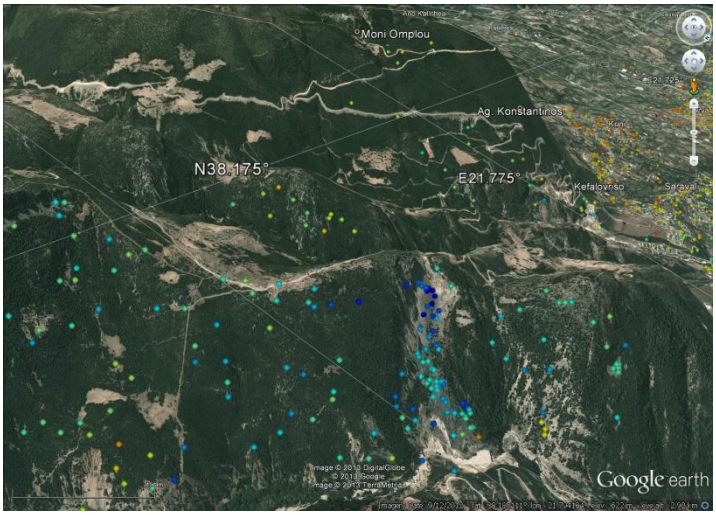

Figure 5-40. 3D of the PSs in a slope of ascending track 415 at the area of Souli.

In Figure 5-41 the 3D view is from the position of the satellite (LOS ascending track 415 from an azimuth of almost 255° and incidence angle of 23°) of the same slope.

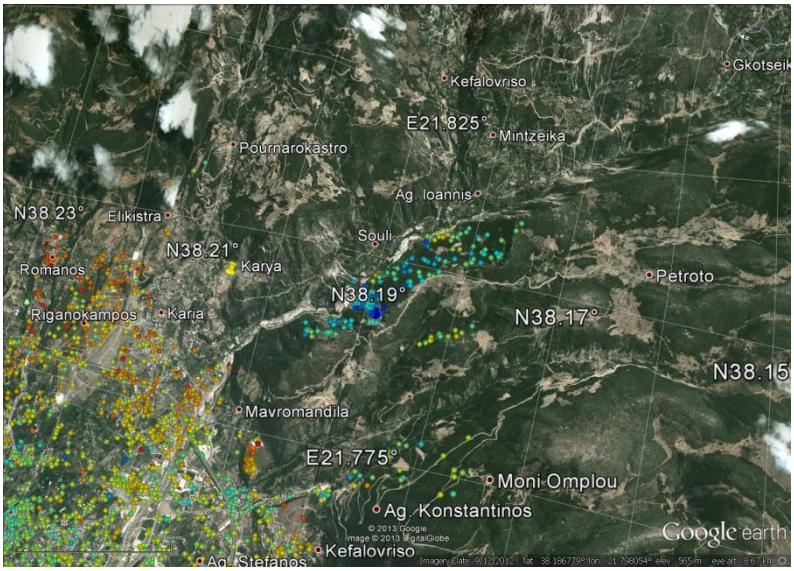

Figure 5-41. 3D view from the position of the satellite (LOS ascending track 415 from an azimuth of almost 255° and incidence angle of 23°) of the PSs at the area of Souli.

5.8.3. Panagopoula

In Figure 5-42 we can detect a deformation (inside white dashed rectangle) and in Alexandri area. We also note that the fault of Psathopyrgos is passing through these deformations. Moreover at Alexandri and Panagopoula there are two small Deltas. The deformation located inside the rectangle in the Panagopoula Landslide. The most PSs are located along the highway.

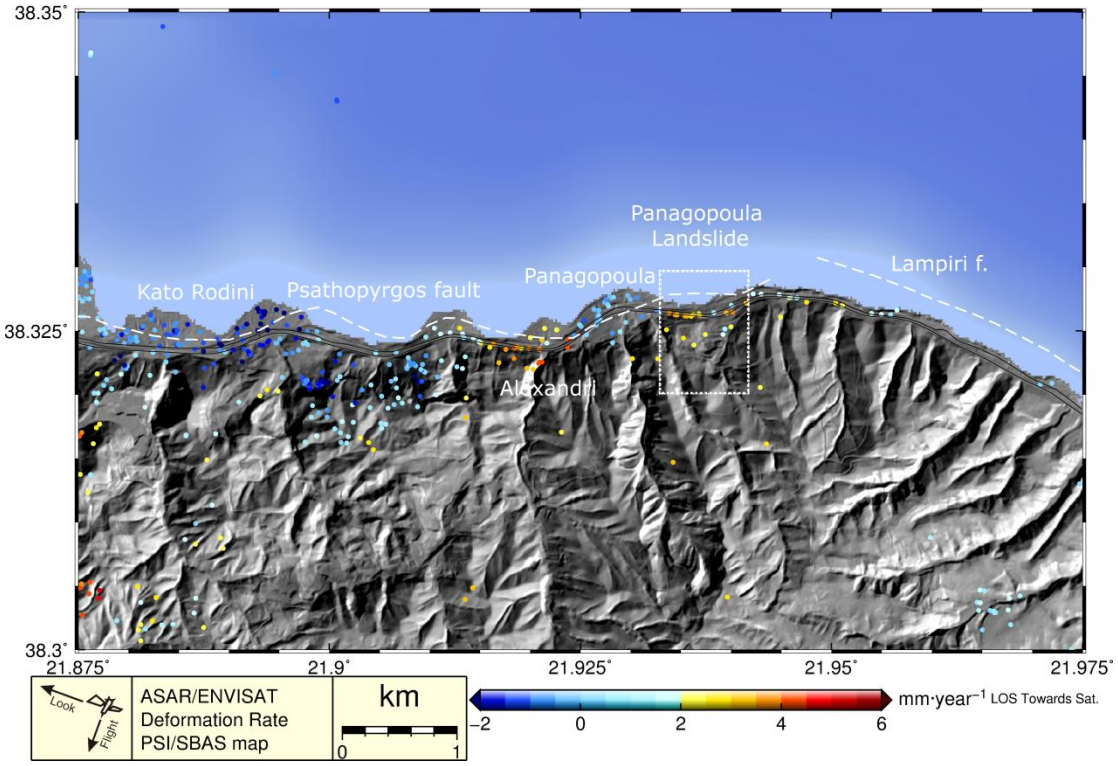

Figure 5-42. PSI/SBAS map of the Panagopoula landslide in the descending LOS direction of track 279 (§2.3.2), with positive values towards satellite

In Figure 5-43 we can also discriminate the Panagopoula Landslide mainly along the highway. The deformation at Alexandri isn't so well defined.

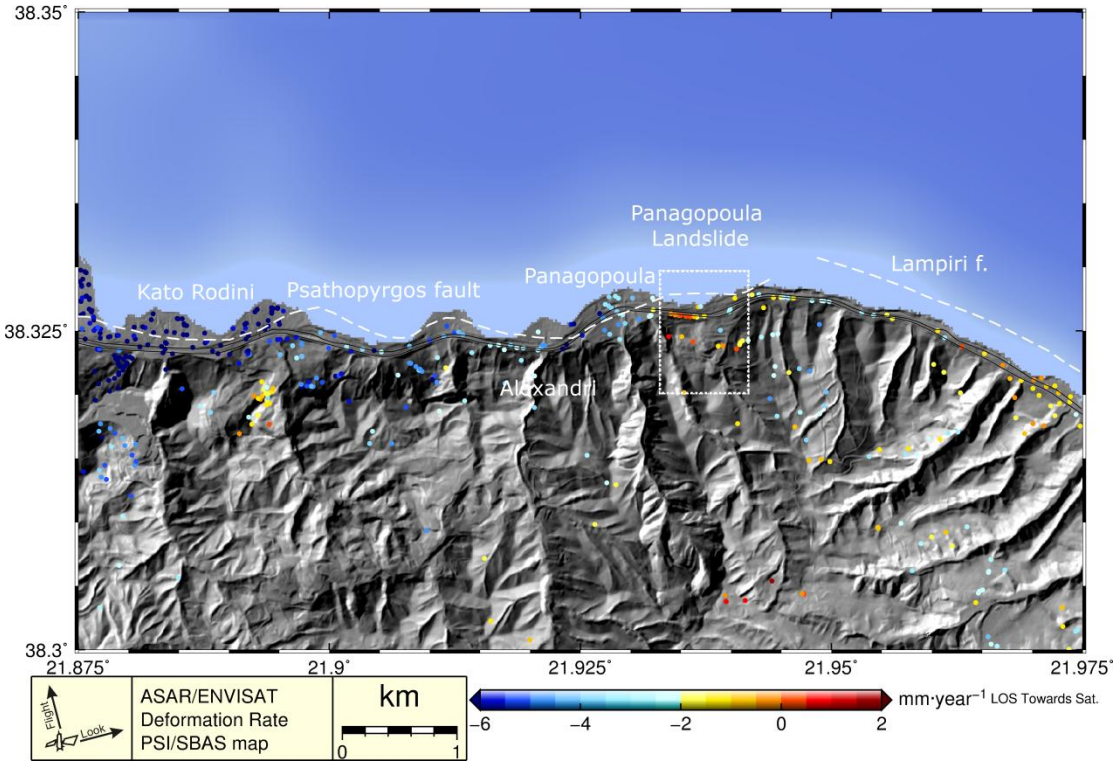

Figure 5-43. PSI/SBAS map of the Panagopoula landslide in the ascending LOS direction of track 415 (§2.3.2), with positive values towards satellite

In Figure 5-44 we can see a view from google-earth.

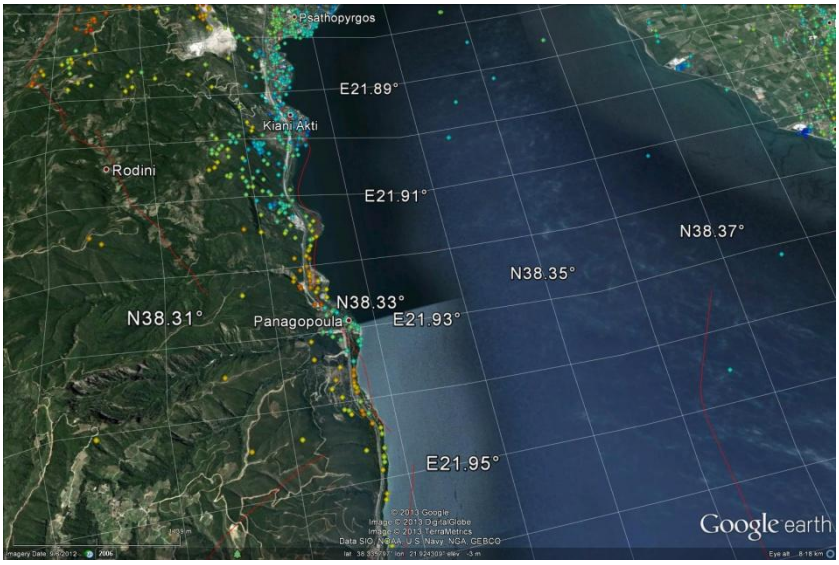

Figure 5-44. 3D representation of the PSs in the descending LOS of track 415 of the Panagopoula Landslide. The viewpoint is simulated to be similar to the LOS of the descending track. 'Red' represents deformation towards satellite.

In Figure 5-45 a simplified engineering geological map and simplified slip sections through instability zone map of the Panagopoula landslide by [Koukis et al., 2009] is shown. The same area is marked with dashed white line in Figure 5-42 and Figure 5-43.

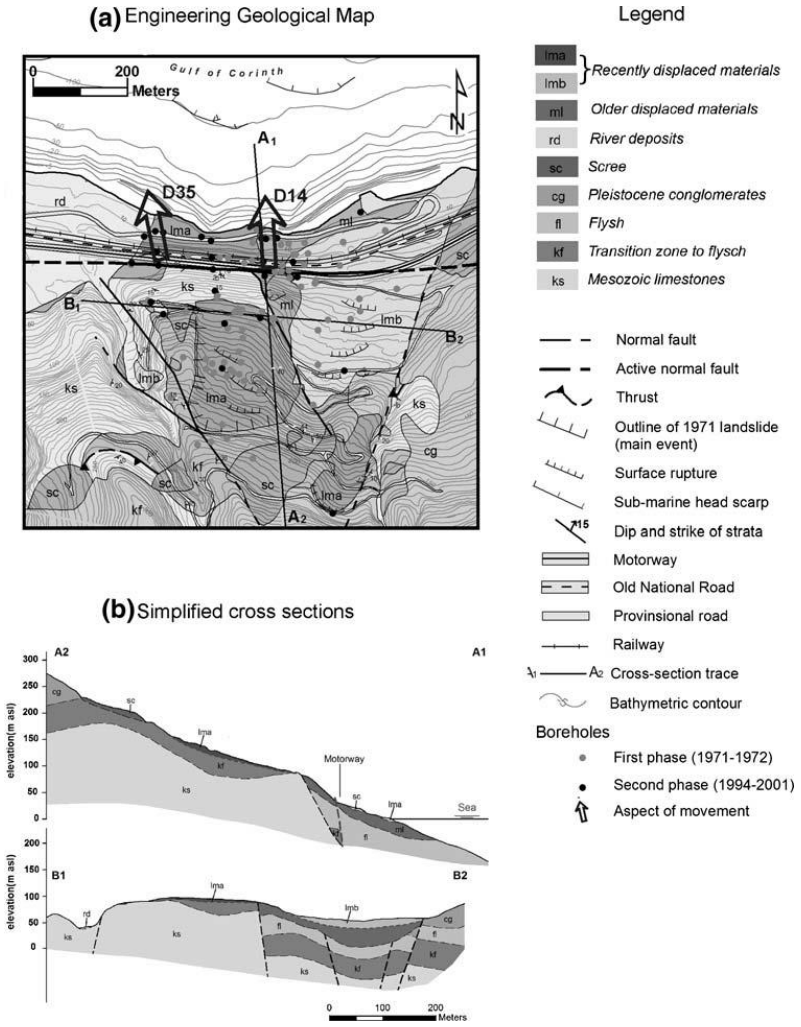

Figure 5-45. Courtesy of [Koukis et al., 2009], (a) Simplified engineering geological map of the Panagopoula landslide, (b) Simplified slip sections through instability zone.

5.9. Interesting features

In Figure 5-46 we can discriminate a special feature located SE of Trihonida lake. Its length is almost 1.5 km. Its extension is large.

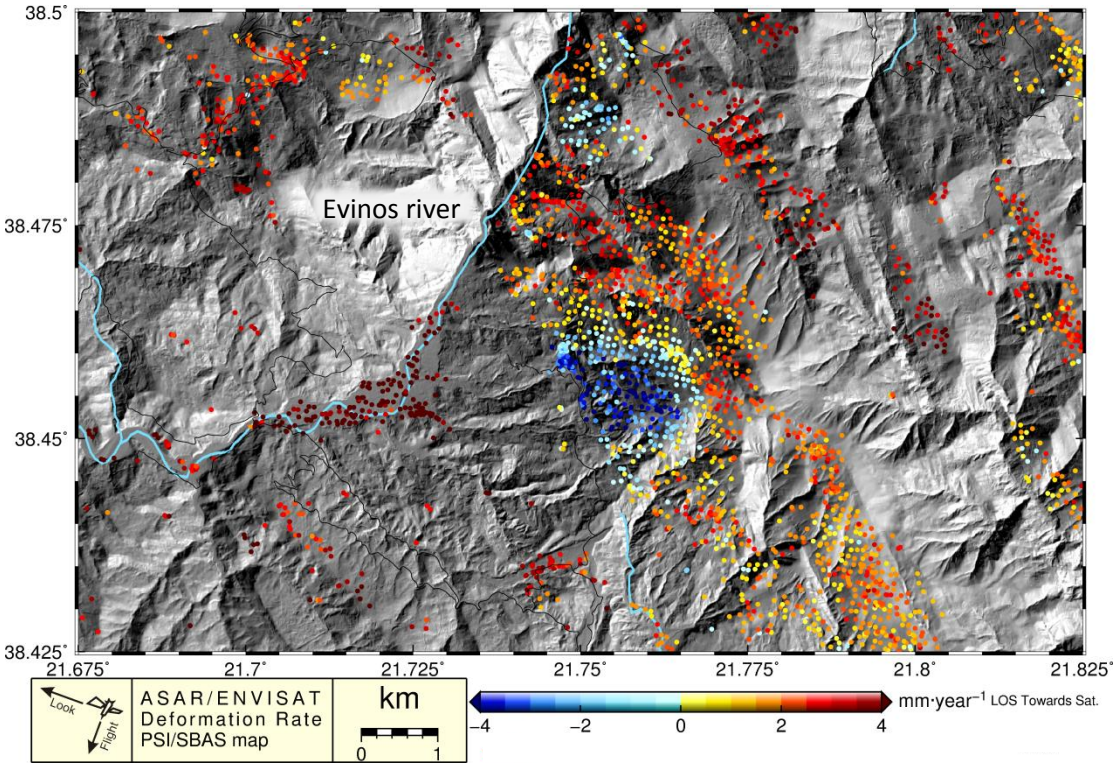

Figure 5-46. PSI/SBAS map in descending LOS direction of an interesting feature.

In we can see the temporal evolution of this feature. The layer underneath is limestone from Pindos mountain. The deformation field is very well concentrated and shaped. It is located in a slope facing west, a fact that renders the deformation very well detectable for the descending pass. From Figure 5-47 we can observe that it is about of an insisting and continuously evolving phenomenon. A rational explanation would be that it is about a creeping slope that could be emerged to landslide. There are also some signs of erosion on the legs of the slope that could amplify this deformation.

In the North area we can spot a smallest deformation on a similarly oriented slope, east of Evinos River, also indicating slope instability.

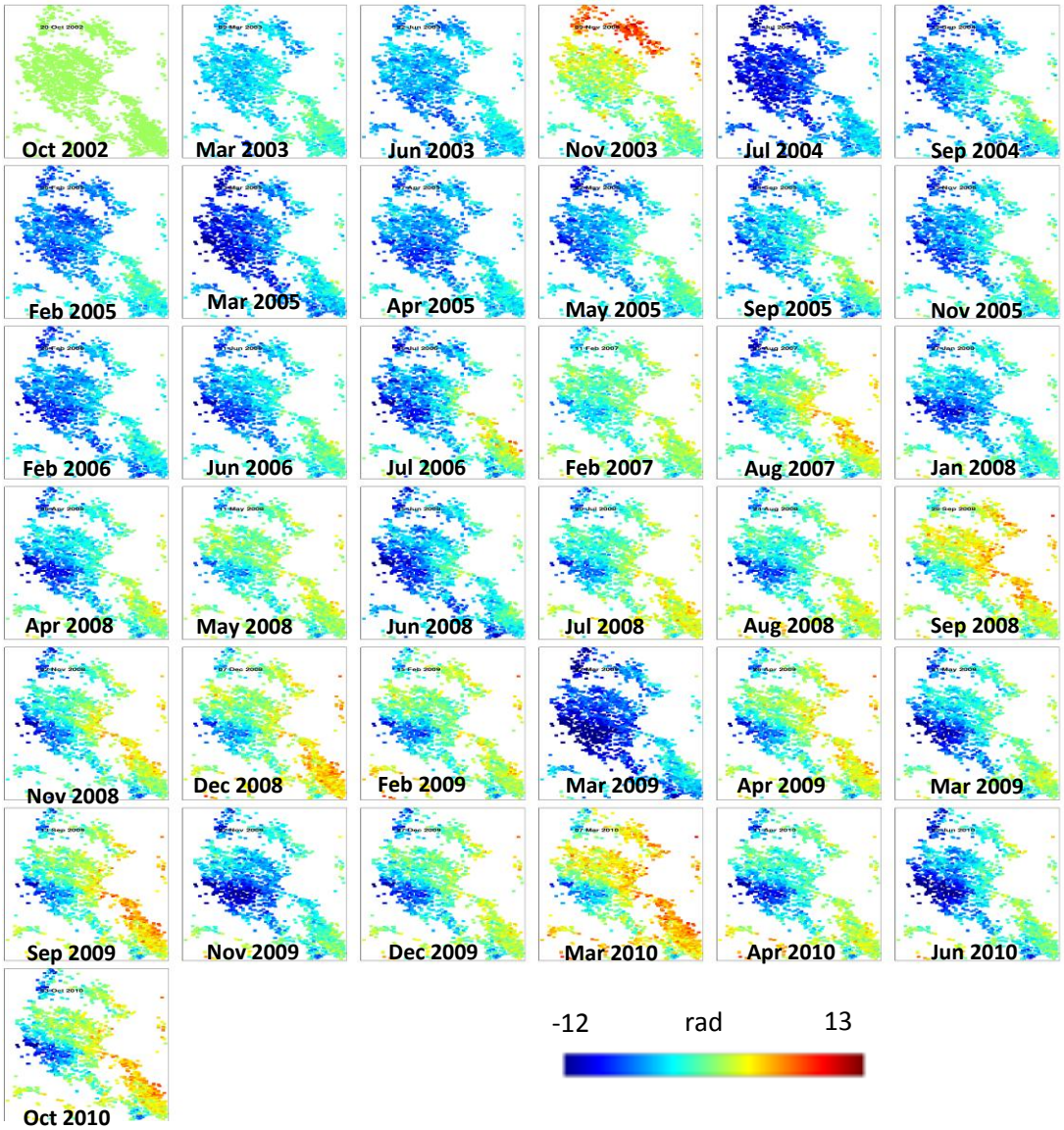

Figure 5-47. The temporal evolution of the 'interesting feature' SE of Trihonida Lake. Its values represent LOS deformation in radians from descending PSI/SBAS track 279, towards satellite. The first image is the reference.

In Figure 5-48 we can discriminate an eye pattern interesting feature that its origin is also in question. It is located east of Trihonida Lake. Its footprint in time is continuous as we can see in Figure 5-49, where the temporal evolution is shown.

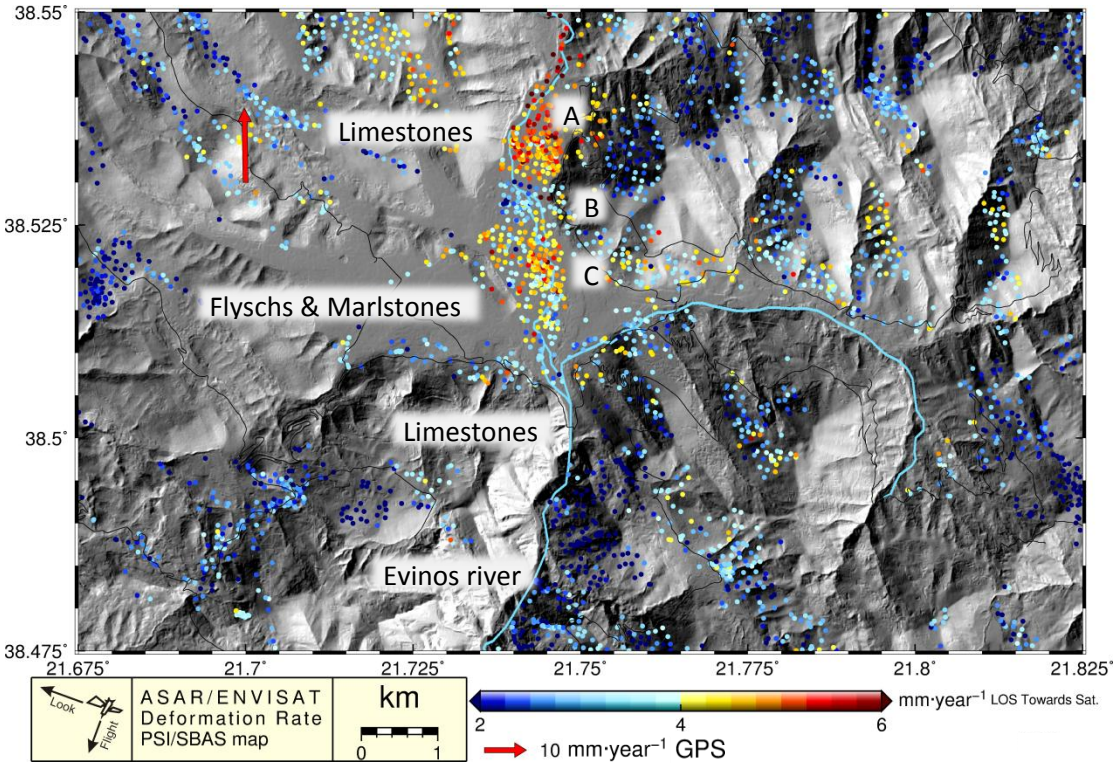

Figure 5-48. PSI/SBAS map in descending LOS direction of an eye patterns interesting feature.

The deformation pattern is located inside the gorge of Evinos River. The layer in the center of our area is consisted of Flyschs and Marlstones, highly erosional, with the layers North and South of it to be mainly Limestones. That explains the alluvial plane in the center leaving exposed riverine sediments. In spot 'A' the river rapidly enters this plane and loses a large part of its fluid dynamic leading to highly deposition of sediments. The in spot 'B' and 'C' there is also some deposits due to the lower fluid dynamic of the river. The Figure 5-49 shows that the deformation is not consistent in time fortifying this hypothesis. This could be a rational explanation of the observed positive deformation in comparison with its surroundings.

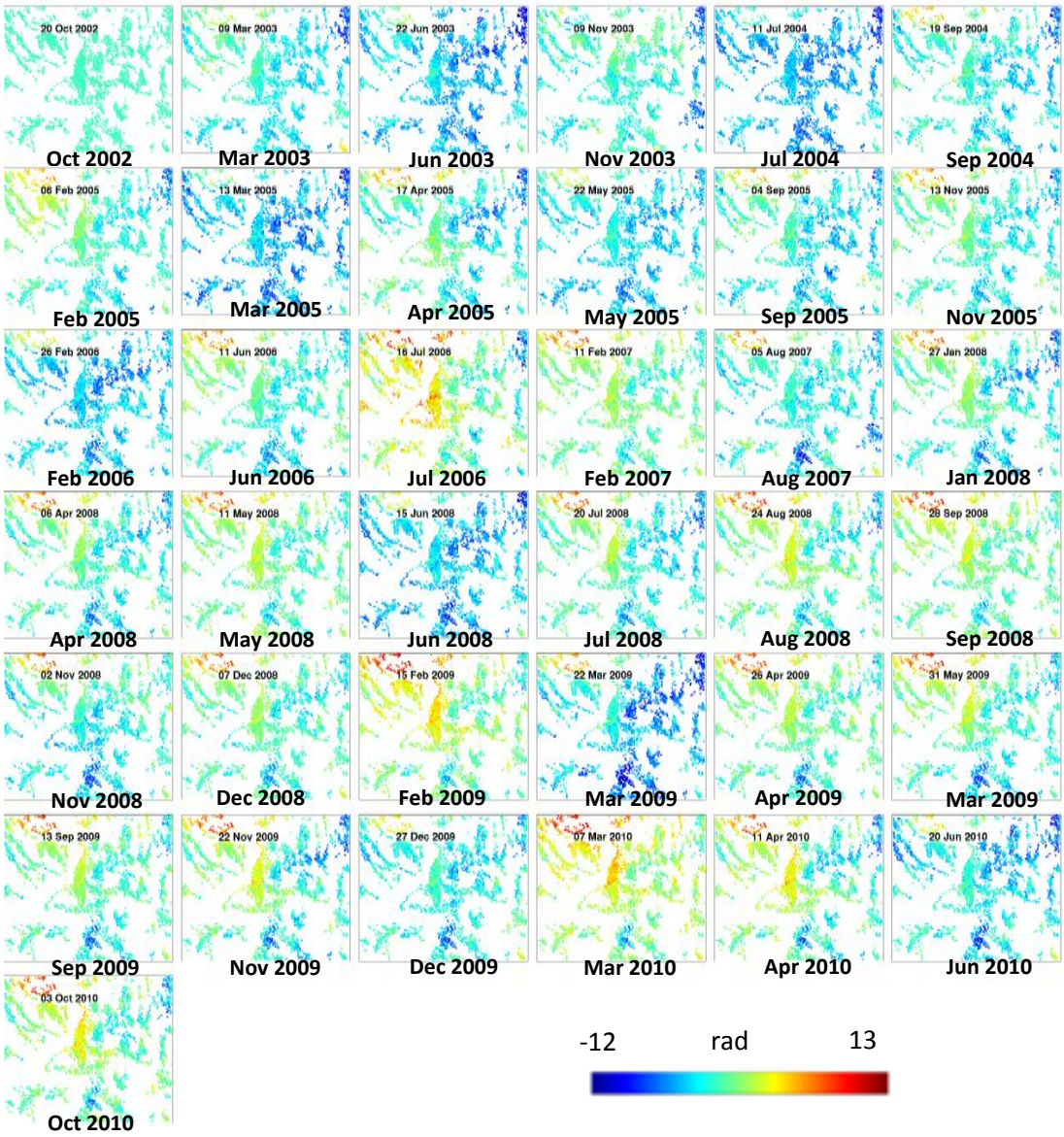

Figure 5-49. Deformation history of the eye pattern feature. The values represent deformation in radians at the LOS of the Track 279 (§2.3.2) towards satellite. The reference image is the first one.

6. Trihonida – Aetoliko

This area fall outside the study area but because of its link with the GoC through the 'triple junction', It will be studied briefly. The PSI/SBAS processing of the NGoC is bounded by the South of Trihonida Lake as we can see from Figure 6-1, thus we don't have processed the whole of Trihonis Lake. In Figure 6-1 and Figure 6-2 we can see the two discontinuities marked as Agrinion f. and Trihonis f. which coincide with the corresponding faults.

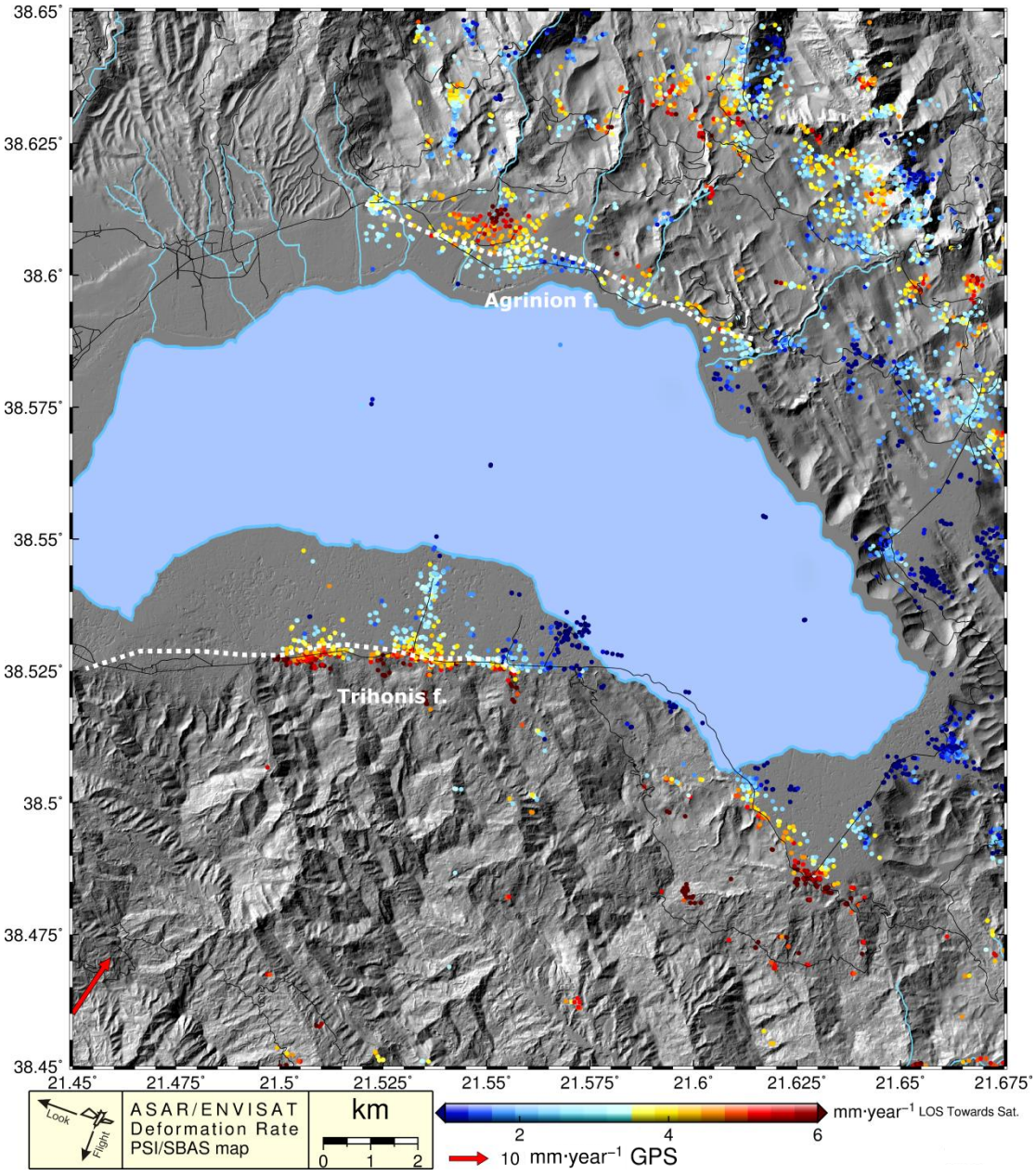

Figure 6-1. PSI/SBAS deformation map of Trihonida Lake, in the descending LOS.

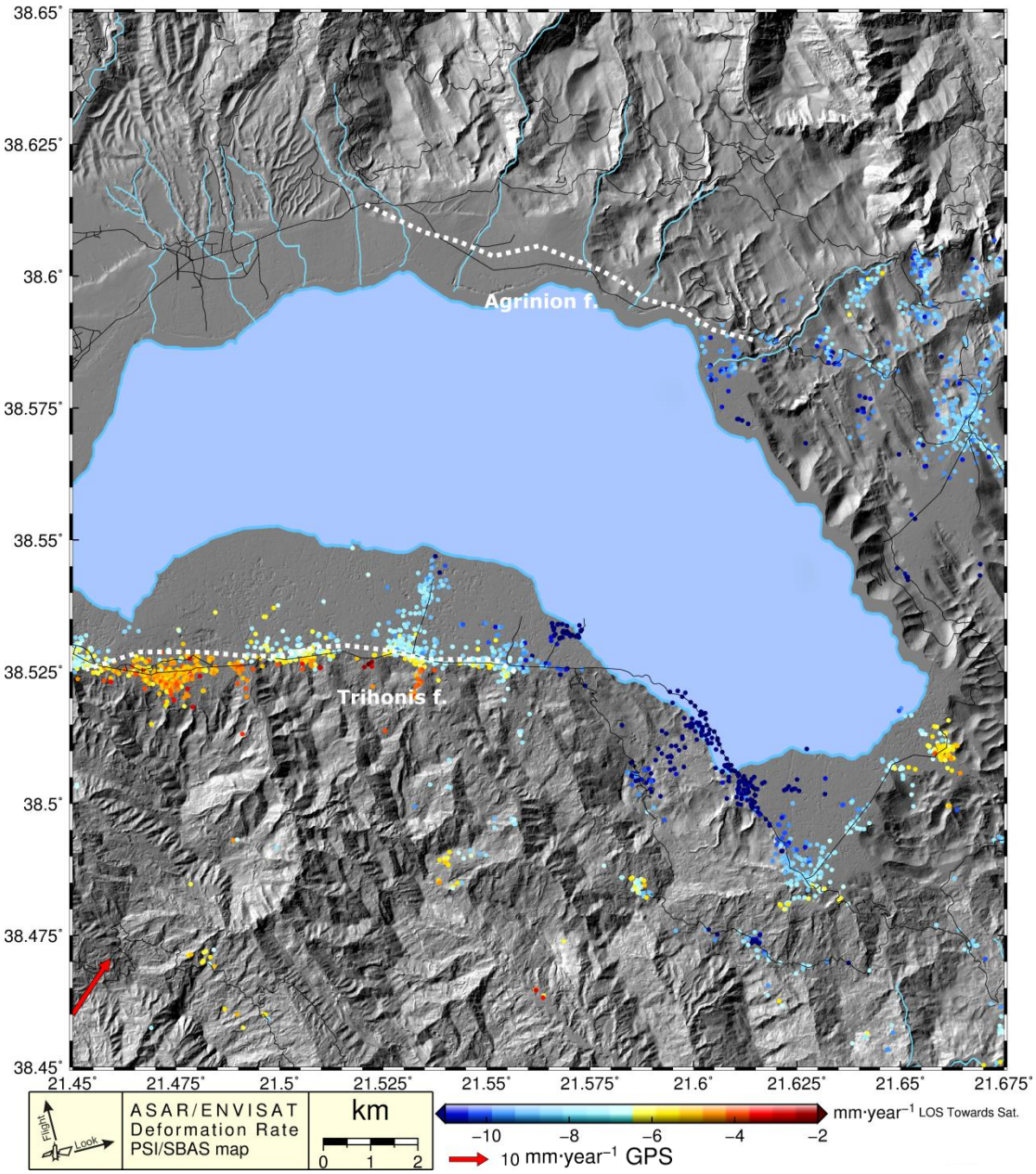

Figure 6-2. PSI/SBAS deformation map of Trihonida Lake, in the ascending LOS.

In Figure 6-3 and Figure 6-4 we can see the UDc and EWc, respectively. For the Trihonis f. we can discriminate the footwall uplifted with ~3 mm year^{-1}. We can also discriminate a small EWc.

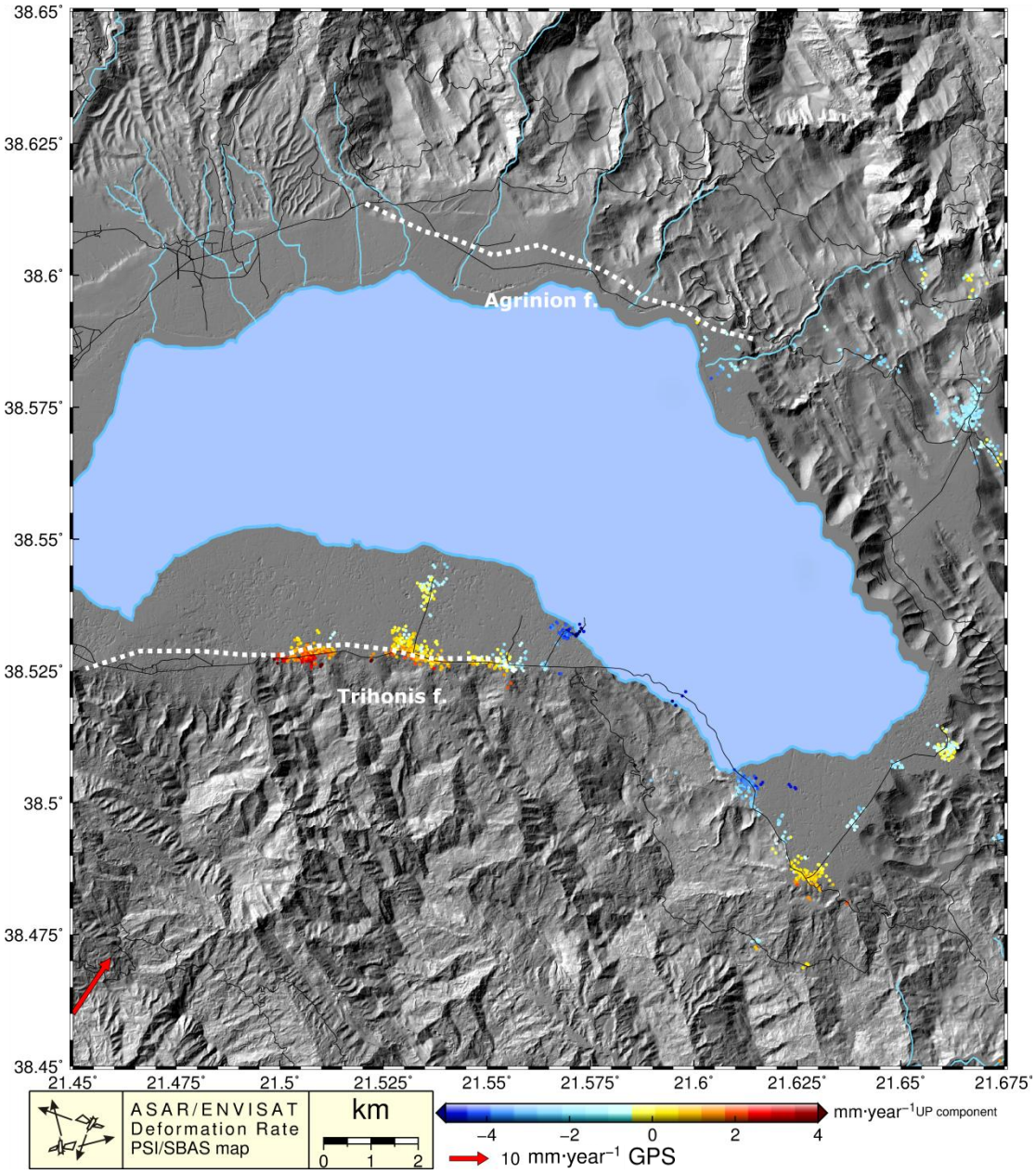

Figure 6-3. PSI/SBAS UDc deformation map of Trihonida Lake.

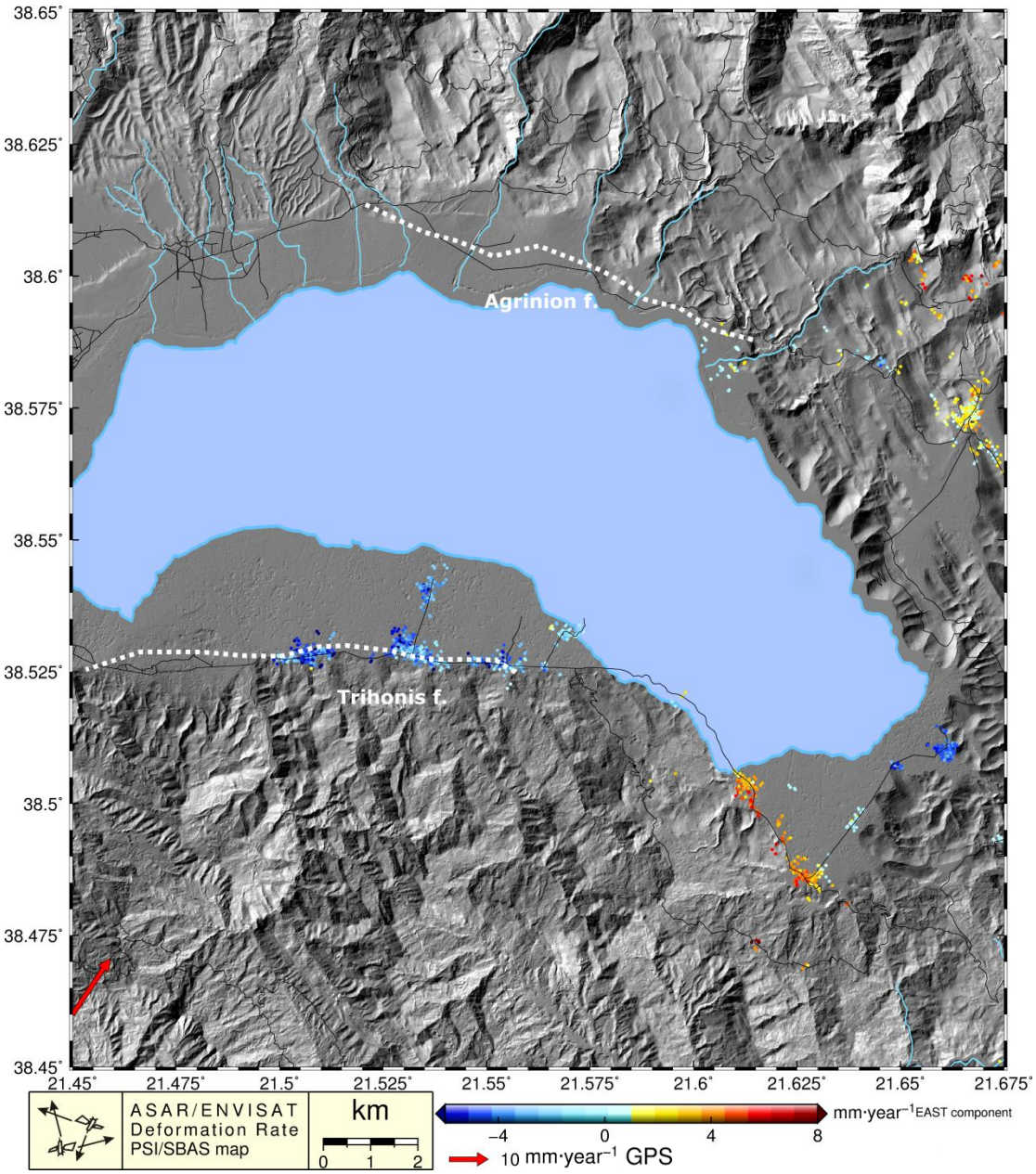

Figure 6-4. PSI/SBAS EWc deformation map of Trihonida Lake.

As mentioned in §2.4.3 the Aetoliko Valley has been processed by different tracks than the GoC. It hasn't been processed so to extract the UDc and EWc or to apply the correction that we had applied in the North and South GoC and the rate values are not referenced. A ramp may exist but the. Our intention was just to investigate the presence to the piece of the triple junction in this area. In Figure 6-5 and Figure 6-6 we can see the two tracks. The azimuth of the LOS of the descending Track no. 50 fits better to the geometry of left-lateral deformation of Katouna-Stamna fault zone.

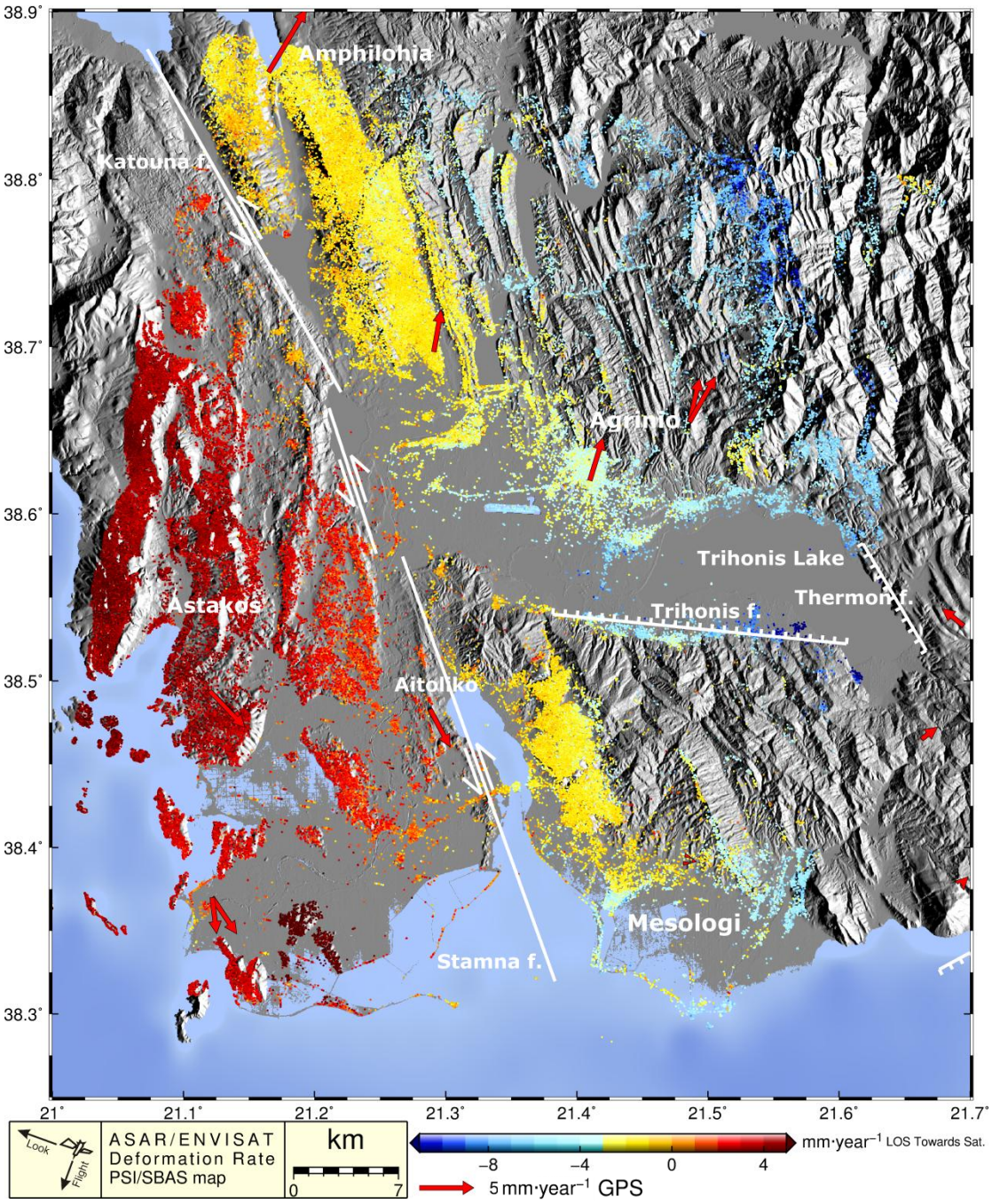

Figure 6-5. The PSI/SBAS map of descending track 50 of Aetoliko area. The red arrows represent the planar GPS measurements in stable Fokida frame.

In the PSI/SBAS rate map of Figure 6-5 we can detect a probable E-W slope trend of the rate values but the abrupt change between the two patches either sides of the fault system

declares indeed a real step and an existing deformation discontinuity. Thus indeed we can confirm the left-lateral deformation of the fault system Katouna and Stamna. The Eastern patch is moving away the satellite where the Western patch moving towards it. In Figure 6-6 we can detect the opposite sign of the deformation as we would expected it but the dynamic range is less since the viewing geometry is not the optimal for this kind of horizontal movement. Moreover the GPS rates in both sides of the fault system validates its activity and its strike-slip deformation. By supposing no vertical deformation we computed the strike slip along across the Katouna-Stamna fz. To be ~2.5 mm year^{-1}.

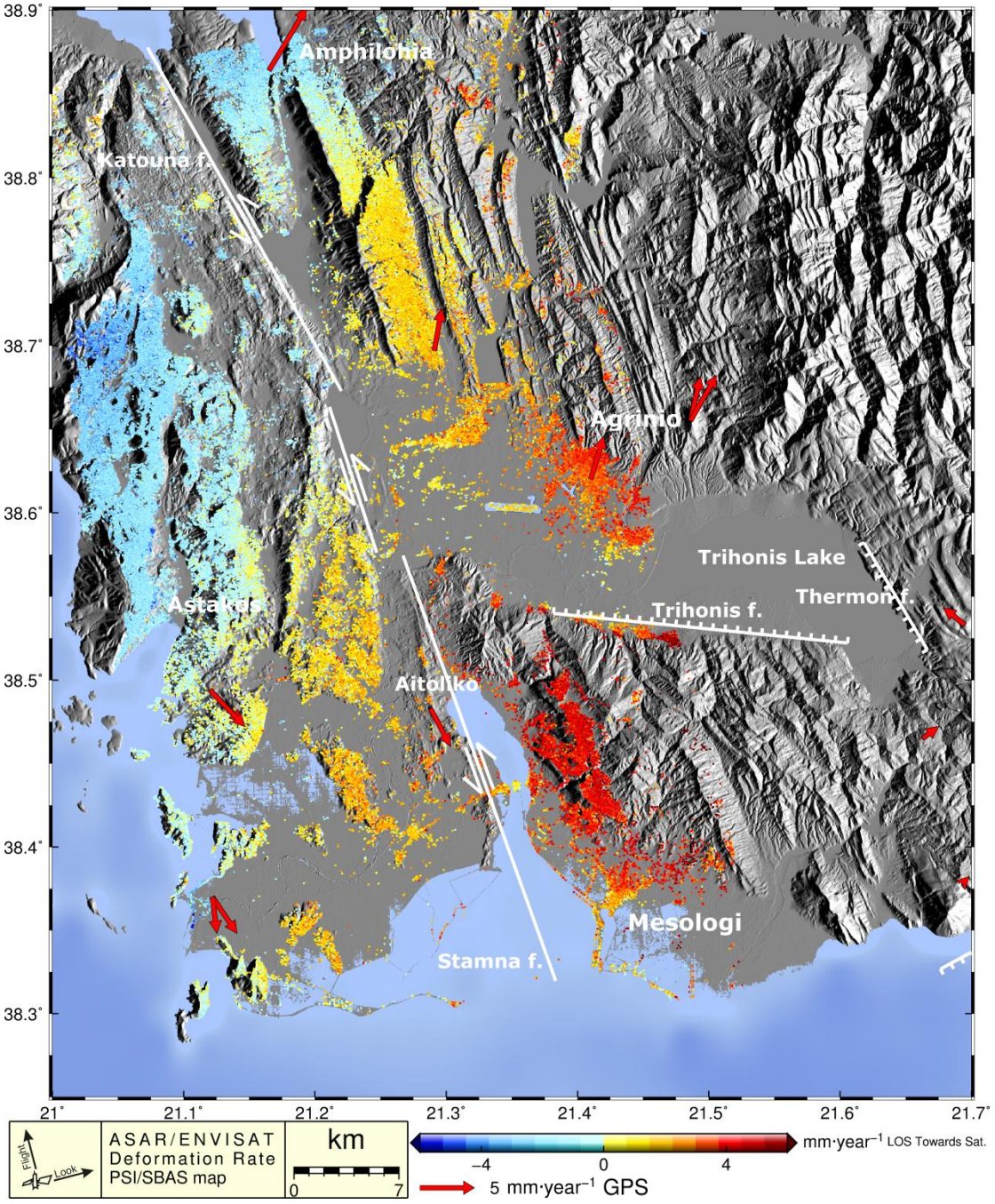

Figure 6-6. The PSI/SBAS map of ascending track 186 of Aetoliko area. The red arrows represent the planar GPS measurements in stable Fokida frame.

[Perouse et al., submitted to Terra Nova] after geological study of the Katouna-Staman fz. Estimates the strike slip left lateral component to be no less than 4 mm year^{-1} (Figure 6-7). The two values are close but a discrepancy exists. A source of the observed discrepancy is the fact that the Aetoliko PSI/SBAS map hasn't be corrected as for the Gulf of Corinth case forcing us to consider the vertical component as zero and neglect any trend along the longitude direction.

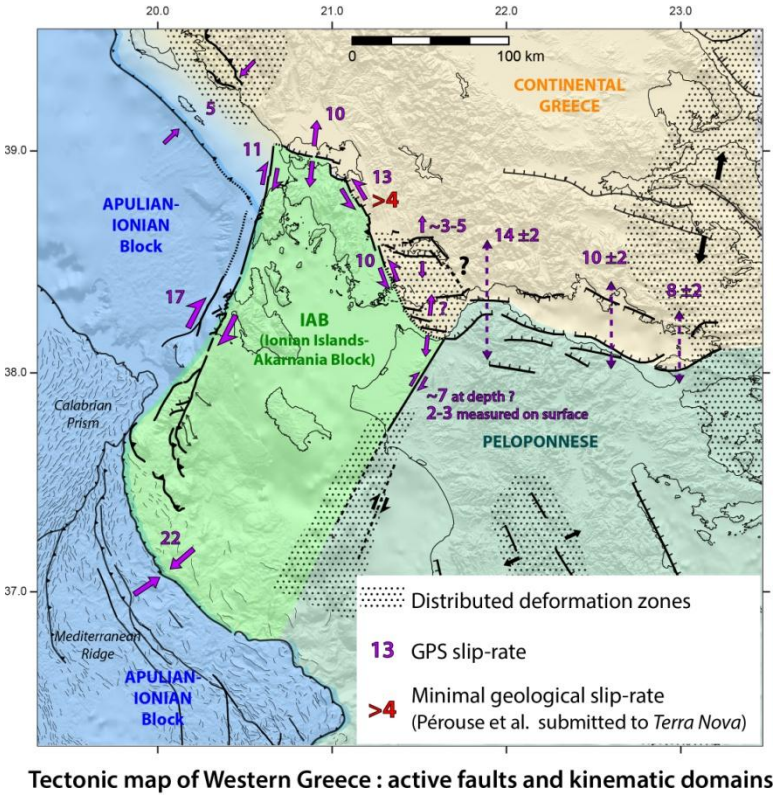

Tectonic map of Western Greece : active faults and kinematic domains

Figure 6-7. Courtesy of [Perouse et al., submitted to Terra Nova]. Tectonic map of Western Greece : active faults and kinematic domains.

7. Conclusions

Active faulting can be detected and measured with SAR Multitemporal interferometry even in the case of mm year^{-1}.

There are many detectable inland active creeping faults in the western Gulf of Corinth.

We have concluded that there is a difficulty for the GPS observations to estimate the locking depth of earthquake events but InSAR can be used to fill this gap.

The multitemporal GPS and SAR interferometry are contaminated with deformation even from distant earthquakes.

The combined use of Multitemporal interferometry and GPS provides very detailed and accurate deformation rate maps in the Up and East component. It is a very powerful tool for the estimation of fault parameters in case of earthquake events, even with no rupture reaching the surface and with ground deformation of the order of few mm.

This study demonstrates the variety of geophysical events occurring in the extended area of the Gulf of Corinth, the complementarity of InSAR and GPS and the wide range of their applications. Moreover, demonstrates the need of the complementarity with seismology and geology.

A triple junction that develops when a spreading center interacts with a convergent margin is a combination of two or more of the following types of boundaries: an active spreading ridge, a transform fault, or a trench. In §1.4, at the broad scale we have described the presence of a triple junction between micro-plates at the boundary between the rift of Corinth to the east and the termination of the Hellenic arc to the west. At the present study we have demonstrated the presence of the pieces of the diffused 'triple junction' feature (Figure 7-1).

Significant ground deformation is observed within the city of Patras itself, due not only to urban subsidence often seen elsewhere, but also to the motion of shallow structures likely to be induced by deep tectonic movements at the junction of the right lateral strike-slip fault linked to the Movri ([Briole et al., in preparation] demonstrates the aseismic right lateral creeping across the NE extension of it), penetrating inland between Rio and Patras (trans-tensional fault of Rio Patras) and the Psathopyrgos normal fault at the entrance of the Corinth Rift. The Rio-Patras fault is a transition, oblique, structure, connecting the strike-slip zone to the south and the extensional area to the east. All these features constitute the NW piece of the triple junction.

We briefly investigated and discussed the Trihonida and Aetoliko valley deformation field in the northwest of the triple junction area.

We have measured the deformation in Nafpaktos and Marathias fault zones, as well as Sellianitika fault zone, Psathopyrgos and Aigion fault in the central piece of the triple Junction (Figure 7-1).

The Helike fault [Ford et al., 2013] is also an accommodate part of the inferred deformation through the triple junction.

The methodology chain followed, using the original PSI/SBAS up to the production of the UDc and EWc, performed well and provided accurate and robust results in an extended area. The original PSI/SBAS data suffers from unhandled low frequency erroneous components that have been minimized. On the contrary, the high frequency spatial discontinuities were visible and could be quantified and qualified from the original PSI/SBAS data but without any absolute reference and in the LOS direction. The robustness of his method has been demonstrated by GPS validation. The A disadvantage of it is the need of common PSs from both tracks.

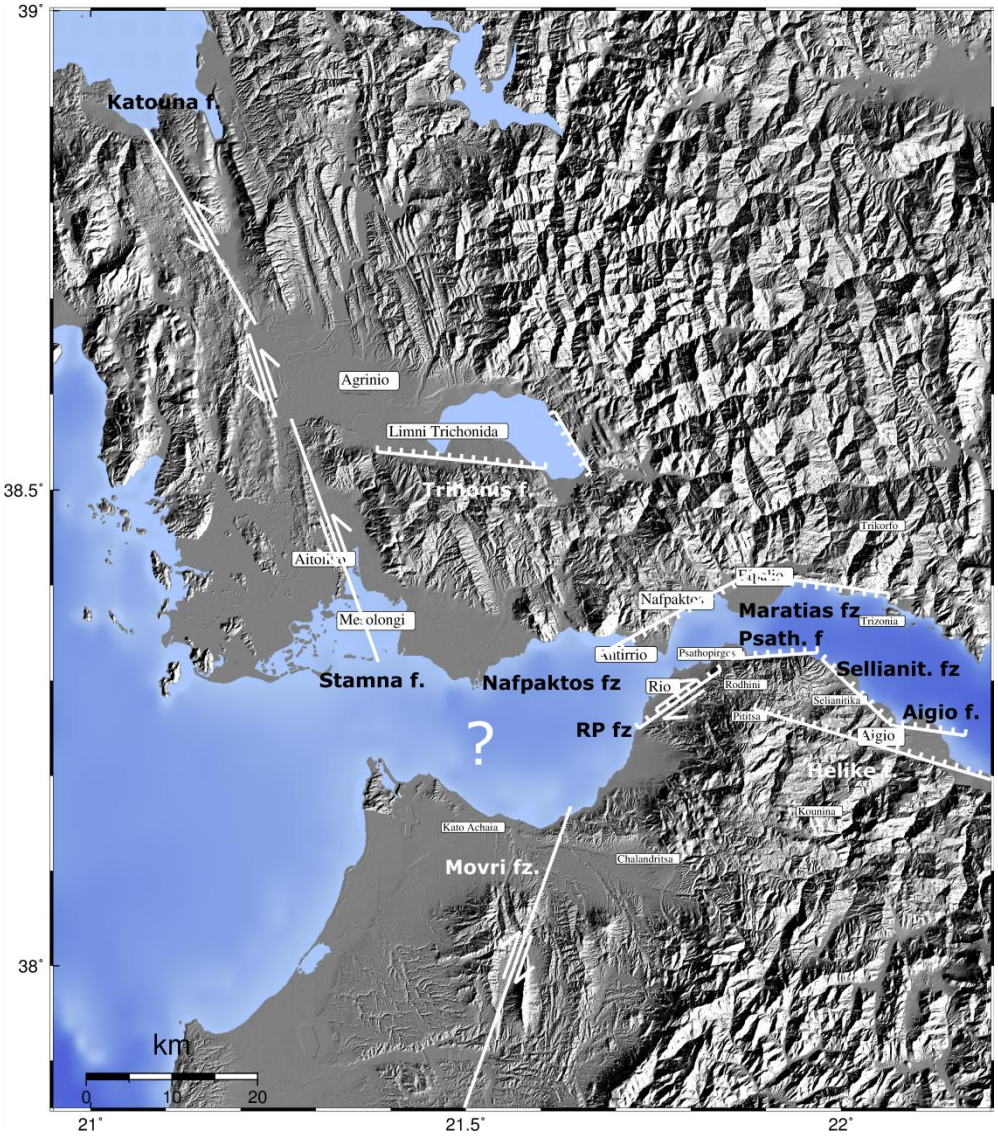

Figure 7-1. The dashed lines indicate the radians of the triple junction. The onshore discontinuities have been investigated in the thesis.

The arrival of the new high resolution SAR sensors as RADASAT-2, Cosmo-SkyMed but mainly TerraSAR-X, (because of more opportunities for data provision to the scientific community), with different incidence angles than the usual I2 mode of ~23° of ASAR/ENVISAT will make

the discrimination of the Cartesian components more imperative, neglecting the difficulty of acquiring both passages at the same area, the same date range.

The city of Patras is suffering from uplifting blocks and localized subsidence. As forth mentioned these occurred in motion of shallow structures and not reaching the microplate boundaries. All the observed discontinuities have been detected and discussed. Rion-Patras fault zone is a highly active creeping oblique fault, dipping North, with many local discontinuities on its hangingwall striking NNW and NW of unknown origin.

Some possible landslides and creeping slopes were visible even if they were limited to a small spatial extent. Deformation caused by riverine sediments seems to be detectable by temporal InSAR.

All the deltas around the Western GoC are subsiding fast, with their rates to increase intensively towards the coast, except the one in Aigion. Indeed the only intensively subsiding block of it, is the one that is located in the hangingwall of the Aigion fault. The rest, located in the footwall, does not subside due to the equilibrium of the tectonic uplifting. On the contrary, it is uplifting with a rate a bit smaller than the city and near the suburbs of Aigion. Many faults lie inside the observed Deltas. Their subsidence component due to the compaction of their old sentiments is added to the tectonic one. From the cross sections we could discriminate the existence of these two mechanisms but not their values.

Our findings in Aigion fault, in Mornos Delta and inside the city of Patras have been compared with remote and insitu observations.

This study has given us many opportunities to advance the current work further and to extend it with more data and in more case studies. Thus, the proposed methodology will be enhanced, increasing the level of accuracy by considering some sources of noise defined also by this study. Additionally, it will be applied to Aetoliko area for the production of high accuracy deformation maps. It can also easily be applied to other areas where data is available.

The temporal evolution of the deformation in certain case studies will be further investigated, to isolate the slow deformation from the fast one (earthquake) and the artefacts.

Modelling of creeping faults (i.e. Rio-Patras, Aigion) will be performed to extract the locking depth and the slip rate.

Modelling will also be used to discriminate the deformation due to tectonics and sentiment compaction where applicable.

Acquisitions from new high resolution SAR sensors as RADASAT-2, Cosmo-SkyMed and TerraSAR-X will bring an extra asset for such applications. Such data is already available.

The interaction with seismologists and geologists will be strengthened and is welcome.

Landslides and creeping slopes which have been detected in the current study will be investigated further with very high resolution SAR data. Such data is already available.

8. Bibliography

Altamimi, Z., Angermann, D., Argus, D., et al. (2001). The terrestrial reference frame and the dynamic Earth. EOS, Transactions of the American Geophysical Union 82(25), pp. 273–279.

Altamimi, Z., Sillard, P., Boucher, C. (2002). ITRF2000: A new release of the international terrestrial reference frame for Earth science application. Journal of Geophysical Research 107(B10): 2214.

Amelung, F., Galloway, D.L., Bell, J.W., Zebker, H.A., Laczniack, R.J. (1999). Sensing the ups and downs of Las Vegas: InSAR reveals structural control of land subsidence and aquifer-system deformation. Geology 27, pp. 483–486.

Avallone, A. (2003). Analyse de dix ans de déformation du rift de Corinthe (Grèce) par géodésie spatiale. PhD Thesis. IPGP: France.

Berardino, P., Fornaro, G., Lanari, R., Sansosti, E. (2002). A new algorithm for surface deformation monitoring based on small baseline differential SAR interferograms. IEEE Transactions on Geoscience and Remote Sensing 40 (11), pp. 2375–2383.

Beutler, G., Drewes, H., Verdun, A. (2004). The new structure of the International Association of Geodesy (IAG) viewed from the perspective of history. Geodesist's Handbook. Journal of Geodesy 77, pp. 560–575.

Blewitt G.(2007). GPS and Space-Based Geodetic Methods. Geodesy: Treatise on Geophysics, Volume 3.11, Elsevier B.V.

Briole, P., Armijo, R., Avallone, A., Bernard, P., Charara, R., Deschamps, A., Dimitrov, D., Elias, P. , Grandin, R. , Ilieva, M., Lambotte, S., Lyon-Caen, H., Meyer, B., Mouratidis, A., Nercessian, A., Papanastassiou, D., Ruegg, J.C., Sokos, E., Sykioti, O. (2008). Multidisciplinary study of the June 8, 2008, Mw=6.4 Andravida earthquake. European Seismological Commission ESC 2008. Hersonissos, Crete, Greece. 7 - 12 September 2008.

Briole, P., De Natale, G., Gaulon, R., Pingue F., Scarpa, R. (1986). Inversion of geodetic data and seismicity associated with the Friuli earthquake sequence (1976-1977). Annales Geophysicae, 4, pp. 481-492.

Briole, P., Rigo, A., Lyon-Caen, H., Ruegg, J., Papazissi, K., Mitsakaki, K., et al. (2000). Active deformation of the Corinth rift, Greece: Results from repeated Global Positioning System surveys between 1990 and 1995. J. Geophys. Res. 2000, 105, pp. 25605–25625.

Casu, F., Manzo, M., Lanari R. (2006).A quantitative assessment of the SBAS algorithm performance for surface deformation retrieval from DInSAR data., Remote Sens. Environ., vol. 102, no. 3/4, pp. 195 -210.

Chen, C., Zebker, H. (2002). Phase unwrapping for large SAR interferograms: Statistical segmentation and generalized network models. IEEE Transactions on Geoscience and Remote Sensing, vol. 40, pp. 1709-1719.

Clarke, P., Davies, R., England, P., Parsons, B., Billiris, H., Paradissis, D., Veis, G., Denys, P., Cross, P., Ashkenazi, V., Bingley, R. (1997). Geodetic estimate of seismic hazard in the Gulf of Korinthos, Geophys. Res. Lett., 24(11).

Colesanti, C., Ferretti, A., Prati C.,Rocca, F. (2003). Monitoring landslides and tectonic motions with the Permanent Scatterers Technique. Engineering Geology 68 (2003), pp. 3–14.

Colesanti, C. and Wasowski, J. (2006). Investigating landslides with space-borne Synthetic Aperture Radar (SAR) interferometry. Engineering Geology 88 (2006) pp. 173-199.

Costantini, M., Malvarosa, F., Minati, F., Pietranera, L., Milillo, G. (2002). A three-dimensional phase unwrapping algorithm for processing of multitemporal SAR interferometric measurements. Proceedings of the IEEE International Geoscience and Remote Sensing Symposium (IGARSS 2002), Toronto (Canada), 24–28 June 2002, vol. 3, pp. 1741–1743.

Costantini, M., Lombardo, P., Malvarosa, F., Minati, F., Pastina, D., Pietranera, L. (2001) Analysis and correction of artifacts on differential SAR interferometry for the study of subsidence phenomena. IGARSS 2001.

Crosetto, M., Castillo, M., Arbiol, R. (2003). Urban subsidence monitoring using radar interferometry: Algorithms and validation. Photogrammetric Engineering and Remote Sensing 69 (7), pp. 775–783.

Ferretti, A., Fumagalli, A., Novali, F., Prati, C., Rocca, F., Rucci, A. (2011). A New Algorithm for Processing Interferometric Data-Stacks: SqueeSAR. IEEE Transactions on Geoscience and Remote Sensing, vol.49, no.9, pp.3460,3470.

Franceschetti, G., Lanari, R. (1999). Synthetic aperture radar processing. CRC Press, Boca Raton.

Elias , P., Sykioti, O., Kontoes, C., Avallone, A., Van Gorp, S., Briole, P., Paradissis, D. (2006). A method for rapid elimination of high frequency signal noise and unwrapping artefacts from interferometric calculation. International Journal of Remote Sensing, Vol. 27, Issue 14, pp. 3079 - 3086.

Duro, J., Inglada, J., Closa, J., Adam, N., Arnaud, A. (2003). High Resolution Differential Interferometry Using Time Series of ERS and Envisat SAR Data. Proceedings of the third International Workshop on ERS SAR Interferometry (FRINGE 2003). Frascati (Italy), 2–5 December 2003.

Ekstrom, G., Dziewonski, A.M., Maternovskaya, N.N. & Nettles, M. (2005). Global seismicity of 2003: centroid-moment-tensor solutions for 1087 earthquakes. Phys. Earth planet. Inter., 148(2–4), pp. 327–351.

Elias, P., Briole, P.,Sykioti, O. (2008) PALSAR/ALOS interferometry in the Gulf of Corinth and Patras (Greece). Comparison with ERS and ASAR/ENVISAT results and GPS measurements, ALOS 2008 PI Symposium, Rhodes, Greece, November 3 - 7, 2008.

Elias, P., Kontoes, C., Papoutsis, I., Kotsis, I., Sakellariou, D., Marinou, A. and Paradissis D. (2009). Permanent Scatterer InSAR analysis and validation in the Gulf of Corinth. Sensors, vol. 9(1), pp. 46-55.

Ferretti, A., Prati, C., Rocca, F. (2000). Nonlinear subsidence rate estimation using Permanent Scatterers in Differential SAR Interferometry. IEEE Transactions on Geoscience and Remote Sensing 38 (5), pp. 2202–2212.

Ferretti, A., Prati, C., Rocca, F. (2001). Permanent Scatterers in SAR Interferometry. IEEE Transactions on Geoscience and Remote Sensing 39 (1), pp. 8–20.

Flotte, N., Sorela, D., Mullerm, C., Tensic, J. (2005). Along strike changes in the structural evolution over a brittle detachment fault: Example of the Pleistocene Corinth–Patras rift (Greece). Techtonophysics, 403, pp. 77– 94.

Ford, M., Boiselet, A., Meyer, N., Lambotte, S., Scotti, O., Lyon-Caen, H., Briole, P., Caumon, G., Bernard, P. (2013). Distribution of deformation on an active normal fault network, NW Corinth rift, EGU Geneal Assembly, 1-5 April, 2013, Vienna, Austria.

Fruneau, B., Rudant, J.-P., Obert, D., Raymond, D. (1999). Small displacements detected by SAR Interferometry in the city of Paris (France). Proc. IGARSS'99, Hamburg, Germany, 28 June - 2 July 1999, pp. 1943-1945.

Ganas, A., Serpelloni, E., Drakatos, G., Kolligri, M., Adamis, I., Tsimi, Ch.,Batsi, E. (2009). The Mw 6.4 SW Achaia (Western Greece) Earthquake of 8 June 2008: Seismological, Field, GPS Observations, and Stress Modeling. Journal of Earthquake Engineering, 13, pp.8, 1101 — 1124.

Gianniou, M. (2011). Detecting permanent displacements caused by earthquakes using data from the HEPOS network. EUREF 2011 Symposium, May 25-28 2011, Chisinau, Moldova.

Gourmelen, N., Amelung, F. (2005). Post-seismic mantle relaxation in the Central Nevada Seismic. Science 310, pp. 1473–1476.

Hammond, WC. (2005). The ghost of an earthquake. Science 310, pp. 1440–1442.

Hanssen, R. (2001) Radar Interferometry and Error Analysis Kluwer Academic Publisher, New York Boston.

Herring T.(2007). Geodesy, Treatise on Geophysics, Volume 3.11, Elsevier B.V.

Hetland, E., Hager, B. (2003). Postseismic relaxation across the Central Nevada Seismic Belt. Journal of Geophysical Research 108: 2394.

Hetland, E., Hager, B. (2006.) The effect of rheological layering on postseismic and interseismic displacements. Geophysical Journal International 166, pp. 277–292.

Hooper, A., Zebker, H., Segall, Kampes, B. (2004). A new method for measuring deformation on Volcanoes and other natural terrains using InSAR persistent scatterers. Geophysical Research Letters 31.

Hooper, A. (2006). Persistent Scatterer Radar Interferometry for Crustal Deformation Studies and Modeling of Volcanic Deformation. PhD Thesis, Stanford University, U.S.A.

Hooper, A., Segall, P., Zebker, H. (2007). Persistent Scatterer InSAR for Crustal Deformation Analysis, with Application to Volcán Alcedo, Galápagos. J. Geophys. Res., 112, B07407.

Hooper, A. (2008). A multi-temporal InSAR method incorporating both persistent scatterer and small baseline approaches. Geophys. Res. Letters, 35.

Hooper A., (2010). Bayesian inversion of wrapped InSAR data for geophysical parameter estimation. Proceedings ESA Living Planet Symposium, Bergen 2010.

Ilieva, M.(2011). Crustal deformations of shallow earthquakes in the Eastern Mediterranean studied by radar interferometry and seismology. PhD Thesis, Ecole Normale Superieure, Paris, France.

Jackson, J.A., D. McKENZIE (1984). Active tectonics of the Alpine-Himalayan belt between Western Turkey and Pakistan. Geophys. J. R. Astron. Soc., 77, pp. 185-264.

Jackson, J., McKenzie, D. (1988). The relationship between plate motions and seismic tremors, and the rates of active deformation in the Mediterranean and Middle East Geophys. J. R. Astron. Soc., 93, pp. 45-73.

Jestin F., Huchon, P., Gaulier, J.M. (1994). The Somalia Plate and the East African rift system: Present-day kinematics, International Geophysical Journal, pp. 116,637-654.

Kalteziotis, N., Koukis, G., Tsiambaos, G., Sabatakakis, N., Zervogiannis, H. (1991). Structural Damage in a Populated Area due to an Active Fault. 2nd International Conference on Recent Advances in Geotechnical Earthquake Engineering and Soil Dynamics, March 11-15, 1991, St. Louis, Missouri.

Kampes, B., M. (2005). Displacement parameter estimation using permanent scatterer Interferometry. Ph.D. Thesis. Delft University of Technology, Holland.

Van der Kooij, M., Hughes, W., Sato, S., Poncos, V. (2006). Coherent target monitoring at high spatial density: Examples of validation results. Eur. Space Agency Spec. Publ., SP-610.

Van der Kooij, M. (1999). Engineering geology landslide investigations and SAR Interferometry. Proceedings of FRINGE'99, Liege, Belgium

Van der Kooij, M. (2003). Coherent target analysis. Proceedings of the third International Workshop on ERS SAR Interferometry (FRINGE 2003), Frascati (Italy), 2–5 December 2003.

McKenzie, D.P. (1970). Plate tectonics of the Mediterranean region, Nature, 226, pp. 239-243.

Kiratzi, A., Sokos, E., Ganas, A., Tselentis, A., Benetatos, C., Roumelioti, Z., Serpetsidaki, A., Andriopoulos, G., Galanis, O., Petrou, P. (2008). The April 2007 earthquake swarm near Lake Trichonis and implications for active tectonics in western Greece Tectonophysics 452, pp. 51–65.

Koukis, G., Sabatakakis, N.,Ferentinou, M., Lainas, S., Alexiadou, X., Panagopoulos, A. (2009). Landslide phenomena related to major fault tectonics: rift zone of Corinth Gulf, Greece. Bull Eng Geol Environ 68, pp. 215–229.

Koukis, G., Sabatakakis, N., Tsiambaos, G., Katrivesis, N. (2005). Engineering geological approach to the evaluation of seismic risk in metropolitan regions: case study of Patras, Greece. Bulletin of Engineering Geology and the Environment, Vol. 64, 3, pp. 219-235.

Kreemer, C., Blewitt, G., Maerten, F. (2006). Co- and postseismic deformation of the 28 March 2005 Nias Mw 8.7 earthquake from continuous GPS data. Geophysical Research Letters 33: L07307.

Lambeck, K. (1988). Geophysical geodesy: The slow deformations of the Earth. Oxford, UK: Clarendon Press.

Lanari, R., Mora, O., Manunta, M., Mallorqui, J.J., Berardino, P., Sansosti, E. (2004). A small baseline approach for investigating deformations on full resolution Differential SAR Interferograms. IEEE Transactions on Geoscience and Remote Sensing 42, pp. 1377–1386.

Li, F.K., Goldstein, R.M. (1990). Studies of multibaseline spaceborne interferometric synthetic aperture radars. Geoscience and Remote Sensing, IEEE Transactions on, 28(1): pp. 88-97.

Lyons, S., Sandwell, D. (2003). Fault creep along the southern San Andreas from Interferometric synthetic aperture radar, permanent scatterers, and stacking, Journal of Geophysical Research, 108 (B1), pp. 2047 – 2070.

Massonnet, D., Briole, P., Arnaud, A. (1995). Deflation of Mount Etna monitored by Spaceborne Radar Interferometry. Nature 375, pp. 567–570.

Massonnet, D., Feigl, K.L. (1998). Radar Interferometry and its application to changes in the Earth's surface. Review of Geophysics 36, pp. 441–500.

DeMets, C., Gordon, R.G., Argus, D.F., Stein, S. (1990). Current plate motions. Geophys. J. Int., 101, pp. 425-478.

Le Mouélic, S., Raucoules, D., Carnec, C., King, C. (2003). A least square adjustments of multitemporal InSAR data: application to the ground deformation of Paris. Photogrammetric Engineering and Remote Sensing 71 (2), pp. 197–205.

Muller, M.D.M. (2011). Analysis of long-term GPS observations in Greece (1993–2009) and geodynamic implications for the Eastern Mediterranean. PhD Thesis. ETH, Switcherland.

Okada, Y., (1985). Surface deformations due to shear and tensile faults in a half-space, Bull. Seism. Soc. Am., pp. 1135-1154.

Palyvos, N., Pantosti, D., Stamatopoulos, L., De Martini, P. (2007). Geomorphological Reconnaissance of the Psathopyrgos and Rion-Patras fault zones (Achaia, NW Peloponnesus). Bulletin of the Geological Society of Greece vol. XXXX, Proceedings of the 11th International Congress, pp. 1586-1598, Athens, May, 2007.

Papadopoulos, G.,Karastathis, V., Kontoes, C., Charalampakis, M., Fokaefs, A., Papoutsis, I. (2010). Crustal deformation associated with east Mediterranean strike–slip earthquakes: The 8 June 2008 Movri (NW Peloponnese), Greece, earthquake (M_w6.4). Tectonophysics 492 (2010), pp. 201–212.

Parcharidis I., Kokkalas, S., Fountoulis, I., Foumelis, M. (2009). Detection and Monitoring of Active Faults in Urban Environments: Time Series Interferometry on the Cities of Patras and Pyrgos (Peloponnese, Greece). Remote Sens. 1, pp. 676-696.

Parcharidis, I., Kourkouli, P., Karymbalis, E., Foumelis, M., Karathanassi V. (2013). Time Series Synthetic Aperture Radar Interferometry for Ground Deformation Monitoring over a Small Scale Tectonically Active Deltaic Environment Mornos, Central Greece). Journal of Coastal Research: Volume 29, Issue 2: pp. 325 – 338.

Perouge, E., Sebrier, M., Braucher, R., Chamot-Rooke, N., Bourles, D., Briole, P., Sorel, D., Dimitrov, D., Arsenikos, S. (2013). Transition from collision to subduction in Western Greece : The Katouna-Stamna active fault system. Submitted to Terra Nova.

Pollitz, F. (1997). Gravitational-viscoelestic postseismic relaxation on a layered spherical Earth. Journal of Geophysical Research 102: pp. 17921–17941.

Reilinger, R., Toksoz, N., King, R., McClusky, S., Jestin F., Huchon, P., Gaulier, J.M. (1994). The Somalia Plate and the East African rift system: Present-day kinematics, Geophys. J. Int., 116, pp. 637-654.

Rigo, A., Lyon-Caen, H., Armijo, R., Deschamps, A., Hatzfeld, D., Makropoulos, K., Papadimitriou, P., Kassaras, I. (1996). A microseismic study in the western part of the Gulf of Corinth (Greece): implications for large-scale normal faulting mechanisms. Geophysical Journal International 126 (3), pp. 663–688.

Rosen, P. A., Hensley, S., Zebker, H.A., Webb, F.H., Fielding, E.J. (1996). Surface deformation and coherence measurements of Kilauea Volcano, Hawaii from SIR-C radar interferometry. J. Geophys. Res., 101, 23, pp. 109-123,125.

Rosen, P.A., Henley, S., Peltzer, G., Simons, M. (2004). Updated repeat orbit interferometry package released. EOS, Trans. Am. geophys. Un., 85(5), 47.

Royden, L. (1993). The tectonic expression of slab pull at continental convergent boundaries. Tectonics, 12, pp. 303-325.

Smith, D., Turcotte D. (eds.) (1993) Geodynamics Series Vol. 25: Contributions of Space Geodesy to Geodynamics: Technology. (ISBN 0-87590-526-9), Washington, DC: American Geophysical Union.

Schmidt, A., Burgmann, R. (2003). Time-dependent land uplift and subsidence in the santa clara valley, california, from a large interferometric synthetic aperture radar data set, Journal of Geophysical Research, 108 (B9), ETG4 – 1.

Stamatopoulos, L., Kontopoulos, N., Voltaggio, M., Branca, M. (2004). Radiochronological data with U/Th method in lagoonal/marine deposits of the NW Peloponnese, Greece. Bull. Geol. Soc. Greece, XXXVI, pp. 1064-1067 (in Greek).

Sonder, L., England, P. (1989). Effects of temperature dependent rheology on large-scale continental extension, J. Geophys. Res., g4, pp. 7603-7619.

Sokos, E., Zahradnik, J., Kiratzi, A., Jansky, J., Gallovic, F., Novotny, O., Kostelecky, J., Serpetsidaki, A., Tselentis, G.-A., (2012).The January 2010 Efpalio earthquake sequence in the western Corinth Gulf (Greece). Tectonophysics 530-531, pp. 299–309.

Stein, S., Wysession, T. (2003). Introduction to Seismology, Earthquakes, and Earth Structure. Blackwell Publishing.

Sykioti, O., Kontoes, C., Elias, P., Sachpazi, M., Paradissis, D. and Kotsis, I., (2003). Ground deformation at Nisyros volcano (Greece), detected by ERS2 SAR differential interferometry. International Journal of Remote Sensing, 24(1), pp. 183-188.

Torge, W. (2001). Geodesy, 3rd edn. Berlin, Germany: Walter de Gruyter.

Tarantola, A., Valette B., (1982). Generalized nonlinear inverse problem solved using the least squares criterion, Rev. Geophys. Space Phys., 20, pp. 219-232.

Usai, S. (2002). A least-squares approach for long-term monitoring of deformations with differential SAR interferometry. Proceedings of the IEEE International Geoscience and Remote Sensing Symposium (IGARSS 2002), Toronto (Canada), 24–28 June 2002, vol. 2, pp. 1247–1250.

Usai, S. (2003). A least squares database approach for SAR interferometric data. *IEEE* Transactions on Geoscience and Remote Sensing, 41 (4), pp. 753–760.

Ward, S., Valensise, G. (1989). Fault parameters and slip distribution of the 1915, Avezzano, Italy earthquake derived from geodetic observations. Bull. Seismol. Soc. Amer., 79, pp. 690–710.

Werner, C., Wegmuller, U., Strozzi, T., Wiesmann, A., (2003). Interferometric Point Target Analysis for Deformation Mapping. Proceedings of the IEEE International Geoscience and Remote Sensing Symposium (IGARSS 2003). Toulouse (France), 21–25 July 2003, vol. 7, pp. 4362–4364.

Werner, C., Wegmuller, U., Wiesmann, A., Strozzi, T., (2003). Interferometric Point Target Analysis with JERS-1 L-band SAR Data. Proceedings of the IEEE International Geoscience and Remote Sensing Symposium (IGARSS 2003). Toulouse (France), 21–25 July 2003, vol. 7, pp. 4359 - 4361 vol.7.

Zebker, H., Rosen P., Goldstein R., Gabriel A., Werner, C., (1994). On the derivation of coseismic displacement fields using Differential Radar Interferometry: the Landers earthquake. Journal of Geophysical Research 99 (B10), pp. 19617–19634.

Zebker, H., Goldstein, R. (1986). Topographic mapping from interferometer synthetic aperture radar observations. Journal of Geophysical Research v91 issue B5, pp. 4993–4999.

Zebker H., Illasenor J. (1992). Decorrelation in Interferometric Radar Echoes, IEEE Transactions on Geoscience and Remote Sensing, 30(5), pp. 950-959.

9. Index